Investigating gene regulatory networks in aortic arch artery development

Catherine Ann Stothard

Submitted in accordance with the requirement for the degree of

Doctor of Philosophy

Institute of Genetic Medicine

Newcastle University

February 2020

Abstract

Developmental defects to the heart and aortic arch arteries are a leading cause of morbidity and occur in 22q11 deletion syndrome (22q11DS) patients. Formation of the aortic arch arteries requires the remodelling of the pharyngeal arch arteries (PAA) which depends on regulated gene expression and the interaction of multiple tissues. *TBX1* has been identified as a leading causative gene in 22q11DS, however, the wide spectrum of defects present in 22q11DS patients suggests that modifier genes may contribute to this phenotypic variation. *Tbx1*, *Pax9* and *Gbx2*, all independently required for cardiovascular development, are co-expressed in the pharyngeal endoderm, a tissue that provides signalling cues during PAA morphogenesis. *Tbx1* and *Pax9* genetically interact and *Gbx2* is downregulated in both *Tbx1*-null and *Pax9*-null mice. The aim of this project was to establish the *Gbx2*-null phenotype and investigate a potential interaction between *Gbx2* and *Pax9* in the pharyngeal endoderm during cardiovascular development.

Gbx2-null mouse embryos presented with 4th PAA-derived defects, such as right aortic arch, as well as outflow tract defects. *Pax9*$^{+/-}$;*Gbx2*$^{+/-}$ mice were crossed to study the interaction between these genes by generating embryos with complex genotypes. The presentation of cardiovascular defects in *Pax9*$^{+/-}$;*Gbx2*$^{+/-}$ mice showed a strong genetic interaction. Likewise, *Pax9* heterozygosity modified the *Gbx2*-null phenotype, both increasing the penetrance of defects and causing the presentation of additional abnormalities. Conditionally deleting *Gbx2* from the endoderm concomitantly with the heterozygous deletion of *Pax9* resulted in cardiovascular defects, highlighting the pharyngeal endoderm as a key tissue in PAA morphogenesis and remodelling.

Mouse models were used to study a potential *Tbx1-Pax9-Gbx2* genetic network in cardiovascular development. *In vitro* models were used to investigate the interaction of *Tbx1* and *Pax9* with the *Gbx2* coding region. The data presented in this thesis suggests that a *Tbx1-Pax9-Gbx2* genetic network exists within the pharyngeal endoderm to control PAA morphogenesis.

Acknowledgments

I would first like extend my sincere gratitude to my supervisor Dr Simon Bamforth for providing the opportunity to perform this research and the continuous guidance and encouragement throughout my PhD project. I would also like to thank my supervisor Professor Deborah Henderson for her expertise and support in this project. Additionally, I would like to thank Dr Helen Phillips and Dr Colin Miles for their valuable comments regarding my research.

I am thankful to the past and present members of the cardiovascular research group for all their help in the lab and practical advice. I am extremely grateful to Dr Kate Bailey, Dr Ramada Khasawneh and Dr Silvia Mazzotta for teaching me during the initial stages of my PhD, with extra special thanks to Kate for having to put up with my questions for the longest! I am grateful to the undergraduate and postgraduate students that have contributed to this project while working alongside me.

I would like to extend my thanks to all the staff at the Institute of Genetic Medicine for the amazing work they do and all the help they have given me for the past three years.

To my friends within the Institute of Genetic Medicine (and the worst “weekly” ice cream club that has ever existed), thank you for providing encouragement and entertainment during my PhD. Thank you to Emily, Kate, Lauren and everyone in the lunchtime crew for making the past three years so enjoyable.

Finally, I would like to thank my parents, Ann and Keith Stothard, for their endless love, support and inspiration.

Table of Contents

Abstract iii

Acknowledgments v

Table of Contents vii

Abbreviations xii

List of Figures xv

List of Tables xix

Chapter 1. Introduction 1

1.1 Cardiovascular development 1

1.1.1 Cardiac neural crest cells 4

1.1.2 The outflow tract 6

1.2 Development of the aortic arch arteries 6

1.2.1 Development and remodelling of the pharyngeal arch arteries 6

1.2.2 The pharyngeal arches 9

1.2.3 Derivative of the pharyngeal arches 11

1.2.4 The role of the pharyngeal endoderm 12

1.3 Signalling pathways in cardiovascular development 13

1.3.1 Notch signalling 13

1.3.2 Fibroblast growth factor signalling 14

1.3.3 Sonic hedgehog signalling 14

1.3.4 Bone morphogenetic protein signalling 15

1.3.5 Wnt signalling 15

1.4 Congenital heart defects 16

1.4.1 22q11 deletion syndrome 20

1.5 Left-right patterning 22

1.6 *Tbx1* 25

1.6.1 The T-box gene family 25

1.6.2 Tbx1 in 22q11 deletion syndrome and cardiovascular development 26
1.7 *Pax9* 31
1.7.1 The paired box gene family 31
1.7.2 Pax9 in cardiovascular development 34
1.8 *Gbx2* 37
1.8.1 The gastrulation homeobox gene family 37
1.8.2 Gbx2 in cardiovascular development 38
1.9 Aims and hypothesis 42
Chapter 2. Materials and Methods 45
2.1 Mouse strains and breeding 45
2.1.1 Gbx2 mice 45
2.1.2 Pax9 mice 46
2.1.3 Pax9Cre mice 47
2.1.4 Tbx1 mice 47
2.1.5 eYFP mice 47
2.1.6 lacZ mice 48
2.2 Embryo dissection 48
2.3 Genotyping 48
2.3.1 DNA extraction 48
2.3.2 Polymerase Chain Reaction 49
2.4 Histology 52
2.4.1 Embryo embedding and sectioning 52
2.4.2 Haematoxylin and eosin staining 54
2.5 Imaging 54
2.5.1 Magnetic resonance imaging 54
2.5.2 High Resolution Episcopic Microscopy 55
2.6 Ink injection 55
2.7 Whole mount *in situ* hybridisation 55

2.7.1 Probe digoxygenin labelling 55
2.7.2 Hybridisation 57
2.8 Immunohistochemistry 58
2.9 RNAScope 59
2.10 Whole mount lacZ Stain 61
2.11 Quantitative Polymerase Chain Reaction of flow sorted cells 61
2.11.1 Cell dissociation and flow sort 62
2.11.2 RNA extraction 63
2.11.3 cDNA synthesis 63
2.11.4 Quantitative polymerase chain reaction 64
2.12 Luciferase Assays 65
2.12.1 JEG3 Cell Culture 65
2.12.2 Luciferase Assays 65
2.12.3 Chromatin Immunoprecipitation Assays 68
2.14 Statistical analysis 70
2.14.1 Chi-squared test 70
2.14.2 Unpaired t-test and one-way ANOVA 71
Chapter 3. Investigating the role of *Gbx2* in cardiovascular development 72
3.1 Introduction 72
3.2 *Gbx2*$^{-/-}$ embryos are underrepresented during development 74
3.3 The *Gbx2*$^{-/-}$ phenotype 74
3.4 Left-right patterning defects in *Gbx2*$^{-/-}$ embryos 81
3.5 Pharyngeal arch artery formation and remodelling in *Gbx2*$^{-/-}$ embryos 88
3.6 Endothelial cell contribution to the pharyngeal arch arteries in *Gbx2*$^{-/-}$ embryos 90
3.7 Discussion 91
Chapter 4. Investigating the *Pax9-Gbx2* interaction during cardiovascular development 98

4.1 Introduction 98
4.2 *Pax9* and *Gbx2* expression *in vivo* 99
4.3 Analysis of the *Pax9/Gbx2* genotypes 105
4.4 The *Pax9*$^{+/-}$;*Gbx2*$^{+/-}$ phenotype 107
4.5 *Pax9* heterozygosity modifies the *Gbx2*$^{-/-}$ phenotype 112
4.6 *Gbx2* heterozygosity modifies the *Pax9*$^{-/-}$ phenotype 123
4.7 Outflow tract defects in complex *Pax9;Gbx2* mutants 130
4.8 Discussion 136
Chapter 5. Investigating the role of *Pax9* and *Gbx2* in the pharyngeal endoderm 140
5.1 Introduction 140
5.2 Validating the *Pax9Cre* allele 141
5.3 The role of *Pax9* and *Gbx2* in the pharyngeal endoderm 144
5.4 Discussion 151
Chapter 6. Investigating the potential *Tbx1-Pax9-Gbx2* genetic network 155
6.1 Introduction 155
6.2 *Tbx1*, *Pax9* and *Gbx2* expression *in vivo* 156
6.3 *Gbx2* heterozygosity does not modify the *Tbx1*$^{+/-}$ phenotype 159
6.4 *Gbx2* heterozygosity does not modify the *Tbx1*$^{+/-}$;*Pax9*$^{+/-}$ phenotype 161
6.5 Investigating the interaction of TBX1 and PAX9 with the *Gbx2* conserved region 163
6.6 Discussion 169
Chapter 7. Final Discussion 174
7.1 Summary of findings and future work 174
7.1.1 Gbx2 as a modifier of 22q11 deletion syndrome 174
7.1.2 The Pax9-Gbx2 interaction in the pharyngeal endoderm 175
7.1.3 The Tbx1-Pax9-Gbx2 network 177
7.1.4 The sensitivity of the 4th pharyngeal arch artery 177

7.1.5 The cause of the 4th PAA defects in Gbx2-/- mice 179
7.2 Conclusion 180
References 194

Abbreviations

22q11DS	22q11 deletion syndrome
ALSA	Aberrant left subclavian artery
ARSA	Aberrant right subclavian artery
AV	Atrioventricular
AVSD	Atrioventricular septal defect
BA	Brachiocephalic artery
BE	Binding element
Bmp	Bone morphogenetic protein
Bp	Base pair
BSA	Bovine serum albumin
CAT	Common arterial trunk
CC	Common carotid arteries
CCTGA	Congenitally corrected transposition of the great arteries
CHD	Congenital heart defects
ChIP	Chromatin immunoprecipitation
CoAoA	Cervical aortic arch
CoRSA	Cervical origin of the right subclavian artery
CRKL	CRK like proto-oncogene
CS	Carnegie stage
CV	Cardiovascular
dAo	Dorsal aorta
ddH2O	Deionised water
DEPC	Diethyl pyrocarbonate
DIG	Digoxygenin
DLA	Dual luciferase assay
DORV	Double outlet right ventricle
dTGA	Dextra-transposition of the great arteries
EDTA	Ethylenediamine tetra-acetic acid
EMT	Epithelial-to-mesenchymal transition

ERG	ETS-related gene
eYFP	Enhanced yellow fluorescent protein
FBS	Fetal bovine serum
Fgf	Fibroblast growth factor
Gbx	Gastrulation brain homeobox
GpDTPA	Gadopentetate dimeglumine
Hh	Hedgehog
HREM	High resolution episcopic microscopy
H&E	Haematoxylin and eosin
IAA	Interrupted aortic arch
ICV	Inferior caval vein
IHC	Immunohistochemistry
IP	Immunoprecipitation
IRSA	Isolated right subclavian artery
Isa	Intersegmental arteries
IVC	Interventricular communication
kb	Kilobase pair
kDa	Kilodaltons
LCC	Left common carotid artery
LCRs	Low copy repeats
LLPM	Left lateral plate mesoderm
LPM	Lateral plate mesoderm
L-R	Left-right
LSA	Left subclavian artery
LV	Left ventricle
Mb	Million base pair
MRI	Magnetic resonance imaging
NCC	Neural crest cells
NICD	Notch intracellular domain
OFT	Outflow tract

PA	Pharyngeal arch
PAA	Pharyngeal arch artery
Pax	Paired box
PBS	Phosphate buffered saline
PCR	Polymerase chain reaction
PFA	Paraformaldehyde
PHF	Primary heart field
PI	Propidium iodide
Pitx2	Paired-like homeodomain transcription factor 2
PSE	Pharyngeal surface ectoderm
PT	Pulmonary trunk
qPCR	Quantitative polymerase chain reaction
RAA	Right aortic arch
RAD	Right arterial duct
RCC	Right common carotid artery
RE-RSA	Retro-oesophageal right subclavian artery
RSA	Right subclavian artery
RV	Right ventricle
SCV	Superior caval vein
SHF	Second heart field
Shh	Sonic hedgehog
Tbx	T-box
TGA	Transposition of the great arteries
Tgf	Transformation growth factor
TSA	Tyramide signal amplification
vgo	Van gogh
VR	Vascular ring
VSD	Ventricular septal defect
Wnt	Wingless/Int

List of Figures

Figure 1.1. Schematic overview of cardiovascular development in mouse. 4
Figure 1.2. Migration of cardiac neural crest cells at mid-embryogenesis. 5
Figure 1.3. Structure of the pharyngeal arch arteries and mature aortic arch. 8
Figure 1.4. Remodelling of the pharyngeal arch arteries to the aortic arch. 9
Figure 1.5. Structure of the pharyngeal arches. 10
Figure 1.6. Schematic showing double outlet right ventricle with an interventricular communication. 17
Figure 1.7. Defects derived from the abnormal development of the 4th pharyngeal arch artery. 19
Figure 1.8. The 22q11.2 deletion region. 21
Figure 1.9. Schematic diagram of the left-right body asymmetry and patterning defects. 23
Figure 1.10. Genetic pathway in left-right patterning. 25
Figure 1.11. Pharyngeal arch and pharyngeal arch artery defects in *Tbx1*-null mice. 27
Figure 1.12. Non-cardiovascular defects present in *Pax9*$^{-/-}$ mice. 34
Figure 1.13. Cardiovascular and pharyngeal arch artery defects in *Pax9*-null mice. 35
Figure 1.14. *Tbx1* and *Pax9* interact in the pharyngeal endoderm during cardiovascular development. 37
Figure 1.15. Graphical hypothesis. 42
Figure 2.1. Schematic diagrams of the *Gbx2* alleles. 46
Figure 2.2. Schematic diagrams of the *Pax9* alleles. 46
Figure 2.3. Schematic diagrams of the *Pax9Cre* allele. 47
Figure 2.4. Schematic showing the experiment plan for qPCR analysis of the pharyngeal arch cells. 62
Figure 3.1. Cardiovascular defects present in *Gbx2*$^{-/-}$ embryos at E15.5. 75
Figure 3.2. Mirror image aortic arch defect present in *Gbx2*$^{-/-}$ embryos. 77
Figure 3.3. Vascular ring defect present in *Gbx2*$^{-/-}$ embryos. 78
Figure 3.4. Transposition of the great arteries present in a *Gbx2*$^{-/-}$ embryo. 79
Figure 3.5. Schematic diagram of the *Gbx2* mouse constructs. 81
Figure 3.6. Left-right patterning defects in *Gbx2*$^{-/-}$ embryos at E15.5. 84

Figure 3.7. HREM reconstructions showing the PAA structure at E10.5 and E11.5 in *Gbx2*$^{-/-}$ embryos. 86
Figure 3.8. *Pitx2* expression in *Gbx2*$^{-/-}$ embryos at E8.5. 87
Figure 3.9. 4th pharyngeal arch artery defects in *Gbx2*$^{-/-}$ embryos at E10.5. 89
Figure 3.10. Endothelial cell disorganisation in *Gbx2*$^{-/-}$ embryos. 90
Figure 3.11. Fate of *Gbx2*$^{-/-}$ embryos. 97
Figure 4.1. Whole mount *in situ* hybridisation for *Pax9* and *Gbx2*. 100
Figure 4.2. *Pax9* and *Gbx2* are expressed within the pharyngeal endoderm. . 101
Figure 4.3. *Gbx2* expression within the pharyngeal arches of *Pax9*$^{-/-}$ embryos at E9.5. 102
Figure 4.4. *Pax9* expression within the pharyngeal arches of *Gbx2*$^{-/-}$ embryos at E9.5. 104
Figure 4.5. Possible genotypes obtained from *Pax9*$^{+/-}$;*Gbx2*$^{+/-}$ cross and key comparisons made in each experiment. 105
Figure 4.6. Cardiovascular defects in *Pax9*$^{+/-}$;*Gbx2*$^{+/-}$ neonates. 108
Figure 4.7. Cardiovascular defects present in *Pax9*$^{+/-}$*Gbx2*$^{+/-}$ embryos. 109
Figure 4.8. 4th pharyngeal arch artery defects in *Pax9*$^{+/-}$;*Gbx2*$^{+/-}$ mice at E10.5. 111
Figure 4.9. Cardiovascular defects present in *Pax9*$^{+/-}$;*Gbx2*$^{-/-}$ neonate. 113
Figure 4.10. *Pax9*$^{+/-}$;*Gbx2*$^{-/-}$ embryos showed cardiovascular defects also present in *Gbx2*$^{-/-}$ embryos. 114
Figure 4.11. Transposition of the great arteries and left-right patterning defects in a *Pax9*$^{+/-}$;*Gbx2*$^{-/-}$ embryo. 115
Figure 4.12. *Pax9*$^{+/-}$;*Gbx2*$^{-/-}$ embryos had defects typical of *Pax9*$^{-/-}$ embryos. .. 117
Figure 4.13. *Pax9*$^{+/-}$;*Gbx2*$^{-/-}$ embryos had thymus defects. 120
Figure 4.14. *Pax9*$^{+/-}$;*Gbx2*$^{-/-}$ embryos do not have cleft palate. 121
Figure 4.15. 4th pharyngeal arch artery defects in *Pax9*$^{+/-}$;*Gbx2*$^{-/-}$ mice at E10.5. 122
Figure 4.16. Cardiovascular defects present in *Pax9*$^{-/-}$ and *Pax9*$^{-/-}$;*Gbx2*$^{+/-}$ neonates. 124
Figure 4.17. Cardiovascular defects present in *Pax9*$^{-/-}$;*Gbx2*$^{+/-}$ embryos. 125
Figure 4.18. Palate and thymus defects present in *Pax9*$^{-/-}$*Gbx2*$^{+/-}$ embryos. ... 127
Figure 4.19. Pharyngeal arch artery defects in *Pax9*$^{-/-}$;*Gbx2*$^{+/-}$ embryos compared to *Pax9*$^{-/-}$ embryos at E10.5. 128

Figure 4.20. 4th pharyngeal arch artery defects present in the *Pax9-/-;Gbx2-/-* embryo et E10.5. 131
Figure 4.21. Defects present in a *Pax9-/-;Gbx2-/-* mouse at P0. 132
Figure 4.22. Cardiovascular defects present in a *Pax9-/-;Gbx2-/-* E15.5 embryo. 133
Figure 4.23. Complex outflow tract defects present in *Pax9-/-;Gbx2+/-* embryos. 134
Figure 4.24. Partial common arterial trunk was present in complex *Pax9;Gbx2* mutants. 135
Figure 5.1. *Pax9Cre* is expressed in the pharyngeal arches from E8.5. 141
Figure 5.2. *Pax9Cre* is expressed within the pharyngeal endoderm. 142
Figure 5.3. qPCR analysis of flow-sorted pharyngeal endoderm cells. 143
Figure 5.4. *Pax9* deletion using the *Pax9Cre* allele recapitulates the *Pax9*-null phenotype. 144
Figure 5.5. *Gbx2* expression in the pharyngeal endoderm of conditional endoderm mutants. 145
Figure 5.6. Cardiovascular defects present in conditional endoderm mutants at E15.5. 146
Figure 5.7. 4th pharyngeal arch artery defects in *Gbx2f/-;Pax9Cre* mice at E10.5. 147
Figure 5.8. Cardiovascular defects in *Gbx2+/f;Pax9Cre* embryos at E15.5. 149
Figure 5.9. 4th pharyngeal arch artery defects in *Gbx2+/f;Pax9Cre* mice at E10.5. 150
Figure 6.1. *Tbx1, Pax9* and *Gbx2* expression in the pharyngeal arches at E9.5. 156
Figure 6.2. *Pax9* and *Gbx2* are downregulated in the pharyngeal endoderm of *Tbx1-/-* embryos. 157
Figure 6.3. *Tbx1* expression *Pax9-/-* and *Gbx2-/-* embryos at E9.5. 158
Figure 6.4. Cardiovascular defects present in *Tbx1+/-* and *Tbx1+/-;Gbx2+/-* embryos at E15.5. 160
Figure 6.5. Cardiovascular defects present in *Tbx1+/-;Pax9+/-* and *Tbx1+/-;Pax9+/-;Gbx2+/-* embryos at E15.5. 162
Figure 6.6. Schematic diagram of the *GBX2* conserved region. 164
Figure 6.7. PAX9 activates the *GBX2* conserved region *in vitro*. 165

Figure 6.8. Location of primer binding sites used in the ChIP assay to target the *Gbx2* conserved region by qPCR. 166
Figure 6.9. Chromatin immunoprecipitation of the *Gbx2* conserved region using E10.5 embryos. 167
Figure 6.10. Chromatin immunoprecipitation of the *Gbx2* conserved region using E9.5 embryos. 168
Figure 7.1. The proposed *Tbx1-Pax9-Gbx2* model in the morphogenesis of the 4th pharyngeal arch artery. 180

List of Tables

Table 1.1. Penetrance of 4th pharyngeal arch artery defects in *Tbx1*$^{+/-}$ mutants during embryogenesis from published data. 28
Table 1.2. Penetrance of 4th pharyngeal arch artery defects observed in conditional heterozygous *Tbx1* mutants at E10.5 in published data. 29
Table 1.3. Penetrance of cardiovascular defects observed in conditional heterozygous *Tbx1* mutants at E15.5-P2 in published data. 31
Table 1.4. Summary of the nine *PAX* genes showing which structural regions are present in each and their chromosomal locations in human and mouse. 32
Table 1.5. Penetrance of 4th pharyngeal arch artery defects observed in conditional homozygous *Gbx2* mutants at E10.5 in published data. 39
Table 2.1. Volume of lysis buffer added to samples for DNA extraction using the proteinase K method. 49
Table 2.2. Primer sequences used for genotyping. 50
Table 2.3. Protocol for processing embryos for wax embedding. 53
Table 2.4. Restriction enzymes and RNA polymerases used to generate *in situ* hybridisation probes. 56
Table 2.5. Primary and secondary antibodies used for immunohistochemistry. 59
Table 2.6. Probes used in RNAScope assays. 60
Table 2.7. Duration of PFA fix for lacZ staining. 61
Table 2.8. Primers used for qPCR analysis. 65
Table 2.9. Plasmids used for each control assay. 67
Table 2.10. Plasmids used in each luciferase experiment investigating the interaction of Tbx1 and Pax9 with the *Gbx2* enhancer region. 68
Table 2.11. Antibodies used in chromatin immunoprecipitation assays. 69
Table 3.1. Reported penetrance of cardiovascular defects in *Gbx2*-null mice in late embryogenesis. 72
Table 3.2. Reported penetrance of 4th pharyngeal arch artery defects in *Gbx2*-null embryos at E10.5. 73
Table 3.3. Embryos (E8.5-15.5) obtained from *Gbx2*$^{+/-}$ X *Gbx2*$^{+/-}$ cross from 42 litters. 74
Table 3.4. Penetrance of cardiovascular defects in *Gbx2*$^{-/-}$ embryos at E15.5. 76

Table 3.5. Comparison of the *Gbx2*$^{-/-}$ phenotype collected in this study compared to previously published data. 80
Table 3.6. Penetrance of left-right patterning defects in *Gbx2*$^{-/-}$ embryos at E15.5. 82
Table 3.7. 4th pharyngeal arch artery defects present in *Gbx2*$^{-/-}$ embryos at E10.5 and E11.5 assessed by HREM. 85
Table 3.8. Penetrance of 4th pharyngeal arch artery defects in *Gbx2*$^{-/-}$ embryos at E10.5 assessed by intracardiac ink injection and HREM. 89
Table 4.1. Mice (E9.5-P0) obtained from the *Pax9*$^{+/-}$;*Gbx2*$^{+/-}$ X *Pax9*$^{+/-}$;*Gbx2*$^{+/-}$ cross from 25 litters. 106
Table 4.2. Mice obtained from *Pax9*$^{+/-}$ X *Gbx2*$^{+/-}$ cross at time of weaning from 46 litters. 107
Table 4.3. Penetrance of cardiovascular defects present in *Pax9*$^{+/-}$;*Gbx2*$^{+/-}$ mice E15.5-P0. 110
Table 4.4. Penetrance of 4th pharyngeal arch artery defects in *Pax9*$^{+/-}$;*Gbx2*$^{+/-}$ embryos at E10.5. 111
Table 4.5. Penetrance of cardiovascular defects at E15.5 in *Gbx2*$^{-/-}$ embryos compared to *Pax9*$^{+/-}$;*Gbx2*$^{-/-}$ embryos. 118
Table 4.6. Penetrance of thymus defects present at E15.5 in *Gbx2*$^{-/-}$ embryos compared to *Pax9*$^{+/-}$;*Gbx2*$^{-/-}$ embryos. 120
Table 4.7. Penetrance of 4th pharyngeal arch artery defects in *Gbx2*$^{-/-}$ and *Pax9*$^{+/-}$;*Gbx2*$^{-/-}$ embryos at E10.5. 123
Table 4.8. Penetrance of cardiovascular defects at E15.5 in *Pax9*$^{-/-}$ embryos compared to *Pax9*$^{-/-}$;*Gbx2*$^{+/-}$ embryos. 126
Table 4.9. Penetrance of 4th pharyngeal arch artery defects in *Pax9*$^{-/-}$ and *Pax9*$^{-/-}$;*Gbx2*$^{+/-}$ embryos at E10.5. 129
Table 4.10. Pharyngeal arch artery defects present at E10.5 in *Pax9*$^{-/-}$ and *Pax9*$^{-/-}$;*Gbx2*$^{+/-}$ embryos. 130
Table 4.11. Penetrance of cardiovascular defects in each genotype at E15.5-P0. 136
Table 5.1. Penetrance of defects at E15.5 in conditional endoderm mutants. 147
Table 5.2. Penetrance of 4th pharyngeal arch artery defects in *Gbx2*$^{f/-}$;*Pax9Cre* embryos at E10.5. 148
Table 5.3. Penetrance of defects at E10.5 and E15.5-P0 in conditional endoderm mutants and global mutant equivalent genotypes. 151

Table 5.4. Penetrance of cardiovascular defects in mutants at mid and late embryogenesis. 153
Table 6.1. Summary of RNAScope gene analysis in *Tbx1*$^{-/-}$, *Pax9*$^{-/-}$ and *Gbx2*$^{-/-}$ mutants. 159
Table 6.2. Cardiovascular defects in *Tbx1*$^{+/-}$ embryos compared to *Tbx1*$^{+/-}$;*Gbx2*$^{+/-}$ embryos at E15.5. 161
Table 6.3. Cardiovascular defects present in *Tbx1*$^{+/-}$;*Pax9*$^{+/-}$ embryos compared to *Tbx1*$^{+/-}$;*Pax9*$^{+/-}$;*Gbx2*$^{+/-}$ embryos at E15.5. 163
Table 6.4. Penetrance of cardiovascular defects in *Tbx1*$^{+/-}$ and *Tbx1*$^{+/-}$;*Gbx2*$^{+/-}$ mice E15.5-P2 in published data. 171
Table A.1. Phenotype of each *Gbx2*$^{-/-}$ mouse at E15.5. 183
Table A.2. Phenotype of each *Gbx2*$^{+/-}$;*Pax9*$^{+/-}$ mouse at E15.5 and P0. 184
Table A.3. Phenotype of each *Gbx2*$^{-/-}$;*Pax9*$^{+/-}$ mouse at E13.5-15.5 and P0. 185
Table A.4. Phenotype of each *Pax9*$^{-/-}$ mouse at E15.5 and P0. 186
Table A.5. Phenotype of each *Pax9*$^{-/-}$;*Gbx2*$^{+/-}$ mouse at E15.5 and P0. 187
Table A.6. Phenotype of each *Pax9*$^{-/-}$;*Gbx2*$^{-/-}$ mouse at E15.5-P0. 187
Table A.7. Phenotype of each *Pax9Cre;Gbx2*$^{f/f}$ mouse at E15.5. 188
Table A.8. Phenotype of each *Pax9Cre;Gbx2*$^{f/-}$ mouse at E15.5. 188
Table A.9. Phenotype of each *Pax9Cre;Gbx2*$^{+/f}$ mouse at E15.5. 189
Table A.10. Phenotype of each *Tbx1*$^{+/-}$ mouse at E15.5. 190
Table A.11. Phenotype of each *Tbx1*$^{+/-}$;*Gbx2*$^{+/-}$ mouse at E15.5. 191
Table A.12. Phenotype of each *Tbx1*$^{+/-}$;*Pax9*$^{+/-}$ mouse at E15.5. 192
Table A.13. Phenotype of each *Tbx1*$^{+/-}$;*Pax9*$^{+/-}$;*Gbx2*$^{+/-}$ mouse at E15.5. 193

Chapter 1. Introduction

1.1 Cardiovascular development

The adult mammalian heart is a muscular pump needed to pump blood around the body. The four chambered heart consists of two atrial chambers which drain into two ventricles. The left ventricle connects to the aorta to deliver oxygenated blood to the systemic circulation. The heart is the first organ to fully develop and function, required to pump blood around the developing embryo. Genetic mutations that alter heart development result in congenital heart defects (CHDs). CHDs are the most prevalent birth defect, affecting nearly 1% of the population, and result in structural defects to the heart and associated vessels (1).

Formation of the heart begins with the specification of the cardiogenic fields which occurs during gastrulation (as reviewed in Brade et al*.,* 2003). A schematic overview is shown in Figure 1.1. Gastrulation occurs at embryonic day (E) 6 in mouse development, during which the three germ layers (endoderm, ectoderm and mesoderm) are formed. The lateral plate mesoderm (LPM) is formed by the migration of cardiac mesoderm progenitors that migrate from the primitive steak to the anterior portion of the embryo. The LPM is divided into the somatic and splanchnic mesoderm. It is from the splanchnic mesoderm that the first cardiac progenitors, namely the primary heart fields, are derived (2-4).

The bilateral primary heart fields form the primary cardiac crescent at E7.5. This then fuses at the ventral midline at E8, forming the linear heart tube. The heart tube is initially composed of a single lining of endothelial cells surrounded by a myocardial layer. At E8.0 in mice, the tube has the ability to beat, irregularly, pumping oxygenated blood and nutrients throughout the embryo (5). The proliferation of primary heart field (PHF) cells and the addition of secondary heart field (SHF) cells causes the rapid growth of the heart tube between E8 and E9 (6, 7).

The SHF is a second group of progenitor cells located in the splanchnic mesoderm. These cells migrate to the heart and subsequently continue to provide progenitors to the heart throughout embryogenesis (6, 7). Myocardial cells from the SHF contribute to the outflow tract (OFT), right ventricle and atria, while the left ventricle is largely

derived from the PHF. By E8.5, the common atrial chamber, primitive left ventricle and bulbous cordis (future right ventricle) can be distinguished.

The heart tube loops rightward from E8.25, following which the atrioventricular (AV) canal develops, separating the atrial and ventricular regions of the heart. During the looping of the heart tube, the chambers of the heart begin to take shape as the pouches of the heart tube balloon out due to cell proliferation (8). For the four chambers of the heart to be defined, the formation of the endocardial cushions is required. The AV cushions will later form the tricuspid and mitral valves. Endocardial cushions also form in the OFT. Pairs of facing cushions extend through the OFT in a spiral formation from the ventricle to the aortic sac, thereby forming the aortic and pulmonary valves.

The primitive heart tube consists of an outer myocardial and inner endothelial layer, between which lies an extracellular matrix, called cardiac jelly, from which the cushions form (9). The process of endocardial cushion formation in the AV canal and OFT occurs via a similar process. Cushions first appear as thickenings of cardiac jelly. These restricted swellings are consequently invaded with mesenchymal cells. The mesenchymal cells are a result of epithelial-to-mesenchymal transition of endocardial cells; a myocardium regulated process called EMT (10).

The primary atrial septum divides the atrial chambers. This is formed by the proliferation of the myocardial layer and is covered by a mesenchymal cap (as reviewed in Moorman and Christoffels, 2003). This mesenchyme fuses with the AV cushions and the vestibular spine completing septation (11). A secondary atrial septum is present in mammals. This is formed from a folding of the atrial wall right of the primary septum (12).

The ventricles are largely separated by the interventricular septum, produced by ballooning of the chambers. However, through a large portion of embryonic development, there remains communication between the two chambers; occurring through a gap at the tip of the incomplete interventricular septum. The completion of ventricular septation occurs around E14.5 (equivalent to Carnegie stage (CS) 20 in humans) with the fusion of the septum to the AV cushions and the proximal OFT cushions; coinciding with septation of the OFT. The fusion of the cushions completes AV and OFT septation. Myocardial cells invade the cushions and, as a result, the mesenchyme of the cushions undergoes myocardialisation, transforming into cardiac muscle to muscularise and support the septa (13, 14).

As well as the SHF, there are other extracardiac contributions made to the developing heart, one being the epicardium. As mentioned, the heart tube consists of a myocardial and endocardial layer. The proepicardium is a cluster of cells, transiently present from E8.5. The progenitors that arise from here form the outermost layer of the heart, called the epicardium, as well as epicardium-derived cells (15). These epicardium-derived cells then differentiate into various cell lineages in the heart, contributing to the formation of fibroblasts and vascular smooth muscle cells (16).

The myocardium lies between the epicardial and endocardial layers of the heart. Cardiomyocytes, with fully differentiated sarcomeres, exist within the chamber walls forming the myocardium which forms two distinct layers: the compact layer and the trabecular layer. The compact layer is a basal layer of myocardium that provides proliferating cells for the developing heart. The thickness of this myocardial layer increases throughout development due to a high rate of cardiomyocyte proliferation and compaction of trabeculae (17).

Trabeculae are organised sheets of cardiomyocytes that form muscular ridges and are lined by endocardial cells (18). They are formed by interaction with the endocardium following the looping of the heart. Trabeculae, found in the ventricles, extend into the cavity of the chamber and are essential in heart development and function. The layer functions to increase surface area, thereby allowing for maximum oxygen and nutrient delivery to the developing heart in the absence of coronary circulation (19). The trabeculae become incorporated into the interventricular septum, papillary muscles and the conduction system of the heart.

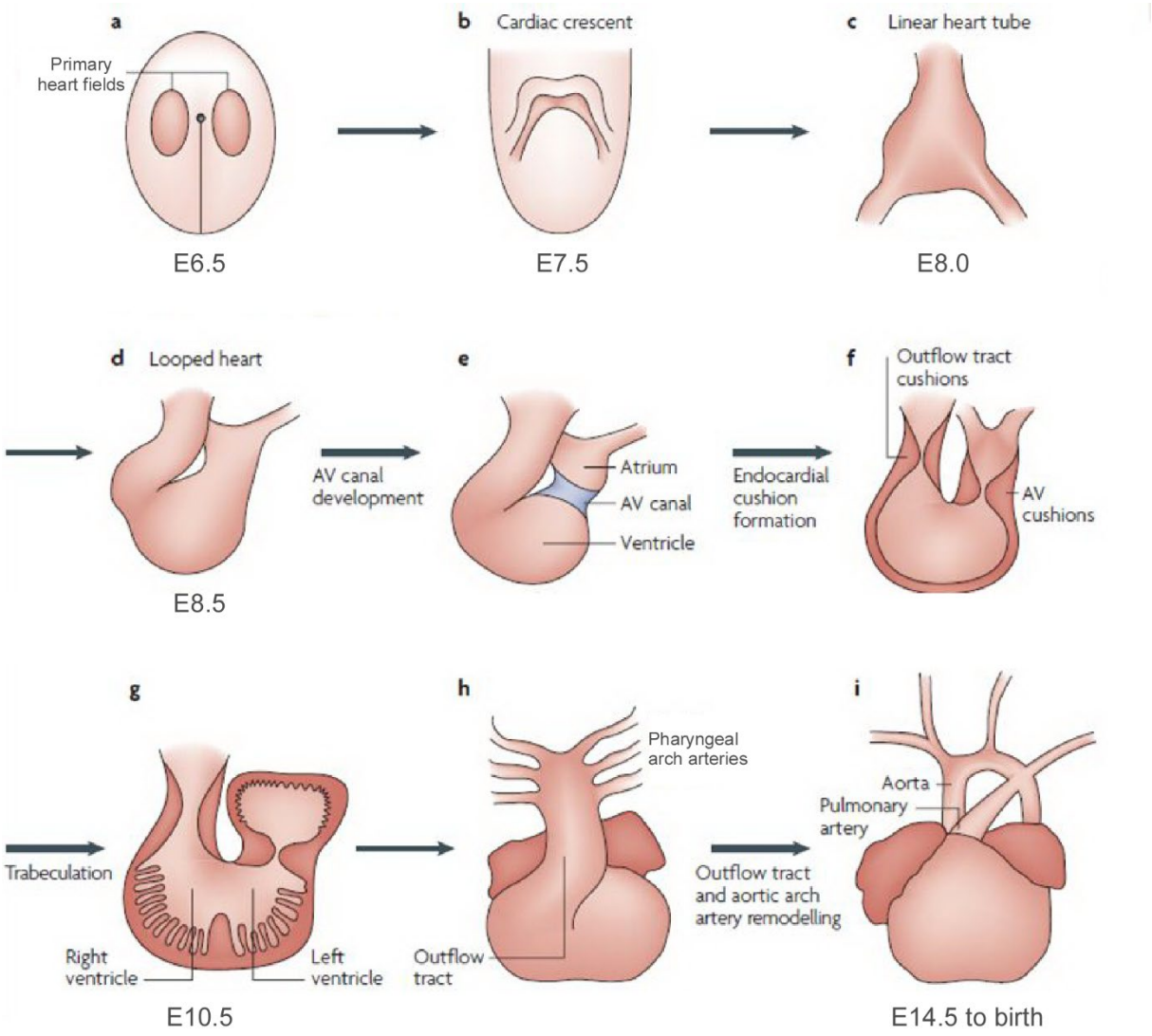

Figure 1.1. Schematic overview of cardiovascular development in mouse.

a) At E6.5, the two PHFs are located laterally to the midline. These migrate to form the cardiac crescent (b) which fuses at the midline generating the linear heart tube (c). The heart tube loops rightward from E8.5 (d) and the AV canal forms, separating the atria and ventricles (e). The AV and OFT endocardial cushions are formed from cardiac jelly (f). Trabeculae form in the myocardial layer from E9.5 (g). Fusion of the endocardial cushions and ballooning of the chambers completes AV and OFT septation, forming the four chambered heart (h,i). Abbreviations: E, embryonic day. Adapted from High and Epstein (2008) (20).

1.1.1 Cardiac neural crest cells

Neural crest cells (NCC) are multipotent cells that originate from the neural tube. There are two divisions of the neural crest; the cranial and trunk. The cardiac NCC are a subset of cranial NCC that originate from the region of the cranial neural fold between the midotic placode and somite 3 (21). NCC migrate to the pharyngeal arches (PA) from the midbrain and hindbrain in three distinct migration streams (22) then

differentiate into smooth muscle to support the developing pharyngeal arch arteries (PAA) (23). The PAA form the aortic arch and great vessels and are discussed in detail in Section 1.2.1. NCC also migrate through the PA to the OFT where they initiate septation (discussed in Section 1.2.2).

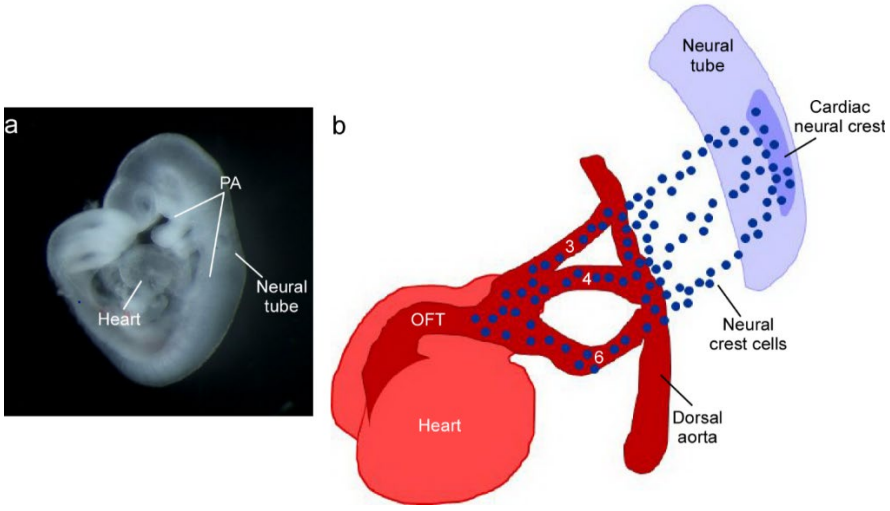

Figure 1.2. Migration of cardiac neural crest cells at mid-embryogenesis.

a) Image of an E9.5 embryo showing the developing heart, PA and neural tube. b) Schematic diagram of the NCC that migrate from the cardiac neural crest in the neural tube. NCC migrate in three streams to the PA where they differentiate into smooth muscle of the PAA (numbered). NCC migrate through the PA to the OFT of the heart. Abbreviations: PA, pharyngeal arches. Adapted from Hutson and Kirby (2007) (24).

The role of NCC is apparent in studies in which the ablation of NCC caused both cardiovascular and non-cardiovascular defects. Non-cardiovascular defects include the aplasia or hypoplasia of the thymus and parathyroid glands (25). NCC contribute to the atrioventricular and semilunar valves as they migrate from the PA into the aorticopulmonary septum and are thereby crucial in the septation of the OFT (26). NCC ablation results in a malpositioning of the OFT. This includes common arterial trunk (CAT), in which OFT has failed to septate into the aorta and pulmonary trunk, and overriding aorta with the aorta positioned centrally over the heart rather than the left ventricle (27, 28).

NCC are also required earlier in heart development during looping of the heart tube. SHF cells that were fated to migrate to the OFT and differentiate into myocardium fail to do so when NCC are ablated. Instead, the SHF cells become proliferative and do not migrate, thereby resulting in a shortened OFT and altered cardiac looping (29).

1.1.2 The outflow tract

In vertebrates, blood leaves the right and left ventricle of the heart via the pulmonary trunk and ascending aorta respectively. These vessels have formed during the septation of the common OFT, a process requiring the interaction of multiple tissues including the myocardium, endocardium and NCC. Failure of the OFT to form correctly results in CHDs including double outlet right ventricle (DORV), CAT and transposition of the great arteries (TGA) (CHDs are discussed further in Section 1.4).

The OFT begins as a singular tube, connecting the primitive ventricles to the PAA. At E9.5, prior to OFT septation, the OFT rotates anticlockwise as the great arteries develop (30). A characteristic dog-leg bend structure is found from E10.5 (around CS12 in humans), which separates the distal (arterial) and proximal (ventricular) regions of the OFT.

Cushions, cardiac jelly filled ridges, form along the OFT in a spiral conformation; from the distal end of the right ventricle to the aortic sac. NCC contribute to OFT cushion formation by migrating through the PA of the embryo and into the OFT where they aid in bulking the cushions. This also acts to initiate OFT septation as the cushions enlarge and then fuse, starting from the distal end of the OFT, which begins to separate the aorta and pulmonary trunk (27).

1.2 Development of the aortic arch arteries

1.2.1 Development and remodelling of the pharyngeal arch arteries

The great vessels and aortic arch structure form from the remodelling of the PAA. By E13.5, the aortic arch system found in the mouse embryo closely resembles that of an adult mouse (Figure 1.3). The ascending aorta takes oxygenated blood from the left ventricle and is connected to the descending aorta by the aortic arch. Arising from the arch is the brachiocephalic artery which branches into the right subclavian artery (RSA) and the right common carotid artery (RCC). The left common carotid (LCC) is the third branch of the aortic arch and the left subclavian artery (LSA) is the fourth. The pulmonary arteries branch from the pulmonary trunk which arises from the right ventricle. The arterial duct connects the pulmonary trunk to the dorsal aorta, allowing blood to bypass the non-functioning lungs during embryogenesis and closes shortly after birth.

The PAA form within the PA of the embryo. There are 5 pairs of PAA, numbered 1 through 4 and 6 according to their corresponding PA. Through evolution, the number of PAA has reduced. The 5th PAA does not form in mammals, existing only transiently during embryogenesis (31). This series of symmetrical pairs of vessels arise from the aortic sac and connect to the dorsal aortae. They asymmetrically remodel to form the double circulatory system.

Prior to E9.5, the arterial trunk extends from the cardiac tube of the heart and splits into paired ventral aortae which connect to the dorsal aortae via a loop, termed the primitive aortic arch. The ventral and dorsal aorta are connected in this way until the 15 somite stage (32). The PAA then form in a cranial to caudal order at the early stages of E9.5 (21-23 somites), with the 3rd clearly present by mid E9.5 (24-26 somites). The 1st and 2nd PAA then regress before E10.5, with the distal portion of the 1st becoming the maxillary process and the 2nd PAA forming a capillary plexus. During the regression of the 1st and 2nd, the 3rd becomes thicker and the 4th is forming at 27-29 somites. The final, and most caudal, PAA to form is the 6th, appearing from 31-34 somite stage. By E10.5 (around 34 somites), 3 pairs of fully-formed vessels (namely the 3rd, 4th and 6th) can be seen connecting the aortic sac to the dorsal aorta (Figure 3).

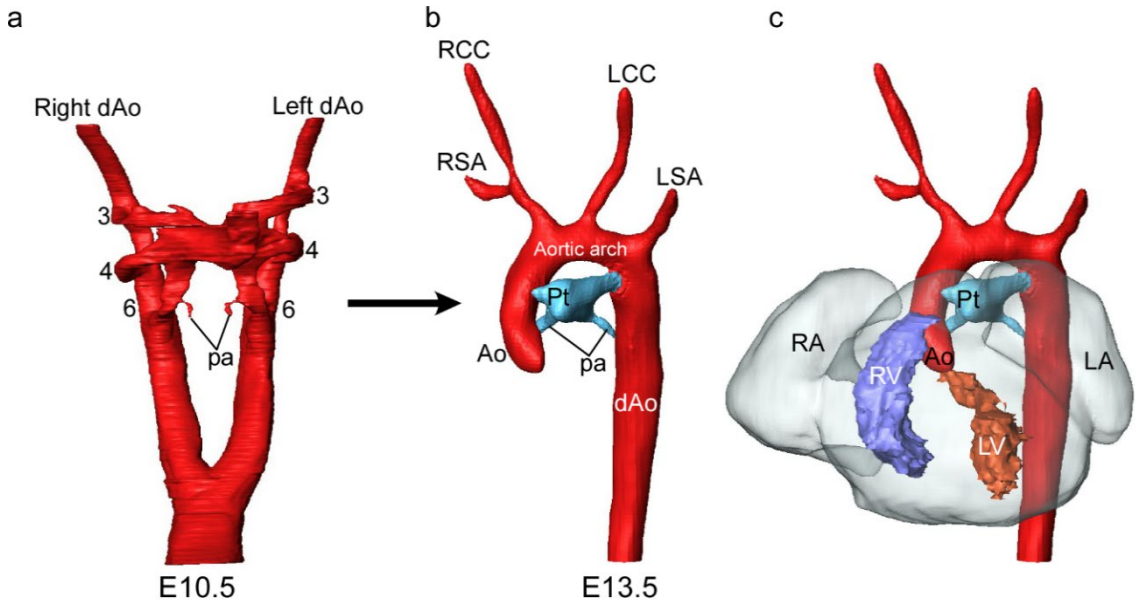

Figure 1.3. Structure of the pharyngeal arch arteries and mature aortic arch.

a) Bilaterally symmetrical structure of the PAA (numbered) at E10.5 prior to remodelling. The PAA remodel asymmetrically from E11.5 to form the mature aortic arch structure (b,c) by E13.5. The left ventricle connects to the aorta which arches leftward to a left sided dorsal aorta (dAo). The brachiocephalic artery (BA) arises from the arch, branching into the RSA and RCC. The LCC and LSA then branch from the arch. The pulmonary arteries (pa) split from the pulmonary trunk (Pt) which connects to the RV. Abbreviations: Ao, aorta; BA, brachiocephalic artery; dAo, dorsal aorta; LCC, left common carotid artery; LSA, left common carotid artery; LV, left ventricle; pa, pulmonary arteries; Pt, pulmonary trunk; RCC, right common carotid artery; RSA, right subclavian artery; RV, right ventricle.

The arrangement of the PAA remains bilaterally symmetrical until E11.5 (41-50 somites), at which point complex remodelling occurs to form the asymmetrical structure of the mature aortic arch (Figure 1.4). The aortic and pulmonary trunk are present at the proximal portion of the aortic sac at E11.5. The distal portion of the aortic sac becomes T-shaped with left and right horns which will form part of the aortic arch and brachiocephalic artery respectively. It is from these horns that the 3rd and 4th PAA dorsally branch while the right 6th PAA begins to regress at this stage. This regression occurs with an increase in apoptosis that spreads from the mesoderm of the PA to the smooth muscle layer of the PAA (33). The portion of the dorsal aorta between the 3rd and 4th PAA (the carotid duct), diminishes by around E12.5 and the right dorsal aorta becomes thin by this stage and has regressed completely by E13. This leaves a bilaterally asymmetrical structure with a single dorsal aorta.

The contribution of each PAA to the aortic arch are shown in Figure 1.4. The left and right common carotid arteries form from the remodelling of the 3rd PAA. The brachiocephalic artery is formed from the right horn of the aortic sac. The proximal portion of the RSA branching from the brachiocephalic artery is formed from the right 4th PAA. The aortic arch forms from the left horn of the aortic sac and the left 4th PAA. While the right 6th regresses, the left 6th forms the arterial duct.

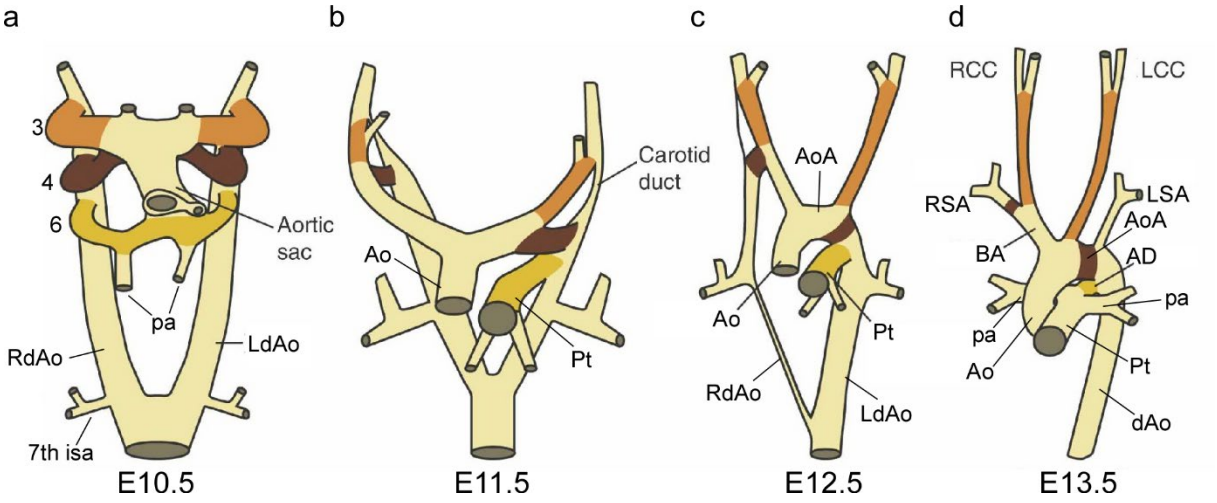

Figure 1.4. Remodelling of the pharyngeal arch arteries to the aortic arch.

The symmetrical structure of the PAA at E10.5 (a), which remodel to form the aortic arch structure. By E11.5 (b) the proximal portion of the aortic sac has septated into the aorta and pulmonary trunk. The 3rd and 4th PAA branch from the horns of the distal aortic sac. The right 6th PAA has regressed and the carotid duct between the 3rd and 4th PAA has started to thin. The right dorsal aorta is regressing by E12.5 (c) and is completely absent by E13.5 (d) showing the mature aortic arch structure. Abbreviations: Ao, aorta; AoA, aortic arch; BA, brachiocephalic artery; dAo, dorsal aorta; isa, intersegmental arteries; LCC, left common carotid artery; LSA, left common carotid artery; LV, left ventricle; pa, pulmonary arteries; Pt, pulmonary trunk; RCC, right common carotid artery; RSA, right subclavian artery; RV, right ventricle. Adapted from Papangeli and Scambler (2012) (34).

1.2.2 The pharyngeal arches

The PAA form within the PA, a transient series of protrusions that form in a cranial to caudal sequence along the embryo (as reviewed by Graham et al., 2001). There are 5 PA, numbered 1-4 and 6, comprised of multiple tissue types, namely the pharyngeal endoderm, ectoderm, mesoderm and NCC (Figure 1.5). The core of each arch is mesenchyme, derived from mesoderm cells and NCC that migrate into the PA. This core is surrounded by epithelial layers, the pharyngeal endoderm on the internal lining

and ectoderm on the outer lining. The epithelial layers form pharyngeal pouches (endoderm) and clefts (ectoderm) between each PA.

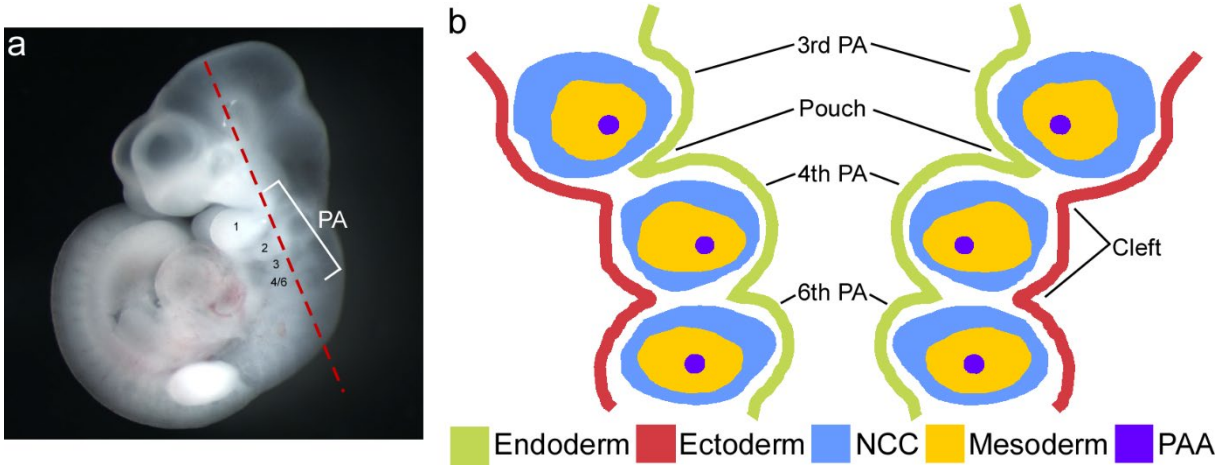

Figure 1.5. Structure of the pharyngeal arches.

(a) The PA (numbered) are visible externally on the embryo. Red dashed line represents the coronal section to obtain (b) a schematic of the structure of PA 3-6. Each arch is composed of an inner lining of endoderm, outer lining of ectoderm. The endoderm forms pouches between the PA and the ectoderm forms clefts. The PAA is within the mesodermal core which is surrounded by NCC. Abbreviations: PA, pharyngeal arches; PAA, pharyngeal arch arteries.

The developing PAA reside in the mesodermal core of the PA. The developing vessels are composed of a layer of endothelial cells surrounded by smooth muscle. The muscle is provided by the differentiation of NCC that migrate into the PA (35). However, the mechanism of the formation of the endothelial lumen is unknown. The reasoning of angiogenesis or vasculogenesis remains an ongoing debate (36, 37). The angiogenesis model proposes that the PAA arise from the dorsal aortae, OFT or another pre-existing vessel. The vasculogenesis models suggests that the endothelial cells arise from *de novo* differentiation in the mesodermal core of the PA.

Prior to the formation of the endothelial lumen, the endothelial cells form a plexus in the PA that is then thought to give rise to the PAA lumen (38, 39). The endothelial plexus is present from 18 somites in the region corresponding to the future caudal PAA (40). It was postulated that the cells of the endothelial plexus arise from the dorsal aorta (36). The 1st and 2nd PAA, were shown to share common progenitors with the dorsal aorta, aortic sac and endocardium, however the caudal PAA (3rd-6th) did not

(40). The endothelium of the cranial and caudal PAA arise from a different origin and mechanism.

In the caudal PAA (3^{rd}-6^{th}), the endothelial cells are mesoderm derived, largely originating from the SHF, but the mechanism whereby these progenitors are recruited to the PA is unknown (40-42). The SHF extends cellular processes towards the gut endoderm which migrate to form the endothelial plexus. Between 30-34 somites, the plexus begins to remodel and the cells coalesce in to the PAA lumen (40). The endothelial cells migrate as angiogenic sprouts to eventually connect the aortic sac to the dorsal aortae (37). The caudal PAA appear to originate through vasculogenesis then grow through angiogenesis. Multiple genes have been implicated in the formation of the caudal PAAs (discussed in Sections 1.6, 1.7 and 1.8), however, the exact mechanism of how these genes direct PAA formation is unknown.

1.2.3 Derivative of the pharyngeal arches

Each of the PAs, as well as the pouches and clefts, contribute to the development of different parts of the body (as reviewed in Grevellec and Tucker, 2010). In vertebrates, the 1^{st} arch forms the jaw and Meckel's cartilage, which will form part of the ear. The 1^{st} cleft and pouch contribute to the eardrum and Eustachian tube of the ear, respectively. The 2^{nd} and 3^{rd} arch provide skeletal structures of the ear and also the hyoid apparatus which anchors the tongue and larynx. The 2^{nd} pouch forms the epithelium of the palatine tonsil, a lymphoid organ. The 4^{th} and 6^{th} PA form the thyroid, arytenoid and cricoid cartilage and the laryngeal muscles. The 3^{rd} and 4^{th} pouches become the thymus, parathyroid glands and the ultimobranchial body.

The neural crest also contributes to the derivatives of the PA, for example in the formation of the connective tissue around the thymus and parathyroid glands (43). NCC ablation results in abnormal thymus and parathyroid development (25), however, it has been shown that the endoderm alone can give rise to the thymus (44).

1.2.4 The role of the pharyngeal endoderm

The development of various structures from the PA requires the interaction between the layers of the arches. It was previously thought that the precise patterning of the arches relied on the neural crest (45). However, the formation of the PA in the absence of the neural crest, as well as their normal patterning, show this not to be the case (46).

The pharyngeal endoderm is required for the patterning and segmentation of the PA and expresses key genes to provide signalling cues during development (47). The pharyngeal pouches are highly regionalised with precise gene expression in different pouches (46). For example Sonic hedgehog (Shh) is expressed in the 2nd pouch (46) and is required to communicate with the head ectoderm to induce patterning of this tissue (48).

Models with altered gene expression within the pharyngeal endoderm have defects to the structure of the PA. This occurs because the formation of the PA relies on the segmentation of the pharyngeal endoderm. This was shown in zebrafish with the *van gogh* (*vgo*) mutant in which the PA did not form. This was independent of NCC defects but occurred with failed pouch segmentation (49). *Vgo* encodes for the zebrafish orthologue of T-box 1 (*Tbx1*), a transcription factor required in cardiovascular development.

Tbx1 is expressed in the pharyngeal endoderm, ectoderm and mesoderm of the PA. In *Tbx1*$^{-/-}$ mice, the pouches do not form and the caudal PAs are absent. This causes defects in the organs derived from the PA, including the thymus and the aortic arch (50). Conditional homozygous *Tbx1* deletion from the pharyngeal endoderm recapitulates the *Tbx1*-null phenotype with failed formation of the caudal PA thereby showing the necessity of the pharyngeal endoderm in PA organisation (51, 52).

The endothelium of the caudal PAA is derived from SHF-mesoderm (40) and the endoderm provides signalling cues to this tissue in PAA formation. *Tbx1* has been shown to induce signals from the endoderm that are then transferred to the underlying mesenchyme to direct PAA development via fibroblast growth factor (Fgf) signalling (53).

The endoderm influences NCC through the expression of the *Fgf* gene family (as discussed in Graham et al*.,* 2005). NCC rely on cues from signalling molecules for migration into the PA. Loss of the *Fgf* receptor, *Fgfr1*, specifically from the pharyngeal

epithelium resulted in failed NCC migration and craniofacial defects (54). *Fgf3* and *Fgf8* signalling from the pharyngeal endoderm is needed to induce NCC (55). Supporting the role of the endoderm in PA development was a study by Couly et al. (2002) which ablated pharyngeal endoderm domains early in chick embryogenesis. The endoderm was found to be essential in providing cues for the specification of facial skeletal elements formed from NCC-derived mesenchyme.

The pharyngeal endoderm is hence a key region in the governing the development of the PAA and other PA derivatives. However, the formation of these tissues is also dependent on gene expression in the other tissues of the PA. Further work is required to infer the tissue specific role of the pharyngeal endoderm.

1.3 Signalling pathways in cardiovascular development

There are multiple signalling pathways implicated in cardiovascular development, including cell-cell signalling or the secretion of signalling proteins (as reviewed in Cesario et al., 2015). This is required for communication between tissue types. For example, the PAA are within the mesoderm and rely on signalling from the surrounding epithelial layers during their formation and remodelling (47, 56).

1.3.1 Notch signalling

Notch is a highly conserved signalling pathway which allows short-range communication between adjacent cells. This communication relies on the expression of transmembrane proteins; Notch receptors and ligands. There are four members of the Notch family of receptors expressed in mammals (Notch1-4). The five ligands expressed by mammals are divided into two families namely Delta-like (consisting of Delta-like 1,3,4) and Jagged (consisting of Jagged1, 2) (as reviewed in High et al., 2007). Upon ligand binding, the Notch receptor is cleaved thereby releasing the Notch intracellular domain (NICD) into the cytoplasm. After translocating to the nucleus, the NICD forms, along with other molecules, a transcriptional complex to activate gene expression of its targets to elicit various downstream responses.

Notch, expressed in the endothelium and NCC, has been implicated in multiple stages during embryogenesis including cell proliferation, differentiation and migration (20). In

the context of cardiovascular development, loss of Notch signalling in the NCC results in aortic arch defects and ventricular septal defects. The abnormal aortic arch patterning arises due to the aberrant NCC migration and reduced differentiation of NCC into smooth muscle cells surrounding the PAA (57).

1.3.2 Fibroblast growth factor signalling

Fgf signalling functions via secreted proteins that can act in a paracrine or endocrine fashion, for local or long-range signalling respectively (58). There are 22 members within the Fgf family in mice and, of the *Fgf* genes, *Fgf8* expression is critical in the development of the PA and their derivatives; required in cardiovascular and craniofacial development.

Fgf8 is expressed prior to gastrulation and complete *Fgf8* knockouts die during this stage (59). By E9.5, *Fgf8* is expressed in the pharyngeal endoderm and ectoderm of the PA (59). *Fgf8* hypomorphic mutants have absent teeth and a truncated tongue, among defects to other craniofacial structures formed from the 1st PA (60). Loss of *Fgf8* also results increased apoptosis of migrating NCC and consequent defects to the cardiovascular OFT such as TGA and DORV (61) (defects are discussed in Section 1.4).

1.3.3 Sonic hedgehog signalling

Of the mammalian hedgehog signalling genes, sonic hedgehog (*Shh*) is the only gene expressed within the PA (62). *Shh* is expressed in the pharyngeal endoderm and *Shh*$^{-/-}$ mice have hypoplastic PA (63). These mutants consequently show severe craniofacial defects in which the eyes, nose and oral features are unidentifiable (64). The hypoplasia of the PA in *Shh*$^{-/-}$ mice causes defects to the PAA and the caudal vessels fail to form (65). The NCC migration streams are also abnormal and in later development these embryos present with common arterial trunk and defects to the aortic arch (65).

1.3.4 Bone morphogenetic protein signalling

Bone morphogenetic proteins (BMPs) belong to the transforming growth factor-β (TGF-β) family of proteins. There are over 20 identified *Bmps,* six of which are expressed in the developing heart (as reviewed in Yuasa et al., 2008). Loss of Bmp signalling in mice, via disruption of the BMP type II receptor, resulted in common arterial trunk, absent semilunar valves and interruption of the aortic arch (66). The lack of OFT septation occurred due to abnormalities in the OFT cushions. The cushions enlarge and fuse to separate the aorta and pulmonary trunk during normal development however, in the *Bmp* mouse mutants, the cushions are smaller.

Bmp4 has been shown to be required in the formation of the OFT and aortic arch. *Bmp4* is expressed in the splanchnic mesoderm, pharyngeal mesoderm and the OFT myocardium (67, 68). The loss of *Bmp4* from the mesoderm using *Nkx2.5Cre* caused PAA remodelling defects and embryos had interrupted aortic arch and abnormal origin of the carotid arteries (68). Defects to the PAA were present at E10.5 in *Bmp4* mutants, with failed smooth muscle recruitment around the vessels, suggesting that *Bmp4* is needed for NCC function.

1.3.5 Wnt signalling

There are 19 identified *WNT* genes in human and mouse which encode secreted glycoproteins that bind receptors to induce intracellular pathways (as reviewed in Komiya and Habas, 2008). There are two division of Wnt signalling, canonical and non-canonical, which are dependent or independent of β-catenin respectively. The non-canonical pathway is independent of β-catenin but the canonical relies on β-catenin to activate target gene expression. The canonical pathways controls gene expression within the epithelial layers of the PA, including *Shh*, *Fgf8* and *Bmp4* expression (69).

The canonical Wnt signalling pathway is active in NCC that migrate to the PA (70) and the survival of NCC depends on this signalling (71). The loss of β-catenin, and hence canonical Wnt signalling, in NCC resulted in severe abnormalities in craniofacial development (72). Inactivation of β-catenin in the mesenchyme of the PA caused defects to the derivatives of the PA, including the thymus, parathyroid glands and the aortic arch arteries (73). These mouse mutants presented with a hypoplastic aorta and aberrant subclavian arteries as well as OFT defects including CAT and DORV (73).

1.4 Congenital heart defects

As the most prevalent birth defect, CHDs are a major cause of morbidity and are caused by both genetic and environmental factors (1, 74). CHDs are structural abnormalities that can affect the heart or the aortic arch arteries.

Conotruncal defects, affecting the OFT and great vessels of the heart, are of the most frequent form of heart defect, present in 30% of CHD cases (75). During development, the common OFT septates into the aorta and pulmonary trunk. The aorta takes oxygenated blood from the left ventricle to deliver to the systemic circulation and the pulmonary trunk takes deoxygenated blood from the right ventricle to deliver to the lungs via the pulmonary arteries. There are multiple CHDs that affect the septation, alignment and overall structure of the OFT and the great vessels.

These defects frequently occur with a ventricular septal defect (VSD), also referred to as an interventricular communication (IVC). The interventricular septum is formed during ballooning of the heart chambers and separates the ventricles (13). The failed fusion of the septum with the endocardial cushions results in communication between the ventricles and the mixing of oxygenated and deoxygenated blood. This results in cyanosis and poor oxygenation in the patient. VSD is a haemodynamic necessity with the conotruncal defect DORV. In DORV, both the aorta and pulmonary trunk are aligned to the right ventricle (76) (Figure 1.6). A deviation of this defect is overriding aorta, in which the aorta is positioned centrally, above the interventricular septum. This also occurs with a VSD resulting in the delivery of poorly oxygenated blood to the systemic circulation.

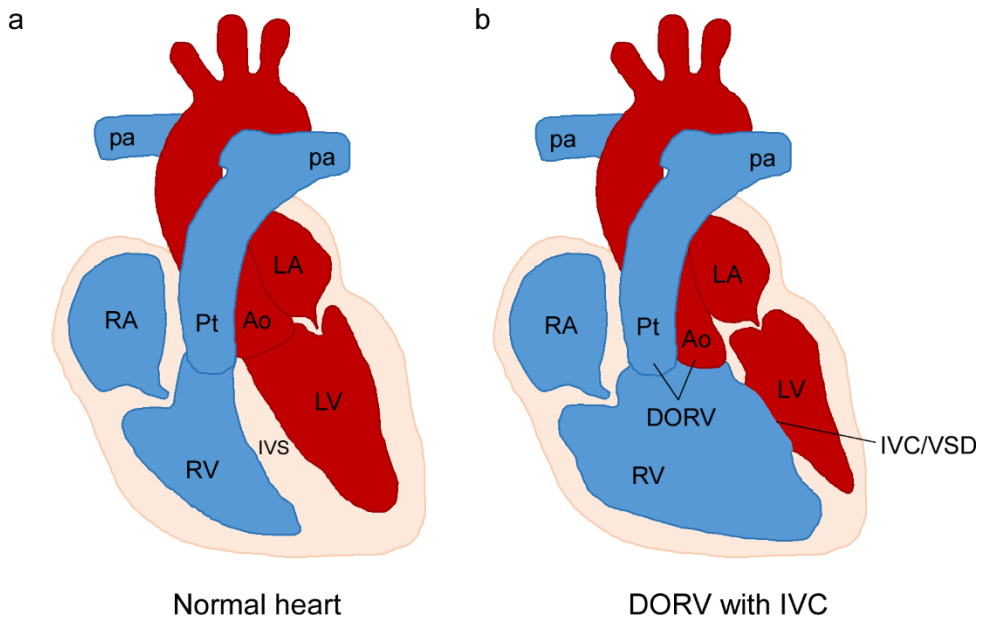

Figure 1.6. Schematic showing double outlet right ventricle with an interventricular communication.

Normal heart (a) with a complete interventricular septum (IVS) separating the right and left ventricles. The aorta and pulmonary trunk arise from the left and right ventricle respectively. Heart with DORV (b) with both the aorta and pulmonary trunk connecting to the right ventricle. The IVS has failed to completely form and there is communication between the ventricles. Abbreviations: Ao, aorta; DORV, double outlet right ventricle; IVC, interventricular communication; IVS, interventricular septum; LA, left atrium; LV, left ventricle; pa, pulmonary arteries; Pt, pulmonary trunk; RA, right atrium; RV, right ventricle; VSD ventricular septal defect.

TGA is one of the most common CHDs, accounting for 34% of conotruncal defects (77). In vertebrates, the aorta and pulmonary trunk are aligned to their respective ventricles following septation and rotation of the common OFT. TGA occurs as a result of this failed rotation causing the misalignment of the vessels; with the aorta arising from the right ventricle and the pulmonary trunk from the left ventricle. Consequently, deoxygenated blood is delivered to the systemic circulation and oxygenated blood is directed to the lungs. VSD is essential for survival in the case of TGA to allow for the mixing of oxygenated and deoxygenated blood heart, as, otherwise, the aorta would carry only deoxygenated blood to the systemic circulation.

CHDs can also occur due to the aberrant formation and remodelling of the PAA. There are 5 pairs of PAA which asymmetrically remodel for form the mature aortic arch structure (discussed in Section 1.2.1). Defects to the 4th PAA are most frequent which therefore affects the derivatives of this vessel (Figure 1.7).

The left 4th PAA contributes to the distal region of the aortic arch. Therefore the absence or hypoplasticity of the left 4th results in interrupted aortic arch (IAA) in which the ascending aorta fails to connect to the descending aorta. There are three forms of IAA depending on the location of the interruption (78). With IAA-A this region is distal to the LSA, in IAA-B, the most common form, the interruption is between the LCC and LSA and IAA-C occurs when the region between the brachiocephalic artery and LCC is interrupted. Right aortic arch (RAA) is another defect that arises due to left 4th PAA abnormalities and the resulting aortic arch extends to the right side of the body (79). In cervical aortic arch (CoAoA), the arch extends abnormally high in the neck and this more commonly occurs with a right sided arch (80) .

A less severe CHD that occurs as a results of the incorrect development of the right 4th PAA is the aberrant origin of the subclavian arteries and often occurs simultaneously with aortic arch defects (79). There are multiple forms of aberrant right subclavian artery (ARSA). The RSA usually branches from the brachiocephalic artery however, in retro-oesophageal RSA (RE-RSA), the RSA branches from a distal portion of the aortic arch then extends to the right side of the body, passing dorsally behind the oesophagus. This defect is viable, although it can result in the compression of the oesophagus and trachea. In isolated RSA (IRSA), the RSA branches from the pulmonary trunk. Cervical origin of the RSA (CoRSA) occurs with the absence of the right 4th PAA and the abnormal persistence of the carotid duct (81). A CoRSA branches as a trifurcation from the RCC high in the neck. The aforementioned subclavian artery defects can also affect the LSA. Aberrant left subclavian artery (ALSA) is frequent with a RAA (79).

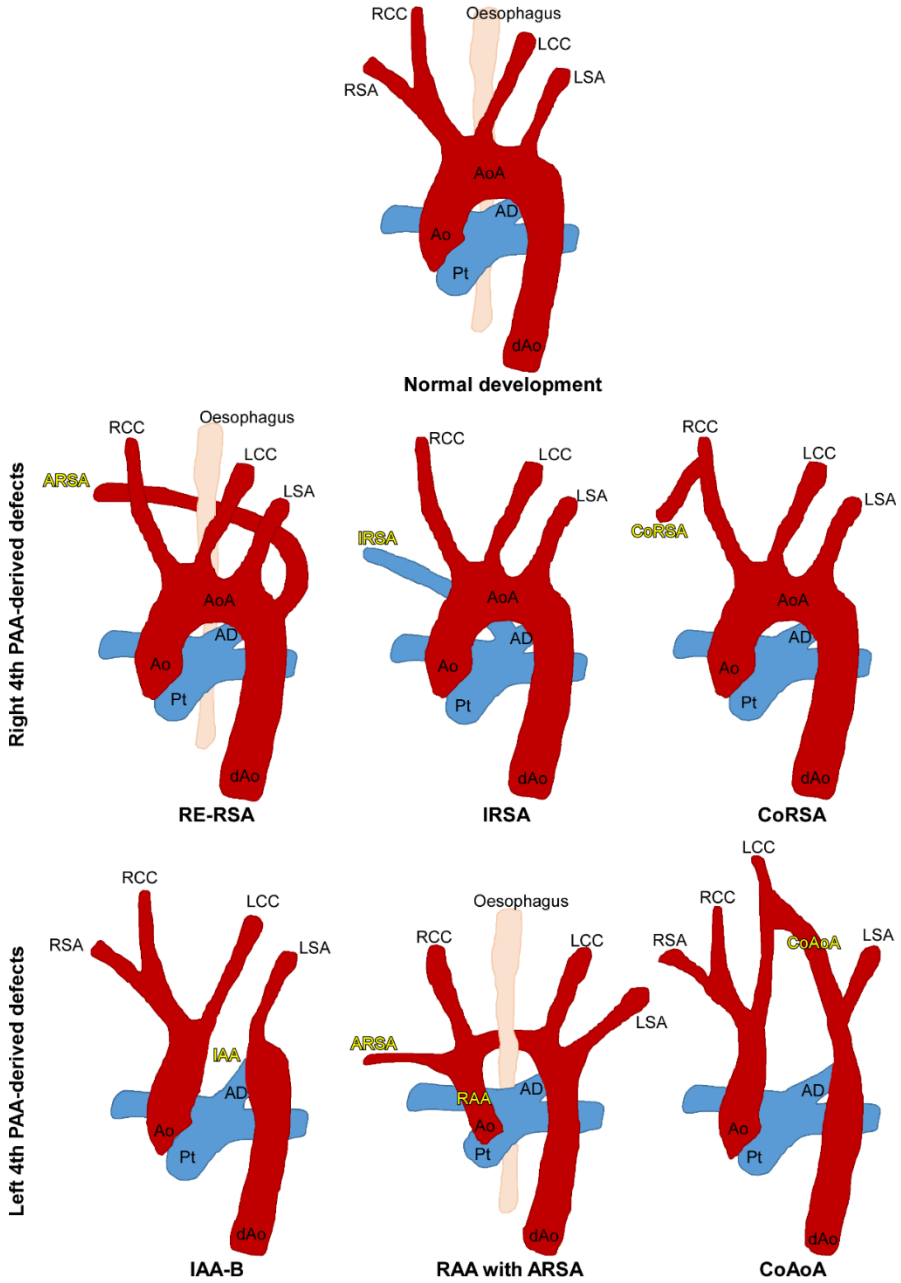

Figure 1.7. Defects derived from the abnormal development of the 4th pharyngeal arch artery.

Normal structure of the aortic arch is shown. Defects to the right 4th PAA affect the subclavian arteries. In RE-RSA, the RSA branches from a distal region of the arch and extends to the right side of the body by passing dorsal to the oesophagus. The RSA branches from the pulmonary trunk in IRSA. A CoRSA branches from the brachiocephalic artery abnormally high in the neck. Defects to the left 4th PAA affect the aortic arch such as IAA with a missing portion of the arch. The arch can be right sided (RAA) or located abnormally high in the neck (CoAoA). Abbreviations: Ao, aorta; AoA, aortic arch; AD, arterial duct; ARSA, aberrant right subclavian artery; dAo, dorsal aorta; CoAoA, cervical aortic arch; CoRSA, cervical right subclavian artery; IAA, interrupted aortic arch; IRSA, isolated right subclavian artery; LCC, left common carotid artery; LSA, left common carotid artery; Pt, pulmonary trunk; RAA, right aortic arch; RE-RSA, retro-oesophageal right subclavian artery; RCC, right common carotid artery; RSA, right subclavian artery.

1.4.1 22q11 deletion syndrome

CHDs occur in 22q11.2 deletion syndrome (DS) which is the most common microdeletion in humans, presenting approximately every 1:4000 live births (82). This microdeletion is linked with several syndromes including DiGeorge Syndrome, velo-cardial syndrome as well as psychiatric disorders (as reviewed in Morrow et al., 2018). The disorder is characterised by facial dysmorphisms, palatal defects, immunodeficiency, speech and learning disabilities as well as cardiovascular defects. Thymus defects are present in 22q11DS which results in immunodeficiency in patients. Parathyroid and endocrine glands, required in calcium and phosphate homeostasis, are also abnormal in 22q11DS patients which results in hypocalcemia.

As the main cause of mortality in 22q11DS, approximately 75% of 22q11DS patients suffer from cardiovascular defects (83, 84). Cardiovascular abnormalities most frequently observed include CAT, tetralogy of Fallot, IAA and VSD (83, 85). The cardiovascular phenotype of 22q11DS patients is varied. In addition to the aforementioned abnormalities, other defects have been observed at a lower frequency including RAA, defects to the subclavian arteries, DORV and TGA (85-89).

In most individuals 22q11DS is a result of a *de novo* deletion between 1.5-3Mb (million base pair) (90). This in turn usually arises due to the non-allelic homologous recombination of low copy repeats (LCRs) on chromosome 22q11.2 (91). Figure 1.8 shows the 22q11.2 region. There are eight LCRs in total (named LCR22A-H) spanning the 22q11.2 region, with 4 LCRs (LCR22A-D) mapping to the 3Mb deletion region. The most common deletion is the 3Mb hemizygous deletion termed LCR22A-D deletion, in which region between LCR22A and LCR22D is lost. This is followed by the shorter 1.5Mb LCR22A-B deletion. 56 protein-encoding genes are known to map to the 3Mb deletion region (92). In addition to this there are seven miRNAs and 10 non-coding genes (91, 92). Of the protein coding genes within this region, *TBX1*, when mutated, has been identified as a leading gene to cause the cardiovascular phenotype in 22q11DS patients (as discussed in section 1.6.2).

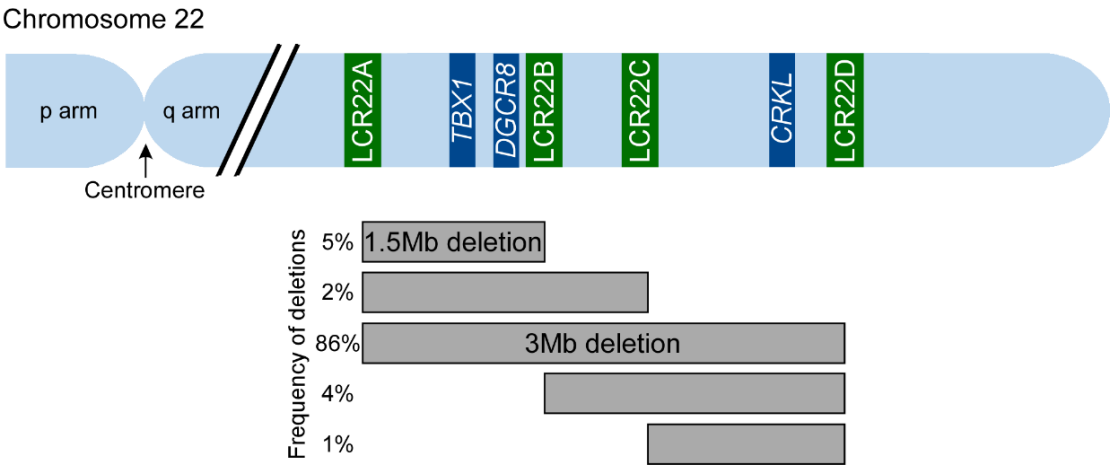

Figure 1.8. The 22q11.2 deletion region.

Schematic of the human 22q11 region showing the location of the LCRs and the common deletions. The reported frequency of the deletions is indicated (91). The 3Mb deletion (LCR22A-D) is the most common in patients. 56 protein-coding genes are included in this deletion, the location of *TBX1, DGCR8* and *CRKL* are shown. Adapted from Lindsay et al., 2001, McDonald-McGinn et al., 2015 and Morrow et al., 2018 (91, 93, 94).

DGCR8, located between LCR22A and LCR22B, is required in the biogenesis of miRNAs. Haploinsufficiency of this gene results in dysregulated miRNA expression in 22q11DS patients therefore disrupting global gene expression. It was proposed that the deletion of *DGCR8* contributes to the neurocognitive, thyroid and cardiovascular defects observed in patients (95).

Another gene of importance in the manifestation of the 22q11DS phenotype is CRK like proto-oncogene (*CRKL*). *CRKL* encodes an adapter protein found within the 3Mb deletion (specifically within the LCR22C-D region) and is required for heart, aortic arch, thymus and parathyroid gland development. Mice null for *Crkl* presented with similar defects found in *Tbx1*-null mice, with CoRSA, IAA and thymus defects, however the 4th PAA-derived defects occurred at a reduced frequency (96). Both these genes are expressed in the PA and it was found that the heterozygous deletion *Tbx1* and *Crkl* in mouse resulted in 22q11DS typical defects (97). The evidence that these genes genetically interact indicates that they act via the same genetic pathway in the manifestiation of 22q11DS.

TBX1 was confirmed as the most likely candidate gene using transgenic mouse models. The *Df1* and *Lgdel* mouse construct has a deletion of over 15 genes, including *Tbx1*, overlapping with the human 22q11 deletion (98-100). Mice heterozygous for

either deletion presented with defects that largely recapitulated the 22q11DS phenotype, with VSD, ARSA and IAA, at a lower penetrance (99, 100). Of the genes in this mouse deletion, *Tbx1* was identified as the cause of the defects as *Tbx1* heterozygosity in mice recapitulated the *Df1* and *Lgdel* heterozygous phenotypes (98, 100).

The large number of genes mutated in the 22q11DS suggests that the phenotype is the result of complex genetic interactions. Approximately 86% of 22q11DS patients have a similar 3Mb deletion however there is high phenotypic variability (91). It has been suggested that there are modifier genes lying outside of this deletion region that contribute to this (101). Further investigations of the genes within and outside of the deletion region are required to investigate the genotype to phenotype relationship of 22q11DS.

1.5 Left-right patterning

Visceral and abdominal organs in vertebrates are positioned asymmetrically, termed *situs solitus* (Figure 1.9). Left-right (L-R) patterning is determined early in embryogenesis and refers to the breaking of symmetry across the L-R body axis (reviewed in Blum et al., 2014). Perturbations in L-R patterning result in defects in the arrangement and structure of these organs, termed heterotaxy. *Situs inversus*, occurring rarely, is the complete mirror arrangement of the visceral and abdominal organs. *Situs ambiguous* is the incomplete reversal of these organs. Heterotaxy can affect the cardiovascular and respiratory system. For example, with right atrial and pulmonary isomerism, the left side of the heart and lungs have failed to adopt their left sided identity. As a result, these organs have a symmetrical structure, both adopting a right sided structure.

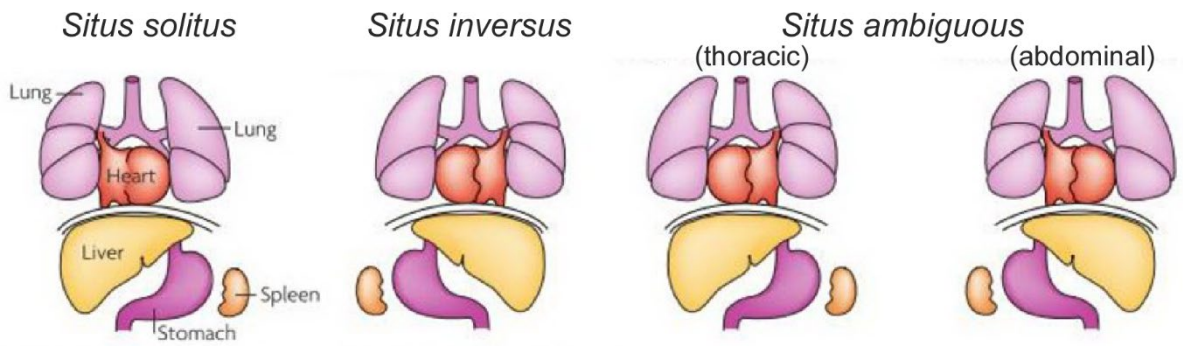

Figure 1.9. Schematic diagram of the left-right body asymmetry and patterning defects.

The normal asymmetric positioning of visceral and abdominal organs is termed *situs solitus*. *Situs inversus* is the complete mirror image reversal of *situs solitus*. *Situs ambigious* is the incomplete reversal of normal organ positions, with only a portion of organs affected. Adapted from Fliegauf et al., 2007 (102).

L-R patterning defects are closely linked with CHDs for example TGA frequently occurs with heterotaxy and has also been linked with 22q11DS (77, 103). Due to inconsistency in the presentation of TGA, its etiology remains uncertain. However, animal models have shown that genes required in L-R patterning are also implicated in the manifestation of TGA (104, 105). Retinoic acid is a signalling molecule necessary for vertebrate development. Altered levels of retinoic acid during embryogenesis have been shown to result in cardiovascular defects; including TGA and DORV (106).

Laterality is established via transient, asymmetric expression of transforming growth factor beta (TGF-β) related proteins. L-R axis determination is initiated via rotating ciliated cells, found at the node of the primitive streak, which cause a leftward nodal flow at E7.5. This nodal flow is required to break symmetry and its absence causes randomised laterality of visceral organs (107, 108).

The induction of signalling molecules within the node activates specific signalling pathways which then allow for the asymmetric morphogenesis of visceral organs. Signals from the node are transferred to the left lateral plate mesoderm (LLPM), where they induce the asymmetric expression of TGF-β related proteins; namely Nodal and Lefty (as reviewed in Shiratori et al., 2014). *Nodal* and *Lefty* are expressed asymmetrically between 2-6 somites in mice. There are two Lefty genes in vertebrates, *Lefty1*, expressed at the midline, and *Lefty2*, in the LLPM. *Nodal* is a left side determinant and its expression in the LLPM induces expression of *Lefty1* and *Lefty2*.

The transient asymmetric expression between these genes is maintained through their stimulatory and antagonist feedback interactions. *Nodal* positively regulates *Nodal* and *Lefty* expression while *Nodal* is restricted to the left side via antagonism from Lefty. Therefore, as *Lefty* expression increases, it will eventually prevent their expression through repressing *Nodal.*

Nodal initiates signalling via TGF-β receptors resulting in the expression of paired-like homeodomain transcription factor 2 (*Pitx2*), among other key genes. Three isoforms are encoded by the *Pitx2* gene; Pitx2a-c. Of these transcripts, *Pitx2c* is expressed asymmetrically and is responsible for L-R determination (109). *Nodal* induces *Pitx2c* in the LLPM and its expression is maintained throughout development by *Nkx2* (110). *Pitx2c* expression in cells causes their derivatives to adopt a left sided morphology (111). Loss of *Pitx2c* results in right isomerism of bilateral organs as well as malposition of the great arteries, including TGA (30, 112). However, *Nodal* is able to act independently of Pitx2 via other pathways as mice with a homozygous *Pitx2* mutation can present with normal heart looping and positioning of the stomach (113).

Nodal has other downstream targets including *Cited2. Cited2*$^{-/-}$ mice present with abnormal cardiovascular and aortic arch development as well as L-R patterning defects including right atrial and pulmonary isomerism (114). In *Cited2*$^{-/-}$ mice, *Nodal* and *Pitx2* expression in the LLPM was absent, among other key factors of the L-R determinant signalling pathway. *Cited2* is a downstream target of Nodal and is also able to feedback to components of the pathway.

Zic3 is another downstream target of *Nodal*. Patients with X-linked heterotaxy have loss of function mutations in *ZIC3. Zic3* is symmetrically expressed in the node and mice deficient for *Zic3* have cardiovascular and L-R patterning defects (115). A subset of *Zic3*$^{-/-}$ mice presented with abnormal *Nodal* and *Pitx2* expression.

Nodal signalling induces a cascade of lateral pathways with multiple components. Bmp signalling is needed for formation of the node and expression of *Nodal* and *Lefty* (116, 117). Adding to the complexity is the involvement of Notch signalling, which is required upstream to induce *Nodal* expression (118).

Figure 1.10 shows the simplified genetic pathways in L-R patterning. Establishment of laterality is a complex process occurring early in embryogenesis. The manifestation of

L-R patterning defects is therefore not straight forward and could arise at multiple levels of these pathways.

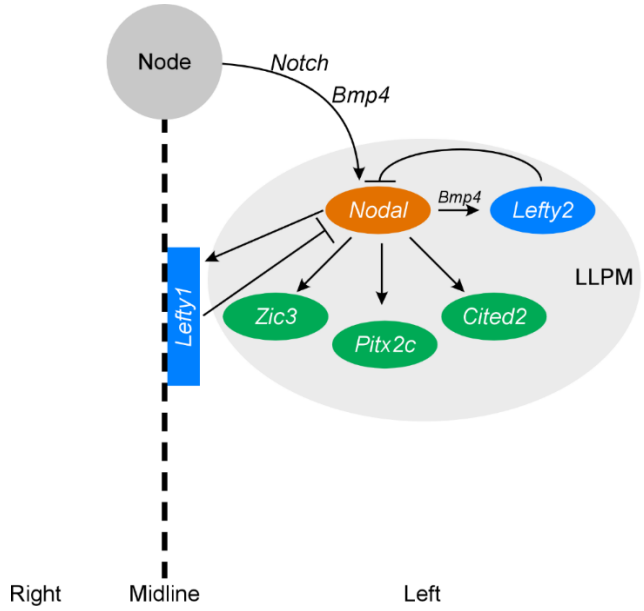

Figure 1.10. Genetic pathway in left-right patterning.

Schematic showing the establishment of laterality initiated in early embryogenesis at the node. Ciliated cells at the primitive streak cause leftward flow which induces signalling pathways from the node. This results in *Nodal* expression in the LLPM which requires Notch and BMP4 signalling. *Nodal* causes *Lefty1* and *Lefty2* expression at the midline and LLPM respectively. *Lefty* antagonises *Nodal* expression. *Nodal* initiates lateral pathways affecting expression of multiple downstream effectors, including *Zic3*, *Pitx2c* and *Cited2*. Adapted from Shiratori et al., 2006 (119).

1.6 *Tbx1*

1.6.1 The T-box gene family

Of the genes in the 22q11DS deletion region, mutations in *TBX1* have been identified as the leading cause of the cardiovascular phenotype. *TBX1* is a member of the T-box gene family which encode transcription factors and are characterised by the T-box domain a conserved DNA-binding domain of 17-26 kilodaltons (kDa) (120, 121). This T-box binding domain binds the T-half site (also termed the T-box binding element), a palindromic consensus sequence (122). The T-box genes each show varying inducing activities which may in part be due to the different preferences for a T-half site of a particular spacing or orientation for each of the T-box proteins (122, 123). T-box genes

generally bind palindromic sequences of the T-box site, however Tbx1 preferentially binds tandem repeats of the sequence (124).

Mutations in T-box genes often result in developmental defects, with the cardiovascular system frequently affected. Mutations in *TBX5* result in Holt-Oram syndrome, in which patients suffer from skeletal and cardiac defects (125). Likewise, *TBX3* mutations are associated with ulnar mammary syndrome which includes cardiac conduction defects (126) and patients with a *TBX20* mutation have atrial septal defect (127). *TBX1* haploinsufficiency, as mentioned, as has been extensively linked with 22q11DS.

Tbx1 is required at multiple stages of development and is expressed throughout embryogenesis. *Tbx1* expression in mice is localised to the mesoderm at E7.5 (128). *Tbx1* is then expressed in the otic vesicle and PA from E8, in the mesoderm, ectoderm and endoderm of the developing embryo (128, 129). Expression is lower at E7.5-8.5 and vastly increases at E9.5 (120), coinciding with the formation of the PAA.

1.6.2 Tbx1 in 22q11 deletion syndrome and cardiovascular development

The necessity of *Tbx1* in embryogenesis has been studied using *Tbx1* mouse models. *Tbx1* deletions result in defects to the cardiovascular system, great arteries, craniofacial region and the thymus, all of which are observed in the 22q11DS phenotype (50, 98, 100). All *Tbx1*$^{-/-}$ mice die at birth with CAT, a severe cardiovascular defect in which the OFT has failed to septate and RAA was also observed (50). Additionally, homozygous mutants had a cleft palate, absent thymus and parathyroid glands. Craniofacial defects affecting the neck region, facial structure and ears were present.

These defects occur due to the failed segmentation of the PA, from which the craniofacial region, thymus and great vessels form (50). The 3rd, 4th and 6th PAA fail to form in *Tbx1*$^{-/-}$ mutants and the dorsal aorta connects directly to the aortic sac (Figure 1.11).

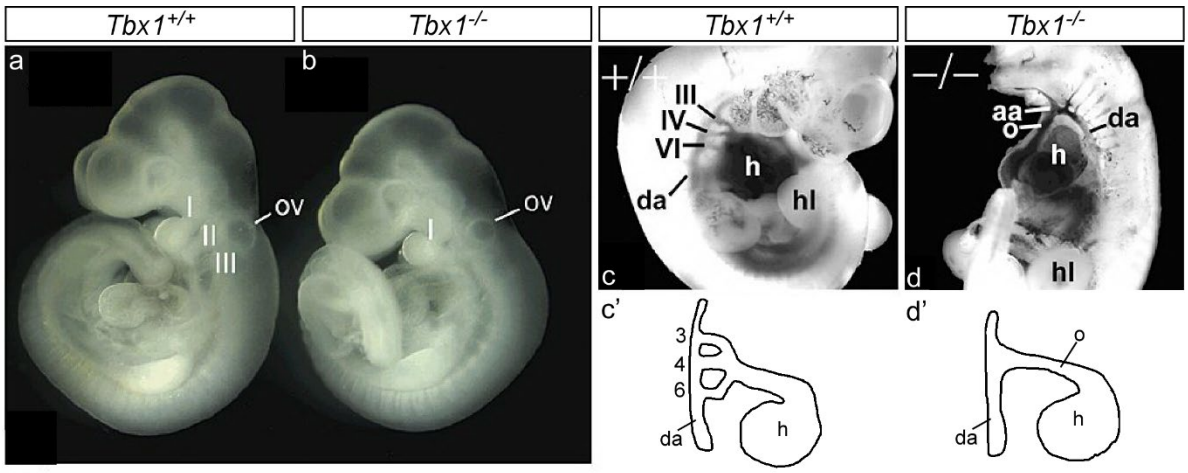

Figure 1.11. Pharyngeal arch and pharyngeal arch artery defects in *Tbx1*-null mice.

The PA are externally visible in the wild type embryo at E10.5 (a). The caudal PA are absent in *Tbx1*$^{-/-}$ embryos (b) due to failed segmentation of the PA. Lateral view of wild type embryo with intracardiac ink injection showing the PAA (numbered) at E10.5 (c) with a diagram of this structure (c'). In *Tbx1*$^{-/-}$ embryos (d), the PAA do not form and a single OFT connects the aortic sac to the dorsal aorta (d'). Abbreviations: aa, aortic arch; da, dorsal aorta; h, heart; hl, hind limb; o, outflow tract; ov, otic vesicle. Adapted from Jerome and Papaioannou (2001) (50).

The *Tbx1*$^{-/-}$ mouse model presents with the phenotypic characteristics observed in the spectrum of defects associated with 22q11DS, however the defects that occur in this mouse are more severe than observed in patients. The *Tbx1* heterozygous mouse model is arguably more reflective of the phenotype observed in patients.

Tbx1$^{+/-}$ mice present with thymus and cardiovascular defects typical of 22q11DS, though at a reduced penetrance when compared to *Tbx1*$^{-/-}$ mutants (53, 97, 130-134). *Tbx1*$^{+/-}$ mice largely have non-lethal defects and are consequently viable. Aberrant origin of the subclavian arteries, with RE-RSA and CoRSA, are frequent defects in *Tbx1*$^{+/-}$ mice. Severe defects, such as IAA, occur in these mice at a reduced frequency. These defects are derived from abnormal 4th PAA development which are hypoplastic or absent in *Tbx1*$^{+/-}$ mutants (34, 50, 53, 98, 129, 130). Defects to the left and right 4th PAA results in IAA and abnormal RSA, respectively.

These defects to the 4th PAA in *Tbx1*$^{+/-}$ mice occur due to the failed formation of smooth muscle around the vessel (130). *Tbx1* is required to signal to post-migratory NCC in the PA to induce differentiation of NCC into smooth muscle cells (23, 135). This lack

of signal in *Tbx1*$^{+/-}$ mutants results in the complete loss or delayed formation of smooth muscle cells around the 4th PAA.

In the *Tbx1*$^{+/-}$ mutants, the frequency of 4th PAA defects is greater at mid-embryogenesis than the aortic arch defects observed later in development. This decrease in defects is well documented in the literature and indicates that the 4th PAA is able to recover during embryogenesis (130). Table 1.1 summarises the penetrance of defects in *Tbx1*$^{+/-}$ mutants throughout development in published data. From E10.5, the penetrance of 4th PAA defects decreases during development, and by E14.5-neonate stage, the penetrance of defects is significantly reduced (chi-squared, $p<0.00001$).

Table 1.1. Penetrance of 4th pharyngeal arch artery defects in *Tbx1*$^{+/-}$ mutants during embryogenesis from published data.

Penetrance of defects are presented as the mean penetrance from the available studies with 95% confidence intervals.

Stage	Penetrance of defects	Reference
E10.5-11	82% (63%-100%) n=127	(56, 97, 130-134)
E11.5	63% (51%-74%) n=76	(34, 130)
E12.5	53% n=30	(125)
E13.5	46% n=30	(34)
E14.5-P2	33% (22-44%) n=181	(34, 56, 97, 129, 131-134)

This phenotypic recovery is specific to cardiovascular defects but not to other 22q11DS-typical features. The *Df1* mouse presents with cardiovascular defects at a reduced penetrance compared to that observed in 22q11DS patients, however the

penetrance of thymus and craniofacial defects between the mouse model and patients does not vary (136).

As *Tbx1* is expressed in the all layers of the PA, excluding the NCC, it was unknown as to which specific tissue *Tbx1* expression is required in PAA morphogenesis. Previous studies have investigated the role of *Tbx1* expression within the tissues of the PA using mouse models with the conditional heterozygous deletion of *Tbx1* using different Cre lines (129, 134). Table 1.2 summarises the published data showing the penetrance of 4th PAA defects at E10.5 in these conditional mutants.

Table 1.2. Penetrance of 4th pharyngeal arch artery defects observed in conditional heterozygous *Tbx1* mutants at E10.5 in published data.

Genotype	Tissue with *Tbx1* heterozygous deletion			Penetrance of 4th PAA defects	Reference
	Endoderm	Ectoderm	Mesoderm		
Tbx1$^{+/-}$	Y	Y	Y	82% (n=127)	(56, 97, 130-134)
Tbx1$^{+/f}$;Mesp1Cre			Y	0 (n=19)	(129)
Tbx1$^{+/f}$;Fgf15Cre	Y	Y		20% (n=34)	(129)
Tbx1$^{+/f}$;AP2αCre		Y		75% (n=17)	(132)
Tbx1$^{+/f}$;Pax9Cre	Y			94% (n=17)	(134)

Combining previously published data, 82% of *Tbx1$^{+/-}$* mutants (n=127) have 4th PAA defects at E10.5 (53, 56, 97, 130-134). The heterozygous deletion of *Tbx1* from the mesoderm using *Mesp1Cre* did not result in any 4th PAA defects suggesting that the expression within the mesoderm is not essential for 4th PAA formation (129). *Fgf15Cre* was used to delete *Tbx1* from the endoderm and ectoderm, resulting in 20% of

embryos (n=34 examined) with a 4th PAA defect (129). This shows that *Tbx1* expression in the pharyngeal epithelia contributes to 4th PAA formation.

Tbx1$^{+/f}$*;AP2αCre* embryos had 4th PAA defects at a penetrance of 75% (n=17 examined), similar to that observed in global *Tbx1*$^{+/-}$ mutants. *AP2αCre* is expressed in the pharyngeal ectoderm and NCC, however as *Tbx1* is not expressed in NCC (128) any defects that occurred can be attributed to the deletion from the ectoderm. Deletion of *Tbx1* from the pharyngeal endoderm using *Pax9Cre* also recapitulated the penetrance of 4th PAA defects in *Tbx1*$^{+/-}$ mutants (134).

The *Tbx1*$^{+/f}$*;AP2αCre* and *Tbx1*$^{+/f}$*;Pax9Cre* mutants were also assessed at E15.5 (Table 1.3). All conditional ectoderm mutants (*Tbx1*$^{+/f}$*;AP2αCre*) had normal cardiovascular defects, while 44% of endoderm mutants (*Tbx1*$^{+/f}$*;Pax9Cre*) were abnormal. The decrease in defects from mid-embryogenesis to late development is likely due to the recovery of the 4th PAA phenotype (130). At late development and neonatal stages, 33% (n=181 collectively examined) of *Tbx1*$^{+/-}$ had cardiovascular defects. Therefore, of these mutants, deletion of *Tbx1* from the pharyngeal endoderm using *Pax9Cre* most closely recapitulated the *Tbx1*$^{+/-}$ phenotype. *Tbx1*$^{+/f}$*;Pax9Cre* mice are also heterozygous for *Pax9*, and the interaction between *Tbx1* and *Pax9* likely increased the penetrance of defects. Nonetheless, this suggests that *Tbx1* and *Pax9* interact in the endoderm during 4th PAA morphogenesis.

Table 1.3. Penetrance of cardiovascular defects observed in conditional heterozygous *Tbx1* mutants at E15.5-P2 in published data.

Genotype	Tissue with *Tbx1* heterozygous deletion			Penetrance of defects at E15.5-P2	Reference
	Endoderm	Ectoderm	Mesoderm		
***Tbx1*$^{+/-}$**	Y	Y	Y	33% (n=181)	(34, 56, 97, 129, 131-134)
Tbx1*$^{+/f}$*;AP2αCre		Y		0 (n=9)	(132)
Tbx1*$^{+/f}$*;Pax9Cre	Y			44% (n=34)	(134)

The varied phenotype observed in 22q11DS patients has led to the suggestion that there are additional genes present outside the deletion region that are also involved in the disorder (101). Transcriptome analysis of the PA of *Tbx1*$^{-/-}$ mice identified differentially expressed genes that were affected by the loss of *Tbx1* (137). This included the downregulation of *paired box 9* (*Pax9*) and *gastrulation brain homeobox 2* (*Gbx2*), transcription factors located outside of the 22q11 deletion region.

1.7 *Pax9*

1.7.1 The paired box gene family

PAX9, found on ch.14q13.3 in humans, belongs to the PAX family of transcription factors which are required during mammalian embryonic development (138). *PAX* genes are primarily expressed during embryogenesis. There are nine genes identified, divided into four groups, all of which share a common motif (139). This motif, the DNA-binding paired domain, is 128 amino acids long and binds specific sequences of DNA (140).

The *PAX* genes vary in the presence of other conserved regions, namely the full homeodomain, the partial homeodomain and the octapeptide motif, which determines to which subgroup they belong (141). Subgroup 1 consisting of *Pax1* and *Pax9* have the octapeptide sequence. *Pax3* and *Pax7*, subgroup 2, encode the full homeodomain and the octapeptide sequence. Subgroup 3 consists of *Pax2*, *Pax5* and *Pax8*, which have a partial homeodomain and the octapeptide motif. The 4th subgroup consists of *Pax4* and *Pax*6, which lack the octapeptide sequence but encodes the full homeodomain (141). The domains present in the PAX proteins allows them bind enhancers to modify downstream transcriptional activity. Table 1.4 summarises the subclasses of *PAX* genes and their chromosome locations.

Table 1.4. Summary of the nine *PAX* genes showing which structural regions are present in each and their chromosomal locations in human and mouse.

Chromosomal locations taken from Wang et al., 2008 (142).

***PAX* gene**	**Subgroup**	**Structural regions present**				**Chromosomal location**	
		Paired domain	**Full homeo-domain**	**Partial homeo-domain**	**Octapeptide motif**	**Human**	**Mouse**
1	I	+	-	-	+	20p11	2
2	III	+	-	+	+	10q25	19
3	II	+	+	-	+	2q35	1
4	IV	+	+	-	-	7q32	6
5	III	+	-	+	+	9p13	4
6	IV	+	+	-	-	11p12	2
7	II	+	+	-	+	1p36.2	4
8	III	+	-	+	+	2q12-14	2
9	I	+	-	-	+	14q12-13	12

The *PAX* genes are required for organogenesis during development. The analysis of human disease and the use of mouse models has implicated various *PAX* genes in the manifestation of genetic syndromes. For example, *PAX2* is needed in the development of the urogenital tract, eyes, ears and central nervous system and *Pax2* knockout mice have hypoplastic kidneys, among other defects to the urogenital tract (143). Patients with heterozygous *PAX2* mutations have renal hypoplasia (144). *PAX3* mutations result in Waardenburg syndrome, characterised by deafness and pigment alterations (145, 146). Chromosomal deletions and mutations that include *PAX9* have resulted in hypodontia, oligodontia, cleft palate and hypothyroidism (147, 148).

Pax9 is a 5 exon gene that maps to ch.12 in mice (149). Exon 3 contains the largest coding region and the paired domain, required for DNA binding. This transcription factor is expressed during embryogenesis and, to a lesser extent, in the adult thymus (150, 151). *Pax9* is expressed from E8.5 in the pharyngeal endoderm, which is required in the formation of the thymus, parathyroid gland and ultimobranchial bodies, structures that fail to form in *Pax9*$^{-/-}$ mice (151, 152). *Pax9* is also expressed in the vertebral column, somites, limb buds, developing nasal process and the NCC-derived mesenchyme that forms the craniofacial regions (151-153). *Pax9* has a role in limb, craniofacial and tooth development and *Pax9*$^{-/-}$ mice die at birth with cleft palate, oligodontia and a supernumary preaxial digit (152). Figure 1.12 shows the defects present in *Pax9*$^{-/-}$ mice.

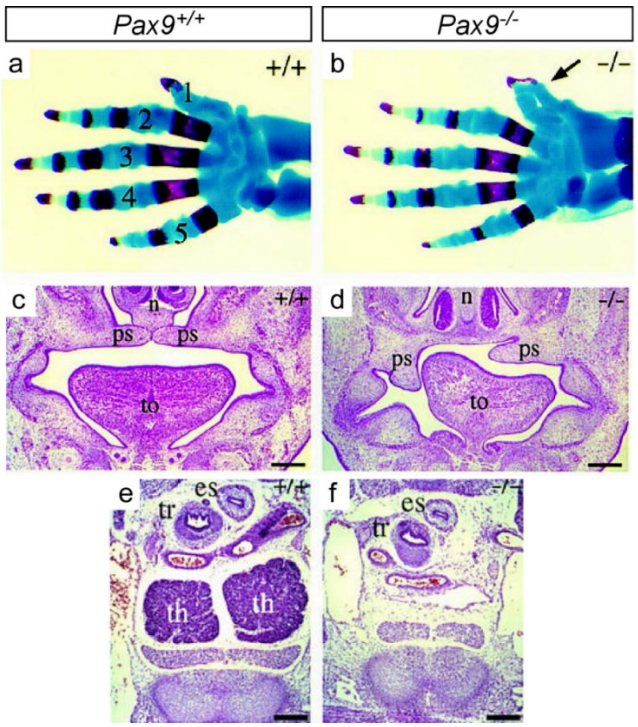

Figure 1.12. Non-cardiovascular defects present in *Pax9*$^{-/-}$ mice.

Skeletal staining of mouse forelimbs (a,b) shows pre-axial digit duplication in *Pax9*$^{-/-}$ mice (b). Coronal sections of wild type embryo (c) shows fused palatal shelves (ps) and tooth (to) formation. The palatal shelves fail to fuse in *Pax9*$^{-/-}$ mice resulting in a cleft palate and tooth development is abnormal (d). The bilobed thymus (th) is normal in wild type embryo (e) but absent in *Pax9*$^{-/-}$ mice (f). Abbreviations: ps, palatal shelf; th, thymus; to, tooth. Adapted from Peters et al., 1998 (152).

1.7.2 Pax9 in cardiovascular development

As well as resulting in oligodontia and craniofacial defects, mutations in *PAX9* have also been implicated in cardiovascular defects. A patient presented with both IAA and the heterozygous deletion of *PAX9* (147). The patient had a small deletion of only three genes (*PAX9*, *NKX2.1*, *NKX2.8*) and had severe cardiovascular defects which included IAA-B, VSD and hypoplasia of the aorta. As *Nkx2.1* and *Nkx2.8* deletions do not result in cardiovascular defects in mice, these genes were excluded as the cause of the cardiovascular phenotype in the patient (154, 155). Schuffenhauer et al. (1999) additionally describe a patient with a proximal ch.14q deletion, which includes *PAX9*, which presented with CAT and pulmonary stenosis.

Previous work in the laboratory used a *Pax9*$^{-/-}$ mouse model to determine the role of *Pax9* in cardiovascular development (134). Analysis of mutant embryos confirmed cardiovascular defects to be the cause of death in these mice. All *Pax9*$^{-/-}$ mice had

cardiovascular defects including: IAA, hypoplastic aorta, ARSA or IRSA, DORV, VSD and absent common carotid arteries (Figure 1.13). These defects overlap with the phenotype of the patient described above.

The defects to the great arteries stemmed from the aberrant formation of the PAAs. By E10.5 in normal development, the 1st and 2nd PAA have regressed leaving the bilaterally symmetrical 3rd, 4th and 6th PAAs. In *Pax9*$^{-/-}$ mice, the 4th PAA was absent at E10.5, resulting in ARSA and IAA later in development. The 3rd PAA was hypoplastic and the 1st and 2nd PAA were abnormally persistent which resulted in the absence of the common carotid arteries. The internal and external carotid arteries branch directly from the great arteries as a result.

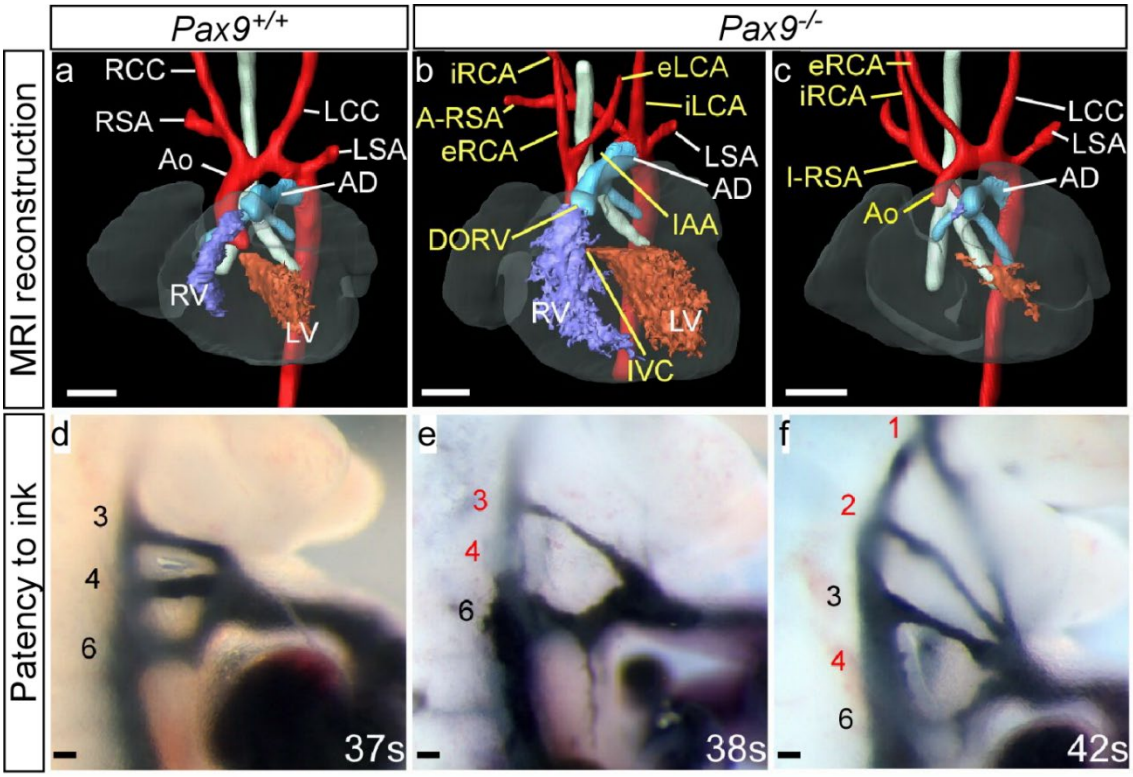

Figure 1.13. Cardiovascular and pharyngeal arch artery defects in *Pax9*-null mice.

Pax9$^{-/-}$ mice have IAA, ARSA, DORV with IVC and absent common carotid arteries resulting in the internal and external carotid arteries branching directly from the great arteries (b). Mutants also have IRSA at a reduced penetrance (c). These defects stem from the aberrant formation of the PAA as shown by intracardiac ink injection. The 4th is absent and the 3rd is frequently hypoplastic in mutants (e,f). The 1st and 2nd PAA regress by E10.5 in wild type mice (d) while they abnormally persist in *Pax9*$^{-/-}$ mice (f). Abbreviations: AD, arterial duct; ALSA, aberrant left subclavian artery; Ao, aorta; ARSA, aberrant right subclavian artery; dAo, dorsal aorta; DORV, double outlet right ventricle; eLCA, external left carotid artery; eRCA, external right carotid artery; IAA, interrupted aortic arch; iLCA, internal left carortid artery; iRCA, internal right carotid

artery; IVC, interventricular communication; LCC, left common carotid artery; LSA, left subclavian artery; LV, left ventricle; RAA, right aortic arch; RCC, right common carotid artery; RSA, right subclavian artery; RV, right ventricle. Adapted from Phillips et al., 2019 (134).

The defects to the caudal PAAs occurred due to reduced smooth muscle investment around these vessels at mid-embryogenesis. NCC differentiate into smooth muscle to support the developing PAA (23) and there were fewer NCC in the 3rd and 4th PA of *Pax9*$^{-/-}$ embryos at E10.5 (134). Consequently, the hypoplastic 3rd PAA was unsupported and collapsed during development. This data confirms the necessity of *Pax9* in PAA morphogenesis and cardiovascular development.

RNA-seq analysis of the pharyngeal region in *Pax9*$^{-/-}$ mice revealed 3863 significantly differentially expressed genes, including the downregulation of *Tbx1* (134). Likewise, *Pax9* was downregulated in *Tbx1*$^{-/-}$ mice (137). Combining the transcriptome analysis of these mutants identified 342 significantly differentiated genes which showed common targets of *Tbx1* and *Pax9* and suggests that these genes act through a common genetic network (134).

This interaction during cardiovascular development was investigated using *Tbx1*$^{+/-}$*;Pax9*$^{+/-}$ mice, which presented with a significantly increased penetrance of 4th PAA defects, including IAA, compared to *Tbx1*$^{+/-}$ mice (134). *Tbx1*$^{+/-}$*;Pax9*$^{+/-}$ mice presented with similar defects to *Tbx1*$^{+/-}$ mice (Figure 1.14), including ARSA, but to a higher penetrance.

Tbx1 is expressed in the endoderm, ectoderm and mesoderm of the PA (128), while *Pax9* is only expressed in the pharyngeal endoderm (134). As both of these genes are expressed in the pharyngeal endoderm of the PA, it was inferred that these genes may function cell-autonomously within this tissue during 4th PAA morphogenesis. The conditional heterozygous deletion of *Tbx1* and *Pax9* in the pharyngeal endoderm in *Tbx1*$^{+/f}$*;Pax9Cre* mice recapitulated the 4th PAA defects in *Tbx1*$^{+/-}$*;Pax9*$^{+/-}$ mice, confirming the role of the pharyngeal endoderm in cardiovascular development (134) (Figure 1.14). This phenotyping and transcriptome analysis suggest that *Tbx1* and *Pax9* function non-hierarchically in 4th PAA morphogenesis and implicates *Pax9* as a 22q11DS phenotype modifier.

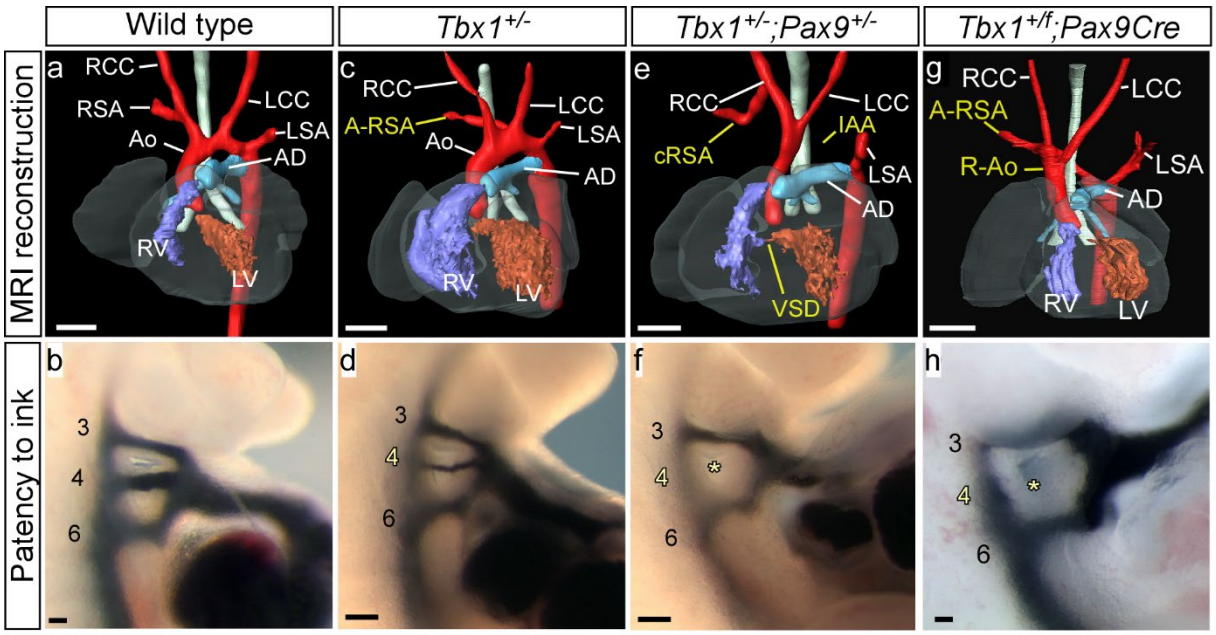

Figure 1.14. *Tbx1* and *Pax9* interact in the pharyngeal endoderm during cardiovascular development.

Tbx1$^{+/-}$;*Pax9*$^{+/-}$ mice (e) had a greater incidence of IAA compared to *Tbx1*$^{+/-}$ mice (c). *Pax9* heterozygosity resulted in a more severe 4th PAA defect in double heterozygous mice (f) compared to *Tbx1*$^{+/-}$ mice (d). The heterozygous deletion of *Tbx1* and *Pax9* in the pharyngeal endoderm (g,h) recapitulated the defects observed in the *Tbx1*$^{+/-}$;*Pax9*$^{+/-}$ global mutants. Adapted from Phillips et al., 2019 (134).

Transcriptome analysis showed the significant downregulation of *Gbx2* in *Tbx1*$^{-/-}$ and *Pax9*$^{-/-}$ mice, suggesting that this gene is a shared downstream target (134, 137). *Gbx2* is a transcription factor expressed in the PA during development with multiple roles in embryogenesis, discussed in the next section.

1.8 *Gbx2*

1.8.1 The gastrulation homeobox gene family

Gbx2 encodes a homeodomain transcription factor. The homeobox, first identified in drosophila, is a DNA sequence of 180 base pairs (156). Homeobox genes encode transcription factors and are characterised by a conserved 60 amino acid DNA-binding domain, termed the homeodomain (157). *GBX1* and *GBX2* are homeobox genes mapped to human ch.7q36 and ch.22q37 respectively that are required in the regulation of embryonic central nervous system development (158).

Gbx1, mapping to ch.5 in mice, is expressed in the developing central nervous system from E8.25, at the ventral zone of the spinal cord at E10.5 and then becomes restricted to the dorsal mantle zone by E12.5 (159). *Gbx1* is needed in the development of the interneurons and motor neurons. *Gbx1*$^{-/-}$ mice survive development but display locomotive defects due to disorganised sensory circuitry in the spinal cord (160, 161).

Gbx2 has 2 exons, with the homeodomain located in exon 2 (162) and is mapped to ch.1 in mice. *Gbx2* is expressed early in embryogenesis during gastrulation at E6 in all germ layers of the posterior region of the embryo (163, 164). From E8.5 *Gbx2* is evident in the pharyngeal endoderm and ectoderm of the PA as well as the mid-hindbrain boundary. From E11.5 *Gbx2* expression is essentially restricted to the central nervous system (163).

To date, there are no cases reported that link human *GBX2* mutations to defects or syndromes. However, mutation studies in mouse embryos have shown that *Gbx2* is required for the specification of the mid-hindbrain; needed for both the correct specification and the normal proliferation of anterior hindbrain precursors at the neural plate stage (165). *Gbx2*-null mice die shortly after birth with irregular brain development including an absent cerebellum. The deletion of *Gbx2* also modified the expression of *Fgf8* and *Wnt1*, both required for the development of the mid-hindbrain organiser.

1.8.2 Gbx2 in cardiovascular development

Investigation of the *Gbx2*$^{-/-}$ mouse has also shown a role of *Gbx2* in cardiovascular development and formation of the great arteries (133, 166). *Gbx2*$^{+/-}$ mice have normal development, but the homozygous deletion of *Gbx2* results in IAA, RAA and ARSA in late term embryos, correlating with absent and hypoplastic 4th PAAs found at E10.5 (133, 166). DORV with IVC was also present in *Gbx2*$^{-/-}$ mutants.

Byrd and Myers (2005) reported NCC migration defects in *Gbx2*-nulls, in which the NCC migrations streams from the spinal cord to the PA were fused and there was consequently fewer NCC in the 4th PA. This disrupted NCC migration did not result in reduced smooth muscle around the PAA, however there was disorganisation of the endothelial cells of the 4th PAA which results in defects to these vessels.

Gbx2 is expressed in the pharyngeal endoderm and ectoderm of the PA (164). Calmont et al. (2009) used conditional mutants to investigate the role of *Gbx2* expression in the

PA epithelia. Table 1.5 summarises the frequency of 4th PAA defects at E10.5 in the *Gbx2*$^{-/-}$ global and conditional mutants.

Table 1.5. Penetrance of 4th pharyngeal arch artery defects observed in conditional homozygous *Gbx2* mutants at E10.5 in published data.

Genotype	Tissue with *Gbx2* homozygous deletion		Penetrance of 4th PAA defects	Reference
	Endoderm	Ectoderm		
***Gbx2*$^{-/-}$**	Y	Y	50% (n=12)	Calmont et al., 2009
Gbx2*$^{f/-}$*;Tbx1Cre	Y	Y	27% (n=11)	
Gbx2*$^{f/-}$*;AP2αCre		Y	47% (n=15)	

Tbx1Cre was used to remove *Gbx2* expression from *Tbx1* expression domains, the endoderm, ectoderm and mesoderm of the PA. As *Gbx2* is not expressed in the pharyngeal mesoderm, any 4th PAA defects present were attributed to the loss of expression from the epithelial layers (164). The frequency of 4th PAA defects in *Gbx2*$^{f/-}$*;Tbx1Cre* mice (27%, n=11 examined) did not recapitulate the defects observed in *Gbx2*$^{-/-}$ mice (50%, n=12 examined). This was likely due to the low efficiency of *Tbx1Cre* recombination in the epithelial layers, which showed chimeric expression of this transgene (133).

The conditional deletion of *Gbx2* from the pharyngeal ectoderm was sufficient to recapitulate the 4th PAA defects observed in global *Gbx2* mutants, with 47% (n=15 examined) of *Gbx2*$^{f/-}$*;AP2αCre* mice showing 4th PAA defects (133). *AP2αCre* is expressed in the pharyngeal ectoderm and NCC, however *Gbx2* is not expressed in NCC (164). The defects in NCC migration observed in *Gbx2*$^{-/-}$ mice were also present in the conditional ectoderm mutants, suggesting that ectodermal *Gbx2* expression is essential in 4th PAA morphogenesis (133). However, the study chose not investigate the conditional ectoderm mutants later in development, reasoning that the 4th PAA phenotype recovers overtime (130). The deletion of *Gbx2* from the ectoderm may not recapitulate the defects observed in late gestation of *Gbx2*$^{-/-}$ mice. Additionally, in

Tbx1$^{-/-}$ embryos, the downregulation of *Gbx2* is more specific to the endoderm (133, 137), therefore the role of the endoderm cannot be excluded.

Gbx2 interacts with other genes known to be required in cardiovascular development (166). *Fgf8*, part of the extracellular signalling Fgf family, has many roles in embryogenesis including heart development and is expressed with *Gbx2* in the pharyngeal endoderm and ectoderm (166). *Fgf8* mutants have OFT defects including DORV and TGA, as well as 4th PAA defects, such as IAA, RAA and ARSA (61). *Gbx2* has been identified as a downstream target of *Fgf8* as *Fgf8* heterozygosity increased the penetrance of cardiovascular defects in *Gbx2*$^{-/-}$ mice. Additionally, while *Gbx2*$^{+/-}$ and *Fgf8*$^{+/-}$ mice show normal development, the combined heterozygosity in *Gbx2*$^{+/-}$*;Fgf8*$^{+/-}$ mice resulted in cardiovascular defects, such as RAA and ARSA (166). This is reminiscent of the interaction between *Tbx1* and *Fgf8*, as *Fgf8* heterozygosity increased the severity of the *Tbx1*$^{+/-}$ cardiovascular phenotype in mice (56).

Gbx2 and *Tbx1* are both expressed in the pharyngeal epithelial layers, and *Gbx2* is a confirmed a downstream target of *Tbx1* (128, 166). As mentioned, *Gbx2* is downregulated in the PA of *Tbx1*$^{-/-}$ mice (137). Calmont et al. (2009) investigated the interaction between these genes in heart development, observing an increase in 4th PAA and cardiovascular defects in *Tbx1*$^{+/-}$*;Gbx2*$^{+/-}$ mice compared to *Tbx1*$^{+/-}$ mice.

T-box sites have been identified within the *Gbx2* locus through which *Tbx1* can regulate *Gbx2* expression (167). Caprio et al. (2014) identified a T-box site in *Gbx2* that *Tbx1* occupies to control *Gbx2* expression by regulating the interaction of transcription factors with *Gbx2*. This region also contains a P53 binding site, through which P53 binds to recruit polycomb repressive complex and the resulting histone methylation causes the silencing of *Gbx2* expression (167). This binding of P53 was dependent on the presence of *Tbx1* suggesting that *Tbx1* occupies *Gbx2* to facilitate transcription factor binding to *Gbx2*.

Pax9 is required in cardiovascular development and has been identified as a potential modifier of the 22q11DS phenotype based on its interaction with *Tbx1* (as discussed in section 1.7.2). *Gbx2* is shared target of *Tbx1* and *Pax9*, downregulated in both *Tbx1*$^{-/-}$ and *Pax9*$^{-/-}$ mutants (134, 137). *Pax9* is also expressed in the pharyngeal endoderm with *Gbx2* however the interaction between these genes has not been investigated.

There is an extensive genetic network within the PA required for PAA morphogenesis and cardiovascular development. Collectively, the studies discussed here have identified the independent requirement of *Tbx1*, *Pax9* and *Gbx2* in the morphogenesis and remodelling of the PAA to form the aortic arch system. As *Tbx1*, *Pax9* and *Gbx2* mutants share an overlapping phenotype with defects primarily affecting the 4th PAA, it could be postulated that these genes share a common network during PAA formation and remodelling.

In the context of the *Gbx2* deletion, the requirement of the ectoderm as a signalling centre has been a point of focus, however the role of *Gbx2* within the pharyngeal endoderm is yet to be studied. As *Pax9* is expressed in only the endoderm of the PA, it is likely that expression in this domain has a key involvement in cardiovascular development. *Tbx1* is also expressed in the endoderm and this tissue provides signalling cues during development (discussed in section 1.2.4). Studies have identified an interaction of *Pax9* and *Gbx2* with *Tbx1*, however the interaction between *Pax9* and *Gbx2*, along with the role of the pharyngeal endoderm, remains undetermined.

1.9 Aims and hypothesis

Patients with 22q11DS present with a broad spectrum of defects, it is therefore postulated that modifier genes lie outside of the deletion region to affect the phenotype. *Gbx2* and *Pax9* have been confirmed to be implicated in cardiovascular development, required for the remodelling of the PAA into the aortic arch system. The precise pathways required during vessel morphogenesis is not completely understood, this project aims to elucidate the complex *Tbx1-Pax9-Gbx2* genetic network and interactions required for the correct development of the cardiovascular system with greater focus on the interaction between *Gbx2* and *Pax9,* within the pharyngeal endoderm, in the formation of the aortic arch arteries.

It is hypothesised that:

Gbx2 and *Pax9* interact cell-autonomously, as part of the *Tbx1* network, within the pharyngeal endoderm in the formation and remodelling of the PAA.

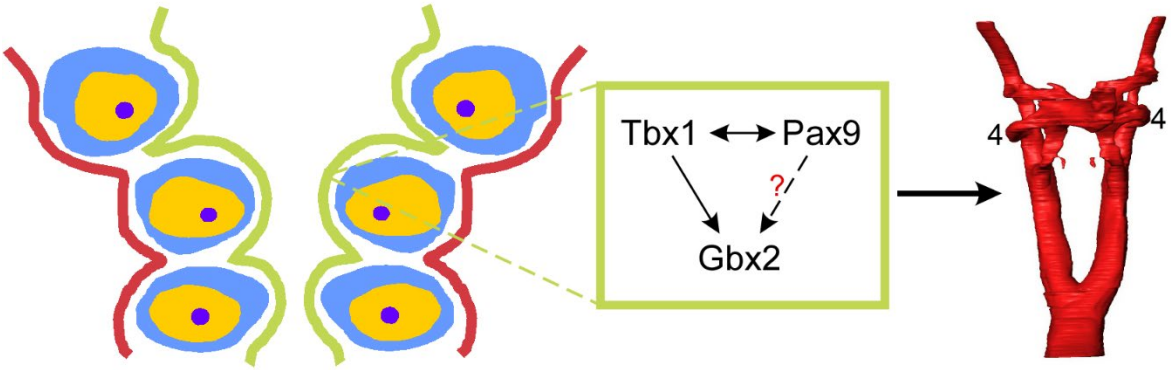

Figure 1.15. Graphical hypothesis.

It is hypothesised that a *Tbx1-Pax9-Gbx2* genetic network exists within the pharyngeal endoderm to control the morphogenesis of the 4th PAA.

The aims of this project are:

1) **To establish the *Gbx2*$^{-/-}$ phenotype on an enriched C57Bl/6 background**

Embryos will be collected at mid-embryogenesis (E10.5) and later in development (E15.5) to perform an in-depth assessment of the PAA and cardiovascular structure.

2) **Investigate the interaction between *Pax9* and *Gbx2* in cardiovascular development**

Wild type, *Pax9*$^{-/-}$ and *Gbx2*$^{-/-}$ embryos will be collected at mid-embryogenesis to analyse *Pax9* and *Gbx2* expression at the time of PAA development to determine gene expression in these mutants.

Embryos with the simultaneous deletion of *Pax9* and *Gbx2* will be collected at E15.5 and E10.5 for phenotyping analysis, the following comparisons will be made:

- *Pax9*$^{+/-}$*;Gbx2*$^{+/-}$ with *Pax9*$^{+/-}$ and *Gbx2*$^{+/-}$, does the combined heterozygosity of *Pax9* and *Gbx2* result in cardiovascular defects?
- *Pax9*$^{+/-}$*;Gbx2*$^{-/-}$ with *Gbx2*$^{-/-}$, does *Pax9* heterozygosity modify the *Gbx2*$^{-/-}$ phenotype?
- *Pax9*$^{-/-}$*;Gbx2*$^{+/-}$ with *Pax9*$^{-/-}$, does *Gbx2* heterozygosity modify the *Pax9*$^{-/-}$ phenotype?
- *Pax9*$^{-/-}$*;Gbx2*$^{-/-}$ with *Pax9*$^{-/-}$ and *Gbx2*$^{-/-}$, do double homozygous mutants display a different phenotype to *Pax9*$^{-/-}$ and *Gbx2*$^{-/-}$ mice?

3) **Investigate the role of *Pax9* and *Gbx2* expression in the pharyngeal endoderm and validate the *Pax9Cre* allele**

The *Pax9Cre* allele will be used with the *Gbx2-flox* allele to remove *Gbx2* expression from the pharyngeal endoderm. The *Pax9Cre* allele will be validated to ensure its specific and successful recombination of floxed alleles. *Gbx2-flox;Pax9Cre* embryos will be collected at E15.5 and E10.5 and compared to *Pax9*$^{+/-}$*;Gbx2*$^{-/-}$ embryos (the global genotype equivalent).

4) Investigate the *Tbx1-Pax9-Gbx2* network

Wild type, *Tbx1*$^{-/-}$, *Pax9*$^{-/-}$ and *Gbx2*$^{-/-}$ embryos will be collected at mid-embryogenesis to analyse *Tbx1*, *Pax9* and *Gbx2* expression at the time of PAA development and determine gene expression in these mutants.

Tbx1$^{+/-}$;*Pax9*$^{+/-}$;*Gbx2*$^{+/-}$ triple heterozygous embryos will be collected at E15.5 to assess the cardiovascular phenotype and determine if *Gbx2* modifies the *Tbx1*$^{+/-}$;*Pax9*$^{+/-}$ phenotype.

An *in vitro* luciferase assay and *in vivo* chromatin immunoprecipitation assay using mouse embryos will be used to determine if Tbx1 and Pax9 can bind and activate the *Gbx2* gene.

Chapter 2. Materials and Methods

2.1 Mouse strains and breeding

Mice were maintained on a C57Bl/6J background and obtained from Jackson Laboratories, unless otherwise stated. All mice were euthanised according to the requirements of the Animals (Scientific Procedures) Act 1986 of the UK government.

2.1.1 Gbx2 mice

Schematic diagrams of the *Gbx2* alleles are shown in Figure 2.1. The *Gbx2* floxed allele has been previously described (168). To create the *Gbx2* floxed allele, a neomycin cassette was used for gene targeting. This neomycin cassette was flanked with *Frt* sites and was removed by Flpe-mediated DNA recombination to create the floxed allele.

The *Gbx2* floxed allele functions as a wild type allele (168). *loxP* sites are positioned in-between exon 1 and 2 and in the non-coding region of exon 2. Cre-mediated recombination of the floxed allele results in the generation of the delete allele in which the majority of exon 2, including the homeodomain, is deleted.

To create the *Gbx2* delete (*Gbx2*$^{-}$) allele, mice carrying a *Gbx2* floxed allele were crossed with *Sox2Cre* transgenic mice. *Sox2Cre* mice express *Cre* recombinase under the control of the *Sox2* promoter, which is active at gastrulation in all embryonic tissues. Mice carrying the *Gbx2* delete allele were then crossed with wild type mice to propagate the *Gbx2* delete allele through the germline and breed out the *Sox2Cre* allele.

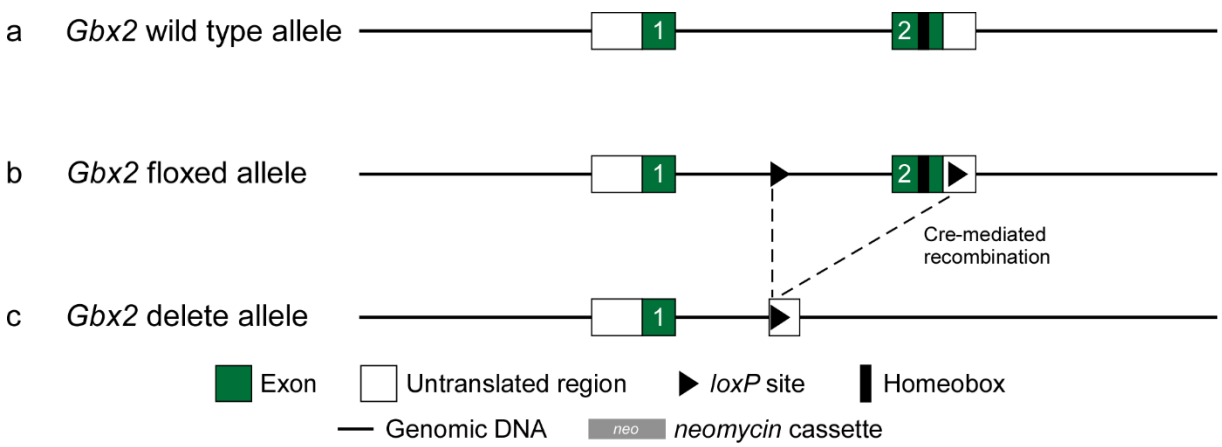

Figure 2.1. Schematic diagrams of the *Gbx2* alleles.

a) Wild type allele with 2 exons. The homeobox is located in exon 2. b) The *Gbx2* floxed allele with a *loxP* site in-between the two exons and a *loxP* site in exon 2. The floxed allele undergoes Cre-mediated recombination to create the delete allele (c). The majority of exon 2, including the homeobox, have been deleted. Adapted from Li et al., 2002 (168).

2.1.2 Pax9 mice

Schematic diagrams of the *Pax9* alleles are shown in Figure 2.2. *Pax9lacZ* mice (152) were obtained from Dr Heiko Peters (Newcastle University, UK). To generate the *Pax9lacZ* allele, the promoterless *Escherichia coli* ATG-lacZ-neomycin-poly(A) cassette was introduced into the ATG-containing exon of *Pax9.* This allowed for *lacZ* expression under the control of the *Pax9* promoter and resulted in a functionally null allele of *Pax9. Pax9*$^{+/-}$ mice carry one copy of the wild type allele and one copy of the *Pax9-lacZ* allele.

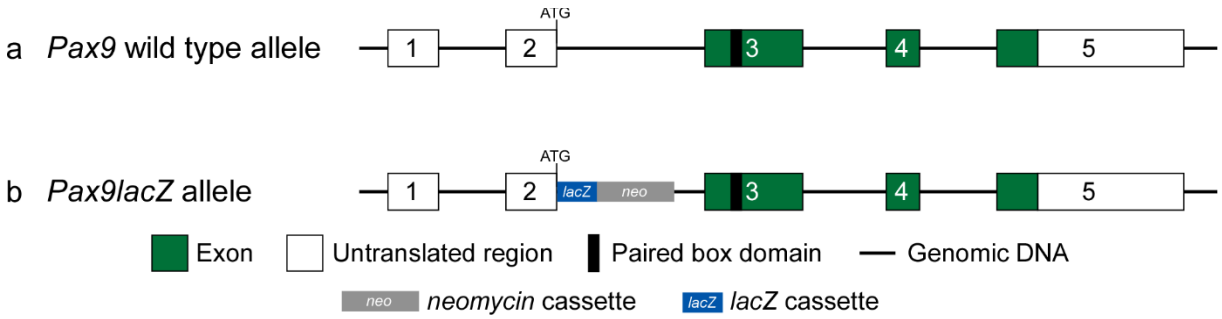

Figure 2.2. Schematic diagrams of the *Pax9* alleles.

a) Wild type *Pax9* allele with 5 exons. The paired box domain is located in exon 3. b) *Pax9lacZ* allele with the *lacZ* and neomycin cassette inserted in-between the ATG-containing exon 2 and exon 3.

2.1.3 Pax9Cre mice

The *Pax9Cre* mouse (134) was obtained from Dr Heiko Peters (Newcastle University, UK). Schematic diagrams of the *Pax9Cre* allele are shown in Figure 2-3. The promoterless *Cre* recombinase gene was inserted, removing the second half of exon 2 and the first half of exon 3. A consensus Kozak sequence was upstream of the *Cre* recombinase gene and *Cre* recombinase is expressed under the control of the *Pax9* promoter. This also generates a functionally null allele of *Pax9.*

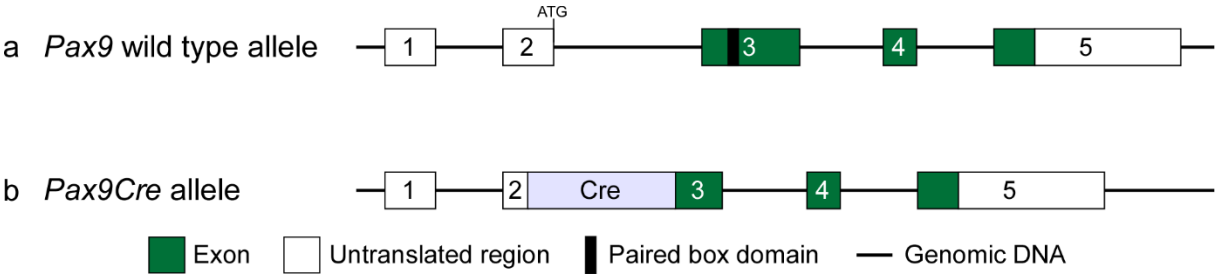

Figure 2.3. Schematic diagrams of the *Pax9Cre* allele.

a) Wild type *Pax9* allele with 5 exons. The paired box domain is located in exon 3. b) *Pax9Cre* allele with the *Cre* recombinase gene inserted. This removes the second half of exon 2 and the first half of exon 3, including the paired box.

2.1.4 Tbx1 mice

The *Tbx1*$^{+/-}$ mouse has been previously described (50). *Tbx1* expression was disrupted by inserting a *loxP*-flanked neomycin cassette into the coding region of *Tbx1*. The targeting cassette replaced the whole *Tbx1* coding region apart from the first 20 amino acids.

2.1.5 eYFP mice

Enhanced yellow fluorescent protein (*eYFP*) reporter mice (*R26ReYFP*) were crossed with *Pax9Cre* mice for the tissue specific investigations of the pharyngeal endoderm. The *eYFP* construct was inserted into the *Rosa26* locus (169) and the stop sequence was flanked by *loxP* sites. Following Cre-mediated recombination, the stop codon is removed and *eYFP* is expressed in the *Cre* expressing tissues.

2.1.6 lacZ mice

The *R26RlacZ* reporter mouse (170) was used to study the expression of *Pax9Cre.* This mouse contains a *lacZ* construct which has a stop codon flanked by *loxP* sites. Following Cre-mediated recombination, the stop codon is removed and *lacZ* is expressed in the *Cre* expressing tissues.

2.2 Embryo dissection

Embryos were collected at time points specific to each experiment with E0.5 defined as noon of the day the vaginal plug was detected. Pregnant females were euthanised according to Schedule 1 via cervical dislocation. The uterus was then dissected and collected in phosphate buffered saline (PBS, pH7.0) or pre-warmed balance HANK solution with EDTA for magnetic resonance imaging (MRI). For E8.5-E11.5 embryos, somites were counted for stage matching. Embryos were imaged using a Leica MZ6 microscope, to detect any externally visible defects, or, for detection of eYFP fluorescence, on a Stemi Axioplan microscope.

2.3 Genotyping

2.3.1 DNA extraction

DNA was extracted from: the yolk sac of embryos aged E9.5-E12.5, the upper limb of embryos aged above E13.5, a section of the tail of euthanised pups or ear notches from adult mice.

For embryonic or neonatal samples, proteinase K was used for DNA extraction. Proteinase K (Sigma), 30µl diluted in 1ml of lysis buffer (50mM KCl, 1.5mM $MgCl_2$, 10mM Tris, 0.45% NP-40, 0.45% Tween-20), was added to samples and incubated at 56°C for 2 hours then at 95°C for 10 minutes to inactivate proteinase K. For volumes of lysis buffer added to samples see Table 2.1. Samples were centrifuged for 1 minute at 1500rpm and stored at 4°C.

Table 2.1. Volume of lysis buffer added to samples for DNA extraction using the proteinase K method.

Sample	Volume of lysis buffer (µl)
E8.5 yolk sac	25
E9.5 yolk sac	50
E10.5 yolk sac	100
E13.5 forelimb	300
E15.5 forelimb	400
Tail	400

For ear notches of adult mice, HotShot DNA extraction was used. 75µl of lysis reagent (0.5mM NaOH, 0.2mM EDTA, pH12) was added to samples then incubated at 95°C for 1 hour. After incubating at room temperature for 10 minutes, 75µl neutralising reagent (Tris-HCl 40mM, pH5.5) was added. Samples were centrifuged for 1 minute at 1500rpm and stored at 4°C.

2.3.2 Polymerase Chain Reaction

2µl of product from DNA extraction was used in each polymerase chain reaction (PCR) for genotyping. A master mix containing the following was made up to amplify the DNA: GoTaq polymerase (Promega), 1x GoTaq reaction buffer (Promega), 0.25mM of each deoxyribnucleotide (dNTP) triphosphate (dATP, dTTP, dGTP, dCTP; Promega), forward and reverse primers specific for each reaction (0.5µm each) and ddH_2O up to a final volume of 20µl. The primers used in PCR reactions for each gene are listed in Table 2.2.

A Veriti Thermal Cycler (Applied Biosystems) was used to carry out the PCR reaction. All reactions, consisting of 30-35 cycles, had a 2 minute denaturation step at 94°C, a 30-40 second annealing step (annealing temperatures listed in Table 2.2) and elongation for 30-40 seconds at 72°C.

Table 2.2. Primer sequences used for genotyping.

Gene	Primer	Sequence	Tm (°C)	Number of cycles	Product Size
Gbx2 **(delete allele)**	Gbx2 Lox1-F	GGAATAGCTGGAGGAGTTGCG	58	35	Wild type: 1615bp Mutant: 268bp
	Gbx2 Lox2-R	TGCTTGGATGTCCACATCTAGG			
Gbx2 **(floxed allele)**	Gbx2 Lox2-F	CTGTTCACGTTAGCAGGTTCGC	58	35	Wild type: 183bp Mutant: 220bp
	Gbx2 Lox2-R	TGCTTGGATGTCCACATCTAGG			
Pax9	P9-Gen2-F1	ACT CAC CGG CCT GCA CCAATTAC	58	35	Wild type: 268bp Mutant: 350bp
	P9-Gen2-R1	TTG TTC TCA CTG AGC CGGCCTGT			
	P9-Gen2-R2	GGA TGT GCT GCA AGG CGATTAAG			
Pax9Cre	P9-Cre F1	ACTCAAGCCTCTTTCAGCCC	60	35	Wild type: 200bp Mutant: ~250bp
	P9Cre R1	GTTGCATCGACCGGTAATGC			
	P9-Gen2-R1	GGA TGT GCT GCA AGG CGATTAAG			
Tbx1	Tbx1.1	TGCATGCCAAATGTTTCCCTG	58	35	Wild type: 196bp Mutant: 450bp
	Tbx1.2	GATAGTCTAGGCTCCAGTCCA			

	Tbx1.3	AGGGCCAGCTCATTCCTCCCAC			
Cre	S1X-A	GCATAACCAGTGAAACAGCATTGCTG	55	30	Mutant ~500bp
	S1X-B	GGACATGTTCAGGGATCGCCAGGCG			
eYFP	eYFP r1	AAAGTCGCTCTGAGTTGTTAT	59	30	Wild type: 500bp Mutant: 250bp
	eYFP r2	GCGAAGAGTTTGTCCTCAACC			
	eYFP r3	GGAGCGGGAGAAATGGATATG			

PCR products were then visualised via gel electrophoresis. 2% (w/v) agarose gels in 1x TAE buffer (40mM Tris, 20mM acetic acid, 1mM EDTA) with 0.5µg/ml ethidium bromide were ran for 40 minutes at 100V then viewed through a UV light transilluminator.

2.4 Histology

2.4.1 Embryo embedding and sectioning

For histological analysis, embryos were fixed in 4% paraformaldehyde (PFA) at 4ºC, then washed in PBS before dehydrating through a graded series of increasing ethanol concentrations, all at room temperature. Prior to wax embedding, embryos were incubated in histoclear (National Diagnostics) at room temperature and then several paraffin wax washes at 60°C. The incubation times for the different embryonic ages are shown in Table 2.3.

8µm sections were taken using a microtome (Leica, RM 2235) and placed on microscope slides covered with warmed water at 37°C. Once the sections had spread, the water was removed and slides were incubated at 37°C overnight to dry.

Table 2.3. Protocol for processing embryos for wax embedding.

Abbreviations: PBS, phosphate buffered saline; PFA, paraformaldehyde.

	E9.5	**E10.5**	**E11.5**	**E15.5**
4% PFA	1 night	1 night	1 night	3 nights
PBS	5 minutes	5 minutes	5 minutes	5 minutes
	5 minutes	5 minutes	5 minutes	5 minutes
50% Ethanol	30 minutes	30 minutes	1 hour	3 hours
70% Ethanol	30 minutes	30 minutes	1 hour	3 hours
	30 minutes	30 minutes	1 hour	3 hours
95% Ethanol	30 minutes	30 minutes	1 hour	3 hours
100% Ethanol	30 minutes	30 minutes	1 hour	3 hours
	30 minutes	1 hour	1 hour	Overnight
Histoclear	10 minutes	15 minutes	20 minutes	30 minutes
	10 minutes	15 minutes	20 minutes	30 minutes
Histoclear/Wax	15 minutes	20 minutes	20 minutes	1 hour
Wax	20 minutes	30 minutes	40 minutes	1 hour
	20 minutes	30 minutes	40 minutes	1 hour
	20 minutes	30 minutes	40 minutes	1 hour
				1 hour

2.4.2 Haematoxylin and eosin staining

8µm sections were stained with haematoxylin and eosin for histological analysis. Wax was removed from the sections by washing in Histoclear for 10 minutes, twice. The sections were then incubated in 100% ethanol twice for 3 minutes and rehydrated in decreasing ethanol concentrations (90%, 70% and 50%) for 2 minutes each. After a 2 minute wash in H_2O, slides were stained with haematoxylin for 10 minutes then rinsed under running water for 5 minutes to remove excess stain. Sections were dipped 4 times in a solution of 1% v/v hydrochloric acid in 70% ethanol. After another wash under running water, slides were stained with eosin (ThermoFisher) for 5 minutes and washed again under running water. Sections were dehydrated by 3 dips in each solution of increasing ethanol concentrations (50%, 70% and 90%) and then incubated twice in 100% ethanol for 3 minutes. Following another two washes in Histoclear for 10 minutes, slides were mounted with Histomount (National Diagnostics) and imaged with a Zeiss Axioplan microscope.

2.5 Imaging

2.5.1 Magnetic resonance imaging

Embryos subject to MRI were aged E15.5. The protocol for MRI has previously been described (171). Embryos were bled out prior to MRI to prevent the high contrast signal from blood interfering with the analysis. Embryos were collected in pre-warmed HANK's solution with 5mM EDTA (10ml/L of HANK's solution). During the bleeding out process, embryos were kept warm via a heat mat to aid bleeding.

Embryos were fixed in 4% PFA at 4ºC for at least 3 days prior to imaging then incubated for a further 4 days in 1ml of 4% PFA containing 4µl of magnevist contrast agent (gadopentetate dimeglumine, Gd-DTPA).

Embryos were fixed in place in a glass tube using 1% agarose made up with water and Gd-DPTA (4µl/ml). A total of 32 embryos, in 8 layers of 4, were stacked in the tube. All embryos had the left forelimb removed to define the left side but in order to identify embryos within each layer, other limbs or the tail were removed from each of the embryos. Embryos were imaged using a 9.4T MR system (Varian, US) (Professor Jürgen Schneider, British Heart Foundation MRI unit, University of Oxford, UK).

To assess the phenotype of the embryos and reconstruct MRI data in a 3-dimensional (3D) model, Amira software (ThermoFisher Scientific) was used, with the voxel size of X-25.4, Y-25.4 and Z-24.4. Following disassembly of the MRI tube, in cases where the analysis was unclear, embryos were embedded, sectioned and stained by H and E staining, as previously described (Section 2.4.2), to ascertain the phenotype and provide finer detail.

2.5.2 High Resolution Episcopic Microscopy

High-resolution episcopic microscopy (HREM) was used to view the structure of the PAA in E10.5 and E11.5 embryos. Embryos were dissected in PBS, fixed in 4% PFA overnight at 4ºC, processed to 70% ethanol at room temperature (described in Section 2.4.1) and embedded in histological embedding material before being subject to imaging (Dr Tim Mohun, Francis Crick Institute). HREM files were analysed using the Amira software (Thermofisher Scientific) to create 3-D reconstructions.

2.6 Ink injection

Intra-cardiac ink injection was used to visualise the PAA at E10.5. Embryos were collected and dissected in PBS. Somites were counted to stage the embryos, with 31-40 somites confirming E10.5. Embryos were pinned in a petri dish filled with 1% agarose and PBS. The peritoneal membrane was removed and Indian ink (diluted 1:1 in water) was injected into the OFT of the heart. Injection was performed using a pulled glass pipette attached to a mouthpiece. Embryos were then imaged on each side using a Leica MZ6 microscope (Leica, Stemi 2000).

2.7 Whole mount *in situ* hybridisation

2.7.1 Probe digoxygenin labelling

The *Gbx2* plasmid probe, *Pax9* plasmid probe and *Pitx2* plasmid probe were donated by Dr Alexandra Joyner (Sloan Kettering Institute, USA), Dr Ralf Kist (Newcastle University, UK) and Dr Dorota Szumska (University of Oxford, UK) respectively.

Plasmid probes contained the full cDNA sequence of their respective target genes. Plasmid probes were linearised with specific restriction enzymes (Table 2.4). 50µl of

digested product was diluted 1:1 in water and an equal volume of phenol chloroform was added. Following centrifugation, chloroform was added to the upper aqueous phase and centrifuged for 5 minutes at 1200rpm. 100% ethanol and 10µl of 3M ammonium chloride was added. The product was centrifuged at 1300rpm for 30 minutes at 4°C and the pellet was washed with 70% ethanol then resuspended in ddH_2O.

Probes were generated from linearised plasmids using a specific RNA polymerase (Table 2.4). Products were labelled with digoxygenin (DIG) according to manufacturer's protocol (Roche) using a mix containing digNTPs, buffer, RNase inhibitor, RNA polymerase, DTT (100mM) to a total volume of 30µl with nuclease free water.

Probes were treated with DNase A for 10 minutes at 37°C before an overnight incubation with lithium chloride at -20°C. The pellet was collected by centrifugation for 30 minutes at 13000rpm at 4°C and washed with 70% ethanol (diethylpyrocarbonate, DEPC). The pellet was resuspended in nuclease free water. An equal volume of formamide was added to stabilise the RNA.

Probes were quantified using a Nanodrop spectrophotometer and ran on a 1% gel at 150V for 10 minutes. Probes were stored at -80°C and denatured at 100°C for 5 minutes in hybridisation solution prior to hybridisation.

Table 2.4. Restriction enzymes and RNA polymerases used to generate *in situ* hybridisation probes.

Gene	Probe	Restriction enzyme	RNA polymerase
Gbx2	Antisense	Hind III	T7
	Sense	Kpn I	T3
Pax9	Antisense	Eco RI	T7
	Sense	BamHI	T3
Pitx2	Antisense	SacI	T3

2.7.2 Hybridisation

Prior to hybridisation, all solutions were treated with DEPC and all tools and materials to be used were treated with RNase Away (ThermoFisher). This removes RNases which would otherwise degrade the RNA probes and RNA of interest.

Embryos were collected at E8.5-9.5 depending on the experiment and dissected in ice-cold DEPC-PBS then fixed overnight in 4% DEPC-PFA. Embryos were washed in DEPC-PBS then dehydrated through a series of increasing methanol solutions (25%, 50%, 75% and 100%, 10 minutes per solution) and stored at -20°C in 100% methanol.

For hybridisation, embryos were rehydrated in a series of methanol solutions (75%, 50% and 25%, 5 minutes per solution) then washed twice in DEPC-PBT (DEPC-PBS, Tween-20) for 5 minutes. Embryos were bleached for 1 hour at room temperature in 6% hydrogen peroxide in DEPC-PBT then washed three times in DEPC-PBT for 5 minutes. Embryos were permeabilised via a 15 minute incubation with proteinase K (10µg/ml, DEPC-PBT) and washed in glycine (2mg/ml, DEPC-PBT) for 5 minutes to inactivate proteinase K and prevent over-digestion of the embryos. Following two 5 minute washes in DEPC-PBT, embryos were fixed for 20 minutes in 0.2% glutaraldehyde/4% DEPC-PFA at room temperature. Embryos were washed again for 5 minutes in DEPC-PBT, twice.

Embryos were transferred to cryovials and incubated with prehybridisation solution (50% formamide, 5x SSC, 0.1% Tween, 50µg/ml Heparin, DEPC-H_2O) for 1 hour at 70°C with gentle rocking. Probes were denatured at 100°C for 5 minutes in hybridisation solution (1µg/ml probe, 50% formamide, 5x SSC pH4.5, 0.1% Tween-20, 50µg/ml Heparin, 50µg/ml yeast tRNA, 100µg/ml salmon sperm DNA, DEPC-H_2O). Hybridisation was performed overnight at 70°C with gentle agitation.

Embryos were washed twice at room temperature for 30 minutes in prewarmed (70°C) solution I (50% Formamide, 5x SSC, 1% SDS, DEPC-H_2O). Solution I was then mixed (1:1 v/v) with solution II (0.5M sodium chloride, 0.01M Tris pH 7.5, 0.1% Tween-20) and the embryos were incubated with this solution for 10 minutes at 70°C .

This was followed by three 5 minute washes in solution II at room temperature, and then 2 incubations with RNase A (100µg/ml, solution II) for 30 minutes at 37°C. 5 minute washes of solution II then solution III (50% formamide, 5x SSC, 0.2% SDS, DEPC-H_2O) at room temperature were performed. This was followed by two 30 minute

washes in solution III at 65°C and three 5 minute rinses in TBST (0.05M Tris pH7.5, 0.15M NaCl, 0.05% Tween-20) at room temperature.

Embryos were blocked with 10% fetal bovine serum (FBS) in TBST for 2.5 hours at room temperature. The block was removed and embryos were incubated overnight at 4°C with 0.5µl/ml Anti-Digoxigenin-AP Fab fragments (Roche) diluted in 1% FBS/TBST.

The following day embryos were washed 5 times in TBST for 1 hour at room temperature and a final wash at 4°C overnight. Five 10 minute washes in NTMT (100M NaCl, 0.1M Tris pH 9.5, 0.1% Tween-20) were performed at room temperature. Development was performed in the dark at room temperature by incubating the embryos in the developing solution (5M NaCl, 2M Tris pH 9.5, 0.1% Tween-20, 20µl/ml NBT/BCIP). Embryos were checked throughout and images of each side of the embryo were taken using a Leica MZ6 microscope (Leica), when development was judged to be complete.

2.8 Immunohistochemistry

Immunofluorescence staining was performed on paraffin sections of E10.5 embryos (embryo preparation is described in Section 2.4.1). Slides were incubated in Histoclear twice for 10 minutes before rehydrating through a graded ethanol series (100%, 100%, 90%, 70% and 50%) for 2 minutes per solution. Slides were washed in PBS for 5 minutes. Antigen retrieval was performed in a pressure cooker for 5 minutes in citrate buffer (0.01M citric acid, pH6). After rinsing slides in running water, slides were washed 3 times in PBS for 5 minutes.

Sections were blocked in 10% FBS/PBS for 30 minutes at room temperature. Primary antibodies (Table 2.5) were diluted in 2% FBS/PBS and incubated on the sections overnight at 4ºC in a humid chamber.

Slides were washed 3 times in PBS for 5 minutes then incubated in secondary antibodies (Table 2.5) diluted 1:200 in 2% FBS in PBS. Slides were incubated in a humid chamber at room temperature for 2 hours.

After washing 3 times in PBS for 5 minutes each, slides were mounted with vectashield with 4',6-diamidino-2-phenylindole (DAPI, Vector laboratories LTD) and stored at 4ºC. Slides were imaged using a Zeiss Axiomager.

Table 2.5. Primary and secondary antibodies used for immunohistochemistry.

Primary antibody	Species and type	Manufacturer	Dilution	Secondary antibody	Manufacturer
ERG1	Rabbit monoclonal	Abcam (ab92513)	1:1000	Donkey anti-rabbit 594	ThermoFisher (A21207)

2.9 RNAScope

RNAScope was performed according to manufacturer's protocol (ACDBio) on paraffin sections of E9.5 and E10.5 embryos (preparation described in Section 2.4.1). Incubations at 40°C were performed using the HybEZ oven to maintain humidity.

Paraffin sections were baked at 60°C for 90 minutes then washed twice for 5 minutes each in Histoclear to remove the wax. Slides were washed twice for 2 minutes in 100% ethanol and air dried. RNAScope hydrogen peroxide was added to sections and incubated at room temperature for 10 minutes. Slides were dipped 5 times in distilled water.

Target retrieval was performed by boiling the slides between 100-104°C in 1X target retrieval buffer (ACDBio) for 5 minutes. Slides were rinsed 3 times in distilled water for 15 seconds then 100% ethanol for 3 minutes before air drying. RNAScope protease plus was added to sections and slides were incubated at 40°C for 5 minutes. Slides were washed 5 times in distilled water.

Probes were warmed to 40°C and left to cool to room temperature before adding to sections and incubating for 2 hours at 40°C. Probes used are listed in Table 2.6. C1 probes were added directly to sections, C2 and C3 probes were diluted 1:50 in probe diluent or in C1 probes before adding to sections.

Table 2.6. Probes used in RNAScope assays.

Probe	Probe type	ACDBio Reference number
Tbx1	C1	481911
Pax9	C2	454321
Gbx2	C3	314351
Cre	C1	312281

Slides were washed in 1X wash buffer (ACDBio) for 2 minutes then incubated overnight in 5X SSC (750mM sodium chloride, 75mM sodium citrate) at room temperature. After two washes in wash buffer, the amplification solutions were hybridised to sections. RNAScope multiplex FL v2 AMP1 was added to sections and incubated at 40°C for 30 minutes then washed twice for 2 minutes in 1X wash buffer. This was repeated with RNAScope multiplex FL v2 AMP2 and finally with a 15 minute incubation with RNAScope multiplex FL v2 AMP3.

Slides were washed twice for 2 minutes then the probe signal was developed. Each probe signal was developed individually by incubating sections with specific HRP solutions (HRP-C1, -C2 or -C3, depending on the probe types used in each assay) for 15 minutes at 40ºC. Slides were washed twice in wash buffer for 2 minutes.

Tyramide signal amplification (TSA) kit (Perkin Elmer) was used to amplify the signal. TSA fluorphores (either cyanine 3 or cyanine 5) were diluted 1:1500 in TSA dilution buffer (ACDBio) and incubated on the sections for 30 minutes at 40ºC. Slides were washed twice in wash buffer for 2 minutes then blocked for 15 minutes with RNAScope multiplex FI v2 HRP blocker at 40ºC. Blocking solution was removed by washing twice in wash buffer for 2 minutes. For experiments that required multiple probes on one slide, this process was repeated using the alternative TSA fluorophore.

DAPI (ACDBio) was added to sections for 30 seconds then slides were immediately mounted using antifade prolong gold mounting media and stored at 4ºC. Slides were imaged using a Zeiss Axioimager.

2.10 Whole mount lacZ Stain

This project used the *Pax9Cre* allele to remove gene expression from the *Pax9* expression domains. To validate this allele, lacZ staining of whole mount embryos was performed. *Pax9Cre* males were crossed with *Rosa26R-lacZ* reporter females and embryos were collected at E8.5 to E11.5. These female mice carry the bacterial *lacZ* gene which, following Cre-mediated recombination, allows the expression of β-galactosidase. This β-galactosidase activity results in the cleaving and oxidation of X-gal in *Pax9* expressing cells, forming a blue product to allow the visualisation of *Pax9Cre* expression.

Embryos were collected and dissected in ice-cold PBS. Following two 5 minute washes in PBS at 4°C, embryos were briefly fixed at room temperature in 4% PFA, the duration of which depended on the age of the embryo (Table 2.7). Embryos were washed three times for 5 minutes in PBS at room temperature then incubated with a staining solution (0.1M phosphate buffer, 0.2M K-ferricyanide, 20mg/ml X-Gal) for 4 hours at 37°C. Embryos were washed again in PBS three times for 5 minutes and imaged using an MZ6 microscope (Leica).

Table 2.7. Duration of PFA fix for lacZ staining.

Age of embryo (E)	Duration of fix (minutes)
8.5	4
9.5	5
10.5	15
11.5	15

2.11 Quantitative Polymerase Chain Reaction of flow sorted cells

To analyse gene expression within the tissues of the PA, cells were dissociated from the PA of *Pax9Cre;eYFP*$^{KI/KI}$ embryos and flow sorted based on Cre-mediated *eYFP* expression. RNA was extracted from the sorted cells and analysed by quantitative

polymerase chain reaction (qPCR). Figure 2.4 shows the breakdown of this experiment.

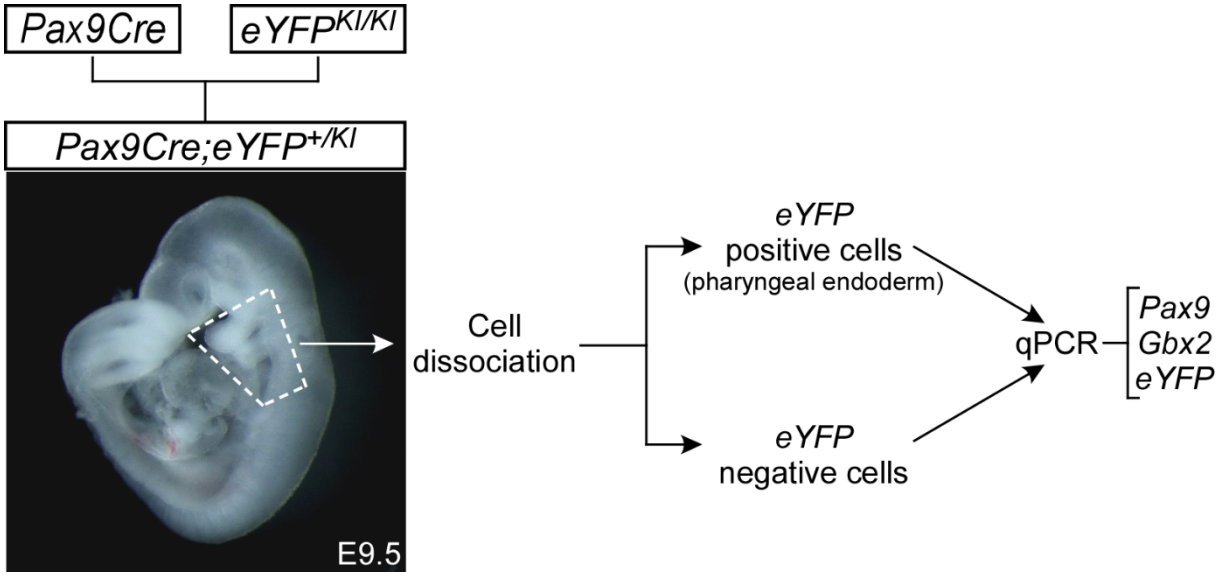

Figure 2.4. Schematic showing the experiment plan for qPCR analysis of the pharyngeal arch cells.

Pax9Cre males were crossed with *eYFP*$^{KI/KI}$ females and embryos were collected at E9.5. Cells were dissociated from the PA region of *Pax9Cre;eYFP*$^{+/KI}$ embryos and flow sorted based on *eYFP* expression. Each cell population was analysed by qPCR for *Pax9*, *Gbx2* and *eYFP*.

2.11.1 Cell dissociation and flow sort

Pax9Cre males were crossed with *eYFP*$^{KI/KI}$ females and embryos were collected at E9.5 in ice-cold PBS. Somites were counted for stage matching and the yolk sac was used for genotyping (described in Section 2.3).

eYFP expressing embryos were identified using a GFP filter on a Stemi Axioplan microscope. The pharyngeal region of fluorescent embryos was dissected (Figure 2.4) for cell dissociation.

Each sample was incubated with 100µl of Accumax (eBioscience) at 37°C with vigorous shaking for 35 minutes. The reaction was stopped by adding 10% FBS/PBS and samples were centrifuged for 5 minutes at 1200rpm then resuspended in filtered 10% FBS/PBS.

Approximate cell count of each sample was determined using a TALI Image-Based Cytometer (ThermoFisher). Cells were stained with propidium iodide (PI) at a concentration of approximately 10µl per million cells. PI was used to mark non-viable cells.

Live *eYFP* positive and live *eYFP* negative cells were sorted fluorescently at 4°C using a Becton Dickinson FACS Aria II with a 100µm nozzle and 20psi sheath pressure. Cells were first gated using FSC-A vs SSC-A then by FSC-A vs FSC-H and FSC-A vs SSC-W to sort singlets. Live cells were collected in 1ml of TRIzol LS (ThermoFisher), ensuring that the volume of cells did not exceed 30% of the volume of TRIzol.

2.11.2 RNA extraction

Sorted cells were incubated with TRIzol LS for 5 minutes at room temperature. 0.2 volumes of chloroform were added to the homogenate, and samples were shaken vigorously for 15 seconds and incubated at room temperature for 3 minutes.

Samples were centrifuged at 12000g for 15 minutes at 4°C. The upper aqueous phase was collected and 1 volume of isopropanol and 2µl of glycogen was added. Following a 10 minute incubation at room temperature, samples were centrifuged at 12000g for 10 minutes at 4°C.

The pellet was washed with 75% ethanol and centrifuged again at 7500g for 5 minutes at 4°C. The ethanol was removed and the pellets were air dried before dissolving in RNase free water and stored at -80°C.

2.11.3 cDNA synthesis

To remove potential DNA contamination, 0.5µg of RNA was incubated with 1µl DNase I (ThermoFisher), DNase I reaction buffer, and DEPC treated water up to 10µl for 15 minutes at room temperature. 1µl EDTA (25mM) was used to inactivate DNase and the sample was heated for 10 minutes at 65°C.

To synthesise the cDNA, 1µl of random primers (Promega) and 1µl dNTPs (10mM, Promega) were added to each sample. This was heated at 65°C for 5 minutes then incubated on ice for at least 1 minute.

First strand buffer, DTT (100mM) and 1µl RNase OUT recombinant RNase inhibitor (Invitrogen) were added, followed by 1µl Superscript III Reverse Transcriptase (ThermoFisher). The reaction mixture was incubated at room temperature for 10 minutes then for 1 hour at 50°C. The reaction was inactivated at 70°C for 15 minutes, briefly centrifuged and stored at -20°C.

2.11.4 Quantitative polymerase chain reaction

Primers to detect mRNA expression using qPCR were designed using PRIMER 3 and specific selection criteria, including: 40-60% guanine-cytosine content, 65-120 base product size and 18-23 base primer size. Specificity was checked using Primer Blast. Primers were tested initially by PCR using water, cDNA and a negative control. Negative controls were generated during cDNA synthesis by omitting the addition of reverse transcriptase. Following the detection of the gene of interest by PCR, qPCR was used to determine primer efficiency.

For each gene analysed a master mix was prepared containing 0.5µl forward primer, 0.5µl reverse primer, 5µl SYBR green master mix (ThermoFisher). Primers targeting GAPDH were used as a housekeeping gene. The primer sequences used are listed in Table 2.1. A negative control using a water template was also used.

For each reaction, 8µl master mix was added to 2µl cDNA and run on a QuantStudio7 Flex Real-Time PCR System (ThermoFisher) on the following protocol: 95ºC for 20 seconds then 40 cycles of 1 second at 95ºC and 20 seconds at 60ºC, followed by a continuous cycle of 15 seconds at 95ºC and 1 minute at 60ºC.

The comparative CT method was used to determine relative gene expression. Each sample was run in triplicate. The triplicate values were averaged and normalised to the average CT of GAPDH for each sample and ΔCT was calculated.

Table 2.8. Primers used for qPCR analysis.

Gene	Forward primer sequence	Reverse primer sequence
GAPDH	TGTGCAGTGCCAGCCTCGTC	TGACCAGGCGCCCAATACGG
eYFP	AGAACGGCATCAAGGTGAACT	GGGGTGTTCTGCTGGTAGTG
Gbx2	CTCGCTGCTCGCTTTCTCT	CTCGTCTTTCCCTTGCCCTC
Pax9	GACCAAGGAGTGAGCGACAG	CCAATCCATTCACTGCGTGC

2.12 Luciferase Assays

2.12.1 JEG3 Cell Culture

Human placental choriocarcinoma (JEG3) cells (ATCC) were used for dual luciferase assays (DLA). Cells were cultured at 37°C with 5% CO_2 and high humidity. High glucose Dulbecco's modified eagle medium (Life Technologies) supplemented with 10% (v/v) FBS (Life Technologies) and 100units/ml of Penicillin and 100µg/ml of Streptomycin (Life Technologies) were used to culture the cells, this was changed every three days.

Cells were cultured in T75 flasks at a density of 15,000 cells/cm^2 and passaged when 80% confluent. The media was removed and the cells were washed with PBS. Cells were detached by 5 minute incubation with 0.05% trypsin in EDTA (Life Technologies) at 37°C. Media was added to deactivate trypsin and cells were collected and centrifuged at 1200rpm for 5 minutes.

2.12.2 Luciferase Assays

Luciferase assays were used to determine if Pax9 and Tbx1 activate the *Gbx2* enhancer region. Assays were performed according to the Dual-Luciferase Reporter Assay System (Promega) manufacturer's protocol.

JEG3 cells were seeded at a density of 100,000 cells per well in 24-well plates in 1ml of media and incubated at 37°C for 24 hours prior to transfection. Transfections were performed in triplicate containing: a DNA mix of plasmids specified for each experiment (Table 2.9 and Table 2.10), Renilla luciferase vector (5ng, as a transfection control),

transfection reagent (jetPrime) in a 2:1 ratio (reagent:DNA) and transfection buffer (jetPrime) up to a total volume of 300µl.

Once the transfection reagent was added to the transfection mix, the mix was incubated at room temperature for 10 minutes prior to adding 100µl, dropwise, to each well for transfection.

The following day, growth media was removed from cultured cells and cells were washed in PBS. Lysis was performed by incubating each well with 100µl of passive lysis buffer (Promega) with gentle rocking for 15 minutes at room temperature. In the case of non-efficient lysis, cells were actively lysed through pipetting. 20µl of the lysate of each well was transferred to an opaque 96-well plate.

The DLA was performed on a GloMax-Multi Detection System (Promega) according to manufacturer's protocol to measure Renilla and Firefly luciferase. 50µl of luciferase assay substrate (Promega) was dispensed into each well and Firefly luciferase was immediately measured. Renilla luciferase was then measured after adding 50µl of Stop and Glo reagent (Promega). Firefly luciferase measurements were normalised against Renilla luciferase measurements.

Each transfection DNA mix included a firefly luciferase expression plasmid (reporter construct) which differed between experiments. Reporter constructs containing a synthetic T-site or Pax binding site were used as a positive control for *TBX1* (2xTtkGl2) (172) and *PAX9* (BMP4) (173) activity, respectively. A vector lacking these synthetic binding sites (tkGl2) was used as a negative control for both TBX1 and PAX9 activity. Table 2.9 shows the plasmids used in each control assay. Transfection was also performed without any DNA or with the empty pcDNA3.1 vector as negative controls. Additionally, the assay was carried out on a media only control.

Table 2.9. Plasmids used for each control assay.

	Condition	0.5µg luciferase plasmid	PAX9 cDNA plasmid	TBX1 cDNA plasmid	pcDNA3.1
Tbx1 positive control	No addition	2xTtkGl2	-	-	0.50µg
	Tbx1	2xTtkGl2	-	0.25µg	0.25µg
Pax9 positive control	No addition	BMP4	-	-	0.50µg
	Pax9	BMP4	0.25µg	-	0.25µg
Tbx1/Pax9 negative control	No addition	tkGl2	-	-	0.50µg
	Tbx1	tkGl2	-	0.25µg	0.25µg
	Pax9	tkGl2	0.25µg	-	0.25µg

To determine if Tbx1 and Pax9 could activate the *Gbx2* conserved region, *TBX1* and/or a *PAX9* cDNA expressing plasmids together with a reporter construct containing the *Gbx2* enhancer region (*Gbx2*-LUC) were in the transfection mix. 0.5µg of a Firefly luciferase expression construct was used in each experiment. The backbone of the plasmid constructs (pcDNA3.1) was used to bring the total DNA to 1µg per transfection mix. Specific plasmids for each experimental condition are shown in Table 2.10.

Table 2.10. Plasmids used in each luciferase experiment investigating the interaction of Tbx1 and Pax9 with the *Gbx2* enhancer region.

Condition	5µg luciferase plasmid	PAX9 cDNA plasmid	TBX1 cDNA plasmid	pcDNA 3.1
No addition	GBX2-LUC	-	-	0.50µg
Tbx1	GBX2-LUC	-	0.25µg	0.25µg
Pax9	GBX2-LUC	0.25µg	-	0.25µg
Tbx1 and Pax9	GBX2-LUC	0.25µg	0.25µg	-

2.12.3 Chromatin Immunoprecipitation Assays

For the chromatin immunoprecipitation (ChIP) assays, wild type CD1 embryos were collected at E9.5 and E10.5 in ice cold PBS and pooled for each experiment; nine embryos at E9.5 and four embryos at E10.5.

Pooled embryos were homogenised in ice cold PBS containing protease inhibitors (Sigma; 1:100) then fixed in 37% formaldehyde for 10 minutes at room temperature. Samples were neutralised in 125mM glycine for 10 minutes at room temperature.

Samples were centrifuged at 4°C for 1 minute at 1200rpm. The pellet was washed twice in PBS and resuspended in 100µl of ChIP lysis buffer (1% SDS, 50mM Tris-HCl, 10mM EDTA) with protease inhibitors (1:100). After incubating for 10 minutes at room temperature, chromatin was sonicated using a Biorupter sonicator (diagenode) for 15 cycles to 200-600bp; assessed by gel electrophoresis. Sonicated samples were centrifuged for 10 minutes at 4°C and the supernatant was collected. Samples were diluted in ChIP lysis buffer to a total volume of 900µl. 10% of the sample was taken for input and stored at -80°C.

Protein G Dynabeads (ThermoFisher) were used for immunoprecipitation (IP). Beads were vortexed prior to use and blocked in blocking buffer (0.5% bovine serum albumin, BSA, in PBS) for 1 hour at 4°C. 200µl blocking buffer as added to the remaining sonicated chromatin and incubated with 100ul of blocked beads for 1 hour at 4°C to preclear the sample. The precleared sample was divided equally into the number of required immunoprecipitations and controls (i.e. Tbx1, Pax9, H3K27ac, IgG, beads

only control). The relevant antibodies were each diluted in 250µl of blocking buffer and incubated with the precleared sample overnight at 4°C. Table 2.11 shows the antibodies used for each immunoprecipitation.

Table 2.11. Antibodies used in chromatin immunoprecipitation assays.

Immunoprecipitation	**Manufacturer**	**Antibody used per immunoprecipitation (µg)**
Tbx1	Abcam, ab18530	5
Pax9	Abcam, ab28538	5
H3K27ac	Abcam, ab4729	3
IgG	Abcam, ab171870	1

The following day, 30ul of blocked beads were added to each immunoprecipitation sample and incubated overnight at 4°C. Prior to elution, each sample was washed 4 times in cold wash buffer (50mM Hepes pH7.6, 500mM LiCl, 1mM EDTA, 0.7% NP-40) and once in TE buffer (10mM Tris pH 8, 1mM EDTA) containing 50mM NaCl. Samples were centrifuged at 300g for 3 minutes at 4°C and any remaining TE buffer was removed.

Samples were eluted in 210µl ChIP elution buffer (50mM Tris-HCl pH8, 10mM EDTA, 1% SDS) for 30 minutes at 65°C 1200rpm. Samples were centrifuged at 16000g for 1 minute and the supernatant was collected.

DNA was extracted from the immunoprecipitation samples and the input. 2µl proteinase K was added to each sample and incubated at 65°C for 2 hours. 200µl PCI (phenol:chloroform:isoamyl alcohol, 25:24:1) was added and the samples were briefly vortexed then centrifuged at 16000g for 5 minutes at room temperature. The upper aqueous phase was collected. 2µl glycoblue (ThermoFisher), 0.5 volumes of 7.5M ammonium acetate and 3.75 volumes of 100% ethanol were added before incubating overnight at 4°C.

Samples were centrifuged for 30 minutes 16000g at 4°C. The pellet was washed twice in 70% ethanol then dried at 42°C. The pellet was resuspended in TE buffer containing 0.1mg/ml RNase A and incubated at 30 minutes at 37°C. Samples were stored at -20°C ready for analysis by qPCR.

Primers were designed to target the *Gbx2* conserved region (forward primer: CAGAGCCCAGATCCCAAGG, reverse primer: TGTGACTCATTAGGCAGCCA). A master mix was prepared containing 0.5µl forward primer, 0.5µl reverse primer, 5µl SYBR green master mix (ThermoFisher). For each reaction, 8µl master mix was added to 2µl DNA and run on a QuantStudio7 Flex Real-Time PCR System (ThermoFisher) on the following protocol: 95ºC for 20 seconds then 40 cycles of 1 second at 95ºC and 20 seconds at 60ºC, followed by a continuous cycle of 15 seconds at 95ºC and 1 minute at 60ºC.

The percentage of input method was used for analysis. Each sample was run in triplicate. The average CT value was normalised to the input sample by subtracting the average CT from the adjusted input value, giving the ΔCT. Percentage of input was then calculated using $100*2^{\Delta CT}$. These values were compared to the IgG negative control to determine if the *Gbx2* conserved region was enriched for Tbx1, Pax9 or H3K27ac.

2.14 Statistical analysis

Statistical significance was assigned with a p value of less than or equal to 0.05.

2.14.1 Chi-squared test

Statistical differences in the penetrance of defects in embryos of different genotypes was calculated using a chi-squared test for associations using IBM SPSS Statistics 25 software. Chi-squared was also used to determine statistical differences in genotype frequency data from mouse crosses using Microsoft Excel.

2.14.2 Unpaired t-test and one-way ANOVA

An unpaired t-test or one-way ANOVA was used to analyse qPCR, DLA and ChIP data using the GraphPad Prism 8 software. If two groups were compared, a t-test was used and if three or more groups were compared, a one-way ANOVA was used.

Data was first tested using a Shapiro-Wilk test to confirm Gaussian distribution of the data. If data passed the normality test, a parametric t-test or one-way ANOVA were used. If data did not pass the normality test, nonparametric tests were used, with a Mann-Whitney test for comparing two groups and a Kruskal-Wallis for comparing three or more groups.

Chapter 3. Investigating the role of *Gbx2* in cardiovascular development

3.1 Introduction

Patients with 22q11DS present with a spectrum of cardiovascular defects that arise due to a 1.5-3Mb deletion on chromosome 22 (90). Of the 45 genes mapped to the 3Mb deletion region, mutations in *Tbx1* have been identified as a leading cause of the cardiovascular phenotype in patients (50, 98). However, the varied phenotype in 22q11DS patients lead to the suggestion that modifier genes exist outside the deletion region (101).

Transcriptome analysis of *Tbx1*$^{-/-}$ mice identified potential downstream targets of *Tbx1* and showed that *Gbx2* was downregulated within the PA (137). *Gbx2* is a transcription factor required for the specification of the midhindbrain. *Gbx2*$^{+/-}$ mice have normal development while *Gbx2*$^{-/-}$ mice die at birth with brain defects (165).

Gbx2 has also been implicated in cardiovascular development as *Gbx2*$^{-/-}$ mice have cardiovascular defects (166). These defects (summarised in Table 3.1) include IAA and VSD, frequent in 22q11DS patients, as well as DORV, RAA and ARSA, which are observed in a subset of patients (83, 88, 89). Conotruncal malformations are present in 22q11DS patients and approximately 20% of foetuses with conotruncal defects were found to have 22q11DS (174).

Table 3.1. Reported penetrance of cardiovascular defects in *Gbx2*-null mice in late embryogenesis.

Abbreviations: ARSA, aberrant right subclavian artery; CV, cardiovascular; DORV, double outlet right ventricle; IAA, interrupted aortic arch; RAA, right aortic arch.

Age	CV defect	DORV	RAA	ARSA	IAA	Reference
E16.5-18.5 n=49	19 (39%)	4 (8%)	7 (14%)	4 (5%)	5 (10%)	Byrd and Meyers, 2005

These defects to the aortic arch arteries arise due to the incorrect development of the 4th PAA, which is frequently hypoplastic or absent in *Gbx2*-null embryos (Table 3.2) (133, 166). This is reminiscent of *Tbx1*$^{+/-}$ mice which have defects specifically to the 4th PAA (34, 50, 53, 98, 129, 130).

Table 3.2. Reported penetrance of 4th pharyngeal arch artery defects in *Gbx2*-null embryos at E10.5.

Abbreviations: PAA, pharyngeal arch artery.

Age	4th PAA defect	Unilateral defect	Bilateral defect	Reference
E10.5 n=12	6 (50%)	6 (50%)	0	Calmont et al., 2009

Tbx1 and *Gbx2* are both expressed in the pharyngeal endoderm and ectoderm of the PA, tissues required in PAA morphogenesis. Further investigation found that *Gbx2* heterozygosity increased the penetrance of cardiovascular defects in *Tbx1*$^{+/-}$ mice, showing that these genes interact in cardiovascular development (133). Likewise, *Gbx2* also interacts with other genes required in cardiovascular development, including *Fgf8* which interacts with *Tbx1* (56, 166).

Few studies have provided an in-depth analysis of the *Gbx2*-null phenotype. However, the presence of 22q11DS defects in *Gbx2*$^{-/-}$ mice and the confirmed interaction with *Tbx1* suggest that *Gbx2* could be a potential modifier of the 22q11DS phenotype. This chapter aimed to establish a baseline cardiovascular phenotype of *Gbx2*-null mice on an enriched C57Bl/6 background. Embryos were collected at E15.5 for MRI and histological analysis. The initial formation of the PAA prior to their remodelling was assessed by immunohistochemistry and intracardiac ink injection at E10.5.

3.2 *Gbx2*$^{-/-}$ embryos are underrepresented during development

For analysis of *Gbx2*$^{-/-}$ mice in this chapter, *Gbx2*$^{+/-}$ embryos were intercrossed and embryos were collected at multiple stages of embryogenesis (E8.5-E15.5) depending on the experiment. Chi-squared was used to determine if the number of embryos observed from this cross differed from the expected Mendelian ratio. There was a highly significant difference (p=0.000004) in the number embryos observed of each genotype compared to expected (Table 3.3). There was a 46% loss of *Gbx2*$^{-/-}$ embryos compared to the expected. When collecting embryos, no reabsorptions or dead embryos were observed therefore it can be assumed that the loss of *Gbx2*$^{-/-}$ embryos occurs very early in embryogenesis. This suggests that *Gbx2* is required early in embryogenesis for normal development.

Table 3.3. Embryos (E8.5-15.5) obtained from *Gbx2*$^{+/-}$ X *Gbx2*$^{+/-}$ cross from 42 litters.

Gbx2 homozygous mutants are highlighted. Statistical significance was analysed using chi-squared.

Genotype	Observed (E8.5-15.5)	Expected
***Gbx2*$^{+/+}$**	61	67.75
***Gbx2*$^{+/-}$**	173	135.5
***Gbx2*$^{-/-}$**	37	67.75
Total	271	
	Chi-squared, p=4x10^{-6}****	

3.3 The *Gbx2*$^{-/-}$ phenotype

Gbx2$^{+/-}$ mice were intercrossed and embryos were collected at E15.5, at which point the structure of the heart and aortic arch arteries closely resembles that of an adult mouse. *Gbx2*$^{-/-}$ embryos (n=25) were collected and analysed by MRI or histology and 64% showed cardiovascular defects (summarised in Table 3.3). Wild type (n=3) and *Gbx2*$^{+/-}$ (n=8) mice collected at E15.5 showed normal cardiovascular development.

As found in previously published data, *Gbx2*$^{-/-}$ embryos had defects indicative of the aberrant development of the 4th PAA. This included RAA and aberrant subclavian

arteries (ARSA and ALSA), present in 24% and 40% of embryos respectively. Aberrant subclavian arteries were either, retro-oesophageal or isolated. Retro-oesophageal subclavian arteries were more frequent (28%). IRSA occurred in 12% of *Gbx2*$^{-/-}$ mice, with the RSA arising from the arterial duct. A right sided arterial duct (RAD) was also present (32%) which either occurred independently or together with RAA.

During development, the right dorsal aorta regresses, with the left persisting to form the mature left sided dorsal aorta. 32% of *Gbx2*$^{-/-}$ mice had a malpositioned dorsal aorta, either right sided or at the midline. 40% of embryos had OFT defects, presenting with DORV and IVC. These key defects are shown in Figure 3.1.

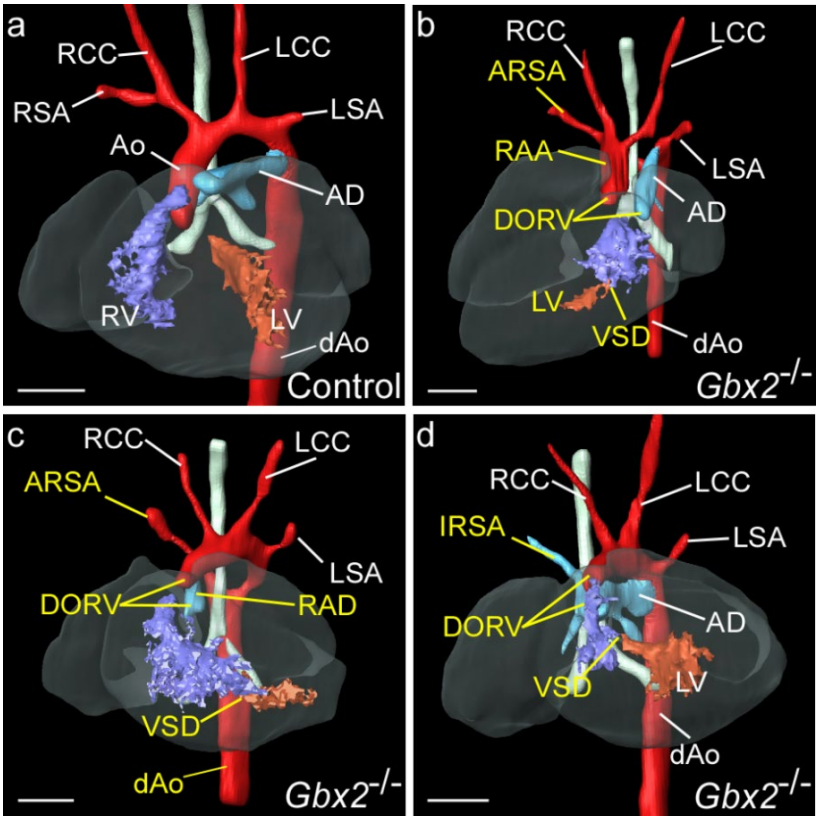

Figure 3.1. Cardiovascular defects present in *Gbx2*$^{-/-}$ embryos at E15.5.

MRI reconstructions of a control embryo (a) showing normal cardiovascular development compared to *Gbx2*$^{-/-}$ embryos (b-d). A portion of embryos showed RAA (b) and a RAD (c), as well as DORV with an IVC (VSD; b-d). The RSA was frequently aberrant (ARSA; b-c) or isolated (IRSA; d). Midline dorsal aorta was also present (c). Abbreviations: AD, arterial duct; Ao, aorta; ARSA, aberrant right subclavian artery; dAo, dorsal aorta; DORV, double outlet right ventricle; IRSA, isolated right subclavian artery; LCC, left common carotid artery; LSA, left subclavian artery; LV, left ventricle; RAA, right aortic arch; RAD, right arterial duct; RCC, right common carotid artery; RSA, right subclavian artery; RV, right ventricle; Tr, trachea; VSD, ventricular septal defect. Scale, 500μm.

Table 3.4. Penetrance of cardiovascular defects in *Gbx2*$^{-/-}$ embryos at E15.5.

ARSA/ALSA includes retro-oesophageal and isolated subclavian arteries. Abbreviations: AA, aortic arch; ALSA, aberrant left subclavian artery; ARSA, aberrant right subclavian artery; CV, cardiovascular; DORV, double outlet right ventricle; IAA, interrupted aortic arch; RAA, right aortic arch; RAD, right arterial duct; TGA, transposition of the great arteries.

	Frequency									
Genotype	**CV Defect**	**DORV**	**VSD**	**IAA**	**RAA**	**RAD**	**ARSA/ ALSA**	**Midline/ Right dAo**	**Mirror image AA**	**TGA**
***Gbx2*$^{-/-}$** n=25	16 (64%)	10 (40%)	12 (48%)	0	6 (24%)	8 (32%)	10 (40%)	8 (32%)	6 (24%)	1 (4%)

In wild type embryos, the brachiocephalic artery branches from a left sided aortic arch and then splits into the RCC and RSA. A mirror image aortic arch, in which both the aortic arch and arterial duct are right sided, was present in 24% of *Gbx2*$^{-/-}$ embryos. Here, the brachiocephalic artery branched into the LCC and LSA (Figure 3.2). This mirror image defect was frequently coupled with an ALSA (Figure 3.2b). Of the *Gbx2*$^{-/-}$ embryos with a mirrored aortic arch (n=6), 50% had ALSA.

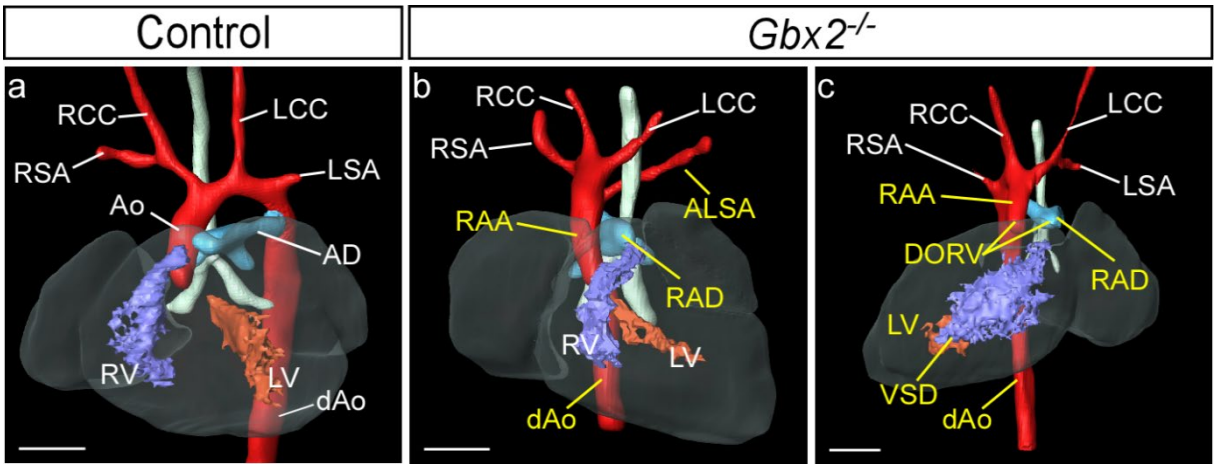

Figure 3.2. Mirror image aortic arch defect present in *Gbx2*$^{-/-}$ embryos.

MRI reconstruction of control embryo (a) with a normal left sided aortic arch and arterial duct. A mirror image aortic arch structure was present in *Gbx2*$^{-/-}$ embryos (b-c) with a RAA, RAD and a right sided dorsal aorta (dAo). This defect frequently occurred with ALSA (b). Abbreviations: AD, arterial duct; ALSA, aberrant left subclavian artery; Ao, aorta; dAo, dorsal aorta; DORV, double outlet right ventricle; LCC, left common carotid artery; LSA, left subclavian artery; LV, left ventricle; RAA, right aortic arch; RAD, right arterial duct; RCC, right common carotid artery; RSA, right subclavian artery; RV, right ventricle; Tr, trachea; VSD, ventricular septal defect. Scale, 500μm.

A vascular ring structure, formed around the oesophagus, was present in 8% of *Gbx2*$^{-/-}$ mice (Figure 6.3). This occurred as an extension of either the aorta or arterial duct, in which the vessel split, extending to both sides of the body, and then connected dorsal to the oesophagus.

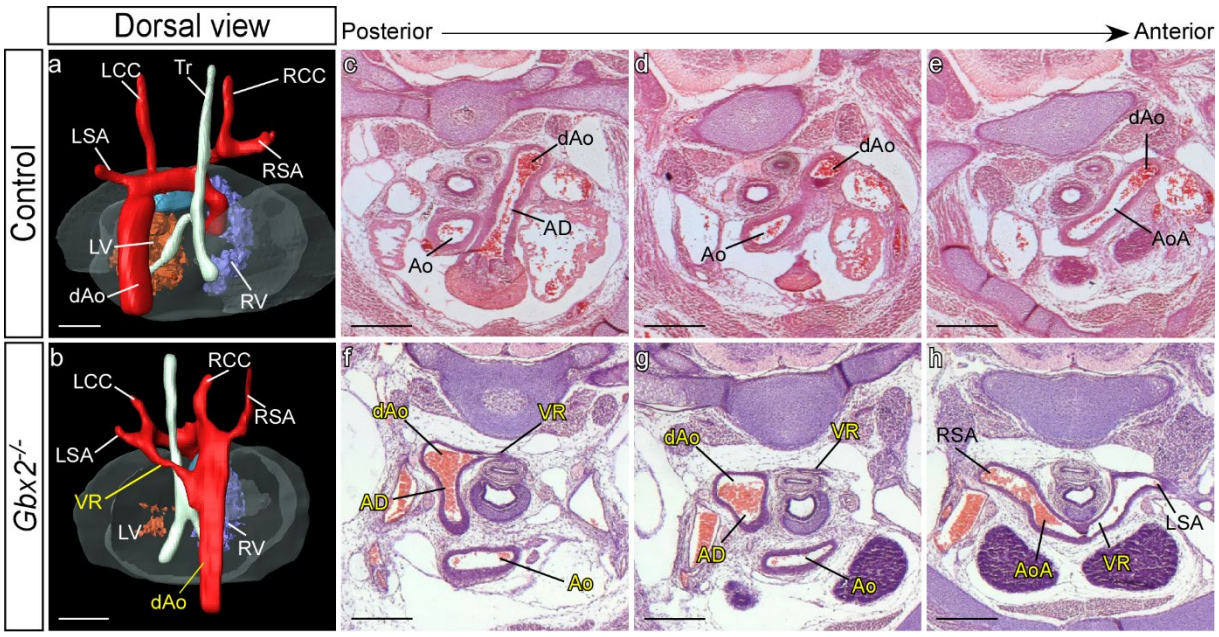

Figure 3.3. Vascular ring defect present in *Gbx2*$^{-/-}$ embryos.

Dorsal view of a control MRI reconstruction (a) and *Gbx2*$^{-/-}$ (b) embryo showing a right sided dorsal aorta (dAo) and a vascular ring (VR) around the oesophagus. H&E stain of transverse control sections (c-e) with the arterial duct and aorta crossing leftward. *Gbx2*$^{-/-}$ embryo sections (f-h) with the aorta splitting into two separate branches crossing to opposite sides of the body to meet dorsal to the oesophagus, forming a VR. Abbreviations: AD, arterial duct; Ao, aorta; AoA, aortic arch; dAo, dorsal aorta; LCC, left common carotid artery; LSA, left subclavian artery; LV, left ventricle; RCC, right common carotid artery; RSA, right subclavian artery; RV, right ventricle; VR, vascular ring. Scale, 500μm.

In normal development, blood flows to the aorta and pulmonary trunk from the left and right ventricles respectively. TGA is a CHD in which the great vessels are associated with the incorrect ventricles. This is dextra-transposition of the great arteries (dTGA), however there are multiple forms of TGA. In congenitally corrected TGA (CCTGA), the ventricles and associated valves reversed, with the LV on the right side of the body and vice versa. Therefore, in CCTGA, the aorta and pulmonary trunk are associated correctly with the morphologically left and right ventricles respectively, but the ventricles are positioned on the wrong side of the body.

TGA was present in one *Gbx2*$^{-/-}$ embryo (Figure 3.4). The aorta was connected to the ventricle on the right and the pulmonary trunk was connected to the ventricle on the left. This defect could not be classified as dTGA or CCTGA as it was difficult to establish whether the ventricle on the left side of the body was morphologically left or right.

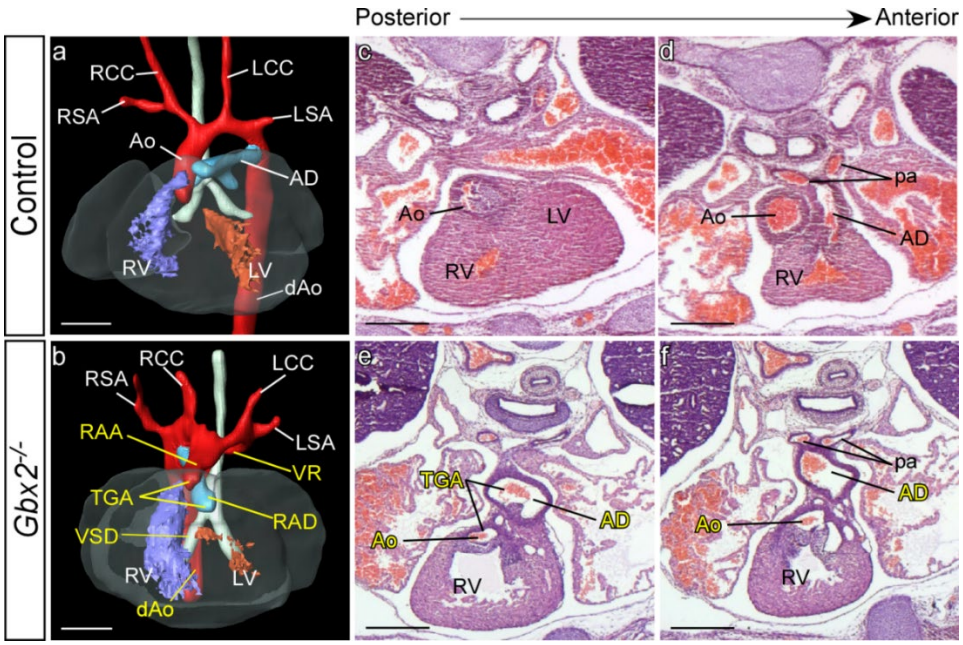

Figure 3.4. Transposition of the great arteries present in a *Gbx2*$^{-/-}$ embryo.

MRI reconstruction of a control (a) and *Gbx2*$^{-/-}$ embryo (b). Control H&E transverse sections (c-d) with the aorta (Ao) clearly arising from the left ventricle (LV; c) and arterial duct (AD) from the right ventricle (RV; d). Mutant embryo has TGA. The aorta arises from the RV (b, e, f) and the arterial duct arises from the LV (b, e, f). Other defects present include: a VR structure around the oesophagus, RAA, RAD and a VSD (b). Abbreviations: AD, arterial duct; Ao, aorta; dAo, dorsal aorta; LCC, left common carotid artery; LSA, left subclavian artery; LV, left ventricle; pa, pulmonary arteries; RAA, right aortic arch; RAD, right arterial duct; RCC, right common carotid artery; RSA, right subclavian artery; RV, right ventricle; TGA; transposition of the great arteries; Tr, trachea; VSD, ventricular septal defect. Scale, 500μm.

The *Gbx2*$^{-/-}$ phenotype was varied. Appendix Table A.1 shows the phenotype of each *Gbx2*$^{-/-}$ embryo collected. There was no obvious correlation in the combination of defects present in each embryo. The most common defect was VSD (48%), which was observed independently and together with other defects (including DORV). Phenotypes ranged from milder defects, such as those affecting the subclavian arteries, to more severe defects with RAA and RAD.

Byrd and Meyers found 39% of *Gbx2*$^{-/-}$ embryos (n=49 examined) had cardiovascular defects at E15.5. This is significantly lower than the 63% penetrance found in this study (analysed by chi-squared, p=0.04). Table 3.5 compares the *Gbx2*-null phenotype from this study and that published by Byrd and Meyers (2005). Similar defects were found in both data sets, including DORV, VSD, ARSA and RAA. However, in most cases, the penetrance of defects was greater in the data collected in this current study.

Table 3.5. Comparison of the *Gbx2*$^{-/-}$ phenotype collected in this study compared to previously published data.

ARSA/ALSA includes retro-oesophageal and isolated subclavian arteries. Statistical significance was analysed using chi-squared for associations. *p<0.05; ***p<0.001. Abbreviations: AA, aortic arch; ALSA, aberrant left subclavian artery; ARSA, aberrant right subclavian artery; CV, cardiovascular; DORV, double outlet right ventricle; IAA, interrupted aortic arch; RAA, right aortic arch; RAD, right arterial duct.

	Frequency					
***Gbx2*$^{-/-}$** E15.5-E18.5	**CV Defect**	**DORV**	**RAA**	**RAD**	**ARSA/ ALSA**	**IAA**
Byrd and Meyers (2005) n=49	19 (39%)	4 (8%)	7 (14%)	7 (14%)	4 (5%)	5 (10%)
Collected data n=25	16* (64%)	10*** (40%)	6 (24%)	8 (32%)	10 (40%)	0

Additional defects were observed in this current study that were not previously reported, namely VR, midline dorsal aorta and ALSA. IAA was reported to occur in 10% of mice in the published data, however this defect was not observed in *Gbx2*$^{-/-}$ mice in this study. This could potentially be due to data interpretation and the classification of defects. For example, a RAA could be classified as IAA as the arch is interrupted on the left side. Nonetheless, the significantly increased penetrance of defects in this current study as well as the presentation of additional defects indicates a more severe phenotype than previously published.

There are multiple factors that could result in this discrepancy in phenotype, including data analysis and genetic background (discussed in section 3.7). Differences in the mouse constructs used could also contribute. Figure 3.5 shows the mouse constructs used in each study.

Both constructs remove the same coding sequence of *Gbx2*, which includes the coding region of exon 2 and the homeobox. However, in the construct used in the Byrd and Meyers study, the neomycin drug selection cassette remains in the construct following recombination of the *Gbx2* coding region. A neomycin cassette was also utilised in the mouse construct used in this study. However, this cassette was flanked by *Frt* sites

and removed by Flpe-mediated recombination to generate the *Gbx2* floxed allele. In both constructs, the floxed region was removed by Cre-mediated recombination of the floxed allele to generate the delete allele.

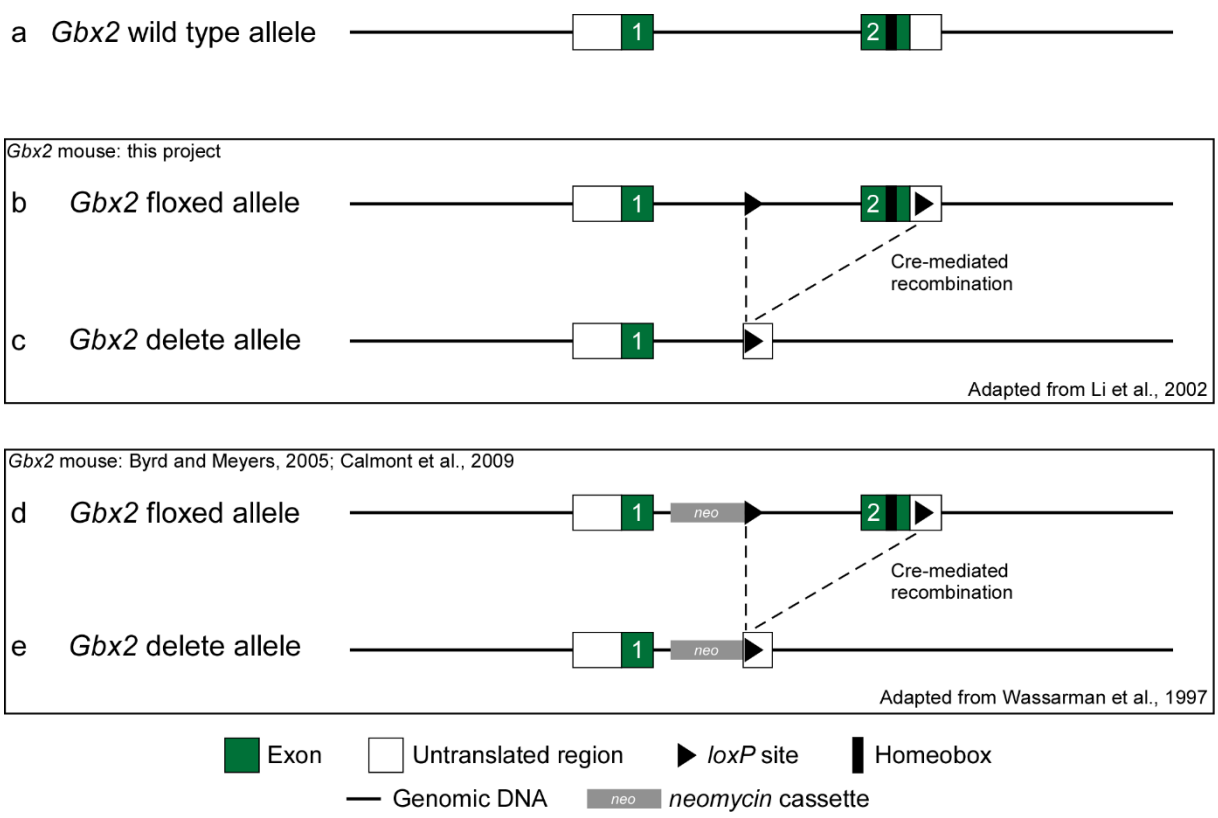

Figure 3.5. Schematic diagram of the *Gbx2* mouse constructs.

a) *Gbx2* wild type allele with 2 exons (numbered). The homeobox is in exon 2. Schematic of the *Gbx2* constructs used in this project (b, c), the Byrd and Meyers (2005) study and the Calmont et al. (2009) study (d, e). In both constructs, the *Gbx2* floxed allele (b, d) has one *loxP* site between exon 1 and 2 and the other is within the non-coding region of exon 2. The floxed allele undergoes Cre-mediated recombination to form the *Gbx2* delete allele (c, e) which has removed the coding region of exon 2, including the homeobox. In the Byrd and Meyers *Gbx2* delete allele (e), the neomycin resistance gene cassette has not been removed.

3.4 Left-right patterning defects in *Gbx2*$^{-/-}$ embryos

L-R patterning is determined early in embryogenesis. L-R patterning defects have not been previously reported in *Gbx2*$^{-/-}$ mice, however 36% of *Gbx2*$^{-/-}$ embryos (n=25 examined) collected in this study had a form of L-R patterning defect. Figure 3.6 shows the L-R patterning defects observed with the penetrance of each defect summarised in Table 3.6.

Right isomerism, in which the left side has failed to adopt left sided identity was present, affecting the atria and lungs. The right lung usually consists of four lobes, namely the cranial, middle, caudal and an accessory lobe that crosses the midline, while the left lung is one singular lobe. Right pulmonary isomerism (RPI) was present in 24% of *Gbx2*$^{-/-}$ mice in which both the right and left lungs had three lobes (Figure 3.6b).

Deoxygenated blood is returned to the heart by the left and right superior caval veins and the inferior caval vein that drain into the right atrium. This was observed in control embryos (n=11, wild type and *Gbx2*$^{+/-}$ embryos) at E15.5. Right atrial isomerism (RAI) in which both the superior caval veins drained into a common atrial chamber was observed in 24% of *Gbx2*$^{-/-}$ embryos (Figure 3.6d). These embryos also had two bilaterally symmetrical inferior caval veins.

Defects to the heart include the aforementioned mirror image aortic arch, found in 24% of *Gbx2*$^{-/-}$ mice (Figure 3.6f). TGA was present in one *Gbx2*$^{-/-}$ embryo (Figure 3.4) and this defect is often associated with L-R patterning defects (104, 105). Additionally, the heart was malpositioned in *Gbx2*$^{-/-}$ mice. The apex of the heart usually points leftward. Mutants showed dextrocardia (8%) with a rightward facing apex (Figure 3.6h). Likewise, mesocardia, in which the heart is positioned centrally, was present in a portion of embryos (32%).

Table 3.6. Penetrance of left-right patterning defects in *Gbx2*$^{-/-}$ embryos at E15.5.

Abbreviations: AA, aortic arch; L-R, left-right; RAI, right atrial isomerism; RPI, right pulmonary isomerism; TGA, transposition of the great arteries.

	Frequency				
Genotype	**L-R patterning defect**	**RPI**	**RAI**	**Dextrocardia**	**Mirror image AA**
***Gbx2*$^{-/-}$** n=24	9 (36%)	6 (24%)	6 (24%)	2 (8%)	6 (24%)

While these L-R patterning defects largely occurred together, RAI, RPI and mirror image aortic arch, also presented independent of other L-R pattering defects. RPI is frequently associated with RAI and cardiovascular defects (175, 176). As was the case here, of the six embryos with RPI, all occurred with a cardiovascular defect and 5/6 occurred with RAI (as shown in Appendix A.1). Heterotaxy can occur in multiple abdominal or visceral organs, however positioning abnormalities were restricted to the heart and lungs in *Gbx2*$^{-/-}$ mice, not the stomach or liver.

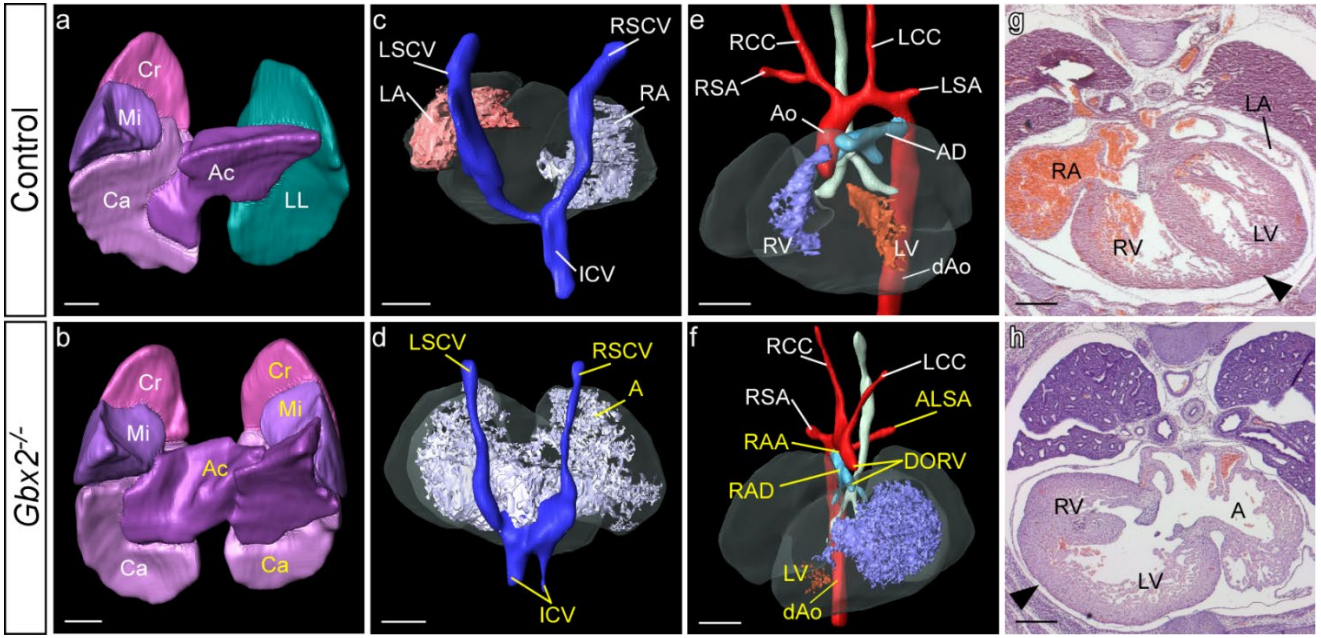

Figure 3.6. Left-right patterning defects in *Gbx2*$^{-/-}$ embryos at E15.5.

MRI reconstructions showing normal lung structure in a control embryo (a). There are four lobes on the right (cranial, Cr; middle, Mi; caudal, Ca) with the accessory lobe (Ac) crossing and the midline and one left lobe (LL). *Gbx2*$^{-/-}$ embryo (b) has RPI, with three lobes also on the left side. Dorsal view of the control heart and pulmonary circulation (c) with the right and left superior vena caval veins (SCV) and the single inferior caval vein (ICV) draining into the right atrium. RAI is present in the mutant (d) the superior caval veins drain into a common atrial chamber (A) and there are two bilaterally symmetrical ICV. A normal aortic arch present in control (e) and a mirror image aortic arch structure in *Gbx2*$^{-/-}$ embryo (f) with RAA, RAD, right sided dorsal aorta (dAo) and an ALSA. H&E stained transverse section of control (g) showing a leftward pointing apex (arrowhead). Dextrocardia was observed in mutants (h) with a rightward pointing apex. Abbreviations: A, atrial chamber; Ac, accessory lobe; AD, arterial duct; ALSA, aberrant left subclavian artery; Ao, aorta; Ca, caudal lobe; Cr, cranial lobe; dAo, dorsal aorta; DORV, double outlet right ventricle; ICV, inferior caval vein; LA, left atrium; LCC, left common carotid artery; LL, left lobe; LSA, left subclavian artery; LSCV, left superior caval vein; LV, left ventricle; RA, right atrium; RAA, right aortic arch; RAD, right arterial duct; RAI, right atrial isomerism; RCC, right common carotid artery; RSA, right subclavian artery; RSCV, right superior caval vein; RV, right ventricle; Tr, trachea; VSD, ventricular septal defect. Scale, 500μm. Lung reconstructions made by Dr Simon Bamforth.

Gbx2$^{-/-}$ embryos were collected at mid-embryogenesis (E10.5 and E11.5) and analysed by HREM to assess the formation of the PAA prior to remodelling. 3D reconstructions of the PAA structure were made from the datasets (Figure 3.7). Six mutants were analysed in total (n=3 at each stage) and two had a PAA defect, summarised in Table 3.7. This included a hypoplastic or absent 4th PAA. At E10.5, two embryos had a unilateral absent 6th PAA as well as a 4th PAA defect. The 6th PAA form in the 31-34 somite stage. These embryos were 34-35 somites and the absence of the 6th PAA could indicate a developmental delay.

Table 3.7. 4th pharyngeal arch artery defects present in *Gbx2*$^{-/-}$ embryos at E10.5 and E11.5 assessed by HREM.

Abbreviations: PAA, pharyngeal arch artery; Th, thin

	Frequency		
	4th PAA defect	**Unilateral defect**	
Age		**Th**	**Absent**
E10.5 n=3	2 (67%)	1 (33%)	1 (33%)
E11.5 n=3	2 (67%)	0	2 (67%)

Additionally, two embryos had a right dorsal aorta with a greater diameter than the left dorsal aorta. The right dorsal aorta usually regresses while the left persists to form the mature dorsal aorta. The enlarged right dorsal aorta could be indicative of a L-R patterning defect, for example the mirror image aortic arch with a right sided dorsal aorta. The penetrance of this early defect correlates with the penetrance of L-R patterning defects at E15.5.

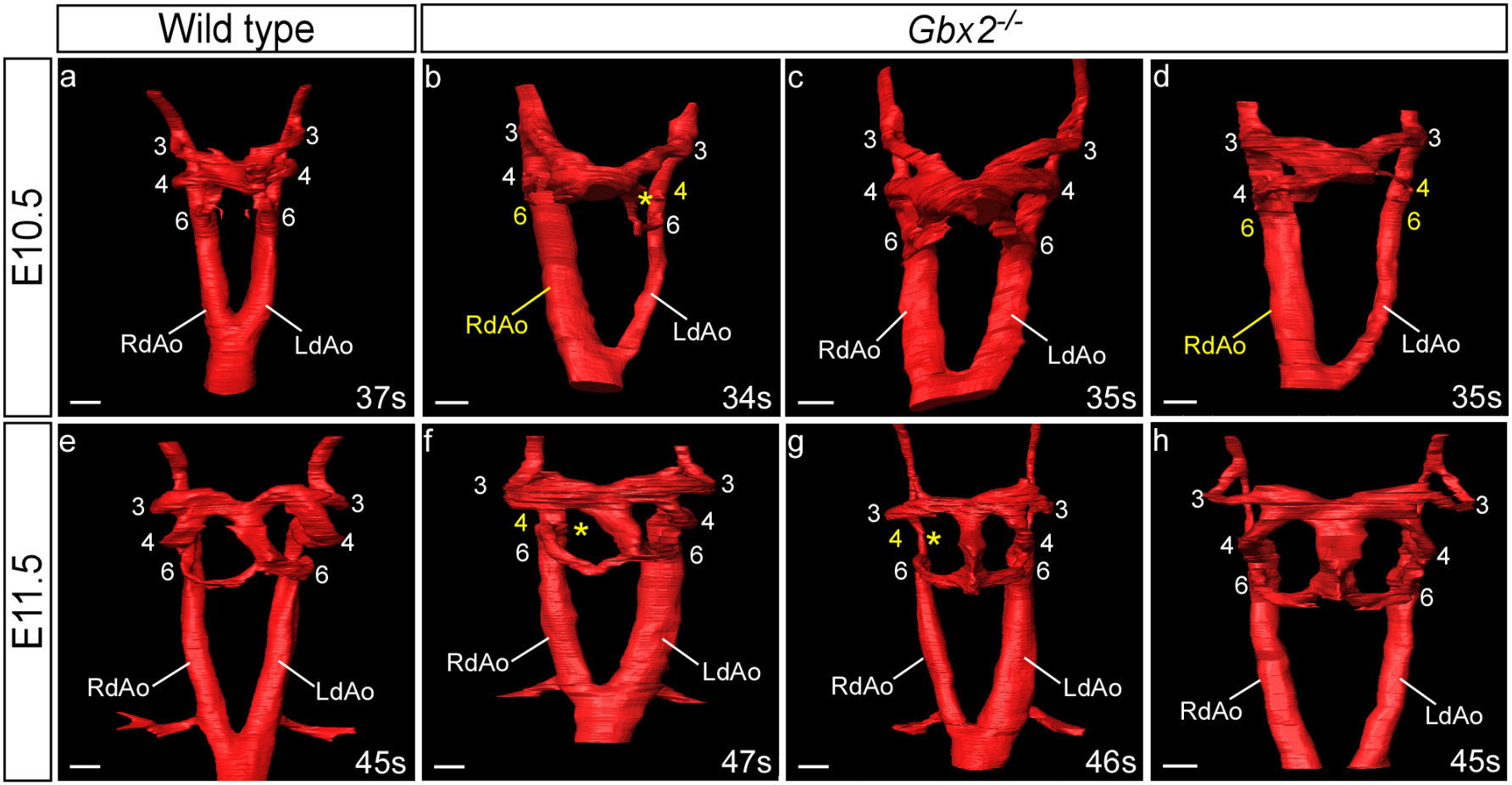

Figure 3.7. HREM reconstructions showing the PAA structure at E10.5 and E11.5 in *Gbx2*$^{-/-}$ embryos.

3D reconstructions of the PAA prior to asymmetric remodelling in wild type E10.5 (a) and E11.5 (e) embryos. There are three pairs of PAA (numbered) connecting the aortic sac to the paired dorsal aorta (dAo). Reconstructions of *Gbx2*$^{-/-}$ embryos at E10.5 (b-d) and E11.5 (f-h). Mutants had an absent (*; b,f,g) or hypoplastic (d) 4th PAA. The 6th PAA were absent in two embryos (b, d). Embryos (b, d) had a right dorsal aorta (RdAo) with a larger diameter than the left dorsal aorta, indicative of a L-R patterning defect. Somite counts (s) indicated. Abbreviations: LdAo, left dorsal aorta; RdAo, right dorsal aorta. Scale, 100μm.

Pitx2c is a key nodal signalling factor, required for L-R determination. Mice deficient for *Pitx2* display L-R patterning defects, including right isomerism (114). Aberrant or reduced *Pitx2c* expression has been found in mouse models with L-R patterning defects. *Cited2*$^{-/-}$ mice show patterning defects reminiscent of *Gbx2*$^{-/-}$ embryos, such as RAI and bilateral inferior caval veins, together with aberrant *Pitx2* expression (114).

Gbx2$^{-/-}$ embryos were collected at E8.5 to assess *Pitx2* expression by whole mount *in situ* hybridisation. There are three isoforms of *Pitx2* (*Pitx2a-c*), which differ in their N-terminal but have an identical C-terminal and homeodomain (109). The probe used detected all isoforms of *Pitx2.* All isoforms are expressed in the head mesoderm at E8.5, whereas only *Pitx2c* is present asymmetrically in the LLPM where it is required for establishing laterality. This was observed in wild type controls (n=3) with clear expression in the head mesoderm and LLPM (Figure 3.8). Expression appears unaffected in *Gbx2*$^{-/-}$ embryos (n=6).

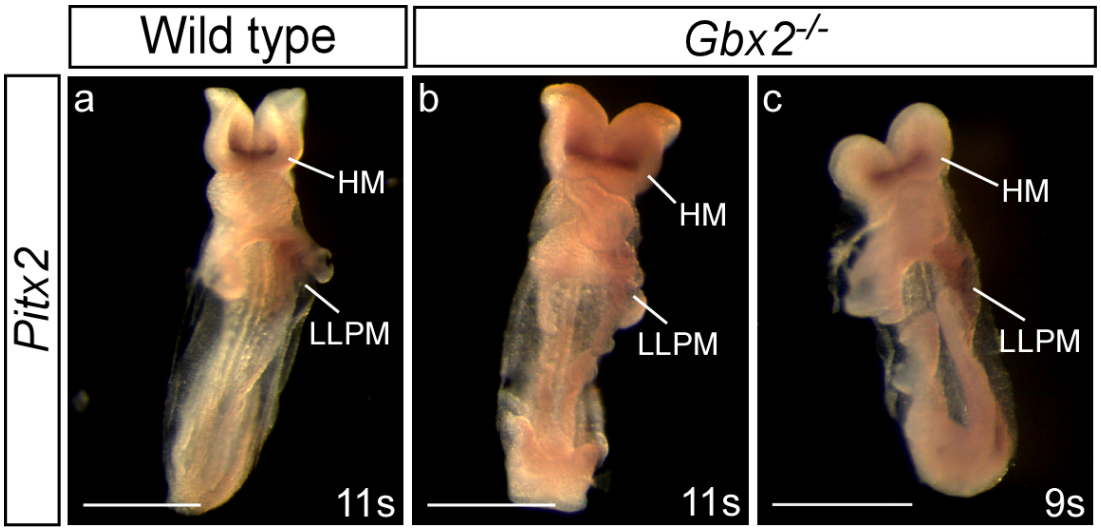

Figure 3.8. *Pitx2* expression in *Gbx2*$^{-/-}$ embryos at E8.5.

Whole mount *in situ* hybridisation using a *Pitx2* probe in wild type (a, n=3) and *Gbx2*$^{-/-}$ (b,c, n=6) embryos at E8.5. *Pitx2* is expressed in the head mesoderm (HM) and left lateral plate mesoderm (LLPM). Expression is unaffected in *Gbx2*$^{-/-}$ embryos. Embryos were between 9-11 somites. Somite counts (s) indicated. Abbreviations: HM, head mesoderm; LLPM, left lateral plate mesoderm. Scale, 500μm.

3.5 Pharyngeal arch artery formation and remodelling in *Gbx2*$^{-/-}$ embryos

The cardiovascular defects present in *Gbx2*$^{-/-}$ mice indicate aberrant formation of the 4th PAA, as confirmed by HREM. To analyse the development of the PAA and determine the penetrance of 4th PAA defects at E10.5, *Gbx2*$^{-/-}$ embryos were collected for intracardiac ink injection to visualise the vessels prior to their remodelling.

No defects were observed in wild type embryos (n=13). Of the 43 *Gbx2*$^{+/-}$ embryos examined, three had a unilateral 4th PAA defect, with a hypoplastic (n=2) or non-patent (n=1) vessel. For two of these embryos, it was the right 4th PAA affected. This would likely result in non-fatal ARSA. Additionally, this penetrance of defects is low, at only 7%. Defects to the 4th PAA have been known to recover during development (as discussed in detail in Section 1.6.2). This recovery could explain the lack of defects present in *Gbx2*$^{+/-}$ embryos at E15.5.

89% (n=9) of *Gbx2*$^{-/-}$ embryos collected displayed abnormal development of the 4th PAA (Figure 3.9). This included either a hypoplastic or non-patent vessel, with defects either unilateral or bilateral. Table 3.8 summarises the 4th PAA defects in *Gbx2*$^{-/-}$ embryos assessed by ink injection and HREM.

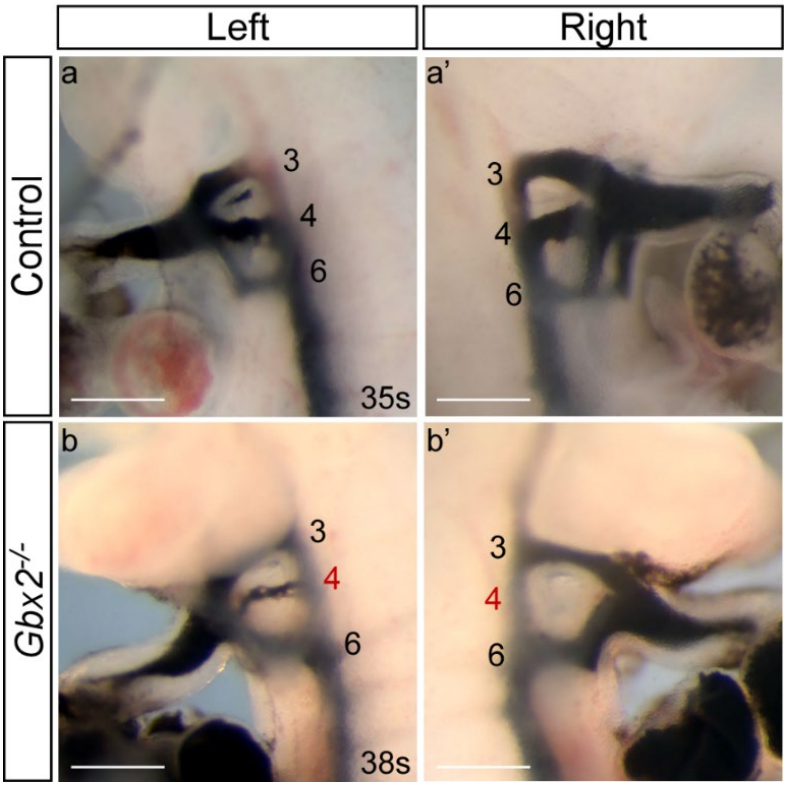

Figure 3.9. 4th pharyngeal arch artery defects in *Gbx2*$^{-/-}$ embryos at E10.5.

Intracardiac ink injection of E10.5 embryos. In control (a) PAA 3-6 (numbered) were patent to ink. *Gbx2*$^{-/-}$ embryos (c) had 4th PAA defects. A hypoplastic left 4th PAA (b) and absent right 4th is shown (b'). Somite counts (s) indicated. Scale, 500μm.

Table 3.8. Penetrance of 4th pharyngeal arch artery defects in *Gbx2*$^{-/-}$ embryos at E10.5 assessed by intracardiac ink injection and HREM.

Abbreviations: NP, non-patent; PAA, pharyngeal arch artery; Th, thin.

	Frequency							
	4th PAA defect	Unilateral defect			Bilateral defect			
Genotype		Defect	Th	NP	Defect	Th-Th	NP-Th	NP-NP
Gbx2$^{-/-}$ n=12	10 (83%)	5 (42%)	1 (8%)	4 (33%)	5 (42%)	0	3 (25%)	2 (17%)

3.6 Endothelial cell contribution to the pharyngeal arch arteries in *Gbx2*$^{-/-}$ embryos

Gbx2$^{-/-}$ embryos were collected at E10.5 to assess the formation of the PAA, specifically the formation of the endothelial lumen. ETS-related gene (ERG) is a transcription factor involved in angiogenesis and the anti-ERG1 antibody reliably detects endothelial cells (177). Immunohistochemistry for anti-ERG1 antibody was used to detect the endothelial cells in the PA of wild type (n=3) and *Gbx2*$^{-/-}$ (n=4) embryos.

In wild type embryos, a clear ring of endothelial cells was present around the 3rd and 4th PAA (Figure 3.10). This was also observed in two *Gbx2*$^{-/-}$ embryos however, two *Gbx2*$^{-/-}$ embryos had a unilateral absent 4th PAA. This occurred together with a disorganised arrangement of endothelial cells in the 4th PA. The endothelial cells failed to form a lumen of the vessel and are instead scattered throughout the 4th PA. The 3rd PAA was unaffected in mutants.

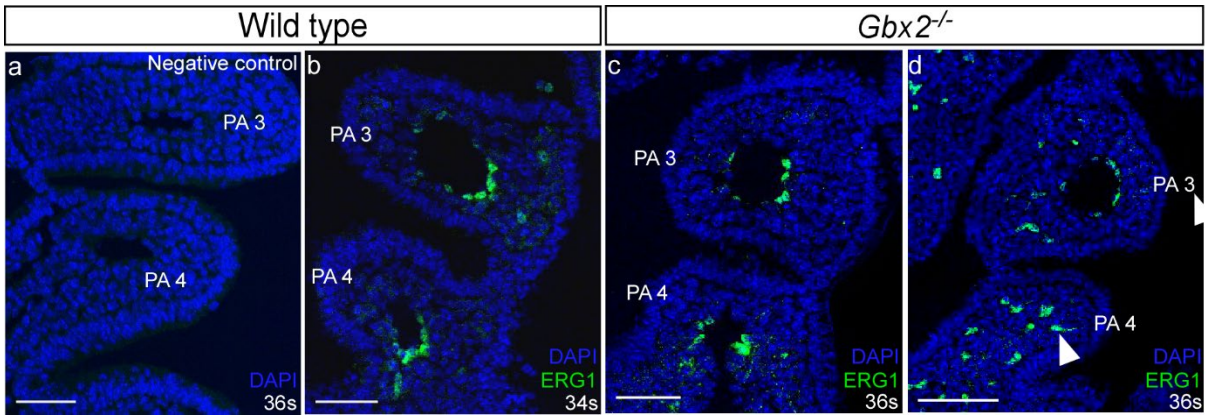

Figure 3.10. Endothelial cell disorganisation in *Gbx2*$^{-/-}$ embryos.

IHC staining with an anti-ERG1 antibody on coronal E10.5 sections of wild type (a) and *Gbx2*$^{-/-}$ (b,c) embryos. (a) Secondary antibody only control. The endothelial cells have formed the lumen in 3rd and 4th PAA in the wild type. *Gbx2*$^{-/-}$ embryo (b) with the endothelial cells normally formed around the PAA. *Gbx2*$^{-/-}$ embryo (c) with normal 3rd PAA formation but the endothelial cells have failed to form a vessel lumen of the 4th PAA. The cells are scattered through the 4th PA (arrowhead). Somite count (s) indicated. Abbreviations: PA, pharyngeal arch. Scale, 50μm.

3.7 Discussion

As found in previously published studies, the data presented in this chapter shows a role for *Gbx2* in cardiovascular development. *Gbx2*$^{-/-}$ mice have defects to the great arteries that stem from the aberrant development of the 4th PAAs, as well as conotruncal and L-R patterning defects.

The penetrance and severity of cardiovascular defects was greater in the mutants collected in this study at both E10.5 and E15.5 compared to previously published data (133, 166). The penetrance of 4th PAA defects at E10.5 was previously reported at 50% (n=12 examined) by Calmont et al. (2009), with all defects being unilateral. In this study, 83% of *Gbx2*$^{-/-}$ embryos (n=12 examined) were abnormal, with 42% of embryos showing a bilateral 4th PAA defect. Likewise, at E15.5, when comparing this study to the Byrd and Meyers (2005) study, there was a significant increase in the penetrance of cardiovascular defects. *Gbx2*$^{-/-}$ mice in this study also presented with previously unreported defects including TGA, VR and L-R patterning defects. The Calmont and Byrd and Meyers study used the same mouse construct which differed from the construct used here (Figure 3.5) which could cause a deviation in phenotype between the studies.

The *Gbx2* mouse construct used in this project differed from that used in the published studies as the *neomycin* selection cassette was removed from the final mutant delete allele. The use of drug selection cassettes has proven invaluable in constructing transgenic models and disrupting gene expression (as reviewed by Hall et al., 2009). Drug selection cassettes are inserted into a genomic clone then into a homologous genetic locus through homologous recombination. The cassette then functions to positively select cells that have acquired the construct. However, such manipulations have been known to alter the expression of nearby genes of the intended target, termed the neighbourhood effect.

The neighbourhood effect was apparent in studies investigating the role of *Mrf4* in myogenesis (as reviewed by Olson et al., 1996). Three mouse models mutated for the same gene showed strikingly different phenotypes (178-180). It was argued that this varied phenotype was not due to a difference in genetic background, as all mouse models were on a C57Bl/129 background. In each case, a *PGKneo* selection cassette was inserted to delete regions of the *Mrf4* protein coding sequence. Each model varied in the sequence deleted and the orientation of the *PGKneo* selection cassette.

The three *Mrf4* mutants differed in the severity of defects, with one model being fatal (179), one showing milder defects (180) and one showing largely normal development (178). It was noted that *Mrf4* was in close proximity to *Myf5* on mouse chromosome 10 (181). Defects were present in the mutants in which the neomycin resistance gene was transcribed in the same direction as the *Myf5* gene (179, 180) and it was postulated that the transcription of the *PGKneo* selection cassette also interfered with expression of *Myf5.*

Wassarman et al. (1997), which first described the *Gbx2* mouse used by Byrd and Meyers, reported that $Gbx2^{flox}$ heterozygotes were indistinguishable from wild type mice. This is because the $Gbx2^{flox}$ allele should function as a wild type allele. However, $Gbx2^{flox}$ homozygote mutants died at birth with abnormalities in hindbrain development. Wassarman et al. (1997) found aberrantly spliced *Gbx2* transcripts in $Gbx2^{flox}$ mice. These transcripts resulted in non-functioning *Gbx2* protein variants and therefore the $Gbx2^{flox}$ homozygotes would carry two non-functioning copies of *Gbx2.* It was suggested that the neomycin cassette interferes with the normal expression of *Gbx2* creating a hypomorphic allele. The neomycin cassette coding sequence contains cryptic splice sites which results in the translation of proteins with altered functionality (182-184) .

Other mouse models have reported that this aberrant splicing alters the amount of wild type mRNA of the target gene and therefore the presentation of a phenotype (182, 185). Kist et al. (2005) inserted a neomycin cassette into the *Pax9* coding sequence to generate two *Pax9* mutant alleles; $Pax9^{neo}$, a hypomorphic allele, and $Pax9^{LacZ}$, a complete *Pax9* knockout. Alternative splice variants were detected in $Pax9^{neo}$ mice which reduced the amount of wild type *Pax9* mRNA present. $Pax9^{+/neo}$ and $Pax9^{+/LacZ}$ heterozygotes had a reduction in wild type *Pax9* mRNA of more than the expected 50%, showing that the presence of the neomycin cassette is interfering with normal splicing.

Pax9 wild type mRNA was reduced to 7% in $Pax9^{neo/LacZ}$ mice compared to wild type mice (185). Previous work in the laboratory compared the cardiovascular defects in $Pax9^{neo/LacZ}$ mice to $Pax9^{LacZ/LacZ}$ mice to determine if the dosage of *Pax9* affected the presentation of the *Pax9*-null phenotype. $Pax9^{LacZ/LacZ}$ ($Pax9^{-/-}$) mice are a complete *Pax9* knockout with no wild type *Pax9* mRNA expression. These mutants all had defects to the thymus and cardiovascular system, this phenotype has been previously

described in Section 1.7.2. The penetrance of cardiovascular defects was 36% (n=14 examined) in *Pax9*$^{neo/LacZ}$ mice while all mice had an abnormal thymus. This shows that the cardiovascular phenotype varies with gene dosage and 7% expression of wild type *Pax9* mRNA was sufficient for a subset of embryos to develop normal cardiovascular systems. The complete penetrance of thymus defects shows that the threshold of *Pax9* mRNA expression for normal development between the thymus and cardiovascular system varies.

This evidence shows that the presence of selection cassettes can modify the presentation of a phenotype and could therefore provide reasoning for the varied *Gbx2*$^{-/-}$ phenotype between studies. The *neomycin* cassette in the Byrd and Meyers construct could have resulted in aberrant splicing or disrupted gene expression of neighbouring genes of *Gbx2.* As the neomycin cassette was removed from the *Gbx2* mouse construct used in this study, this effect should not affect results obtained in this study and phenotyping analysis is arguably more reliable.

Genetic background is known to affect the presentation of a phenotype (136). Both data sets were maintained on C57Bl/6 background in the aforementioned studies that have analysed the *Gbx2*-null phenotype. Byrd and Meyers used mice that were 99% enriched and mice in this study were between 86-99% enriched on a C57Bl/6 background. However, the Calmont study used mice on a mixed background at only 50% C57Bl/6. Additionally, the mouse substrain was not provided in the published literature.

Data analysis and interpretation could affect the described *Gbx2*-null phenotypes. The Byrd and Meyers study primarily analysed embryos using dissection of near-term embryos and it is possible that some defects could have been overlooked. This project used several methodologies (MRI, HREM, histology, ink injection) to provide an arguably more in-depth analysis of the *Gbx2*$^{-/-}$ phenotype at multiple embryonic stages.

Part of the *Gbx2*$^{-/-}$ phenotype includes defects derived from the abnormal development of the 4th PAA, namely RAA and ARSA. Ink injection and HREM analysis showed that 73% of *Gbx2*$^{-/-}$ embryos had an absent 4th PAA at E10.5-11.5. IHC labelling endothelial cells showed that the absence of the 4th PAA was accompanied by the disorganisation of the endothelial cells. As discussed in Section 1.2.2, the mechanism of PAA formation is unknown and the debate of angiogenesis against vasculogenesis is ongoing (36, 37). However, in the caudal PAs (3rd-6th), the endothelial cells were found to be largely

derived from SHF-mesoderm progenitors and so the caudal PAAs originate through *de novo* vasculogenesis (36, 40). These endothelial cells form a plexus within the PA prior to lumenisation. The exact mechanism of this remodelling is unknown although it has been proposed that the vessel grows through angiogenesis as the endothelial cells migrate as angiogenic sprouts (37).

In the *Gbx2*$^{-/-}$ embryos, the endothelial cells have been successfully recruited to the PA but have failed to remodel to form a vessel lumen. This endothelial cell disorganisation was also observed by Byrd and Meyers (2005) *Gbx2*$^{-/-}$ mutants. NCC were not investigated in the *Gbx2*$^{-/-}$ mice in this study, however Byrd and Meyers noted a reduction in the NCC within the caudal PAAs. It was concluded that the reduction in NCC was responsible for endothelial cell organisation, although the role of *Gbx2* in vessel lumenisation could also be independent of NCC.

Hrt1 and *Hey1* of the Hairy-related transcription factor family are downstream mediators of Notch signalling. *Hrt1* and *Hey1* mutants present with RAA, IAA and ARSA due to the abnormal development of the 4th PAAs (186). A disorganisation of the endothelial cells was also observed in the 4th PAA of *Hrt1* and *Hey1* mutants. This occurred with reduced expression the Notch ligand *Jag1* specifically within the abnormal 4th PAA endothelial cells. The involvement of *Gbx2* together with Notch signalling in PAA morphogenesis has not been investigated, however Notch pathway genes are expressed with *Gbx2* in the developing hindbrain (46, 187). *Gbx2* is required in defining the midhindbrain boundary and impaired Notch signalling not only reduced *Gbx2* expression in the hindbrain but also shifted the midhindbrain boundary. It could be postulated that *Gbx2* and the Notch signalling pathway also interact in the formation of the 4th PAA lumen, as disruption of either results in endothelial cell disorganisation.

Several transcription factors, as well as *Gbx2*, are expressed in the pharyngeal endoderm, this includes *Hox* and *Tbx* gene families (as discussed in Graham et al., 2005). The transcription factors provide signalling cues from the endoderm for PA organisation and PAA formation (46, 47, 51, 188) (as discussed in Section 1.2.4). Alterations in the precise expression pattern within the pharyngeal endoderm disrupts the formation of the pharyngeal pouches which in turn disrupts segmentation of the PA (46, 188). For example, deletion of *Tbx1* from the pharyngeal endoderm prevented pouch formation and therefore PAA formation (51). The loss of *Gbx2* expression from

the endoderm in *Gbx2*$^{-/-}$ embryos could affect the signalling cues from this tissue during 4th PAA formation thereby resulting in defects to this vessel.

Another component to consider in the explanation for 4th PAA defects in *Gbx2*$^{-/-}$ embryos is the potential lack of flow-induced arteriogenesis. Blood flow has been shown to induce blood vessel formation and has a role in the asymmetric remodelling of the PAA. A study by Yashiro et al. (2007) observed that blood flow was significantly greater in the left dorsal aorta than the right dorsal aorta during the remodelling of the PAA which contributed to the regression of the right dorsal aorta. Likewise, it was found that continuous blood flow through the left 6th PAA was essential for the persistence of this vessel while there was reduced blood flow in the right 6th PAA. The decreased blood flow resulted in reduced levels of platelet derived growth factor and vascular endothelial growth factor receptor in the regressing vessels, both of which are required in blood vessel formation (189). In the context of *Gbx2*$^{-/-}$ embryos, it could be a reduced blood flow directed to the 4th PAA which is causing the impaired formation of the 4th PAA.

As the exact mechanism of PAA formation is unknown, it is difficult to infer the role of *Gbx2* in PAA morphogenesis. *Gbx2* could input at various stages of PAA formation, for example at the level of lumenisation either independently of, or through NCC recruitment. In *Gbx2*$^{-/-}$ the precise expression pattern within the endoderm will be altered. This could result in aberrant signalling cues from the pharyngeal endoderm during PAA formation result in abnormal 4th PAA development.

L-R patterning defects were present in *Gbx2*$^{-/-}$ mice. As discussed in Section 1.5, laterality is determined through multiple, lateral signalling cascades initiated at the node from E7.5 (107, 108). *Pitx2* is a key signalling factor in one of these pathways and mice deficient for *Pitx2* present with laterality defects reminiscent of those present in *Gbx2*$^{-/-}$ mice (109, 114). However, *Pitx2* expression was analysed in these mutants and did not differ from controls. Therefore, the reason for these defects in *Gbx2*$^{-/-}$ mice is unknown.

Gbx2 is expressed early in development and breaking of symmetry begins at E7.5 at the node and there are many complex pathways and interactions required during the establishment of the L-R axis (112). It is possible that *Gbx2* could interact with other components of these signalling cascades such as Notch signalling or retinoic acid siganlling, both required in L-R determination. Altered retinoic acid signalling results in

cardiovascular defects observed in *Gbx2* mutants including DORV and TGA (106). More work is required to determine the role of *Gbx2* in PAA morphogenesis and L-R axis determination.

There is incomplete penetrance of cardiovascular defects in *Gbx2*$^{-/-}$ mice and the individual defects present in each embryo also varied. Incomplete penetrance is a feature of many mouse models and genetic syndromes. As stated, 22q11DS patients display a broad phenotype, varying in the defects present and their penetrance (84). The basis of this variability is not completely understood but the presence of genetic modifiers outside of the 1.5 and 3Mb deletion region, such as *Fgf8,* are thought to contribute (101, 190).

Genetic background also has a major effect on the presentation of a phenotype. The *Df1/+* mouse, which largely resembles the 1.5Mb deletion in 22q11 deletion in patients, was analysed on multiple genetic backgrounds and the penetrance of cardiovascular defects ranged from 16% to 50% at E15.5 (136). Discrepancies in phenotypes analysed on different genetic backgrounds are evident in the *Cited2*$^{-/-}$ mouse model, which have cardiovascular and L-R patterning defects (114). Analysis of this mutant on an enriched C57Bl/6 background compared to a mixed background showed a significant increase in the frequency of L-R patterning defects. This correlated with a greater reduction in *Pitx2c* expression in the mice on an enriched background, whereas *Pitx2c* expression on the mixed background was unaffected.

Another explanation for the incomplete penetrance is the ability of the 4th PAA to recover during development (discussed in Section 1.6.2). This was evident in the *Gbx2*$^{-/-}$ mice collected as the penetrance of 4th PAA defects was greater at E10.5 (91%) than E15.5 (64%). This recovery is well documented in *Tbx1*$^{+/-}$ mouse models (130). *Df1/+* mice presented with cardiovascular defects at a reduced penetrance when compared to patients. However, non-cardiac defects in *Df1/+* mice did not recover during development showing the recovery to be specific to cardiovascular development.

Gbx2$^{-/-}$ phenotyping shows that these embryos either: develop normally, have 4th PAA-derived defects or present with simultaneous L-R patterning and 4th PAA-derived defects (Figure 3.11). However, the number of *Gbx2*$^{-/-}$ embryos obtained from the *Gbx2*$^{+/-}$ mouse cross was significantly lower than expected showing that over 50% of *Gbx2*$^{-/-}$ embryos are lost prior to E8.5 in early embryogenesis. The 4th PAA begins to

form from around E9.5 although the establishment of the L-R axis precedes this, beginning at the node of the primitive streak from E7. L-R patterning defects are largely a result of abnormalities at the node (119). The *Gbx2*$^{-/-}$ 4th PAA defects (RAA and ARSA) and L-R patterning defects (RPI and RAI) are not embryonically lethal. This suggests that *Gbx2* expression is required earlier than both the specification of the PAA and determination of L-R patterning and the deletion of *Gbx2* can result in embryonic lethality. *Gbx2* is expressed in all three germ layers at gastrulation at E6 (163), however the role of *Gbx2* expression at this stage is unknown.

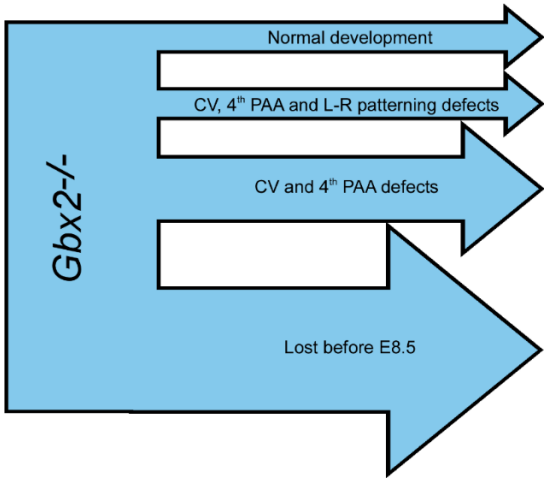

Figure 3.11. Fate of *Gbx2*$^{-/-}$ embryos.

A large portion of *Gbx2*$^{-/-}$ embryos are lost before E8.5. The mutants that survive past this point either develop normally or present with cardiovascular and 4th PAA defects. Of the mutants with cardiovascular defects, L-R patterning defects were present in a subset of embryos.

In conclusion, the work in this chapter provides an in-depth analysis of the cardiovascular phenotype of *Gbx2*$^{-/-}$ mice. The phenotype shows incomplete penetrance and appears to be susceptible to the 4th PAA recovery. IAA and VSD are prominent features of phenotype of 22q11DS, with a prevalence of 5-20% and 10-50% respectively (85). While at a lower penetrance, RAA, defects to the subclavian arteries, DORV and TGA also present in patients (85-87). *Gbx2*$^{-/-}$ mice did not have IAA, however shared overlapping features with the other defects in 22q11DS patients implicating *Gbx2* as a potential genetic modifier of this disease.

Chapter 4. Investigating the *Pax9-Gbx2* interaction during cardiovascular development

4.1 Introduction

Pax9 is a transcription factor expressed in the PA during mid-embryogenesis. Previous studies have identified the role of *Pax9* in thymus, limb and craniofacial development (148, 152), as discussed in Section 1.7.1.

A role of *Pax9* in cardiovascular development has also been identified as chromosomal deletions of *PAX9* are associated with cardiovascular defects. A patient with a hemizygous *PAX9* deletion had IAA, VSD and a hypoplastic aorta (147). The role of *Pax9* was investigated using the *Pax9*-null mouse model, with all mice presenting with cardiovascular defects (134). *Pax9*-null mice present with multiple cardiovascular and OFT defects, namely; IAA, ARSA, absent common carotid arteries, hypoplastic aorta, DORV and VSD. Cleft palate and an absent thymus are also typical of *Pax9*-null mice (152). The shared cardiovascular phenotype in *Pax9*-null mice and patients with chromosomal *PAX9* deletions confirm the loss of *PAX9* to be the cause of defects in these patients. These patients share features of the 22q11DS phenotype, namely IAA and VSD.

Transcriptome analysis of the pharyngeal region of *Tbx1*$^{-/-}$ mice showed downregulation of *Pax9* (137). *Pax9* is expressed in the pharyngeal endoderm of the PA, along with *Tbx1,* and these genes interact during cardiovascular development (134). *Pax9* heterozygosity increased the penetrance of cardiovascular defects in *Tbx1*$^{+/-}$ mice. This suggests an interaction between these genes in cardiovascular development and implicates *Pax9* as a potential modifier of the 22q11DS phenotype.

The work presented in Chapter 3, and previously published studies, has confirmed the role of *Gbx2* in cardiovascular development (133, 166). The *Gbx2*$^{-/-}$ cardiovascular phenotype was varied and mice presented with a range of defects including RAA, ARSA, VSD, DORV and TGA. Additional defects were present including a mirror image aortic arch and L-R patterning defects.

Gbx2 is a potential shared target of *Pax9* and *Tbx1,* as transcriptome analysis of the pharyngeal region of *Pax9*-null and *Tbx1*-null embryos showed a downregulation of *Gbx2* (134, 137). *Pax9* was shown to interact with *Tbx1* within the pharyngeal endoderm (134). The *Pax9*$^{-/-}$ and *Gbx2*$^{-/-}$ phenotype share overlapping features including DORV, VSD, ARSA suggesting that these genes act via the same genetic network. As *Pax9* and *Gbx2* are both expressed within the pharyngeal endoderm, it was surmised that these genes could interact during PAA morphogenesis.

This chapter aims to investigate the potential interaction between *Pax9* and *Gbx2.* Wild type, *Pax9*$^{-/-}$ and *Gbx2*$^{-/-}$ embryos were collected at mid-embryogenesis for gene expression analysis. To investigate an interaction in cardiovascular development, *Pax9*$^{+/-}$;*Gbx2*$^{+/-}$ mice were intercrossed and embryos with the simultaneous deletion of both genes were analysed by MRI and histology at E15.5 and intracardiac ink injection at E10.5.

4.2 *Pax9* and *Gbx2* expression *in vivo*

Wild type embryos were collected at E8.5 and E9.5 for whole mount *in situ* hybridisation using *Pax9* and *Gbx2* probes to show the expression of these genes during embryogenesis (Figure 4.1).

At E8.5 and E9.5 *Pax9* was detected in the PA. *Pax9* is required in the development of the thymus, parathyroid gland and ultimobranchial bodies, all of which are derivatives of the pharyngeal pouches within the PA (detailed in Section 1.2.3).

At E8.5, *Gbx2* was present in the PA, tail bud and midhindbrain boundary region with expression present in the otocyst by E9.5. *Gbx2* has a role in brain development, required for the specification of the midhindbrain (165). *Gbx2* is also required in the formation of the inner ear, which is formed from the otocyst (191).

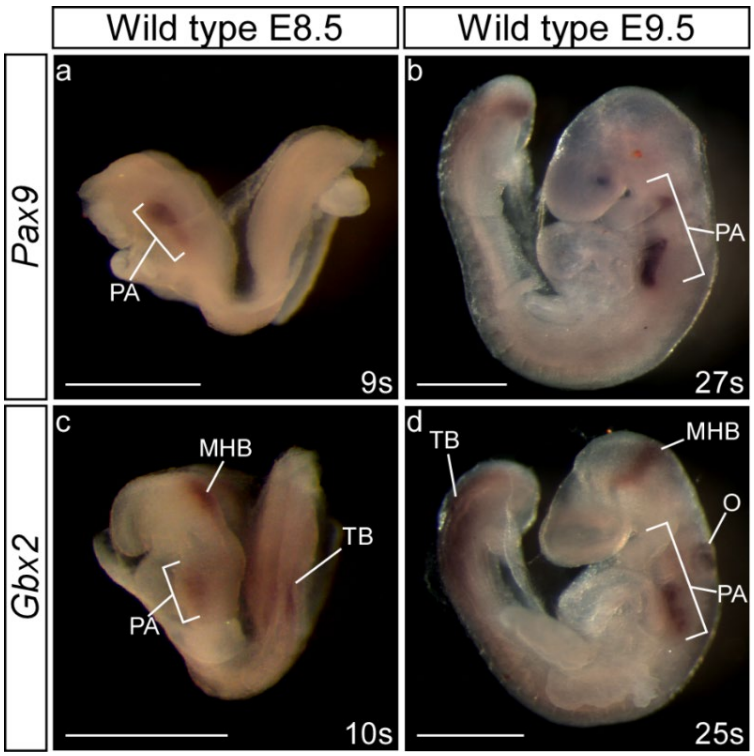

Figure 4.1. Whole mount *in situ* hybridisation for *Pax9* and *Gbx2*.

Wild type embryos were collected at E8.5 and E9.5 for whole mount *in situ* hybridisation using a *Pax9* (a-b) or *Gbx2* (c-d) probe. *Pax9* expression was restricted to the pharyngeal arches (PA) at both stages. *Gbx2* was expressed in the PA, midhindbrain boundary region (MHB) and tail bud (TB) at E8.5 with additional expression in the otocyst (O) by E9.5. Somite counts (s) indicated. Abbreviations: MHB, midhindbrain boundary; O, otocyst; pp, pharyngeal pouches; TB, tail bud. *Pax9* probe: E8.5; n=3 embryos between 9-11 somites, E9.5; n=8 embryos between 24-27 somites. *Gbx2* probe: E8.5; n=3 embryos between 10-11 somites, E9.5; n=3 embryos between 24-26 somites. Scale, 500μm.

E9.5 wild type embryos (n=4) were sectioned and labelled with *Pax9* and *Gbx2* RNAScope probes to determine tissue specific expression within the PA (Figure 4.2). Both genes were expressed in the pharyngeal endoderm, with *Gbx2* also expressed in the pharyngeal ectoderm. Expression of both *Pax9* and *Gbx2* is notably higher in the caudal arches (3rd and 4th PA) when compared to the 2nd arch. The 2nd PAA regress during development while the 3rd and 4th persist to form the common carotid arteries and the subclavian arteries or the aortic arch respectively. *Pax9*$^{-/-}$ and *Gbx2*$^{-/-}$ mice have 4th PAA defects and their increased expression in the caudal arches reinforces the role of these genes in the development of the 4th PAA.

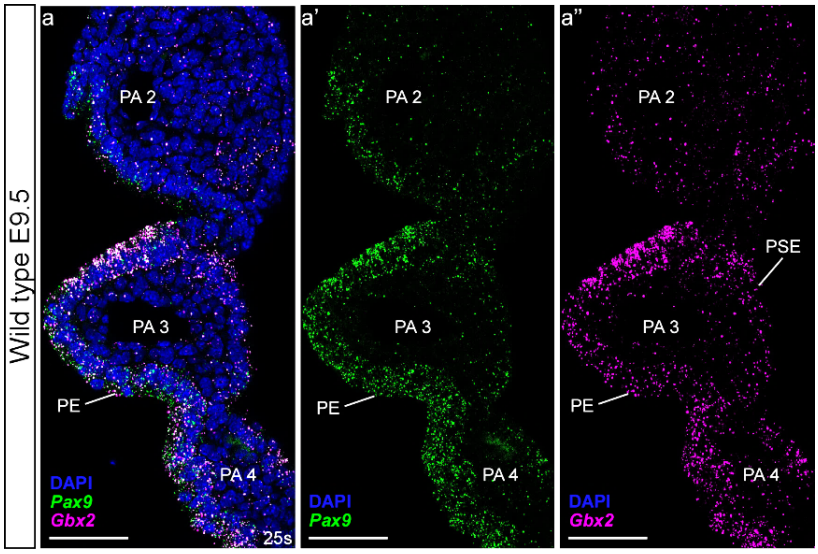

Figure 4.2. *Pax9* and *Gbx2* are expressed within the pharyngeal endoderm.

Pax9 and *Gbx2* RNAScope probes were used on wild type E9.5 sections (n=4, 24-25 somites). Both genes are expressed within the pharyngeal endoderm layer (PE). *Gbx2* is also expressed in the pharyngeal surface ectoderm (PSE). Somite counts (s) indicated. Abbreviations: PA, pharyngeal arch; PE, pharyngeal endoderm; PSE, pharyngeal ectoderm. Scale, 50μm.

RNASeq and qPCR analysis of *Pax9*$^{-/-}$ embryos showed downregulation of *Gbx2* in the PA at E9.5 (134). *Pax9*$^{-/-}$ embryos were collected at E9.5 for *in situ* hybridisation and RNAScope to determine the tissue specific downregulation of *Gbx2* (Figure 4.3). Whole mount *in situ* hybridisation showed that *Gbx2* expression was reduced specifically in the PA of *Pax9*$^{-/-}$ embryos while expression was maintained in the otocyst, tailbuds and midhindbrain region. *Gbx2*-labelled sections of *Pax9*$^{-/-}$ embryos revealed that *Gbx2* was reduced in the pharyngeal endoderm and ectoderm layer of the PA.

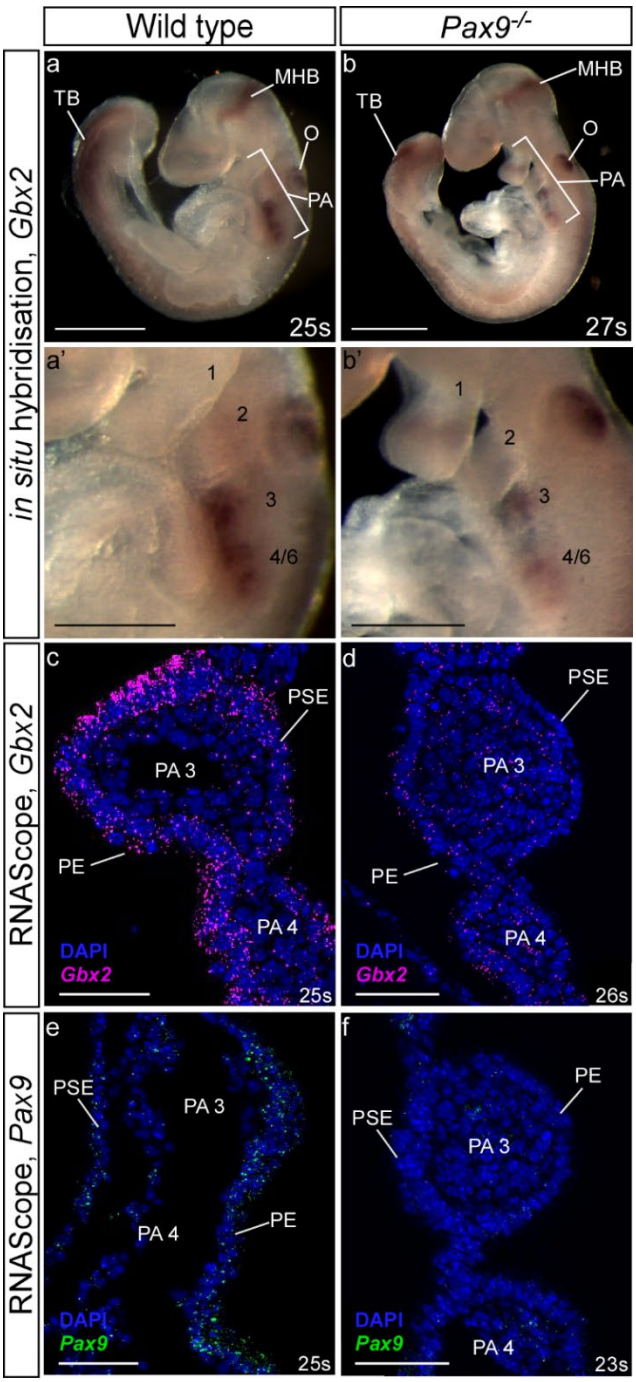

Figure 4.3. *Gbx2* expression within the pharyngeal arches of *Pax9*$^{-/-}$ embryos at E9.5.

Gbx2 in situ hybridisation in wild type (a, n=3, 24-26 somites) and *Pax9*$^{-/-}$ (b, n=3, 25-27 somites) embryos at E9.5. *Gbx2* expression is reduced specifically in the PA of *Pax9*$^{-/-}$ embryos (b') compared to wild types (a'). Expression is maintained in the midhindbrain (MHB), otocyst (O) and tail bud (TB) of *Pax9*$^{-/-}$ embryos (b). RNAScope for *Gbx2* on wild type (c, n=5, 24-28 somites) and *Pax9*$^{-/-}$ (d, n=3, 23-26 somites) sections. *Gbx2* is downregulated in the pharyngeal endoderm (PE) and pharyngeal ectoderm (PSE) of *Pax9*$^{-/-}$ embryos. RNAScope for *Pax9* in wild type (e, n=6, 24-28 somites) and *Pax9*$^{-/-}$ embryos (f, n=3, 23-26 somites) confirms loss of *Pax9* expression in *Pax9*-nulls. Somite counts (s) indicated. Abbreviations: PA, pharyngeal arch; PE, pharyngeal endoderm; PSE, pharyngeal ectoderm. Scale: a-b, 500μm; a'-b', 250 μm; c-d, 50μm.

Gbx2$^{-/-}$ embryos were collected at E9.5 to investigate *Pax9* expression by *in situ* hybridisation and RNAScope (Figure 4.4). Initially, *Pax9* expression was thought to be unaffected in *Gbx2*$^{-/-}$ embryos as whole mount *in situ* hybridisation showed that *Pax9* expression was maintained in the PA of these mutants. RNAscope was used to label E9.5 sections for *Pax9* expression. On closer inspection, *Pax9* is reduced in the pharyngeal endoderm of *Gbx2*$^{-/-}$ embryos.

The downregulation of *Pax9* and *Gbx2* in *Gbx2*$^{-/-}$ and *Pax9*$^{-/-}$ embryos, respectively, suggests an interaction between these genes. The downregulation of *Pax9* in *Gbx2*-null embryos was not detected by whole mount *in situ* hybridisation but required a closer analysis of sections. Conversely, whole mount *in situ* hybridisation showed a large reduction of *Gbx2* expression in *Pax9*-null embryos. The degree in which *Gbx2* was downregulated appears to be greater than the reduction in *Pax9* expression. This could indicate a hierarchy in the signalling pathway in which *Pax9* largely acts upstream of *Gbx2* and *Gbx2* feeds back to *Pax9.*

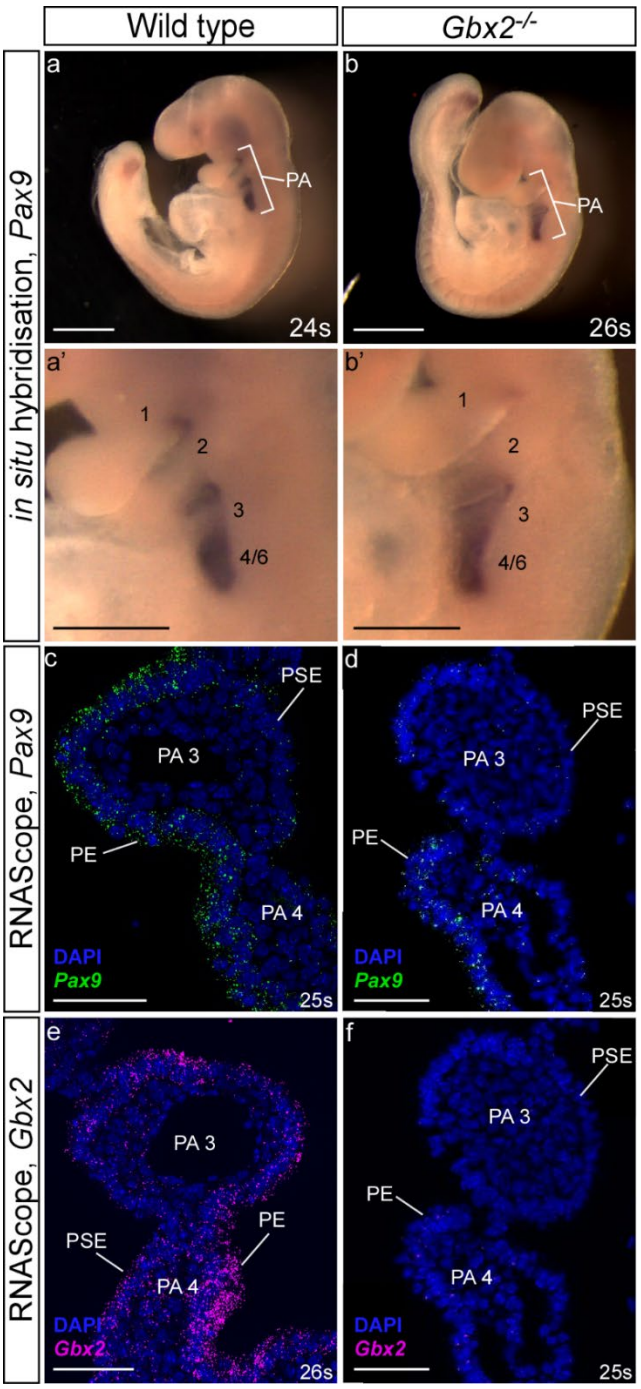

Figure 4.4. *Pax9* expression within the pharyngeal arches of *Gbx2*$^{-/-}$ embryos at E9.5.

Pax9 in situ hybridisation in wild type (a, n=8, 24-27 somites) and *Gbx2*$^{-/-}$ (b, n=5, 23-26 somites) embryos at E9.5. There is no observed difference in *Pax9* expression in the PA of *Gbx2*$^{-/-}$ embryos. RNAScope for *Pax9* in wild type (c, n=6, 24-28 somites) and *Gbx2*$^{-/-}$ (d, n=3, 25-27 somites) sections. *Pax9* is downregulated in the pharyngeal endoderm (PE) of *Gbx2*$^{-/-}$ embryos. RNAScope for *Gbx2* in wild type (e, n=5, 24-28 somites) and *Gbx2*$^{-/-}$ embryos (f, n=3, 25-27 somites) confirms loss of *Gbx2* expression in *Gbx2*-nulls. Somite counts (s) indicated. Abbreviations: MHB, midhindbrain boundary; O, otocyst; PA, pharyngeal arch; PE, pharyngeal endoderm; pp, pharyngeal pouches; PSE, pharyngeal surface ectoderm; TB, tail bud. Scale: a-b, 500μm; a'-b', 250 μm; c-d, 50μm.

4.3 Analysis of the *Pax9/Gbx2* genotypes

Gene expression analysis of *Pax9*$^{-/-}$ and *Gbx2*$^{-/-}$ embryos showed a downregulation of *Gbx2* and *Pax9* respectively. This suggests that these genes may function in a regulatory pathway during development. To investigate this interaction specifically during cardiovascular development, *Pax9*$^{+/-}$*;Gbx2*$^{+/-}$ mice were intercrossed and embryos of various genotypes (Figure 4.5) were collected at E15.5 and E10.5 to assess cardiac and PAA structure respectively. Due to the availability of mice, embryos were also obtained from a *Pax9*$^{+/-}$*;Gbx2*$^{+/-}$ X *Gbx2*$^{+/-}$ and a *Gbx2*$^{+/-}$ X *Gbx2*$^{+/-}$ (for the collection of *Gbx2*$^{+/-}$ and *Gbx2*$^{-/-}$ embryos) mouse cross.

The key comparisons made in this experiment were *Gbx2*$^{-/-}$ against *Pax9*$^{+/-}$*;Gbx2*$^{-/-}$ embryos and *Pax9*$^{-/-}$ against *Pax9*$^{-/-}$*;Gbx2*$^{+/-}$ to determine if *Pax9* heterozygosity modified the *Gbx2*$^{-/-}$ phenotype or if *Gbx2* heterozygosity modified the *Pax9*$^{-/-}$ phenotype respectively. *Pax9*$^{+/-}$ and *Gbx2*$^{+/-}$ have not been reported to show any cardiovascular defects (134, 166). *Pax9*$^{+/-}$*;Gbx2*$^{+/-}$ were collected to determine if the combined heterozygosity of both genes results in a cardiovascular phenotype.

Wild type (n=3), *Pax9*$^{+/-}$ (n=16), and *Gbx2*$^{+/-}$ (n=8) embryos we analysed at E15.5 and all had normal development of the cardiovascular system, thymus and craniofacial region.

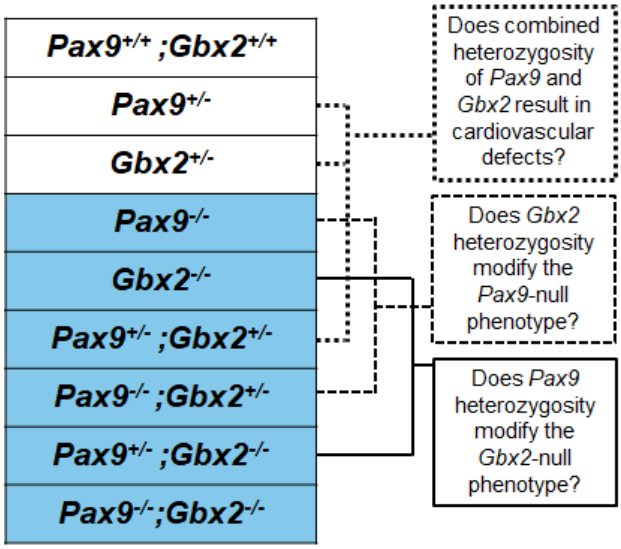

Figure 4.5. Possible genotypes obtained from *Pax9*$^{+/-}$*;Gbx2*$^{+/-}$ cross and key comparisons made in each experiment.

Genotypes that present with cardiovascular defects are highlighted.

Chi-squared was used to determine any deviation in the embryos collected from the expected Mendelian ratio in the *Pax9*$^{+/-}$;*Gbx2*$^{+/-}$ X *Pax9*$^{+/-}$;*Gbx2*$^{+/-}$ cross (Table 4.1). There was a significant difference (p=0.00012) in the number of observed mice against expected with various genotypes being under or over represented. Interestingly, the mutants with a homozygous deletion of *Gbx2* were all under-represented by over 50%. A 72% loss of *Pax9*$^{-/-}$;*Gbx2*$^{-/-}$ mice was observed. The observed number of *Pax9*$^{+/-}$, *Gbx2*$^{+/-}$ and mutants with homozygous deletion of *Pax9* (*Pax9*$^{-/-}$ and *Pax9*$^{-/-}$;*Gbx2*$^{+/-}$ mice) did not greatly differ from expected. This loss of *Gbx2* homozygote mutants was observed previously in the *Gbx2*$^{+/-}$ X *Gbx2*$^{+/-}$ cross (Table 3.3). This confirms the early loss of *Gbx2*$^{-/-}$ homozygous mutants during early embryogenesis.

Table 4.1. Mice (E9.5-P0) obtained from the *Pax9*$^{+/-}$;*Gbx2*$^{+/-}$ X *Pax9*$^{+/-}$;*Gbx2*$^{+/-}$ cross from 25 litters.

Gbx2 homozygous mutants are highlighted. Statistical significance was analysed using chi-squared.

Genotype	Observed (E9.5-P0)	Expected
***Pax9*$^{+/+}$;*Gbx2*$^{+/+}$**	16	10.75
***Pax9*$^{+/-}$**	20	21.5
***Gbx2*$^{+/-}$**	23	21.5
***Pax9*$^{-/-}$**	9	10.75
***Gbx2*$^{-/-}$**	5	10.75
***Pax9*$^{+/-}$;*Gbx2*$^{+/-}$**	67	43
***Pax9*$^{-/-}$;*Gbx2*$^{+/-}$**	19	21.5
***Pax9*$^{+/-}$;*Gbx2*$^{-/-}$**	10	21.5
***Pax9*$^{-/-}$;*Gbx2*$^{-/-}$**	3	10.75
Total	172	
	Chi-squared, p=1.12x10^{-4}***	

4.4 The *Pax9*$^{+/-}$;*Gbx2*$^{+/-}$ phenotype

To generate *Pax9*$^{+/-}$;*Gbx2*$^{+/-}$ mice, *Pax9*$^{+/-}$ and *Gbx2*$^{+/-}$ mice were intercrossed. *Pax9*$^{+/-}$;*Gbx2*$^{+/-}$ mice survive to weaning and breeding age, however there was a significant reduction (chi-squared test, p=0.035) in number of observed *Pax9*$^{+/-}$;*Gbx2*$^{+/-}$ weaned mice compared to expected (Table 4.2). It is worth noting that there is also a larger representation of *Gbx2*$^{+/-}$ mice from this cross which will be reflected in the p-value.

Table 4.2. Mice obtained from *Pax9*$^{+/-}$ X *Gbx2*$^{+/-}$ cross at time of weaning from 46 litters.

Statistical significance was analysed using chi-squared.

Genotype	Observed (3 weeks old)	Expected
***Pax9*$^{+/+}$;*Gbx2*$^{+/+}$**	79	76.75
***Pax9*$^{+/-}$**	74	76.75
***Gbx2*$^{+/-}$**	95	76.75
***Pax9*$^{+/-}$;*Gbx2*$^{+/-}$**	59	76.75
Total	307	
	Chi-squared, p=0.035	

From the *Pax9*$^{+/-}$ X *Gbx2*$^{+/-}$ cross, there were neonates that died on the day of birth. Dead neonates, and littermate controls, were collected for gross dissection at postnatal day (P) 0. Genotyping showed all dead pups (n=4) to be *Pax9*$^{+/-}$;*Gbx2*$^{+/-}$. Additionally, these mice presented with cardiovascular defects including RAA, IAA and ARSA (Figure 4.6). RAA is typical of *Gbx2*$^{-/-}$ mice while IAA is observed in *Pax9*$^{-/-}$ mice. ARSA is a defect common to both mutants. Wild type (n=8), *Pax9*$^{+/-}$ (n=9) and *Gbx2*$^{+/-}$ (n=10) littermates showed no cardiovascular defects.

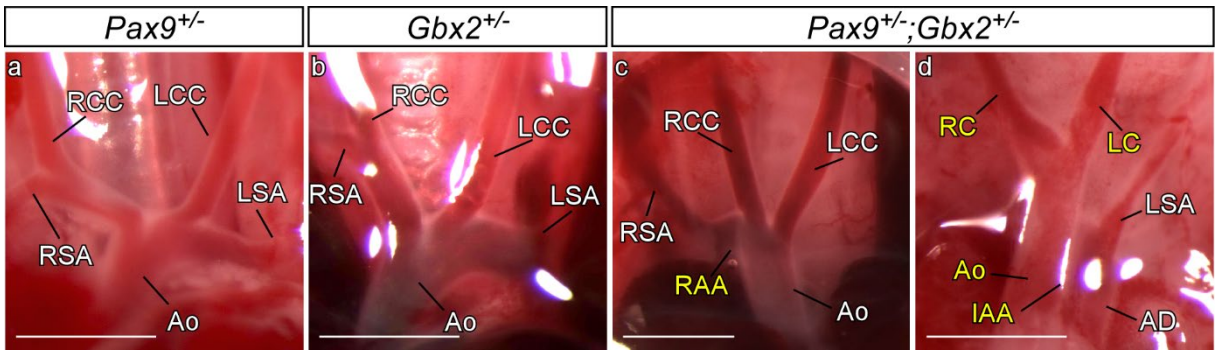

Figure 4.6. Cardiovascular defects in *Pax9*$^{+/-}$;*Gbx2*$^{+/-}$ neonates.

Dissection of P0 pups showed normal aortic arch structure in *Pax9*$^{+/-}$ (a, n=9) and *Gbx2*$^{+/-}$ (b, n=10) mice. *Pax9*$^{+/-}$;*Gbx2*$^{+/-}$ mice (c-d, n=4) had defects including RAA (c) and IAA with an assumed retro-oesophageal RSA (ARSA; d). Abbreviations: AD, arterial duct; Ao, aorta; ARSA, aberrant right subclavian artery; IAA, interrupted aortic arch; LC, left carotid artery; LCC, left common carotid artery; LSA, left subclavian artery; RC, right carotid artery; RAA, right aortic arch; RCC, right common carotid artery; RSA, right subclavian artery. Scale, 1mm.

Pax9$^{+/-}$;*Gbx2*$^{+/-}$ mice were intercrossed to collect *Pax9*$^{+/-}$;*Gbx2*$^{+/-}$ embryos at E15.5 for MRI and histological analysis. This allowed complete assessment of the cardiovascular phenotype and an analysis of a larger number of embryos. No defects were observed in wild type (n=3), *Pax9*$^{+/-}$ (n=16) or *Gbx2*$^{+/-}$ (n=8) at E15.5. Appendix Table A.2 shows the phenotype of each *Pax9*$^{+/-}$;*Gbx2*$^{+/-}$ mouse collected.

At E15.5, 13% (n=15 examined) of *Pax9*$^{+/-}$;*Gbx2*$^{+/-}$ embryos had cardiovascular defects. One embryo had ARSA and the other had RAA and ARSA (Figure 4.7). ARSA is present in both *Pax9*$^{-/-}$ and *Gbx2*$^{-/-}$ mice while RAA is only observed in *Gbx2*$^{-/-}$ mice.

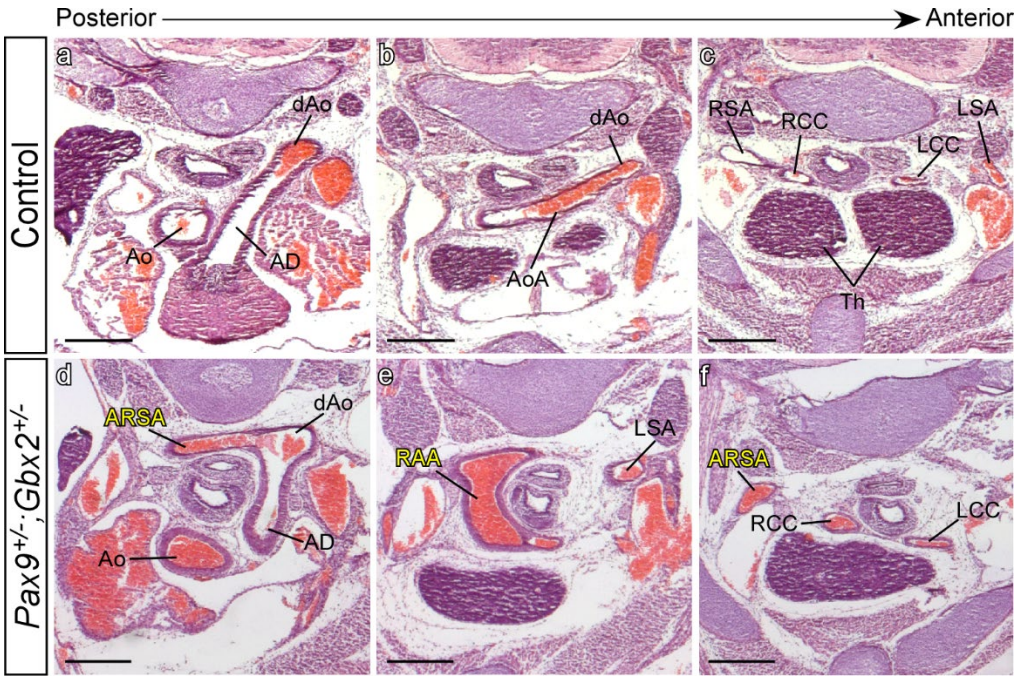

Figure 4.7. Cardiovascular defects present in *Pax9*$^{+/-}$*Gbx2*$^{+/-}$ embryos.

H&E stained E15.5 transverse sections of control embryo (a-c) with normal cardiovascular structure. *Pax9*$^{+/-}$*;Gbx2*$^{+/-}$ embryo (d-f) with ARSA (d) and RAA (e). Abbreviations: AD, arterial duct; Ao, aorta; ARSA, aberrant right subclavian artery; dAo, dorsal aorta; LCC, left common carotid artery; LSA, left subclavian artery; pa, pulmonary arteries; RAA, right aortic arch; RCC, right common carotid artery; RSA, right subclavian artery; RV, right ventricle; Th, thymus. Scale, 500μm.

Table 4.3 summarises the defects in *Pax9*$^{+/-}$*;Gbx2*$^{+/-}$ mice at E15.5 and P0. Combining with the mice collected at P0, 21% of *Pax9*$^{+/-}$*;Gbx2*$^{+/-}$ mice (n=28 examined, E15.5-P0) had cardiovascular defects. This penetrance of defects correlates with the loss of *Pax9*$^{+/-}$*;Gbx2*$^{+/-}$ mice at weaning as there was a 23% decrease in the number of observed double heterozygotes compared to expected.

Table 4.3. Penetrance of cardiovascular defects present in *Pax9*$^{+/-}$;*Gbx2*$^{+/-}$ mice E15.5-P0.

ARSA includes retro-oesophageal subclavian arteries. Abbreviations: ARSA, aberrant right subclavian artery; ALSA, aberrant left subclavian artery; CV, cardiovascular; DORV, double outlet right ventricle; IAA, interrupted aortic arch; RAA, right aortic arch; VSD, ventricular septal defect.

	Frequency			
Age	**CV Defect**	**IAA**	**RAA**	**ARSA**
E15.5 n=16	2 (13%)	0	1 (7%)	2 (13%)
P0 n=12	4 (33%)	2 (17%)	2 (17%)	1 (8%)

Intracardiac ink injection was used to visualise the PAA prior to remodelling. No defects were observed in wild type (n=13) or *Pax9*$^{+/-}$ (n=5) embryos. *Gbx2*$^{+/-}$ embryos had a low penetrance of 4th PAA defects (7%, n=43 examined), however these embryos did not have defects later in development (n=18, E15.5-P0) therefore these defects appear to recover (as discussed in Section 3.5).

4th PAA abnormalities were present in 30% of *Pax9*$^{+/-}$;*Gbx2*$^{+/-}$ embryos (n=63 examined) (Figure 4.8). Only the 4th PAA was affected, with unilateral defects more frequent. Embryos had either a hypoplastic or absent 4th PAA (Table 4.4).

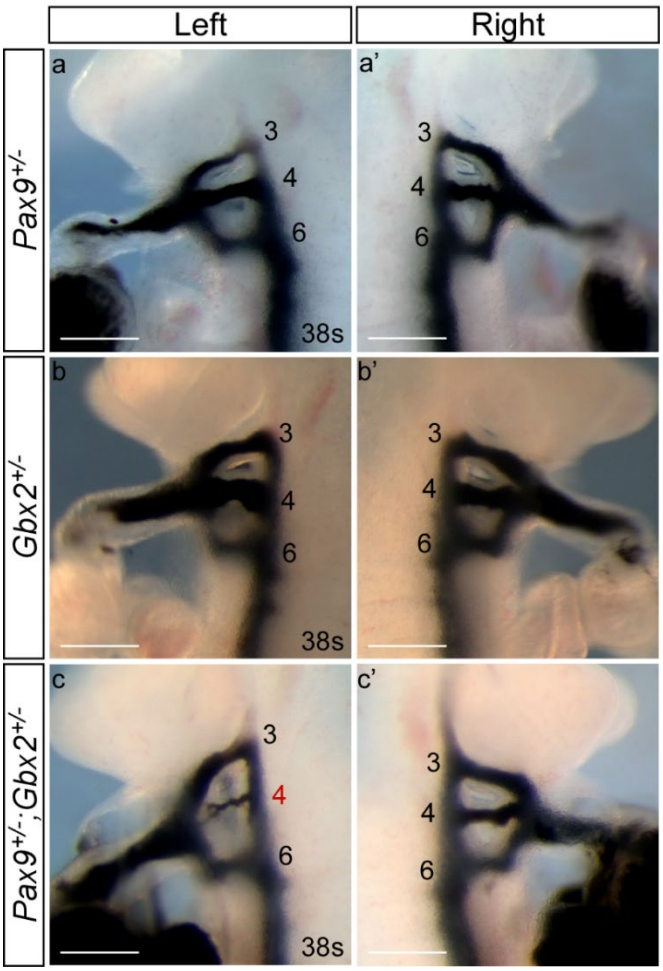

Figure 4.8. 4th pharyngeal arch artery defects in *Pax9*$^{+/-}$;*Gbx2*$^{+/-}$ mice at E10.5.

Intracardiac ink injection of E10.5 embryos in *Pax9*$^{+/-}$ (a) and *Gbx2*$^{+/-}$ (b) embryos, PAA 3-6 (numbered) were patent to ink. *Pax9*$^{+/-}$;*Gbx2*$^{+/-}$ (c) had 4th PAA defects. A hypoplastic left 4th PAA is shown (c). Scale, 500μm.

Table 4.4. Penetrance of 4th pharyngeal arch artery defects in *Pax9*$^{+/-}$;*Gbx2*$^{+/-}$ embryos at E10.5.

Abbreviations: NP, non-patent; PAA, pharyngeal arch artery; Th, thin.

	Frequency							
	4th PAA defect	Unilateral defect			Bilateral defect			
Genotype		Defect	Th	NP	Defect	Th-Th	NP-Th	NP-NP
Pax9$^{+/-}$;*Gbx2*$^{+/-}$ n=63	20 (32%)	13 (21%)	7 (11%)	6 (10%)	7 (11%)	0	3 (5%)	4 (6%)

4.5 *Pax9* heterozygosity modifies the *Gbx2*$^{-/-}$ phenotype

The presentation of cardiovascular defects in *Pax9;Gbx2* double heterozygotes suggests an interaction between these genes in cardiovascular development. To determine if *Pax9* heterozygosity modifies the *Gbx2*-null phenotype, *Gbx2*$^{-/-}$ mice were compared to *Pax9*$^{+/-}$*;Gbx2*$^{-/-}$ mice. Appendix Table A.3 shows the phenotype of each *Pax9*$^{+/-}$*;Gbx2*$^{-/-}$ mouse collected.

Timed matings, intercrossing *Pax9*$^{+/-}$*;Gbx2*$^{+/-}$ mice, were set up to collect embryos at E10.5 and E15.5. Due to the nature of mouse breeding, mice were collected at P0 from missed vaginal plugs. From these missed plugs, any pups that died on the day of birth were collected, along with euthanised control littermates, for dissection to analyse the structure of the aortic arch.

One *Pax9*$^{+/-}$*;Gbx2*$^{-/-}$ mouse was collected, along with euthanised control littermates (Figure 4.9). This *Pax9*$^{+/-}$*;Gbx2*$^{-/-}$ mouse was found dead on the day of birth with cardiovascular defects. The mutant had IAA, absent LCC, ARSA and an absent thymus. IAA, absent common carotid arteries and absent thymus were not defects found in *Gbx2*$^{-/-}$ embryos (n=25 at E15.5). These are all defects of the *Pax9*$^{-/-}$ phenotype, showing that *Pax9* heterozygosity has modified the *Gbx2*$^{-/-}$ phenotype.

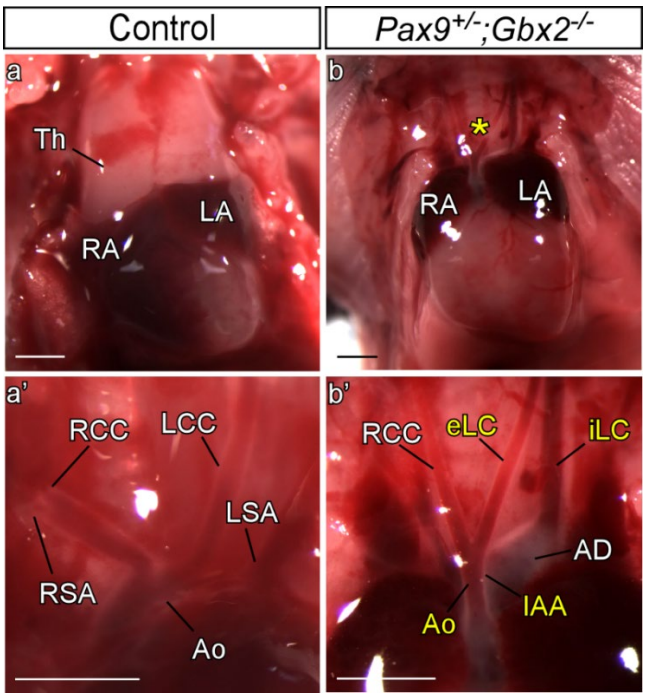

Figure 4.9. Cardiovascular defects present in *Pax9*$^{+/-}$*;Gbx2*$^{-/-}$ neonate.

Dissection of control (a) and *Pax9*$^{+/-}$*;Gbx2*$^{-/-}$ (b) P0 pups. Control has thymus present above the heart (a, Th). The thymus is absent in the mutant (b, *). Normal aortic arch structure is present in control (a'). The mutant (b') has IAA and an assumed ARSA. The LCC is absent and the internal and external left carotid arteries branch from directly from the great vessels. Abbreviations: AD, arterial duct; Ao, aorta; ARSA, aberrant right subclavian artery; eLC, external left carotid artery; IAA, interrupted aortic arch; iLC, internal left carotid artery; LC, left carotid artery; LCC, left common carotid artery; LSA, left subclavian artery; RC, right carotid artery; RAA, right aortic arch; RCC, right common carotid artery; RSA, right subclavian artery. Scale, 1mm.

Embryos were collected at 15.5 and analysed by MRI and histology. One litter collected was found to be E13.5. From this litter, five *Pax9*$^{+/-}$*;Gbx2*$^{-/-}$ embryos were collected and included in the analysis. By this stage the remodelling of the aortic arch is complete and so any aortic arch defects can be reliably determined in the mutant embryos at E13.5. The interventricular septum may not have completely formed by this stage and so isolated VSD cannot reliably be assessed. However, if the E13.5 embryos presented with DORV, it was concluded that the embryo also had a VSD, as this is a haemodynamic necessity with DORV.

All *Pax9*$^{+/-}$*;Gbx2*$^{-/-}$ embryos (n=13) had defects, a significant increase (Fishers exact test, p=0.016) in penetrance compared to *Gbx2*$^{-/-}$ mice (64%, n=25). Defects previously observed in *Gbx2*$^{-/-}$ embryos were present, including RAA, RAD, right dorsal aorta, ARSA, mirror image aortic arch, DORV and VSD (Figure 4.10).

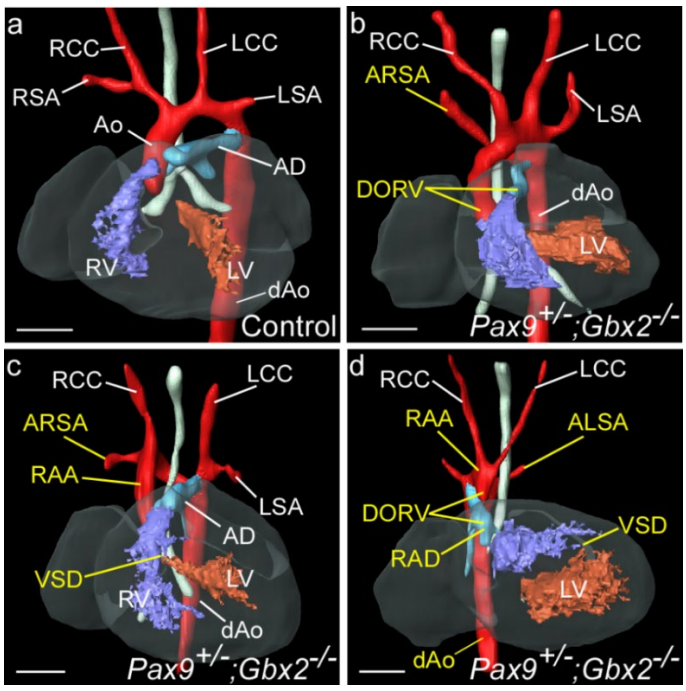

Figure 4.10. *Pax9*$^{+/-}$*;Gbx2*$^{-/-}$ embryos showed cardiovascular defects also present in *Gbx2*$^{-/-}$ embryos.

MRI data reconstructions of control (a) and *Pax9*$^{+/-}$*;Gbx2*$^{-/-}$ (b-d) E15.5 embryos. Control shows normal aortic arch structure. *Pax9*$^{+/-}$*;Gbx2*$^{-/-}$ embryos had the same defects as *Gbx2*$^{-/-}$ mice including DORV with an IVC (VSD; b, d), ARSA (b, c) and RAA (c, d). A mirror image aortic arch structure with an RAA, RAD, right sided dorsal aorta and ALSA is present (d). Abbreviations: AD, arterial duct; ALSA, aberrant left subclavian artery; Ao, aorta; ARSA, aberrant right subclavian artery; dAo, dorsal aorta; DORV, double outlet right ventricle; LCC, left common carotid artery; LSA, left subclavian artery; LV, left ventricle; RAA, right aortic arch; RAD, right arterial duct; RCC, right common carotid artery; RSA, right subclavian artery; RV, right ventricle; Tr, trachea; VSD, ventricular septal defect. Scale, 500μm.

Pax9$^{+/-}$*;Gbx2*$^{-/-}$ mice had L-R patterning defects (38%) at a similar penetrance to *Gbx2*$^{-/-}$ mice (36%). Like the *Gbx2*$^{-/-}$ mice, right isomerism was restricted to the heart and lungs. 31% of *Pax9*$^{+/-}$*;Gbx2*$^{-/-}$ mice had RPI and 24% had RAI. A *Pax9*$^{+/-}$*;Gbx2*$^{-/-}$ embryo presented with RPI, RAI and TGA, among other cardiovascular defects (Figure 4.11). The arterial duct is right sided, the RSA is aberrant, extending behind the oesophagus and the dorsal aorta is positioned at the midline rather than the left. In this embryo, the arterial duct arises from the ventricle on the left side of the body and the aorta from the ventricle on the right side of the body (TGA). Observing the ventricle morphology, the ventricle on the right looks to morphologically represent the left ventricle, as it is larger with a thick ventricular wall, therefore this embryo could specifically have CCTGA.

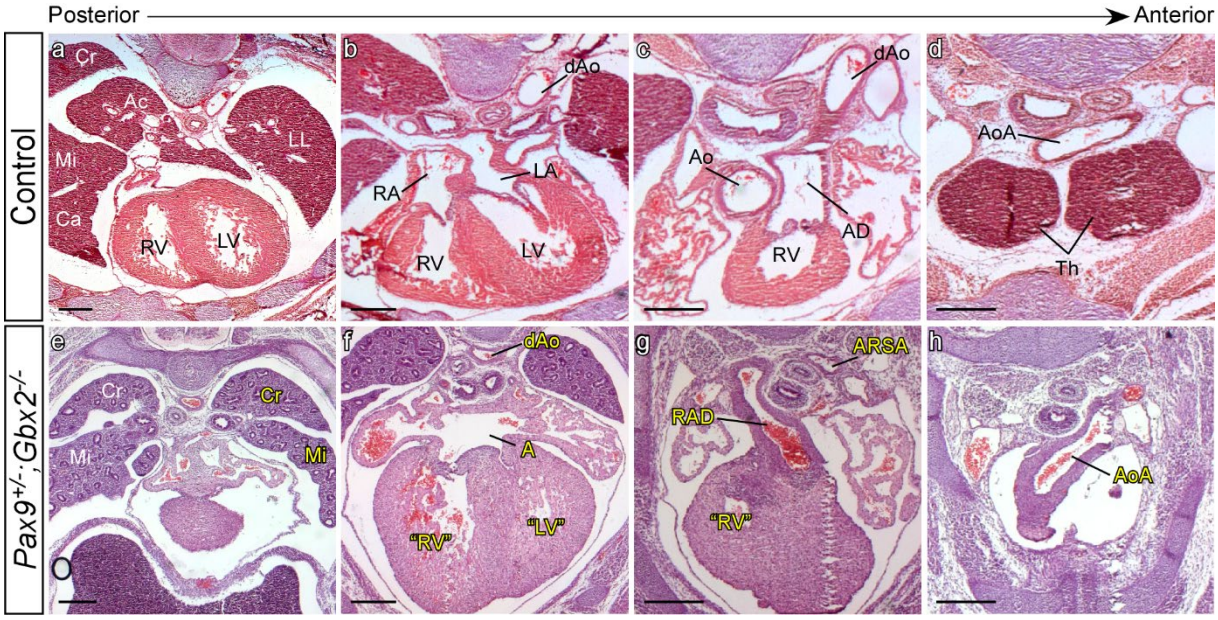

Figure 4.11. Transposition of the great arteries and left-right patterning defects in a *Pax9*$^{+/-}$;*Gbx2*$^{-/-}$ embryo.

H&E stain of E15.5 transverse sections of a control (a-d) and *Pax9*$^{+/-}$;*Gbx2*$^{-/-}$ embryo (e-h). Control has four lobes in the right lung (Cr, Mi, Ca, Ac; a) and single left lobe (LL; a). Mutant has RPI with a symmetrical lung structure and multiple lobes on each side (e). Control showing a four chamber heart with two distinct atria (b). Mutant had RAI with a common atrial chamber (A; f). In the control the AD crosses leftward, connected to the RV (c) and the aortic arch (AoA; d) is left sided. The mutant has a RAD extending from the left sided ventricle ("LV"; g) and the aorta from the right sided ventricle ("RV"). Abbreviations: A, atrium; Ac, accessory lobe; AD, arterial duct; Ao, aorta; AoA, aortic arch; ARSA, aberrant right subclavian artery; Ca, caudal lobe; Cr, cranial lobe; dAo, dorsal aorta; LL, left lobe; LV, left ventricle; Mi, middle lobe; RAD, right arterial duct; RV, right ventricle; Th, thymus; Scale 500µm.

OFT defects, namely DORV, are frequent in *Gbx2*$^{-/-}$ and *Pax9*$^{-/-}$ mice. Partial common arterial trunk (pCAT) was present in one (8%) *Pax9*$^{+/-}$;*Gbx2*$^{-/-}$ embryo in which the OFT has failed to completely septate into the aorta and pulmonary trunk. This was not observed in *Pax9*$^{-/-}$ or *Gbx2*$^{-/-}$ mice. This defect is discussed in more detail in section 4.7.

As well as these abnormalities, *Pax9*$^{+/-}$;*Gbx2*$^{-/-}$ embryos also had defects typical of *Pax9*$^{-/-}$ mice as 31% had IAA (Figure 4.12). 24% of *Gbx2*$^{-/-}$ mice (n=25) had RAA, but none had IAA. *Pax9*$^{+/-}$ mice (n=16, E15.5) have normal cardiovascular development but the heterozygosity of *Pax9* is causing the presentation of *Pax9*$^{-/-}$ defects in *Pax9*$^{+/-}$;*Gbx2*$^{-/-}$ mice.

Pax9$^{-/-}$ mice also have absent common carotid arteries occurring due to the collapse of the 3rd PAA together with the abnormal persistence of the 1st and 2nd PAA (134). As a result, the internal and external carotid arteries branch directly from the aortic arch. Defects to the common carotid arteries were not present in *Gbx2*$^{-/-}$ embryos. Absent common carotid arteries was observed in two *Pax9*$^{+/-}$*;Gbx2*$^{-/-}$ embryos (15%). Both of these embryos also had IAA and thymus defects, all frequent in *Pax9*$^{-/-}$ embryos. This defect was unilateral in one embryo, with a missing RCC, and bilateral in the other mutant (Figure 4.12).

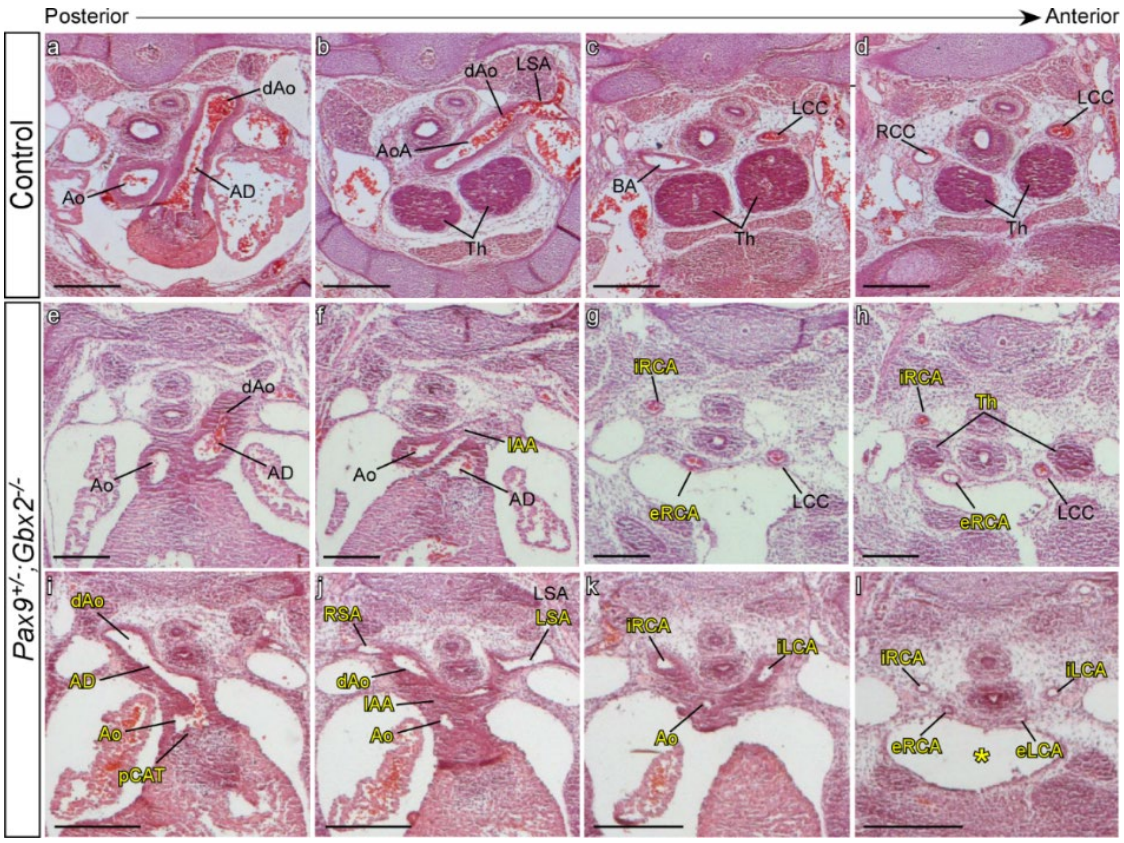

Figure 4.12. *Pax9*$^{+/-}$*;Gbx2*$^{-/-}$ embryos had defects typical of *Pax9*$^{-/-}$ embryos.

H&E stain of transverse sections of a control embryo (a-d) and *Pax9*$^{+/-}$*;Gbx2*$^{-/-}$ embryos (e-h, i-l). In the control, the arterial duct (AD) arises from the RV and crosses leftward, connecting with the dorsal aorta (dAo, a). The LSA branches from the left sided aortic arch (AoA, b). The LCC and the brachiocephalic artery (BA), which splits into the RSA and RCC (d), branch from the AoA (c). One mutant has pCAT and a RAD (i). Both mutants have IAA (f,j) as the ascending aorta has failed to connect to the dorsal aorta. Mutants also have absent common carotid arteries, either unilateral (h) or bilateral (l) in which the internal and external carotid arteries have branched directly from the arch. The thymus is hypoplastic and vestigial in one mutant (h) and absent in the other mutant embryo (*; l). Abbreviations: AD, arterial duct; Ao, aorta; AoA, aortic arch; BA, brachiocephalic artery; dAo, dorsal aorta; eLCA, external left carotid artery; eRCA, external right carotid artery; IAA, interrupted aortic arch; iLCA, internal left carotid artery; iRCA, interal right carotid artery; LCC, left common carotid artery; LSA, left subclavian artery; LV, left ventricle; pa, pulmonary arteries; pCAT, partial common arterial trunk; RAA, right aortic arch; RAD, right arterial duct; RCC, right common carotid artery; RSA, right subclavian artery; RV, right ventricle; Th, thymus. Scale 500μm.

Table 4.5. Penetrance of cardiovascular defects at E15.5 in *Gbx2*$^{-/-}$ embryos compared to *Pax9*$^{+/-}$;*Gbx2*$^{-/-}$ embryos.

Pax9 heterozygosity increased the penetrance of cardiovascular defects overall. The penetrance of DORV, VSD, RAA, ARSA/ALSA, VR, malpositioned dorsal aorta and right dorsal aorta increased. *Pax9*-null typical defects (IAA and absent CC) were present in *Pax9*$^{+/-}$;*Gbx2*$^{-/-}$ mice. Defects observed in *Pax9*$^{-/-}$ mice are highlighted. ARSA/ALSA includes retro-oesophageal, isolated and cervical origin of the subclavian arteries. Statistical significance was analysed using chi-squared for associations. *p<0.05; **p<0.01. Abbreviations: AA, aortic arch; ARSA, aberrant right subclavian artery; ALSA, aberrant left subclavian artery; CC, common carotid arteries; CV, cardiovascular; dAo, dorsal aorta; DORV, double outlet right ventricle; IAA, interrupted aortic arch; L-R, left-right; RAA, right aortic arch; RAD, right arterial duct; VR, vascular ring; VSD, ventricular septal defect.

	Frequency												
Genotype	**CV Defect**	**DORV**	**VSD**	**IAA**	**RAA**	**RAD**	**VR**	**ARSA**	**ARSA/ ALSA**	**Absent CC**	**Midline/ Right dAo**	**Mirror image AA**	**L-R patterning defect**
***Gbx2*$^{-/-}$** n=25	16 (64%)	10 (40%)	12 (48%)	0	6 (24%)	8 (32%)	2 (8%)	7 (28%)	10 (40%)	0	8 (32%)	6 (24%)	9 (36%)
***Pax9*$^{+/-}$;*Gbx2*$^{-/-}$** n=13	13* (100%)	7 (54%)	10 (77%)	4** (31%)	4 (31%)	3 (23%)	3 (21%)	8* (62%)	9 (69%)	2 (15%)	5 (38%)	1 (8%)	5 (38%)

As well as causing the presentation of defects found in *Pax9*$^{-/-}$ embryos (namely IAA and absent common carotid arteries), *Pax9* heterozygosity also increased the penetrance of multiple defects in *Pax9*$^{+/-}$*;Gbx2*$^{-/-}$ mice compared to *Gbx2*$^{-/-}$ mice Table 4.5. The penetrance DORV, VSD, IAA, RAA, ARSA (chi-squared test, p=0.045), ALSA, absent CC, VR and malpositioned dorsal aorta were all increased. The defects with increased penetrance were largely those typical of *Pax9*$^{-/-}$ mice; namely IAA, ARSA, absent CC, DORV and VSD. The overall penetrance of cardiovascular defects as well as the penetrance of IAA and ARSA was significantly increased. *Pax9* heterozygosity has increased the severity of the *Gbx2*$^{-/-}$ phenotype.

The thymus is derived from the 3rd and 4th pouch endoderm (44). An absent thymus is typical of *Pax9*$^{-/-}$ mice while *Pax9*$^{+/-}$ mice have normal thymus development. Mild thymus defects were observed in 8% of *Gbx2*$^{-/-}$ mice (n=25). These defects were a bilaterally hypoplastic thymus or a unilateral defect in which the right lobe was vestigial, located abnormally high in the pharynx. *Pax9* heterozygosity significantly increased (chi-squared test, p<0.0001) the penetrance of thymus defects in *Pax9*$^{+/-}$*;Gbx2*$^{-/-}$ embryos compared to *Gbx2*$^{-/-}$ embryos.

77% of *Pax9*$^{+/-}$*;Gbx2*$^{-/-}$ embryos (n=14) at E15.5 had an abnormal thymus. Table 4.6 summarises the thymus defects observed compared to *Gbx2*$^{-/-}$ embryos. Defects were either unilateral or bilateral, with a larger proportion of *Pax9*$^{+/-}$*;Gbx2*$^{-/-}$ embryos showing bilateral defects (54%). Thymus lobes were either absent, hypoplastic or vestigial (Figure 4.13). The most common defect in *Pax9*$^{+/-}$*;Gbx2*$^{-/-}$ embryos was an absent thymus, either bilateral (Figure 4.12) or unilateral (Figure 4.13), with 54% penetrance overall.

Table 4.6. Penetrance of thymus defects present at E15.5 in *Gbx2*$^{-/-}$ embryos compared to *Pax9*$^{+/-}$;*Gbx2*$^{-/-}$ embryos.

Statistical significance was analysed using chi-squared for associations. *p<0.05; **p<0.01; ****p<0.0001.

	Frequency					
	Thymus defect	Bilateral defect	Unilateral defect	Type of thymus defect		
Genotype				Absent	Hypo-plastic	Vestigial
***Gbx2*$^{-/-}$** n=25	2 (8%)	1 (4%)	1 (4%)	0	0	1 (4%)
***Pax9*$^{+/-}$;*Gbx2*$^{-/-}$** n=13	10**** (77%)	7** (54%)	3* (23%)	7*** (54%)	2 (15%)	3 (23%)

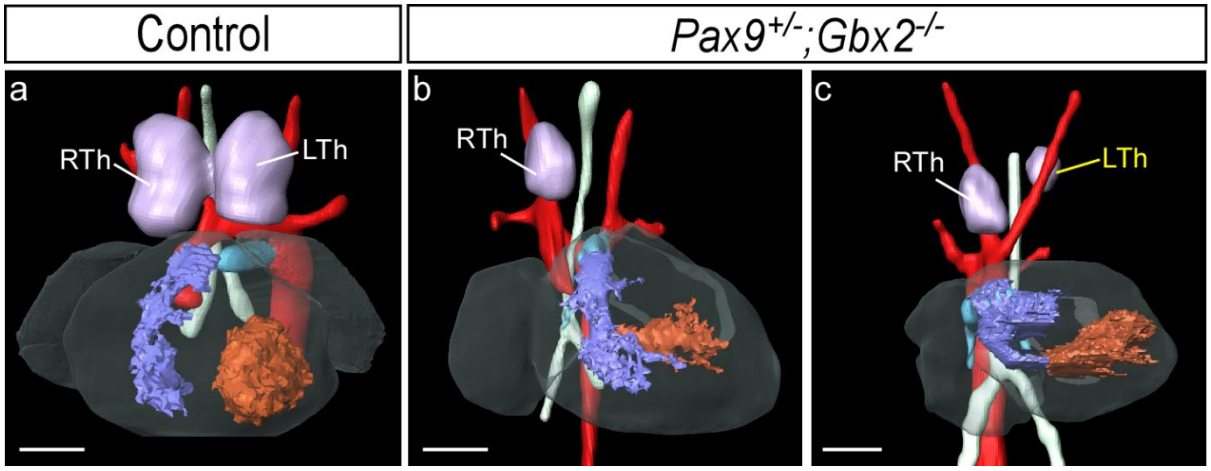

Figure 4.13. *Pax9*$^{+/-}$;*Gbx2*$^{-/-}$ embryos had thymus defects.

MRI reconstructions of control (a) and *Pax9*$^{+/-}$;*Gbx2*$^{-/-}$ (b-c) embryos. Control has a normal bilobed thymus. Mutant with an absent left lobe (b) and a mutant with a vestigial, hypoplastic left lobe (c). Abbreviations: LTh, left thymus lobe; RTh, right thymus lobe. Scale, 500μm

Pax9 is expressed in the cranial NCC (151) and, as a result, *Pax9*$^{-/-}$ mice have a cleft palate where the palatal shelves fail to fuse in development. This defect was not found in *Gbx2*$^{-/-}$ mice. Coronal sections of MRI datasets of *Pax9*$^{+/-}$;*Gbx2*$^{-/-}$ embryos (n=13) were examined and none had a cleft palate (Figure 4.14).

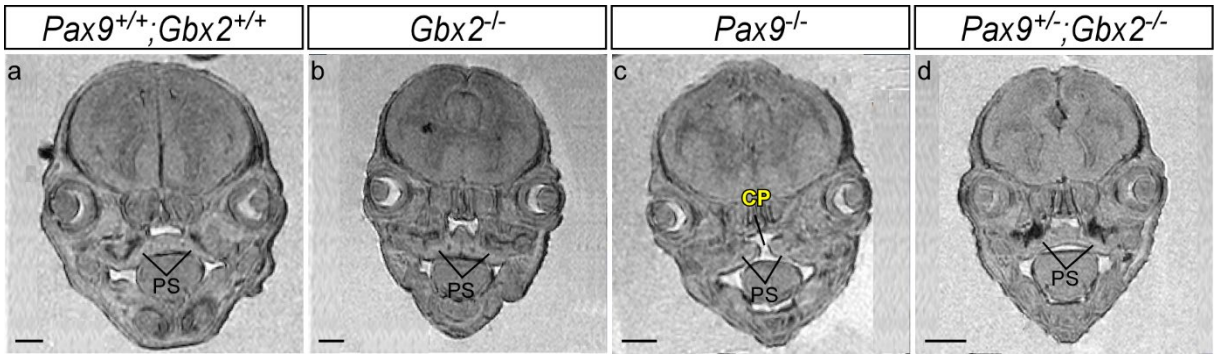

Figure 4.14. *Pax9*$^{+/-}$;*Gbx2*$^{-/-}$ embryos do not have cleft palate.

Coronal snapshots of E15.5 embryos showing the correct fusion of the palatal shelves (PS) in wild type (a), *Gbx2*$^{-/-}$ *and Pax9*$^{+/-}$;*Gbx2*$^{-/-}$ embryos. The palatal shelves fail to fuse in *Pax9*$^{-/-}$ embryos and a cleft palate (CP) is present. Abbreviations: CP, cleft palate; PS, palatal shelves. Scale, 500μm.

Embryos were collected at E10.5 for ink injection to analyse the structure of the PAA prior to remodelling. All *Pax9*$^{+/-}$;*Gbx2*$^{-/-}$ embryos (n=7) had a 4th PAA defect, with the vessels being either thin or completely non-patent to ink (Figure 4.15). This was expected as *Pax9*$^{+/-}$;*Gbx2*$^{-/-}$ embryos had 4th PAA-derived defects at E15.5 and both *Pax9*$^{-/-}$ and *Gbx2*$^{-/-}$ mice have 4th PAA defects.

Pax9$^{-/-}$ embryos also present with a hypoplastic 3rd PAA along with persistent 1st and 2nd PAAs which result in absent common carotid arteries later in development. At E10.5, no *Pax9*$^{+/-}$;*Gbx2*$^{-/-}$ embryos had defects to the 1st, 2nd or 3rd PAA. At E15.5, two *Pax9*$^{+/-}$;*Gbx2*$^{-/-}$ embryos had absent common carotid arteries (Figure 4.12) which is a lower penetrance when compared to the 92% penetrance of 4th PAA-derived defects observed. Therefore the absence of defects to the 1st, 2nd or 3rd PAA at E10.5 could reflect the lower penetrance of absent common carotid arteries observed in later development.

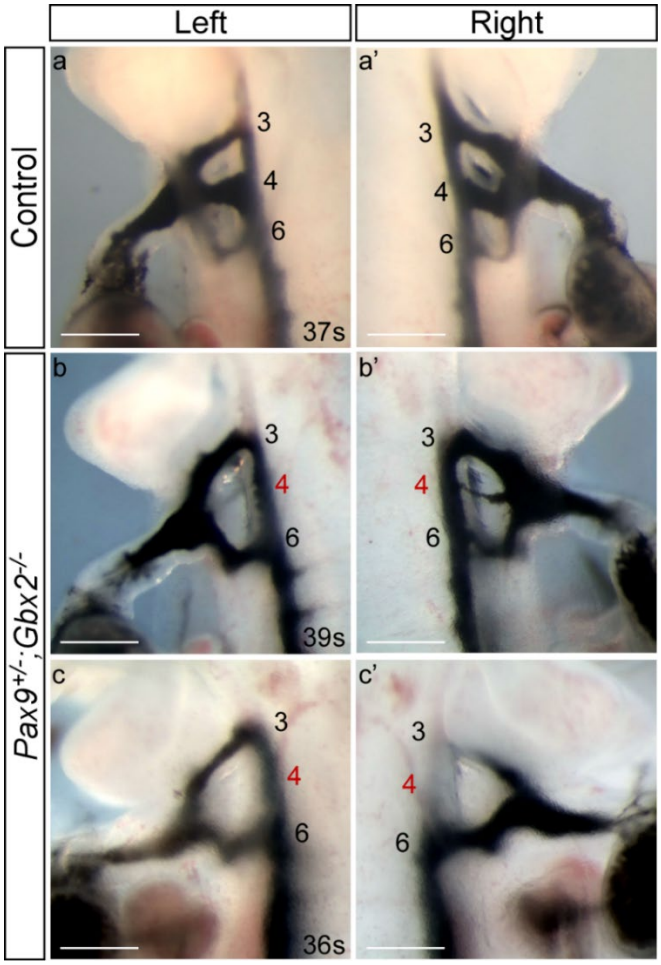

Figure 4.15. 4th pharyngeal arch artery defects in *Pax9*$^{+/-}$;*Gbx2*$^{-/-}$ mice at E10.5.

Intracardiac ink injection of E10.5 embryos. In control embryos (a), PAA 3-6 (numbered) were patent to ink. *Pax9*$^{+/-}$;*Gbx2*$^{-/-}$ embryos (c) had 4th PAA defects. 4th PAA were either hypoplastic (b') or absent (b,c,c'). Scale, 500μm.

The penetrance of 4th PAA defects in *Pax9*$^{+/-}$;*Gbx2*$^{-/-}$ embryos (100%; n=7) was higher than observed in *Gbx2*$^{-/-}$ embryos (83%; n=12) (Table 4.7). There was a greater proportion of *Pax9*$^{+/-}$;*Gbx2*$^{-/-}$ embryos with a bilateral defect rather than a unilateral defect. *Pax9* heterozygosity resulted in more severe 4th PAA abnormalities in *Pax9*$^{+/-}$;*Gbx2*$^{-/-}$ embryos.

Table 4.7. Penetrance of 4th pharyngeal arch artery defects in *Gbx2*$^{-/-}$ and *Pax9*$^{+/-}$;*Gbx2*$^{-/-}$ embryos at E10.5.

Gbx2$^{-/-}$ embryos were analysed by HREM and ink injection. *Pax9*$^{+/-}$;*Gbx2*$^{-/-}$ embryos were analysed by ink injection. Statistical significance was analysed by chi-squared for associations. Abbreviations: NP, non-patent; PAA, pharyngeal arch artery; Th, thin.

	Frequency							
	4th PAA defect	Unilateral defect			Bilateral defect			
Genotype		Defect	Th	NP	Defect	Th-Th	NP-Th	NP-NP
***Gbx2*$^{-/-}$** n=12	10 (83%)	5 (42%)	1 (8%)	4 (33%)	5 (42%)	0	3 (25%)	2 (17%)
***Pax9*$^{+/-}$;*Gbx2*$^{-/-}$** n=7	7 (100%)	1 (14%)	1 (14%)	0	6 (86%)	0	2 (29%)	4 (57%)

4.6 *Gbx2* heterozygosity modifies the *Pax9*$^{-/-}$ phenotype

The increased penetrance and severity of defects in *Pax9*$^{+/-}$;*Gbx2*$^{-/-}$ mice shows that *Pax9* heterozygosity modified the *Gbx2*$^{-/-}$ phenotype. Here, *Pax9*$^{-/-}$ mice were compared to *Pax9*$^{-/-}$;*Gbx2*$^{+/-}$ mice to determine whether *Gbx2* heterozygosity modified the *Pax9*$^{-/-}$ phenotype.

Pax9$^{-/-}$ (n=2) and *Pax9*$^{-/-}$;*Gbx2*$^{+/-}$ (n=2) neonates were collected at P0 due to missed plugs from the *Pax9*$^{+/-}$;*Gbx2*$^{+/-}$ X *Pax9*$^{+/-}$;*Gbx2*$^{+/-}$ cross and analysed by gross dissection (Figure 4.16). All of these mutants died on the day of birth with IAA, ARSA and an absent thymus, defects frequently observed in *Pax9*$^{-/-}$ mice (134). The defects present in the *Pax9*$^{-/-}$;*Gbx2*$^{+/-}$ mice did not deviate from the *Pax9*$^{-/-}$ phenotype.

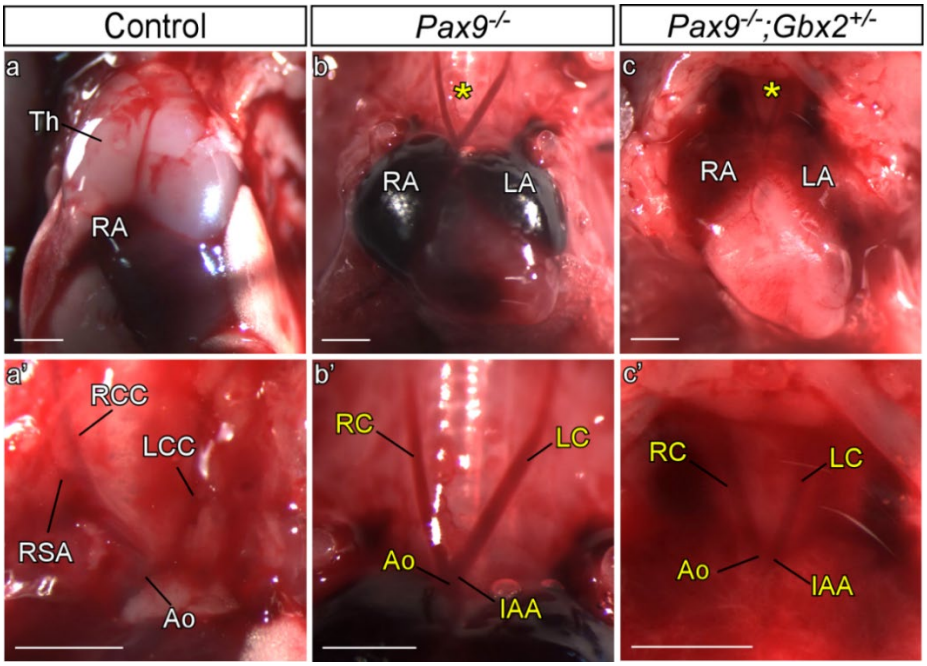

Figure 4.16. Cardiovascular defects present in *Pax9*$^{-/-}$ and *Pax9*$^{-/-}$;*Gbx2*$^{+/-}$ neonates.

Dissection of control (a), *Pax9*$^{-/-}$ (b) and *Pax9*$^{-/-}$;*Gbx2*$^{+/-}$ (c) P0 pups. Control has thymus present above the heart (a, Th). The thymus is absent in the both mutants (b-c, *). Normal aortic arch structure is present in control (a'). The mutants (b'-c') have IAA and an assumed ARSA. Abbreviations: AD, arterial duct; Ao, aorta; ARSA, aberrant right subclavian artery; IAA, interrupted aortic arch; LC, left carotid artery; LCC, left common carotid artery; LSA, left subclavian artery; RC, right carotid artery; RAA, right aortic arch; RCC, right common carotid artery; RSA, right subclavian artery. Scale, 1mm.

Pax9$^{-/-}$ and *Pax9*$^{-/-}$;*Gbx2*$^{+/-}$ embryos were collected at E15.5. As observed in previous datasets (134), all *Pax9*$^{-/-}$ embryos collected at E15.5 (n=7) had an absent thymus, cleft palate and cardiovascular defects. The cardiovascular defects include IAA, hypoplastic aorta, ARSA, IRSA, absent common carotid arteries, DORV and VSD (Figure 4.17b). The defects present in each individual *Pax9*$^{-/-}$ and *Pax9*$^{-/-}$;*Gbx2*$^{+/-}$ embryo is detailed in Appendix Table A.4 and A.5 respectively.

The cardiovascular phenotype of *Pax9*$^{-/-}$;*Gbx2*$^{+/-}$ embryos (n=7) was largely indistinguishable from *Pax9*$^{-/-}$ embryos, with 6/7 embryos showing the typical *Pax9*$^{-/-}$ phenotype (Figure 4.17). One *Pax9*$^{-/-}$;*Gbx2*$^{+/-}$ embryo had RAA, as well as ARSA and DORV with an IVC (Figure 4-18). RAA was not observed in *Pax9*$^{-/-}$ embryos, but was present in 24% of *Gbx2*$^{-/-}$ mice.

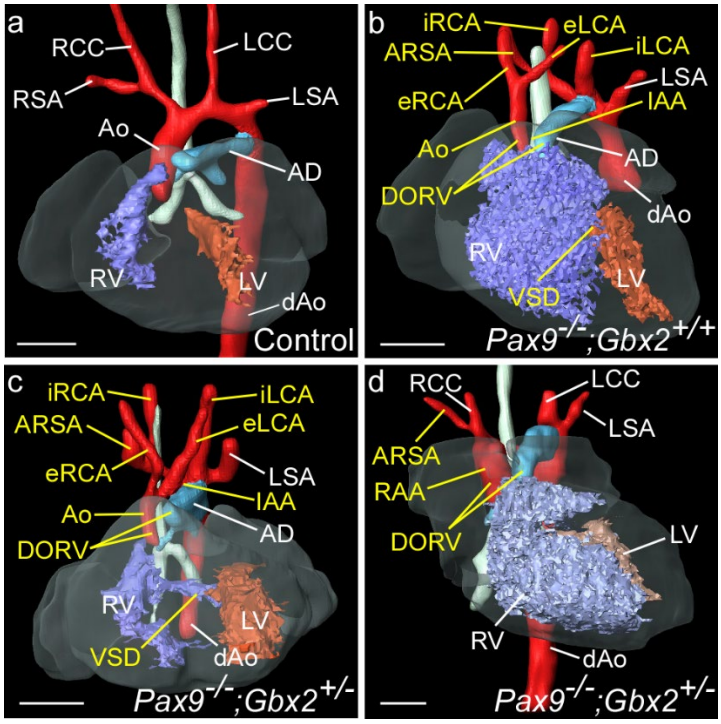

Figure 4.17. Cardiovascular defects present in *Pax9*$^{-/-}$;*Gbx2*$^{+/-}$ embryos.

MRI data reconstructions of control (a), *Pax9*$^{-/-}$ (b) and *Pax9*$^{-/-}$;*Gbx2*$^{+/-}$ (c-d) E15.5 embryos. Control (a) shows normal aortic arch structure. *Pax9*$^{-/-}$ embryo (b) has DORV with an IVC, a hypoplastic aorta, IAA and ARSA. The common carotid arteries are absent resulting in the internal and external carotid arteries (iRCA, eRCA, iLCA, eLCA) arising directly from the great arteries. This phenotype was recapitulated in *Pax9*$^{-/-}$;*Gbx2*$^{+/-}$ embryos (c). One *Pax9*$^{-/-}$;*Gbx2*$^{+/-}$ embryo deviated from the *Pax9*$^{-/-}$ phenotype presenting with RAA, DORV, VSD and ARSA (d). Abbreviations: AD, arterial duct; ALSA, aberrant left subclavian artery; Ao, aorta; ARSA, aberrant right subclavian artery; dAo, dorsal aorta; DORV, double outlet right ventricle; eLCA, external left carotid artery; eRCA, external right carotid artery; IAA, interrupted aortic arch; iLCA, internal left carortid artery; iRCA, internal right carotid artery; LCC, left common carotid artery; LSA, left subclavian artery; LV, left ventricle; RAA, right aortic arch; RCC, right common carotid artery; RSA, right subclavian artery; RV, right ventricle; Tr, trachea; VSD, ventricular septal defect. Scale, 500μm

Pax9$^{-/-}$;*Gbx2*$^{+/-}$ (29%, n=7) embryos also had pCAT, an OFT tract defect present in *Pax9*$^{+/-}$;*Gbx2*$^{-/-}$ embryos (14%, n=7) but not *Pax9*$^{-/-}$ or *Gbx2*$^{-/-}$ embryos (discussed in more detail in section 4.7).

Gbx2$^{-/-}$ and *Pax9*$^{+/-}$;*Gbx2*$^{-/-}$ mice had L-R patterning defects affecting the heart and lungs. No left right patterning defects were observed in *Pax9*$^{-/-}$;*Gbx2*$^{+/-}$ embryos showing that the heterozygous deletion of *Gbx2* is insufficient to cause L-R patterning defects.

Table 4.8 compares the penetrance of cardiovascular defects in *Pax9*$^{-/-}$ and *Pax9*$^{-/-}$;*Gbx2*$^{+/-}$ embryos. In both genotypes, all embryos had cardiovascular defects. However, there was a non-significant increase in the penetrance of each defect (excluding IAA) in *Pax9*$^{-/-}$;*Gbx2*$^{+/-}$ embryos compared to *Pax9*$^{-/-}$ embryos. *Gbx2* heterozygosity has potentially modified the *Pax9*$^{-/-}$ phenotype, however this dataset is limited by small sample numbers.

Table 4.8. Penetrance of cardiovascular defects at E15.5 in *Pax9*$^{-/-}$ embryos compared to *Pax9*$^{-/-}$;*Gbx2*$^{+/-}$ embryos.

Statistical significance was analysed by chi-squared for associations. ARSA includes retro-oesophageal and isolated subclavian arteries. Abbreviations: AA, aortic arch; ARSA, aberrant right subclavian artery; ALSA, aberrant left subclavian artery; CC, common carotid artery; CV, cardiovascular; DORV, double outlet right ventricle; IAA, interrupted aortic arch; RAA, right aortic arch; VSD, ventricular septal defect.

	Frequency						
Genotype	**CV Defect**	**DORV**	**VSD**	**IAA**	**RAA**	**ARSA**	**Absent CC**
***Pax9*$^{-/-}$** n=7	7 (100%)	4 (57%)	5 (71%)	6 (86%)	0	5 (71%)	4 (57%)
***Pax9*$^{-/-}$;*Gbx2*$^{+/-}$** n=7	7 (100%)	5 (71%)	7 (100%)	6 (86%)	1 (14%)	6 (86%)	6 (86%)

Coronal and transverse sections of MRI datasets and H&E sections of *Pax9*$^{-/-}$;*Gbx2*$^{+/-}$ embryos at E15.5 were used to assess the palate and thymus development respectively. As observed in *Pax9*$^{-/-}$ embryos, all *Pax9*$^{-/-}$;*Gbx2*$^{+/-}$ embryos (n=7) had a cleft palate and an absent thymus (Figure 4.18).

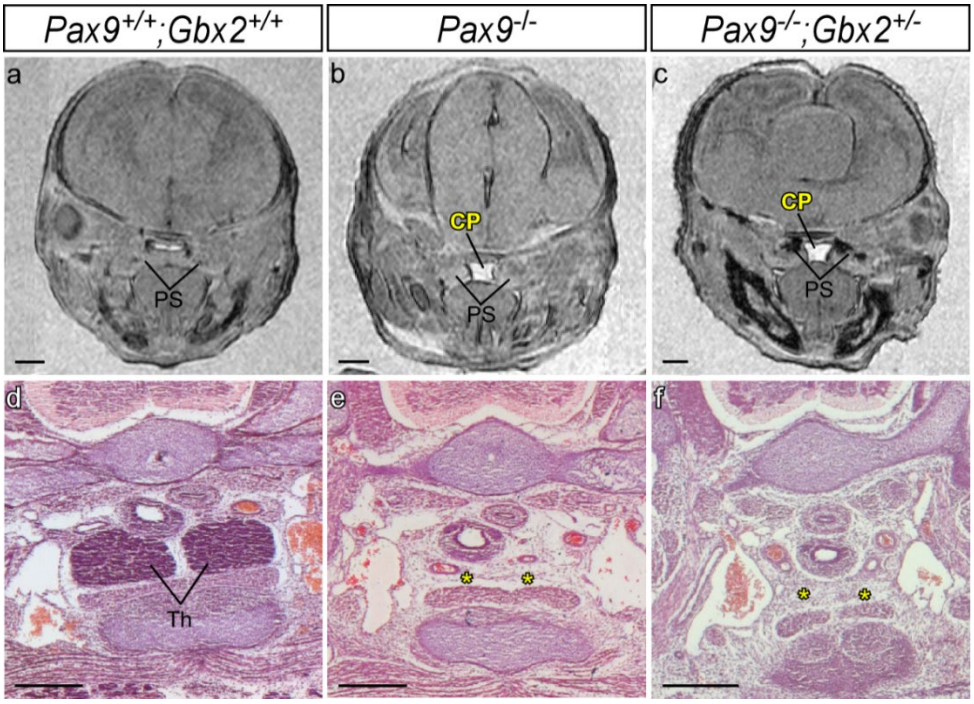

Figure 4.18. Palate and thymus defects present in *Pax9*$^{-/-}$*Gbx2*$^{+/-}$ embryos.

Coronal sections (a-c) of E15.5 embryos. Palatal shelves (PS) have fused in the wild type (a) embryo. In *Pax9*$^{-/-}$(b), and *Pax9*$^{-/-}$*Gbx2*$^{+/-}$ (c) embryos, the palatal shelves have failed to fuse and there is a cleft palate (CP). H&E stained transverse sections of E15.5 embryos (d-f). A bilobed thymus is present in the wild type embryo (d) whereas both lobes are absent in *Pax9*$^{-/-}$(*, e), and *Pax9*$^{-/-}$*Gbx2*$^{+/-}$ (*, f) embryos. Abbreviations: CP, cleft palate; PS, palatal shelves; Th, thymus. Scale, 500μm.

Pax9$^{-/-}$ and *Pax9*$^{-/-}$*Gbx2*$^{+/-}$ embryos were collected at E10.5 for ink injection to analyse the structure of the PAA prior to remodelling (Figure 4.19). *Pax9*$^{-/-}$ embryos of the same genetic background as this study collected previously in the laboratory, published in Phillips et al. (2019), were included in this dataset.

All *Pax9*$^{-/-}$ (n=14) and *Pax9*$^{-/-}$*Gbx2*$^{+/-}$ (n=6) embryos had 4th PAA defects. The 4th PAA defects are summarised in Table 4.9. There was no significant difference in presentation of hypoplastic or absent 4th PAAs between these genotypes. However in all *Pax9*$^{-/-}$;*Gbx2*$^{+/-}$ embryos, the 4th PAA was bilaterally absent compared to *Pax9*$^{-/-}$ embryos in which 28% of mice presented with the less severe unilateral or hypoplastic 4th PAA.

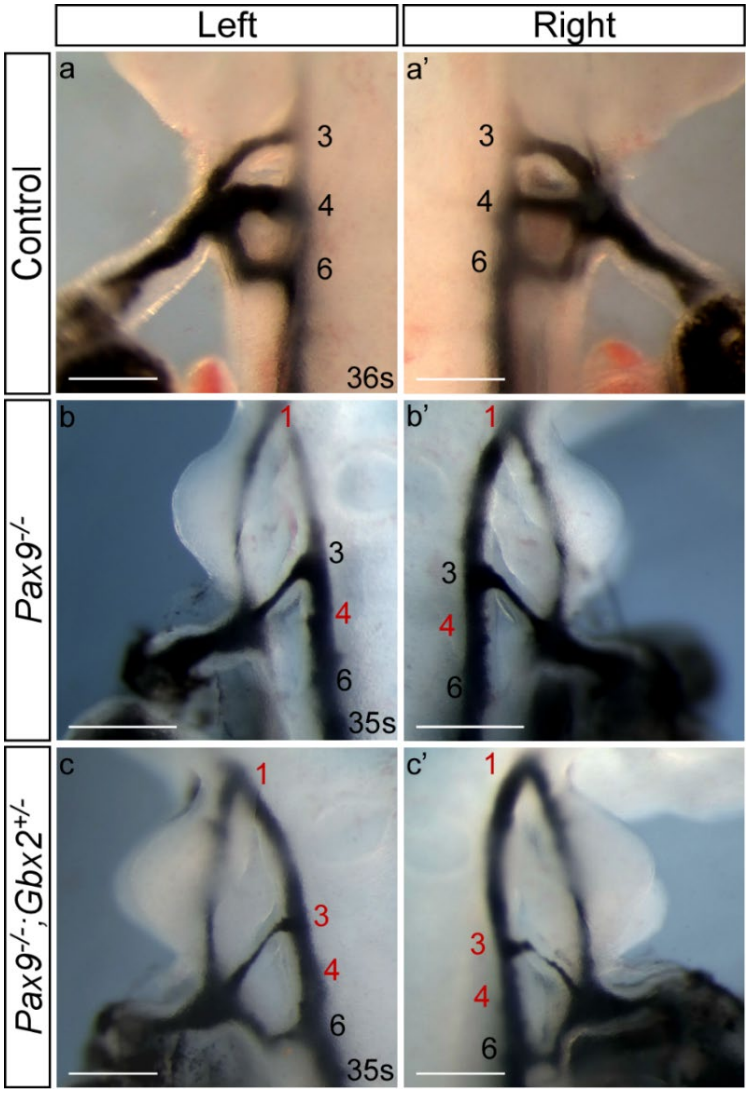

Figure 4.19. Pharyngeal arch artery defects in *Pax9*$^{-/-}$;*Gbx2*$^{+/-}$ embryos compared to *Pax9*$^{-/-}$ embryos at E10.5.

Intracardiac ink injection of E10.5 embryos. In control embryos (a), PAA 3-6 (numbered) were patent to ink. *Pax9*$^{-/-}$ (b) with a bilaterally absent 4th PAA and persistent 1st PAA, the 6th PAA are forming. *Pax9*$^{-/-}$;*Gbx2*$^{+/-}$ mutant (b) has bilaterally persistent 1st PAAs, hypoplastic 3rd PAAs and absent 4th PAAs. Scale, 500μm.

Table 4.9. Penetrance of 4th pharyngeal arch artery defects in *Pax9*$^{-/-}$ and *Pax9*$^{-/-}$;*Gbx2*$^{+/-}$ embryos at E10.5.

Statistical significance was analysed by chi-squared for associations. Abbreviations: NP, non-patent; PAA, pharyngeal arch artery; Th, thin.

	Frequency							
	4th PAA defect	Unilateral defect			Bilateral defect			
Genotype		Defect	Th	NP	Defect	Th-Th	NP-Th	NP-NP
Pax9$^{-/-}$ n=14	14 (100%)	1 (7%)	1 (7%)	0	13 (93%)	0	3 (21%)	10 (71%)
Pax9$^{-/-}$;*Gbx2*$^{+/-}$ n=6	6 (100%)	0	0	0	6 (100%)	0	0	6 (100%)

Persistent 1st and 2nd PAA and hypoplastic 3rd PAA were frequently observed in both genotypes. There was a non-significant increase in the penetrance of persistent 1st PAA in *Pax9*$^{-/-}$;*Gbx2*$^{+/-}$ embryos compared to *Pax9*$^{-/-}$ embryos (Table 4.10). This could reflect the increased incidence in absent common carotid arteries observed at E15.5 (86% in *Pax9*$^{-/-}$*Gbx2*$^{+/-}$ embryos and 57% in *Pax9*$^{-/-}$ embryos, Table 4.8).

Table 4.10. Pharyngeal arch artery defects present at E10.5 in *Pax9*$^{-/-}$ and *Pax9*$^{-/-}$;*Gbx2*$^{+/-}$ embryos.

Statistical significance was analysed by chi-squared for associations. Abbreviations: PAA, pharyngeal arch arteries.

	Defect			
Genotype	**4th PAA**	**3rd PAA**	**2nd PAA**	**1st PAA**
***Pax9*$^{-/-}$** n=14	14 (100%)	10 (71%)	3 (21%)	9 (64%)
***Pax9*$^{-/-}$;*Gbx2*$^{+/-}$** n=6	6 (100%)	6 (100%)	1 (17%)	6 (100%)

4.7 Outflow tract defects in complex *Pax9;Gbx2* mutants

The number of *Pax9*$^{-/-}$;*Gbx2*$^{-/-}$ mice obtained from the *Pax9*$^{+/-}$;*Gbx2*$^{+/-}$ X *Pax9*$^{+/-}$;*Gbx2*$^{+/-}$ cross significantly deviated from expected (Table 4.1). From 25 litters and 172 embryos, 11 (rounded from 10.75) *Pax9*$^{-/-}$;*Gbx2*$^{-/-}$ mice were expected, however only three *Pax9*$^{-/-}$;*Gbx2*$^{-/-}$ mice were collected; one at E10.5, E15.5 and P0.

The *Pax9*$^{-/-}$;*Gbx2*$^{-/-}$ embryo at E10.5 was analysed by intracardiac ink injection to view the structure of the PAA prior to remodelling. The mutant had a bilateral defect, with both 4th PAAs non-patent to ink (Figure 4.20), as was observed in *Pax9*$^{-/-}$ and *Gbx2*$^{-/-}$ embryos.

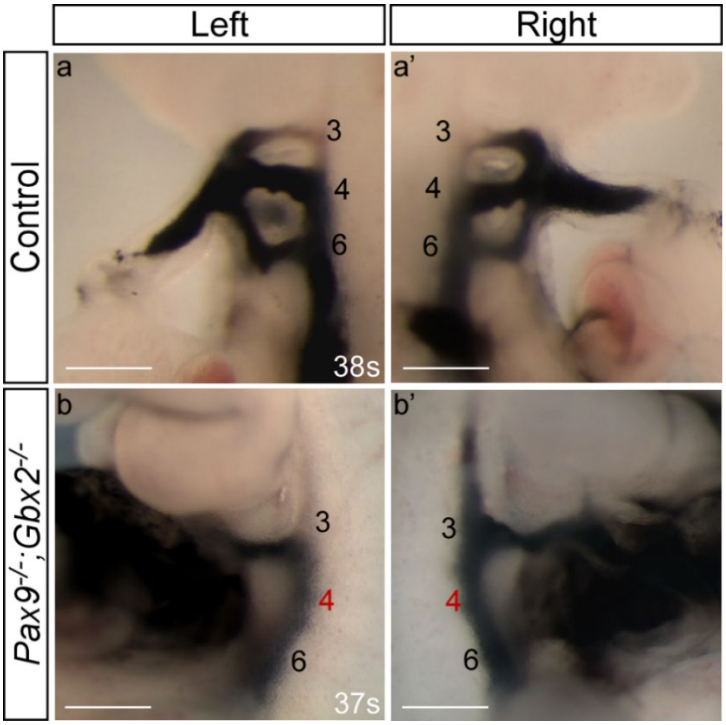

Figure 4.20. 4th pharyngeal arch artery defects present in the *Pax9*$^{-/-}$;*Gbx2*$^{-/-}$ embryo et E10.5.

Intracardiac ink injection of E10.5 control (a) and *Pax9*$^{-/-}$;*Gbx2*$^{-/-}$ (b) embryo. PAA 3-6 (numbered) were patent to ink in the control. *Pax9*$^{-/-}$;*Gbx2*$^{-/-}$ mutant has bilaterally absent 4th PAAs. Scale, 500μm.

The *Pax9*$^{-/-}$;*Gbx2*$^{-/-}$ P0 mouse died on the day of birth, collected in a litter from a missed plug. Dissection of the mutant and control littermates showed severe cardiovascular defects as the cause of death in the mutant while littermate controls showed no defects (Figure 4.21). The *Pax9*$^{-/-}$;*Gbx2*$^{-/-}$ mouse had an absent thymus, IAA and an IRSA branching from the pulmonary trunk. IAA is a prominent phenotype of *Pax9*$^{-/-}$ mice. IRSA was present in *Pax9*$^{-/-}$ (14%) and *Gbx2*$^{-/-}$ (12%) mice.

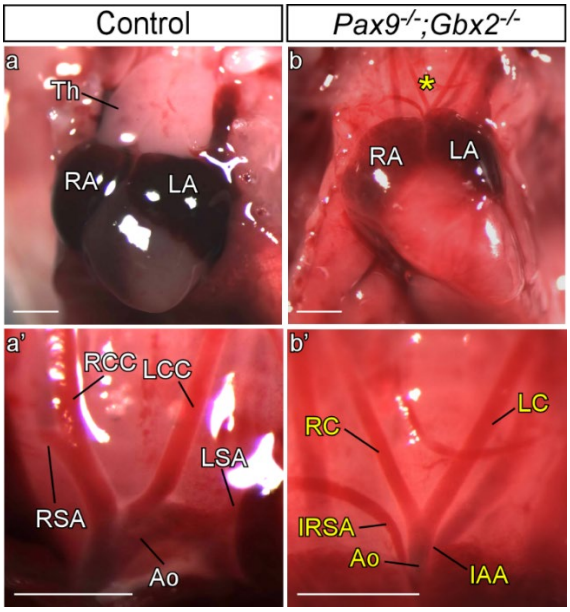

Figure 4.21. Defects present in a *Pax9*$^{-/-}$;*Gbx2*$^{-/-}$ mouse at P0.

Dissection of control (a) and *Pax9*$^{-/-}$;*Gbx2*$^{-/-}$ (b) mouse at P0. Control has a bilobed thymus (Th) positioned above the heart (a). The thymus is absent (*) in the *Pax9*$^{-/-}$;*Gbx2*$^{-/-}$ mouse (b). Normal aortic arch structure is present in the control (a'). The mutant has IAA and IRSA (b'). The carotid arteries branch from the ascending aorta. Abbreviations: Ao, aorta; IAA, interrupted aortic arch; IRSA, isolated right subclavian artery; LC, left carotid artery; LCC, left common carotid artery; LSA, left subclavian artery; RAA, right aortic arch; RC, right carotid artery; RCC, right common carotid artery; RSA, right subclavian artery; Th, thymus. Scale, 1mm.

MRI and histological analysis of the *Pax9*$^{-/-}$;*Gbx2*$^{-/-}$ mouse at E15.5 showed multiple cardiovascular defects (Figure 4.22, Appendix Table A.6). These defects largely resemble the *Pax9*$^{-/-}$ phenotype with absent common carotid arteries, IRSA and VSD. As well as communication between the ventricles, the mutant also had atrioventricular septal defect (AVSD), as the atrioventricular septum has failed to fuse with the endocardial cushions and there is complete communication between all four chambers of the heart.

During development, the aorta and pulmonary trunk form from the septation of the common OFT. OFT defects, namely DORV, were present in *Pax9*$^{-/-}$ and *Gbx2*$^{-/-}$ mice. The *Pax9;Gbx2* double knockout had CAT in which the aorta and pulmonary trunk have failed to septate. This defect was not present in *Pax9*$^{-/-}$ or *Gbx2*$^{-/-}$ mice. Here, the CAT arises from the right ventricle and arches leftward. The subclavian arteries and internal and external carotid arteries branch directly from the arch.

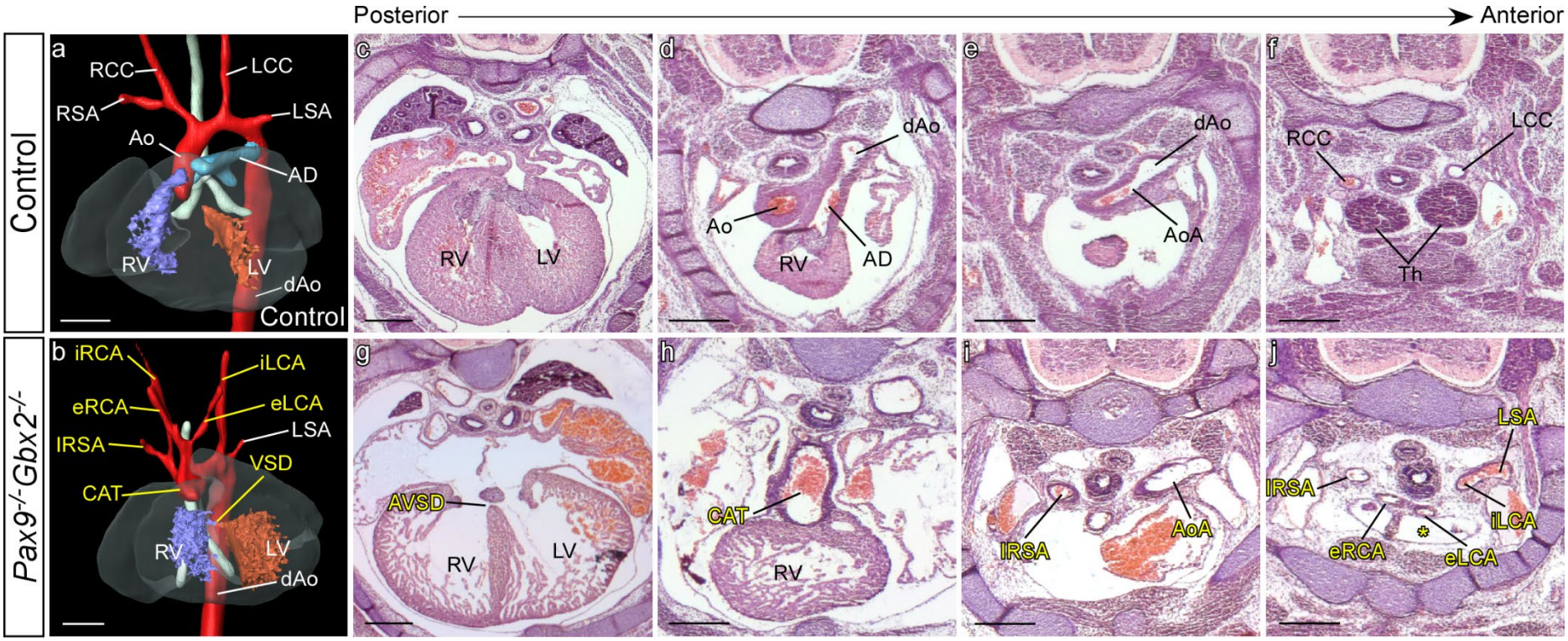

Figure 4.22. Cardiovascular defects present in a *Pax9*$^{-/-}$;*Gbx2*$^{-/-}$ E15.5 embryo.

MRI reconstructions (a-b) and H&E stained transverse sections (c-j) of control (a, c-f) and *Pax9*$^{-/-}$;*Gbx2*$^{-/-}$ (b, g-j) embryos. The OFT has failed to septate in the mutant and CAT (a,h) with AVSD (g) is present. There is an IRSA (b, i) with the RSA branching from the CAT. The common carotid arteries are absent resulting in the internal and external carotid arteries (iRCA, eRCA, iLCA, eLCA; b,j) arising directly from the great arteries. The thymus is absent (*; j). Abbreviations: AD, arterial duct; Ao, aorta; AVSD, atrioventricular septal defect; CAT, common arterial trunk; dAo, dorsal aorta; DORV, double outlet right ventricle; eLCA, external left carotid artery; eRCA, external right carotid artery; IAA, interrupted aortic arch; iLCA, internal left carortid artery; iRCA, internal right carotid artery; IRSA, isolated right subclavian artery; LCC, left common carotid artery; LSA, left subclavian artery; LV, left ventricle; RAA, right aortic arch; RCC, right common carotid artery; RSA, right subclavian artery; RV, right ventricle; Th, thymus; Tr, trachea. Scale, 500μm.

pCAT was present in *Pax9*$^{-/-}$;*Gbx2*$^{+/-}$ (29%, n=7 examined) and *Pax9*$^{+/-}$;*Gbx2*$^{-/-}$ (7%, n=13 examined) mutants at E15.5 (Figure 4.23 and Figure 4.24). This is a form of CAT in which the OFT has septated, but after leaving the heart. The pulmonary trunk connects to the right ventricle and the aorta has branched from the pulmonary trunk. The simultaneous deletion of *Pax9* and *Gbx2* has resulted in severe OFT defects with complete CAT.

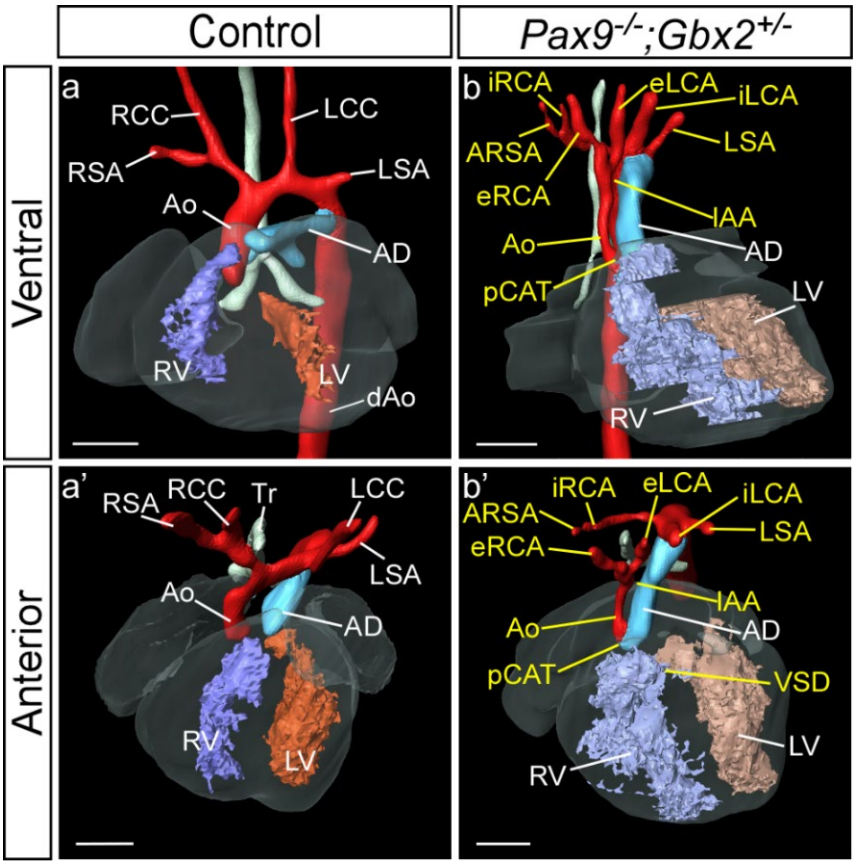

Figure 4.23. Complex outflow tract defects present in *Pax9*$^{-/-}$;*Gbx2*$^{+/-}$ embryos.

MRI reconstructions of control (a) and *Pax9*$^{-/-}$;*Gbx2*$^{+/-}$ (b) embryos with ventral (a-b) and anterior (a'-b') views. The outflow tract has failed to septate in the mutant and pCAT with IVC (VSD) (b) is present. The mutant embryo also has ARSA, IAA and the common carotid arteries are absent resulting in the internal and external carotid arteries (iRCA, eRCA, iLCA, eLCA) arising directly from the great arteries. Abbreviations: AD, arterial duct; Ao, aorta; ARSA, aberrant right subclavian artery; dAo, dorsal aorta; eLCA, external left carotid artery; eRCA, external right carotid artery; IAA, interrupted aortic arch; iLCA, internal left carortid artery; iRCA, internal right carotid artery; LCC, left common carotid artery; LSA, left subclavian artery; LV, left ventricle; pCAT, partial common arterial trunk; RAA, right aortic arch; RCC, right common carotid artery; RSA, right subclavian artery; RV, right ventricle; Th, thymus; Tr, trachea; VSD, ventricular septal defect. Scale, 500μm.

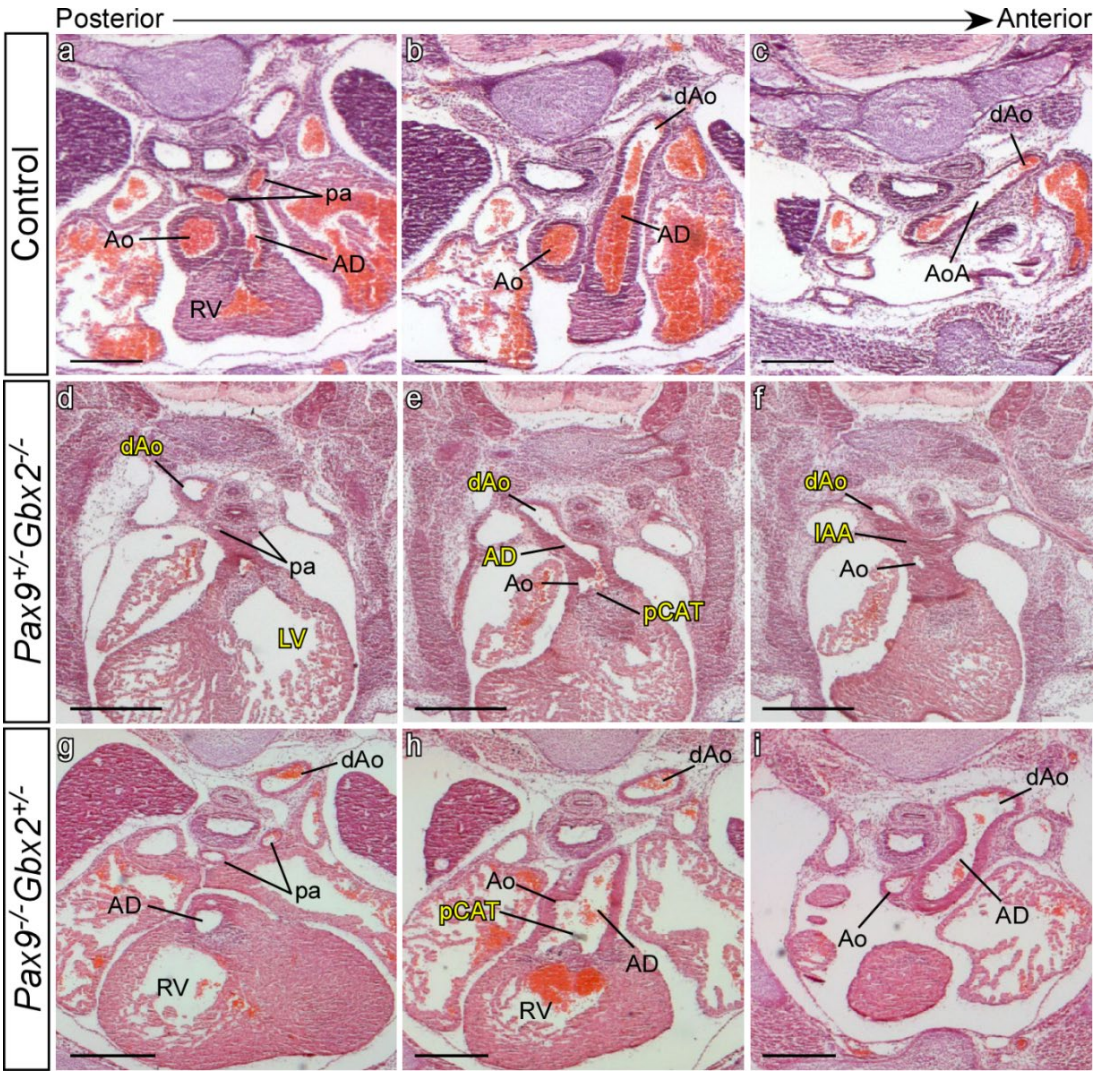

Figure 4.24. Partial common arterial trunk was present in complex *Pax9;Gbx2* mutants.

H&E stained transverse sections of E15.5 control (a), *Pax9*$^{+/-}$*;Gbx2*$^{-/-}$ (b) and *Pax9*$^{-/-}$*;Gbx2*$^{+/-}$ (c) embryos. The aorta and arterial duct arise from the left and right ventricles respectively in the control (a,b). In both mutant embryos, the OFT has failed to septate completely. A partial common arterial trunk (pCAT; e,h) is present, with the aorta branching from the arterial duct after leaving the heart from the right ventricle as a common vessel. Abbreviations: AD, arterial duct; Ao, aorta; AoA, aortic arch; dAo, dorsal aorta; LV, left ventricle; pCAT, partial common arterial trunk; pa, pulmonary arteries; RV, right ventricle. Scale, 500μm

4.8 Discussion

The data presented in this chapter shows that *Pax9* and *Gbx2* interact in cardiovascular development. This is apparent from the phenotyping data. Table 4.11 summarises the penetrance of cardiovascular defects in each mutant genotype discussed in this chapter at E15.5-P0.

Table 4.11. Penetrance of cardiovascular defects in each genotype at E15.5-P0.

The genotypes that present with a cardiovascular phenotype are highlighted.

Genotype	Frequency of cardiovascular defects
$Pax9^{+/+};Gbx2^{+/+}$	0/20
$Pax9^{+/-}$	0/25
$Gbx2^{+/-}$	0/18
$Pax9^{-/-}$	9/9 (100%)
$Gbx2^{-/-}$	16/25 (64%)
$Pax9^{+/-};Gbx2^{+/-}$	6/28 (21%)
$Pax9^{-/-};Gbx2^{+/-}$	9/9 (100%)
$Pax9^{+/-};Gbx2^{-/-}$	14/14 (100%)
$Pax9^{-/-};Gbx2^{-/-}$	2/2

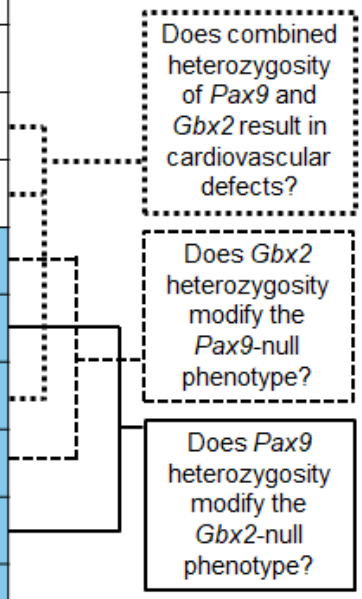

Combined heterozygosity of *Pax9* and *Gbx2* resulted in cardiovascular defects. Interestingly, the deletion of *Pax9* and *Gbx2* appear to have equally contributed to the double heterozygous phenotype. RAA is frequent in $Gbx2^{-/-}$ mice, while $Pax9^{-/-}$ mice usually present with IAA. $Pax9^{+/-};Gbx2^{+/-}$ mice had RAA and IAA, both with a penetrance of 7% (n=28 examined).

Pax9 heterozygosity modified the $Gbx2^{-/-}$ phenotype as the $Pax9^{+/-};Gbx2^{-/-}$ cardiovascular phenotype had complete penetrance, significantly higher than the penetrance of the $Gbx2^{-/-}$ phenotype (64%). *Pax9* heterozygosity resulted in the presentation of $Pax9^{-/-}$ defects in $Pax9^{+/-};Gbx2^{-/-}$ embryos. The frequency of several individual defects was increased, including RAA, VR and malpositioned dorsal aorta.

However, the defects with significantly increased penetrance in *Pax9*$^{+/-}$;*Gbx2*$^{-/-}$ mice were those typical of *Pax9*$^{-/-}$ mice, namely IAA, absent common carotid arteries, thymus defects as well as VSD and ARSA, with the latter common to both *Pax9*$^{-/-}$ and *Gbx2*$^{-/-}$ mice.

Modifier genes can produce either additive or synergistic effects (192). In the case of *Pax9* and *Gbx2*, the modification has resulted in both additive and synergistic effects. The combined deletion of both genes resulted in an increase in the penetrance of previously observed defects, one example being the increased occurrence of VSD in *Pax9*$^{+/-}$;*Gbx2*$^{-/-}$ mice compared to *Gbx2*$^{-/-}$ mice. This is suggestive of an additive effect. However, the penetrance of defects in *Pax9*$^{+/-}$;*Gbx2*$^{-/-}$ mice (100% penetrance of cardiovascular defects) was greater than the sum of the defects in *Gbx2*$^{-/-}$ (64% penetrance of cardiovascular defects) and *Pax9*$^{+/-}$ (no cardiovascular defects) mice. This suggests a synergistic effect, as does the presentation of pCAT in *Pax9*$^{+/-}$;*Gbx2*$^{-/-}$ mice which was not present in *Gbx2*$^{-/-}$ mice.

The modification of the *Pax9*$^{-/-}$ phenotype by *Gbx2* heterozygosity was more subtle. The overall penetrance of cardiovascular defects in *Pax9*$^{-/-}$ and *Pax9*$^{-/-}$;*Gbx2*$^{+/-}$ mice was the same at 100%, however there was an increase in the penetrance of the majority of individual cardiovascular defects; including DORV, VSD and RAA which are frequent in *Gbx2*$^{-/-}$ mice.

The *Pax9*-null phenotype shows complete penetrance, and *Pax9*$^{-/-}$ embryos usually present with a similar array of defects. The *Gbx2*-null phenotype, however, is varied with incomplete penetrance. Due to this reduced penetrance, any deviation from the *Gbx2* phenotype is easier to observe. Nonetheless, the interaction of *Pax9* targeting *Gbx2* appears to be stronger than *Gbx2* targeting *Pax9.* This was also shown in gene expression analysis. The downregulation of *Gbx2* in *Pax9*$^{-/-}$ embryos was more pronounced than the downregulation of *Pax9* in *Gbx2*$^{-/-}$ embryos. This indicates a hierarchal pathway in which *Pax9* largely acts upstream of *Gbx2* and *Gbx2* is able to feedback to act to *Pax9*. This differs from the interaction between *Tbx1* and *Pax9* which interact in a non-hierarchal pathway during cardiovascular development (134).

A similar interaction was observed between *Gbx2* and *Fgf8. Fgf8* is a signalling molecule that shares expression domains in the pharyngeal endoderm and ectoderm with *Gbx2* (59, 166). *Fgf8* has been suggested as a 22q11DS modifier gene as it is required in cardiovascular development and interacts with *Tbx1* during 4th PAA

morphogenesis (56, 61, 193). *Gbx2* and *Fgf8* heterozygotes have normal development, but the combined double heterozygosity results in defects including RAA and ARSA (166) as was observed in *Pax9*$^{+/-}$;*Gbx2*$^{+/-}$ mice. *Fgf8* heterozygosity increased the penetrance of cardiovascular defects in *Gbx2*$^{-/-}$ mice. Additionally, *Gbx2*$^{-/-}$;*Fgf8*$^{+/-}$ mice had thymus defects, frequent in *Fgf8*$^{-/-}$ mice. This is reminiscent of the interaction of *Pax9* with *Gbx2.*

As well as defects derived from the aberrant formation of the PAA, *Pax9* and *Gbx2* mutants also displayed OFT defects. Conotruncal defects are frequent in patients with CHD, occurring in 30% of cases (194) and approximately 20% of these cases had the 22q11 deletion (174). DORV is a prominent feature of *Pax9*$^{-/-}$ and *Gbx2*$^{-/-}$ mice and was also present in complex *Pax9;Gbx2* mutants (*Pax9*$^{-/-}$;*Gbx2*$^{+/-}$ and *Pax9*$^{+/-}$;*Gbx2*$^{-/-}$ mice). These complex mutants also had pCAT, a more severe OFT defect. The *Pax9;Gbx2* double knockout collected at E15.5 had CAT, which is frequent in *Tbx1*-null mutants (50).

Septation of the common OFT requires the interaction of NCC, the epicardium and the myocardium of the OFT. The myocardium of the OFT is derived from the SHF and septation is initiated by the infiltration of NCC into the OFT cushions (6, 27). It follows that mutations that affect the SHF and NCC migration can result in OFT defects, including CAT (28, 195).

It was postulated that pCAT and CAT occurred in the complex mutants as a result of altered NCC. NCC behave abnormally in *Pax9*$^{-/-}$ mice which have fewer NCC in the caudal PA (134). Likewise, *Gbx2*$^{-/-}$ mice show aberrant migration of NCC (133, 166). The NCC were not investigated in complex *Pax9;Gbx2* mutants, but both *Pax9* and *Gbx2* are independently required for normal NCC function. It could therefore be postulated that the combined homozygous deletion of both genes exacerbates the NCC phenotype, resulting in severe OFT defects.

A complex genetic network exists within the SHF and mutations in these genes results in OFT defects. *Tbx1* and *Fgf8* are both expressed in the anterior portion of the SHF and CAT occurs in *Tbx1*$^{-/-}$ and *Fgf8* hypomorphic mutants (61, 195, 196). The *Pax9*$^{-/-}$;*Gbx2*$^{-/-}$ double knockout also had AVSD, a defect that primarily occurs due to perturbations to the SHF (197, 198). The presence of AVSD and the complete lack of OFT septation could suggest that the CAT in the complex mutants is SHF-derived rather than NCC-derived.

This raises the question as to how the deletion of *Pax9* and *Gbx2*, expressed together in the pharyngeal endoderm, could result in a SHF-derived defect. A subset of cardiac progenitors express *Islet1*, the expression of which is required for the progenitors to contribute to the development of OFT, right ventricles and right atria. There has been no report of *Pax9* and *Gbx2* expression within the SHF. However, there are *Islet1*-expressing progenitor cells in the pharyngeal endoderm as well as the SHF (197, 199). Additionally, Park et al. (2006) found that *Fgf8* expression in the mesoderm is needed for OFT alignment while expression in the pharyngeal endoderm is needed for OFT septation. This role of progenitors within the pharyngeal endoderm could explain the presence of CAT that occurs with the simultaneous loss of *Pax9* and *Gbx2.*

Previous work in the laboratory used *Islet1Cre* to remove *Pax9* from *Islet1* expressing cells. All *Pax9*$^{f/-}$*;Isl1Cre* mice (n=9) had the *Pax9*$^{-/-}$ phenotype, with an absent thymus and pre-axial digit duplication. *Pax9*$^{f/-}$*;Isl1Cre* mice all presented with cardiovascular defects that overlapped with *Pax9*$^{-/-}$ mice, namely IAA, ARSA, IRSA, DORV and VSD. As *Islet1* is not expressed in the cranial NCC, *Pax9*$^{f/-}$*;Isl1Cre* did not present with cleft palate. This data shows that deletion of *Pax9* from *Islet1* expressing pharyngeal endoderm cells is sufficient to recapitulate the *Pax9*$^{-/-}$ cardiovascular phenotype. *Pax9* expression within these progenitor cells is required in the development of the septated OFT and great arteries. The exact origin of the OFT defects in complex *Pax9;Gbx2* mutants is difficult to dissect as the NCC and SHF share overlapping roles during cardiovascular development.

The data in this chapter demonstrates a strong interaction between *Pax9* and *Gbx2,* uncovering another part of the complex genetic network required in PAA morphogenesis. The phenotyping and gene expression analysis suggest that *Pax9* is upstream of *Gbx2* and *Gbx2* is able to feed back in to the network. The next chapter sought to investigate the pharyngeal endoderm as the site of this interaction.

Chapter 5. Investigating the role of *Pax9* and *Gbx2* in the pharyngeal endoderm

5.1 Introduction

The mature aortic arch forms from the remodelling of the PAA. This depends on tightly regulated gene expression and the interaction of the multiple tissue types of the PA, which consist of an inner lining of pharyngeal endoderm, an outer lining of pharyngeal ectoderm and a mesodermal core.

The pharyngeal endoderm has been shown to be crucial in the segmentation and patterning of the PA (discussed in Section 1.2.4). Precise gene expression in the endoderm is also required to provide signalling cues to NCC during PAA morphogenesis (47). The role of *Tbx1* within the layers of the PA has been investigated using conditional *Tbx1* mutants and, from these mutants, the heterozygous deletion of *Tbx1* from the pharyngeal endoderm most closely recapitulated the global *Tbx1*$^{+/-}$ phenotype at E15.5 (discussed in Section 1.6.2).

Gbx2 is expressed in the pharyngeal endoderm and ectoderm of the PA (164). The role of *Gbx2* expression in the pharyngeal ectoderm has already been investigated by Calmont et al. (2009) (discussed in Section 1.8.2). While the conditional *Gbx2* deletion from the ectoderm resulted in 4th PAA defects at E10.5, the Calmont study neglected to report analyses of these embryos in late embryogenesis, reasoning that the 4th PAA phenotype recovers during development. The effect of a *Gbx2* deletion from the pharyngeal ectoderm in late development cannot therefore be concluded.

Pax9 expression within the PA is restricted to the pharyngeal endoderm and the deletion of *Pax9* from this tissue results in cardiovascular defects, including IAA, ARSA and DORV (134). Gene expression analysis of wild type embryos confirmed the overlapping expression of *Pax9* and *Gbx2* in the pharyngeal endoderm at E9.5 (Section 4.2), during which the PAA are beginning to form. The data presented in Chapter 4 also confirmed an interaction between *Pax9* and *Gbx2* during cardiovascular development. It is therefore possible that these genes interact cell-autonomously within this tissue during PAA morphogenesis.

The aim of this chapter was to investigate the interaction of *Pax9* and *Gbx2* specifically within the pharyngeal endoderm. In order to remove *Gbx2* expression from the pharyngeal endoderm, the *Gbx2*-floxed allele was used in combination with the *Pax9Cre* allele. The *Pax9Cre* allele was validated before collecting *Pax9Cre;Gbx2-flox* embryos for phenotyping at E10.5 and E15.5.

5.2 Validating the *Pax9Cre* allele

The *Pax9Cre* allele has been used previously in the laboratory. The data conducted in this section validated the *Pax9Cre* allele and was included in published work (134). The *Pax9Cre* allele expresses *Cre* recombinase under the control of the *Pax9* promoter (Section 2.1.3). The insertion of the *Cre* recombinase gene removed part of the coding region of exon 2 and 3, therefore the allele is functionally null in terms of *Pax9* activity.

To validate the *Pax9Cre* allele, *Pax9Cre* males were crossed with *Rosa26R-lacZ* reporter females. Embryos were collected between E8.5 to E11.5 and stained for lacZ expression. Expression was observed within the PA of the embryos from E8.5 as well as in the vertebral column and nasal process from E10.5 (Figure 5.1). *Gbx2* is expressed from E8.5 in the PA (Figure 4.1), therefore *Pax9Cre* is expressed early enough for recombination of the *Gbx2* floxed allele.

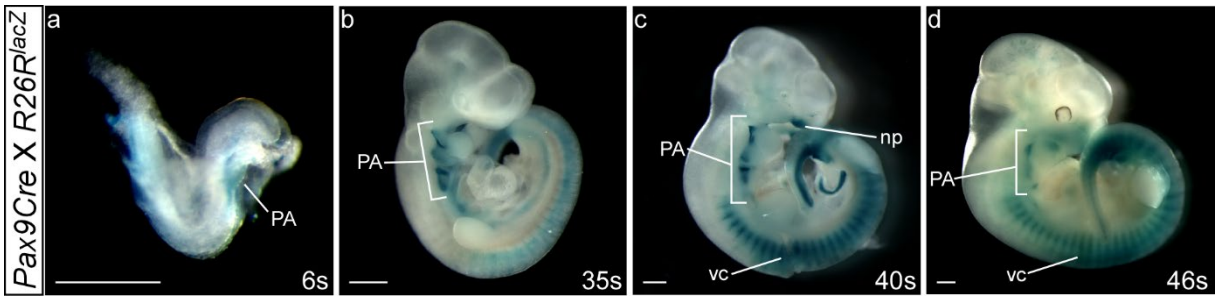

Figure 5.1. *Pax9Cre* is expressed in the pharyngeal arches from E8.5.

Xgal staining of *lacZ* expression in *Pax9Cre;R26R-LacZ* embryos from E8.5-11.5. Expression in the pharyngeal arches is clear from E8.5 (a). By E10.5 (c) expression is observed in the nasal process (np) and vertebral column (vc). Somite counts (s) indicated. Abbreviations: PA, pharyngeal arches; np, nasal process; vc, vertebral column**.** Scale, 500μm.

Pax9Cre embryos (n=3) were collected at E9.5 and coronal sections were stained by RNAScope using a *Cre* and a *Pax9* probe to confirm *Cre* expression within the *Pax9* expression domains (Figure 5.2). *Pax9* and *Cre* had overlapping expression, specifically within the endoderm layer of the PA.

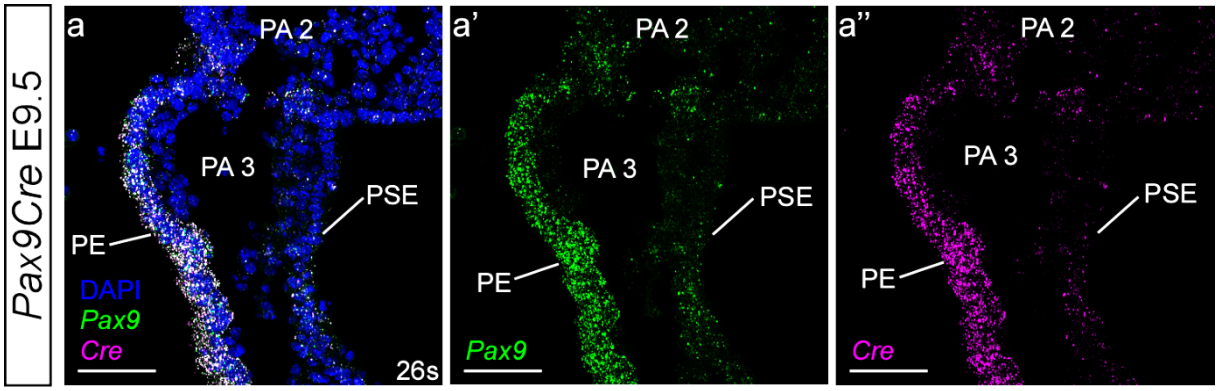

Figure 5.2. *Pax9Cre* is expressed within the pharyngeal endoderm.

Pax9 and *Cre* RNAScope probes were used on coronal E9.5 sections of a *Pax9Cre* embryo (n=3, 26 somites). *Cre* was expressed the pharyngeal endoderm (PE) of the PA with *Pax9.* Abbreviations: PA, pharyngeal arch; PE, pharyngeal endoderm; PSE, pharyngeal ectoderm. Scale, 50μm.

To further validate the *Pax9Cre* allele, pharyngeal endoderm cells were collected from *Pax9Cre;eYFP*$^{+/KI}$ embryos at E9.5 and analysed by qPCR (Figure 5.3). Cells were dissociated from the PA region of the embryos and flow sorted based on Cre-mediated *eYFP* expression. Gene expression within *eYFP*-positive (pharyngeal endoderm) and *eYFP*-negative (remaining pharyngeal arch tissue) cell populations were analysed by qPCR for *Pax9*, *eYFP* and *Gbx2*. The *eYFP* positive-cells were significantly enriched for *Pax9* and *eYFP* compared to *eYFP*-negative cells confirming the cells to be the *Pax9*-expressing pharyngeal endoderm cells.

Gbx2 expression in these cell populations was also investigated to quantitatively analyse expression in each tissue. The *eYFP*-negative cells represent the pharyngeal surface ectoderm, mesoderm and NCC within the PA. *Gbx2* is expressed in the pharyngeal endoderm and ectoderm of the PA, consequently the *eYFP*-negative cells represent the *Gbx2* expression within the ectoderm. *Gbx2* expression was significantly higher in the pharyngeal endoderm, showing that most *Gbx2* is expressed in the pharyngeal endoderm, highlighting the importance of this tissue.

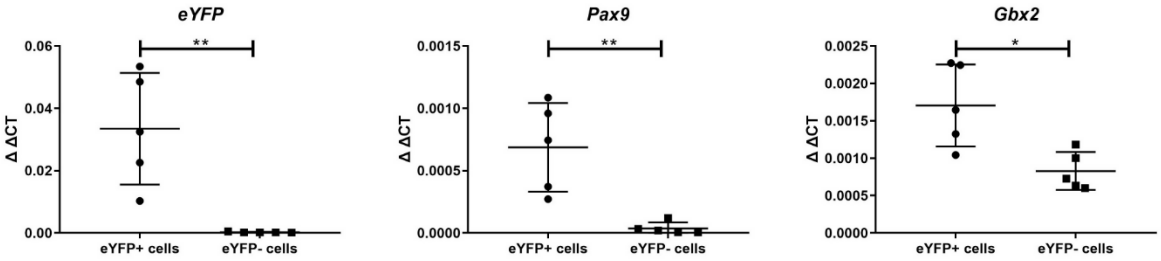

Figure 5.3. qPCR analysis of flow-sorted pharyngeal endoderm cells.

Cells were dissociated from the PA of E9.5 *Pax9Cre;eYFP*$^{+/KI}$ embryos (n=5, 23-27 somites) based on Cre-mediated *eYFP* expression and analysed by qPCR. (a) qPCR analysis confirmed the *eYFP*-positive cells to be enriched for *eYFP* while the *eYFP*-negative cells did not express *eYFP*. (b) Only the *eYFP*-positive cells were enriched for *Pax9*. (c) *Gbx2* expression was significantly higher in the *eYFP*-positive cell population, representing the pharyngeal endoderm, compared to the *eYFP*-negative cell population. Statistical analysis was calculated using an unpaired t-test, *p<0.05; **p<0.01.

Pax9Cre males were crossed with *Pax9*$^{f/f}$ females to collect *Pax9*$^{Cre/f}$ mice and *Pax9*$^{+/f}$ littermate controls (Figure 5.4). The *Pax9*^{flox} allele contains *loxP* sites flanking exon 1 and 2 of *Pax9*, the recombination of this region was sufficient to recapitulate the phenotype of *Pax9*$^{-/-}$ mice (153). *Pax9*$^{Cre/f}$ mice should be indistinguishable from *Pax9*$^{-/-}$ mice, as the *Pax9Cre* allele is functionally null in the context of *Pax9* and will also recombine the *Pax9*^{flox} allele.

All *Pax9*$^{Cre/f}$ mice (n=5) died on the day of birth, presenting with the *Pax9*-null phenotype. Upon direct observation, the mutants had a bloated abdomen and pre-axial digit duplication. Embryos were examined at E15.5 and all presented with a cleft palate, absent thymus and cardiovascular defects. The cardiovascular defects matched that observed in *Pax9*-nulls; IAA, ARSA, absent common carotid arteries, VSD and DORV. This not only shows the successful recombination of the *Pax9* floxed allele by *Pax9Cre*, but also confirms that the *Pax9Cre* allele is functionally null in terms of *Pax9* activity.

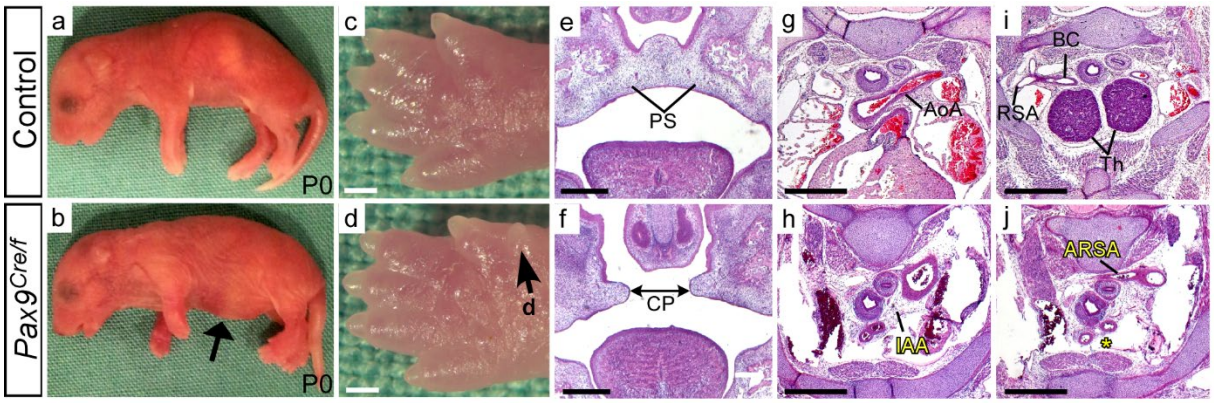

Figure 5.4. *Pax9* deletion using the *Pax9Cre* allele recapitulates the *Pax9*-null phenotype.

Pax9Cre and *Pax9f/f* mice were crossed to generate $Pax9^{Cre/f}$ mice. $Pax9^{Cre/f}$ mice (n=5) died on the day of birth with a bloated abdomen (arrow; b) compared to euthanised control (a). $Pax9^{Cre/f}$ mice had pre-axial digit duplication (arrow; d). H&E stained coronal sections of E15.5 control (e) with normal fused palatal shelves (PS). A cleft palate (CP) is present in the $Pax9^{Cre/f}$ embryo (f). H&E stained transverse E15.5 sections show typical *Pax9*-null defects including IAA (h), ARSA (j) and an absent thymus (*, j). Abbreviations: AoA, aortic arch; ARSA, aberrant right subclavian artery; BC, brachiocephalic artery; RSA, right subclavian artery; Th, thymus. Images a-d from Dr Ralf Kist, Newcastle University. Scale, 500μm.

5.3 The role of *Pax9* and *Gbx2* in the pharyngeal endoderm

To remove *Gbx2* expression from the pharyngeal endoderm, the $Gbx2^{flox}$ allele was used in combination with the *Pax9Cre* allele. $Gbx2^{f/f}$ females were crossed with *Pax9Cre;*$Gbx2^{+/f}$ males to generate *Pax9Cre;*$Gbx2^{f/f}$ embryos. The *Pax9Cre* allele is functionally null, therefore this genotype allowed the investigation of the *Gbx2* endoderm deletion in the context of *Pax9* heterozygosity.

Of the 16 *Pax9Cre;*$Gbx2^{f/f}$ embryos collected, two embryos (13%) had cardiovascular defects (detailed in Appendix Table A.7). One embryo had ARSA and the other had DORV with IVC. With this genotype, two *Gbx2* floxed alleles must be recombined by *Pax9Cre.* It was thought that this could reduce the presentation of the cardiovascular phenotype.

$Gbx2^{f/f}$ females were crossed with *Pax9Cre;*$Gbx2^{+/-}$ males to generate *Pax9Cre;*$Gbx2^{f/-}$ embryos, in which *Cre* must only recombine one *Gbx2* floxed allele. These embryos are null for *Gbx2* in the endoderm and heterozygous for *Gbx2* in the remaining *Gbx2* expression domains, namely the pharyngeal ectoderm. As $Gbx2^{+/-}$ embryos

(n=18, E15.5-P0) did not present with cardiovascular defects, any abnormalities present in *Pax9Cre;Gbx2*$^{f/-}$ embryos were attributed to the deletion of *Gbx2* and *Pax9* within the pharyngeal endoderm specifically rather than the global *Gbx2* heterozygosity.

Prior to phenotyping, *Pax9Cre;Gbx2*$^{f/-}$ embryos (n=5) were collected at E9.5 and sections were stained for *Gbx2* by RNAScope to confirm downregulation of *Gbx2* in the mutant embryos (Figure 5.5). In the wild type embryos (n=5), *Gbx2* expression was observed in the pharyngeal endoderm and ectoderm. Expression was higher in the endoderm, which was also observed through *Gbx2* qPCR analysis of flow sorted PA cells (Figure 5.3).

In the *Pax9Cre;Gbx2*$^{f/-}$ embryos the majority of *Gbx2* expression from the pharyngeal endoderm was lost (Figure 5.5). There was also reduced expression in the pharyngeal ectoderm, however, this was expected as these embryos are also heterozygous for *Gbx2* in the ectoderm. This data and the robust expression of *Cre* in *Pax9* expression domains (Figure 5.2) show that *Pax9Cre* is successfully recombining *Gbx2* specifically in the pharyngeal endoderm.

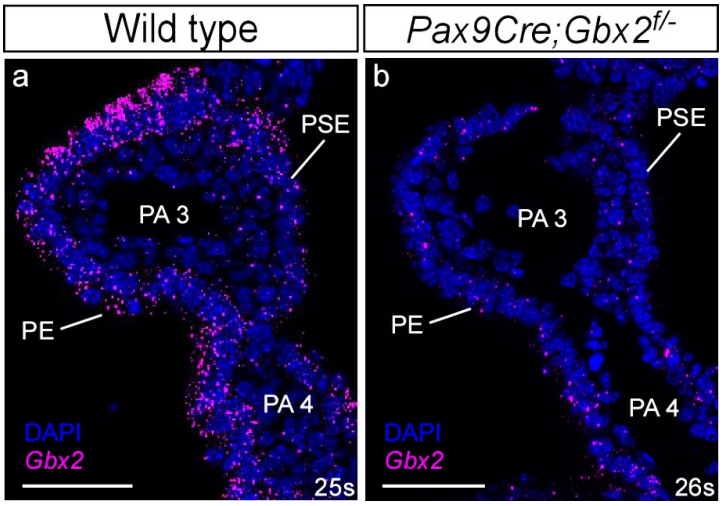

Figure 5.5. *Gbx2* expression in the pharyngeal endoderm of conditional endoderm mutants.

Gbx2 RNAScope probe was used on coronal E9.5 sections of a wild type (a, n=5, 24-28 somites) and *Pax9Cre;Gbx2*$^{f/-}$ embryo (b, n=5, 26-29 somites). *Gbx2* was reduced in pharyngeal endoderm (PE) compared to the wild type. Abbreviations: PA, pharyngeal arch; PE, pharyngeal endoderm; PSE, pharyngeal ectoderm. Scale, 50μm.

Pax9Cre;Gbx2$^{f/-}$ embryos were collected at E15.5 to analyse the cardiovascular and aortic arch structure by MRI (Figure 5.6). Appendix Table A.8 shows the phenotype of each *Pax9Cre;Gbx2*$^{f/-}$ embryo collected. Analysis showed that 21% of *Pax9Cre;Gbx2*$^{f/-}$ embryos (n=14 examined) had cardiovascular defects, an increase compared to 13% in *Pax9Cre;Gbx2*$^{f/f}$ embryos which suggests that the *Cre* recombination efficiency is affected by the presence of multiple floxed alleles. The defects present in *Pax9Cre;Gbx2*$^{f/-}$ embryos were reminiscent of the *Gbx2*$^{-/-}$ and *Pax9*$^{+/-}$*;Gbx2*$^{-/-}$ phenotype. RAA was present in one embryo (7%) and ARSA, the most frequently observed defect (21%), was present in three embryos. Absent LCC was present in one embryo (Figure 5.6) a defect that was observed in *Pax9*$^{+/-}$*;Gbx2*$^{-/-}$ embryos and is typical of *Pax9*$^{-/-}$ embryos. Table 5.1 summarises the defects present in *Pax9Cre;Gbx2*$^{f/-}$ embryos.

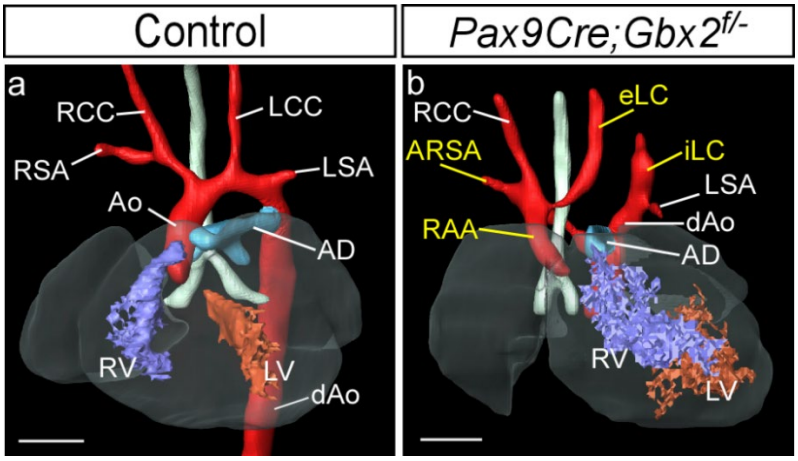

Figure 5.6. Cardiovascular defects present in conditional endoderm mutants at E15.5.

MRI data reconstructions of control (a) and *Pax9Cre;Gbx2*$^{f/-}$ (b) E15.5 embryos. Control shows normal aortic arch structure. *Pax9Cre;Gbx2*$^{f/-}$ with a RAA, ARSA and an absent LCC. Abbreviations: AD, arterial duct; Ao, aorta; ARSA, aberrant right subclavian artery; dAo, dorsal aorta; LCC, left common carotid artery; LSA, left subclavian artery; LV, left ventricle; RAA, right aortic arch; RCC, right common carotid artery; RSA, right subclavian artery; RV, right ventricle; Tr, trachea; VSD, ventricular septal defect. Scale, 500μm.

Table 5.1. Penetrance of defects at E15.5 in conditional endoderm mutants.

ARSA includes retro-oesophageal subclavian arteries. Abbreviations: ALSA, aberrant left subclavian artery; ARSA, aberrant right subclavian artery; CV, cardiovascular; dAo, dorsal aorta; DORV, double outlet right ventricle; IAA, interrupted aortic arch; RAA, right aortic arch; VSD, ventricular septal defect.

	Frequency				
Genotype	**CV Defect**	**IAA**	**RAA**	**ARSA**	**Thymus Defect**
Pax9Cre;Gbx2$^{f/-}$ n=14	3 (21%)	0	1 (7%)	3 (21%)	0

Pax9Cre;Gbx2$^{f/-}$ embryos were collected at E10.5 for ink injection to analyse the structure of the PAA (Figure 5.7). 50% of embryos (n=14 examined) had 4th PAA defects confirming the necessity of *Pax9* and *Gbx2* expression in the pharyngeal endoderm for 4th PAA morphogenesis. Defects, summarised in Table 5.2, included either hypoplastic or absent vessels, both unilateral and bilateral (Figure 5.7).

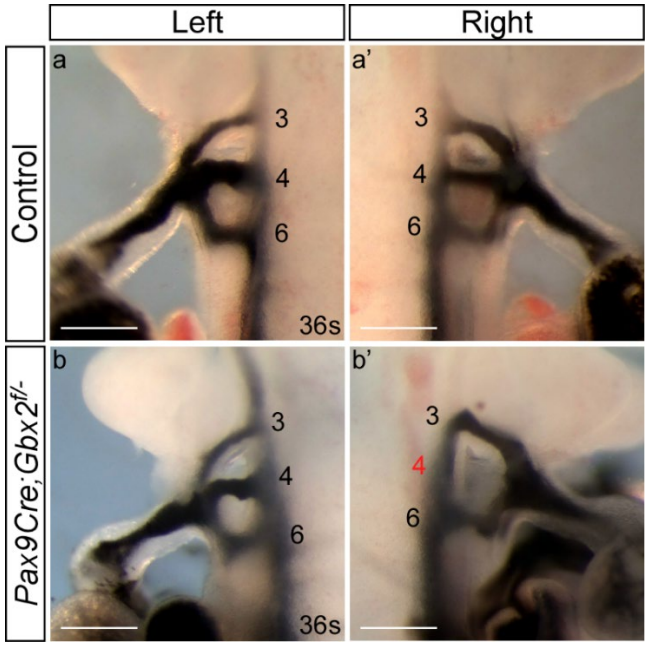

Figure 5.7. 4th pharyngeal arch artery defects in *Gbx2$^{f/-}$;Pax9Cre* mice at E10.5.

Intracardiac ink injection of E10.5 embryos. In the control embryos (a), PAA 3-6 (numbered) were patent to ink. *Gbx2$^{f/-}$;Pax9Cre* embryos (b) had 4th PAA defects. An absent right 4th PAA is shown (b'). Scale, 500μm.

Table 5.2. Penetrance of 4th pharyngeal arch artery defects in *Gbx2$^{f/-}$;Pax9Cre* embryos at E10.5.

Abbreviations: PAA, pharyngeal arch artery; NP, non-patent; Th, thin.

	Frequency							
	4th PAA defect	Unilateral defect			Bilateral defect			
Genotype		Defect	Th	NP	Defect	Th-Th	NP-Th	NP-NP
Gbx2$^{f/-}$;Pax9Cre (n=14)	7 (50%)	5 (36%)	2 (14%)	3 (22%)	2 (14%)	1 (7%)	0	1 (7%)

As *Pax9$^{+/-}$;Gbx2$^{+/-}$* mice presented with cardiovascular defects (21%, n=28 examined, Section 4.4), *Pax9Cre;Gbx2$^{+/f}$* embryos were analysed to determine if heterozygosity of these genes within the pharyngeal endoderm resulted in cardiovascular defects. *Pax9Cre;Gbx2$^{+/f}$* are heterozygous for *Pax9* and *Gbx2* only in the pharyngeal endoderm. At E15.5, 1 out of 15 (7%) *Pax9Cre;Gbx2$^{+/f}$* embryos had cardiovascular defects. This embryo had a mirror image aortic arch, with a RAA and RAD (Figure 5.8, Appendix Table A.9). The mirror image defect was observed in *Gbx2$^{-/-}$* (24%, n=25 examined) and *Pax9$^{+/-}$;Gbx2$^{-/-}$* (8%, n=14 examined) embryos.

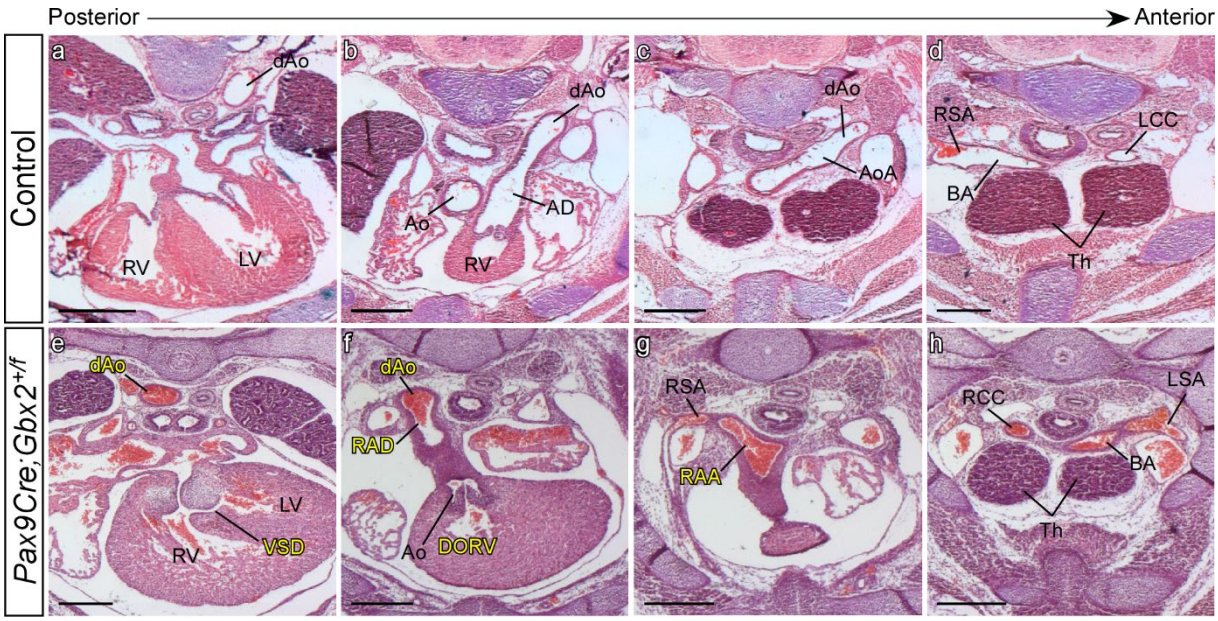

Figure 5.8. Cardiovascular defects in *Gbx2$^{+/f}$;Pax9Cre* embryos at E15.5.

H&E stain of E15.5 transverse sections of a control (a-d) and *Gbx2$^{+/f}$;Pax9Cre* embryo (e-h). In the control, the AD and aortic arch (AoA) cross to the left (b,c). The brachiocephalic artery (BA) branches from the arch and splits into the RSA and RCC (d). The LCC branches from aortic arch (d). The mutant embryo has DORV (f) and an IVC (e). The arterial duct (RAD) and aortic arch (RAA) cross to the right (f,g) connecting to a right dorsal aorta (dAo). The BA splits in to the LSA and LCC (h). Abbreviations: AD, arterial duct; Ao, aorta; AoA, aortic arch; BA, brachiocephalic artery; dAo, dorsal aorta; DORV, double outlet right ventricle; LCC, left common carotid artery; LSA, left subclavian artery; LV, left ventricle; RAA, right aortic arch; RAD, right arterial duct; RCC, right common carotid artery; RSA, right subclavian artery; RV, right ventricle; Th, thymus. Scale 500μm.

Pax9Cre;Gbx2$^{+/f}$ embryos were collected for intracardiac ink injection at E10.5 (Figure 5.9). 4th PAA defects were present in 11% (n=19 examined) of the *Pax9Cre;Gbx2$^{+/f}$* embryos. One embryo had a unilateral hypoplastic 4th and one had bilaterally non-patent 4th PAAs.

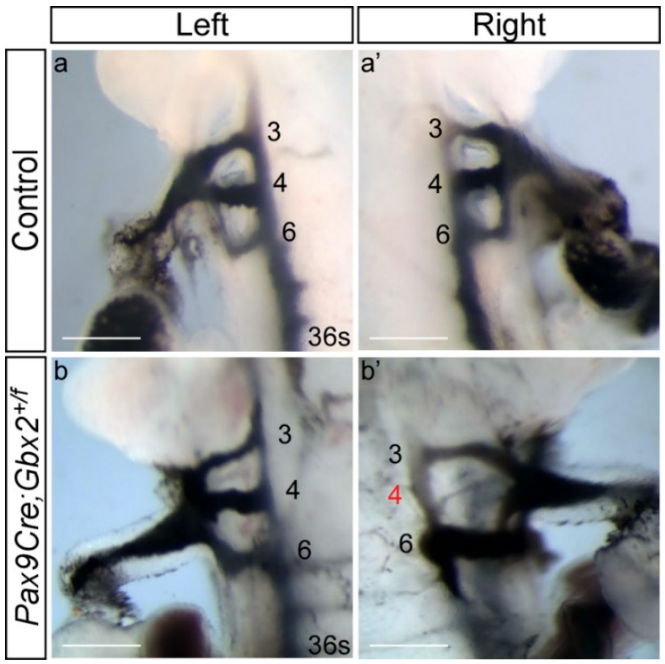

Figure 5.9. 4th pharyngeal arch artery defects in *Gbx2$^{+/f}$;Pax9Cre* mice at E10.5.

Intracardiac ink injection of E10.5 embryos. In control embryos (a), PAA 3-6 (numbered) were patent to ink. *Pax9Cre;Gbx2$^{+/f}$* embryo (b) had 4th PAA defects. A hypoplastic right 4th PAA is shown (c). Scale, 500μm.

Table 5.3 summarises the penetrance of cardiovascular defects at E10.5 and E15.5 in conditional endoderm mutants and their global mutant equivalent genotypes. The penetrance of cardiovascular defects in endoderm mutants differed to the global mutants, particularly at E15.5. However, it is worth noting the reduced penetrance of defects at E15.5 compared to E10.5 in the conditional mutants showing that these mutants show recovery of the 4th PAA phenotype during development. This is discussed in more detail in the next section. The presentation of defects in conditional endoderm mutants shows that expression of *Pax9* and *Gbx2* within the pharyngeal endoderm is essential for PAA morphogenesis and remodelling.

Table 5.3. Penetrance of defects at E10.5 and E15.5-P0 in conditional endoderm mutants and global mutant equivalent genotypes.

Statistical significance between global and condition mutants was analysed by chi-squared for associations. ****p<0.0001. Abbreviations: CV, cardiovascular.

Genotype	Mutant	Penetrance of 4th PAA defects at E10.5	Penetrance of CV defects at E15.5
Pax9Cre;Gbx2$^{f/-}$	Endoderm *Gbx2*-null and *Pax9*-het	50% (n=14)	21% (n=14)
Pax9$^{+/-}$;Gbx2$^{-/-}$	Global *Gbx2*-null and *Pax9*-het	100% (n=7)	100%**** (n=14)
Pax9Cre;Gbx2$^{+/f}$	Endoderm *Gbx2*-het and *Pax9*-het	11% (n=19)	7% (n=15)
Pax9$^{+/-}$;Gbx2$^{+/-}$	Global *Gbx2*-het and *Pax9*-het	30% (n=63)	21% (n=28)

5.4 Discussion

The data presented in this chapter shows that *Pax9* and *Gbx2* expression is required in the pharyngeal endoderm for 4th PAA morphogenesis. Deleting *Gbx2* from the endoderm resulted in the same cardiovascular defects observed in *Gbx2$^{-/-}$* and *Gbx2$^{-/-}$;Pax9$^{+/-}$* mice. There was a discrepancy in the penetrance of these defects in *Pax9Cre;Gbx2$^{f/-}$* mutants compared to *Pax9$^{+/-}$;Gbx2$^{-/-}$* mutants.

A potential cause for this difference is due to Cre efficiency. Cre lines are rarely 100% efficient and successful Cre-mediated recombination relies on the effective expression of Cre in the tissue of interest. An example of a Cre with poor expression is *Tbx1Cre*. A study used *Tbx1Cre* to remove *Gbx2* expression from the pharyngeal mesoderm, endoderm and ectoderm, however this did not recapitulate the global *Gbx2* mutant phenotype (133). Analysis of *Tbx1Cre* embryos showed sparse *Cre* expression within the epithelial layers at the time of 4th PAA specification which resulted in reduced recombination of *Gbx2* and presentation of cardiovascular defects.

RNAscope showed that *Gbx2* was successfully recombined in the pharyngeal endoderm of *Pax9Cre;Gbx2*$^{f/-}$ mutants, although residual expression may remain within the tissue. Validation of the *Pax9Cre* allele confirmed specific expression in the pharyngeal endoderm from E8.5, coinciding with *Gbx2* expression. However, the time required for effective *Gbx2* recombination could have allowed for the expression of Gbx2 protein. This residual *Gbx2* expression or Gbx2 protein could have allowed normal cardiovascular development in a portion of mutants. Additionally, the lower penetrance of defects in *Pax9Cre;Gbx2*$^{f/-}$ mutants could be a result of the remaining *Gbx2* expression in the pharyngeal ectoderm.

A potential explanation for the low penetrance of defects in *Pax9Cre;Gbx2*$^{f/-}$ mutants in late embryogenesis is the recovery of the 4th PAA during development. This is a well-documented process in *Tbx1*$^{+/-}$ mutants in which the penetrance of defects to the 4th PAA decreases throughout embryogenesis (130) (discussed in Section 1.6.2). Previous work in the laboratory has investigated the interaction between *Tbx1* and *Pax9* within the pharyngeal endoderm (134). The *Pax9Cre* allele was used to generate conditional heterozygous *Tbx1* mutants. The incidence of cardiovascular defects in *Tbx1* conditional endoderm mutants (*Tbx1*$^{+/f}$*;Pax9Cre* mice) was significantly greater at E10.5 (92%, n=17 examined) compared to later in development (33%, n=18 examined).

This recovery was apparent in the mutants collected in this study, including the *Pax9Cre;Gbx2*$^{f/-}$ mutants which showed a 50% (n=14 examined) penetrance of 4th PAA defects at mid-embryogenesis compared to 21% (n=14 examined) in late embryogenesis. Table 5.4 shows the penetrance of 4th PAA defects at E10.5, assessed by ink injection and HREM, compared to the penetrance of cardiovascular defects observed at E15.5, assessed by MRI and histology, in the mutants collected in this study. The recovery of 4th PAA defects was apparent in all mutants that showed incomplete penetrance at E15.5; this includes all the *Gbx2* mutants (excluding *Pax9*$^{+/-}$*;Gbx2*$^{-/-}$ and *Pax9*$^{-/-}$*;Gbx2*$^{+/-}$ mice which show complete penetrance at E15.5).

Table 5.4. Penetrance of cardiovascular defects in mutants at mid and late embryogenesis.

The mutants that show a recovery in 4th PAA defects are highlighted. Statistical significance was analysed by chi-squared and Fisher's exact test.

	Penetrance of defects (%)	
Genotype	**E10.5**	**E15.5-P0**
***Gbx2*$^{-/-}$**	10/12 (83%)	16/25 (64%)
***Pax9*$^{-/-}$**	3/3 (100%)	9/9 (100%)
***Pax9*$^{+/-}$*;Gbx2*$^{+/-}$**	19/63 (30%)	6/28 (21%)
***Pax9*$^{+/-}$*;Gbx2*$^{-/-}$**	7/7 (100%)	14/14 (100%)
***Pax9*$^{-/-}$*;Gbx2*$^{+/-}$**	6/6 (100%)	9/9 (100%)
***Pax9Cre;Gbx2*$^{f/-}$**	7/14 (50%)	3/14 (21%)
***Pax9Cre;Gbx2*$^{+/f}$**	2/19 (11%)	1/15 (7%)

It was found that abnormal 4th PAAs in *Tbx1*$^{+/-}$ mutants at E10.5 are underdeveloped due to lack of differentiation of NCC into smooth muscle cells around the vessel (130). The exact mechanism of the 4th PAA recovery is unknown, however it is proposed that developmental cues between E11.5 and E13.5 allow for the delayed differentiation of smooth muscle cells which promotes the recovery of defective vessels (130). Milder 4th PAA defects, such as hypoplasticity rather than absence of the 4th PAA, are found more likely to recover (34, 130). Of the seven *Pax9Cre;Gbx2*$^{f/-}$ embryos with a 4th PAA defect at E10.5, 43% had a hypoplastic 4th PAA. *Tbx1* and *Gbx2* share a role in 4th PAA morphogenesis and potentially an overlapping mechanism in the recovery of this vessel, resulting in the reduced penetrance of 4th PAA-derived defects in late embryogenesis.

The deletion of *Gbx2* from the pharyngeal endoderm resulted in 4th PAA defects, however, as *Gbx2* is expressed in the pharyngeal endoderm and ectoderm, it was unlikely that deleting *Gbx2* from the pharyngeal endoderm would result in full penetrance of defects, as the ectoderm must also have a role in PAA development. Calmont et al. (2009) studied the role of *Gbx2* within the pharyngeal ectoderm using

Ap2αCre to create conditional homozygous ectoderm mutants. Mutants were analysed at E10.5 and 47% (n=15 examined) had a 4th PAA defect. However, the study did not provide phenotyping data for conditional ectoderm mutants later in development, reasoning that the 4th PAA phenotype recovers overtime. It could be that ectoderm mutants did not display a cardiovascular phenotype later in development, or that the penetrance of defects was very low.

In the data collected here, 50% of *Pax9Cre;Gbx2$^{f/-}$* embryos (n=14) had a 4th PAA defect at E10.5, a similar finding to the 47% penetrance in conditional ectoderm mutants at E10.5 in the Calmont study. Likewise, the distribution of unilateral and bilateral 4th PAA defects in conditional endoderm and ectoderm mutants was the same. In both of these conditional mutant genotypes, of the embryos with a 4th PAA defect, 71% had a unilateral defect and 29% had a bilateral defect. It is most likely true that *Gbx2* expression in the endoderm and ectoderm share a role in cardiovascular development. Ectodermal *Gbx2* expression was sufficient to allow for normal cardiovascular development in many of the *Pax9Cre;Gbx2$^{f/-}$* mutants in this study, thereby reducing the penetrance of defects overall.

As the *Pax9Cre;Gbx2$^{f/-}$* mice are also heterozygous for *Pax9*, it is difficult to completely evaluate the role of the pharyngeal endoderm. The presence of defects in these mutants could be due to the tissue-specific loss of *Gbx2* expression from the pharyngeal endoderm, or the genetic interaction between *Gbx2* and *Pax9*. The use of alternative *Cre* lines, such as *Sox17Cre* (200), could be used to investigate the independent role of *Gbx2* within the pharyngeal endoderm. The data presented in Chapter 4 confirmed the interaction between *Pax9* and *Gbx2.* Combined with the phenotyping data in this chapter, the data overall shows that *Pax9* and *Gbx2* interact cell-autonomously within the pharyngeal endoderm.

Chapter 6. Investigating the potential *Tbx1-Pax9-Gbx2* genetic network

6.1 Introduction

Mutations in *Tbx1* have been identified as a leading cause of the cardiovascular phenotype in 22q11DS (50, 98, 100). This phenotype is largely recapitulated in *Tbx1*$^{+/-}$ mouse models which have ARSA and VSD as well as more severe defects, such as IAA, though at a reduced frequency (50, 100, 130). *Pax9* is a potential modifier of the 22q11DS phenotype and *Pax9* heterozygosity has been shown to increase the severity of the *Tbx1*$^{+/-}$ phenotype (134). *Tbx1*$^{+/-}$;*Pax9*$^{+/-}$ mice have a significantly increased penetrance of IAA compared to *Tbx1*$^{+/-}$ mice. IAA is a prominent feature of 22q11DS, as one of the most commonly observed CHD in patients (85).

Tbx1 and *Pax9* appear to interact in a non-hierarchal pathway within the pharyngeal endoderm to control 4th PAA morphogenesis (134). *Gbx2* is downregulated in the pharyngeal endoderm of *Tbx1*$^{-/-}$ and *Pax9*$^{-/-}$ mutants and could be a potential shared downstream target of these genes (133, 134, 137). The data presented in Chapter 4 and 5 suggest that *Pax9* and *Gbx2* interact cell-autonomously in the pharyngeal endoderm. Likewise, *Gbx2* has been shown to interact with *Tbx1*, as *Gbx2* heterozygosity increased the penetrance of cardiovascular defects in *Tbx1*$^{+/-}$ mice (133). All these genes have been shown to interact and are all independently required in cardiovascular development.

The downregulation of *Gbx2* in *Tbx1* and *Pax9* mutants suggests that *Tbx1* and *Pax9* act upstream of *Gbx2.* However, gene expression analysis (Section 4.2) showed that *Pax9* is downregulated in *Gbx2*-null embryos, suggesting that *Gbx2* could feedback and act on *Pax9.* The expression of *Tbx1* in *Gbx2*$^{-/-}$ mutants has not yet been investigated.

Tbx1, *Pax9* and *Gbx2* mouse mutants share overlapping phenotypic features, suggesting that they may act through a common genetic network. This chapter aimed to investigate the potential *Tbx1-Pax9-Gbx2* genetic network in cardiovascular development. *Tbx1, Pax9* and *Gbx2* mutants were collected at E9.5 to analyse gene expression. To investigate this network *in vivo*, *Tbx1*$^{+/-}$;*Pax9*$^{+/-}$;*Gbx2*$^{+/-}$ embryos were

collected at E15.5 to determine if *Gbx2* heterozygosity modified the *Tbx1*$^{+/-}$;*Pax9*$^{+/-}$ cardiovascular phenotype. Finally, the mechanism of this interaction was investigated using luciferase and ChIP assays.

6.2 *Tbx1*, *Pax9* and *Gbx2* expression *in vivo*

Wild type embryos (n=3) were collected at E9.5 and sectioned to determine *Tbx1* co-expression with *Pax9* and *Gbx2* (Figure 6.1). RNAscope confirmed *Tbx1* to be expressed in the pharyngeal endoderm, ectoderm and mesoderm of the PA. *Tbx1* had overlapping expression with *Pax9* and *Gbx2* in the pharyngeal endoderm and with *Gbx2* in the ectoderm. All genes are expressed within the pharyngeal endoderm, highlighting the importance of this tissue in PAA morphogenesis.

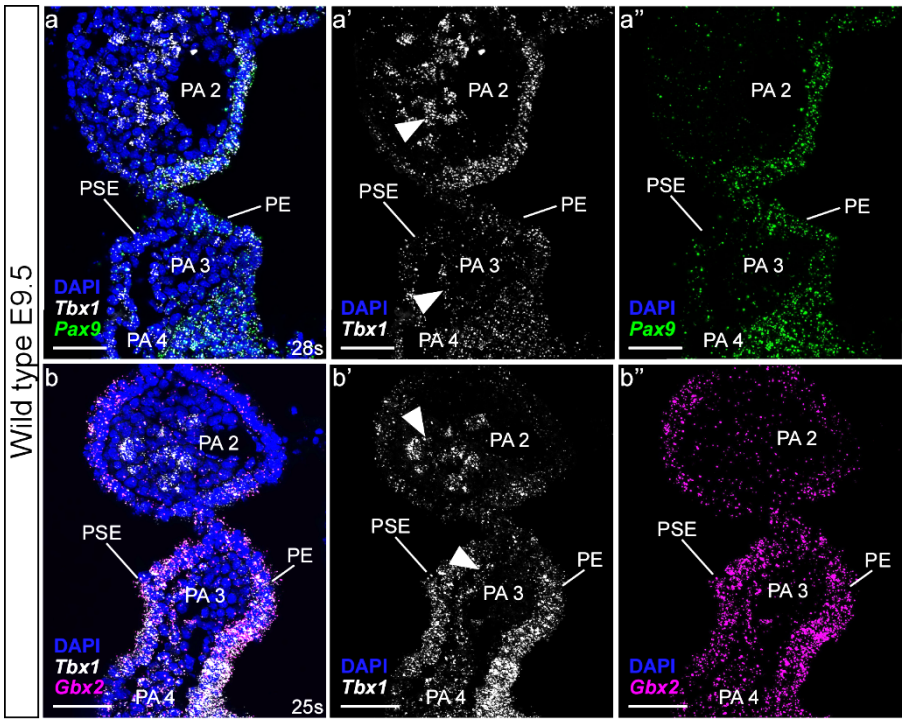

Figure 6.1. *Tbx1, Pax9* and *Gbx2* expression in the pharyngeal arches at E9.5.

Tbx1, Pax9 and *Gbx2* RNAScope probes were used on wild type E9.5 sections (n=3, 24-28 somites). a) *Tbx1* and *Pax9* co-stain shows overlapping expression within the pharyngeal endoderm (PE). *Tbx1* was also detected in the pharyngeal ectoderm (PSE) and mesodermal core of the PA (arrowhead). b) *Tbx1* and *Gbx2* co-stain shows overlapping expression in the pharyngeal endoderm and ectoderm. Somite counts (s) indicated. Abbreviations: PA, pharyngeal arch; PE, pharyngeal endoderm; PSE, pharyngeal surface ectoderm. Scale, 50μm.

Microarray analysis has shown that *Pax9* and *Gbx2* are downregulated in *Tbx1*$^{-/-}$ embryos (133, 137). Wild type (n=3) and *Tbx1*$^{-/-}$ (n=3) embryos were collected at E10.5 then sectioned and stained for *Tbx1, Pax9* and *Gbx2* by RNAScope to determine the tissue specific downregulation (Figure 6.2). At E10.5, *Tbx1, Pax9* and *Gbx2* are still expresed in their specific expression domains within the PA of wild type embryos. In *Tbx1*$^{-/-}$ embryos, the caudal PA fail to segment and are absent. Consequently, the defined PA structure is unrecognisable in *Tbx1*$^{-/-}$ sections, but a lining of endoderm can be observed down the midline of the embryo. *Pax9* and *Gbx2* were downregulated in the pharyngeal endoderm of *Tbx1*$^{-/-}$ mice.

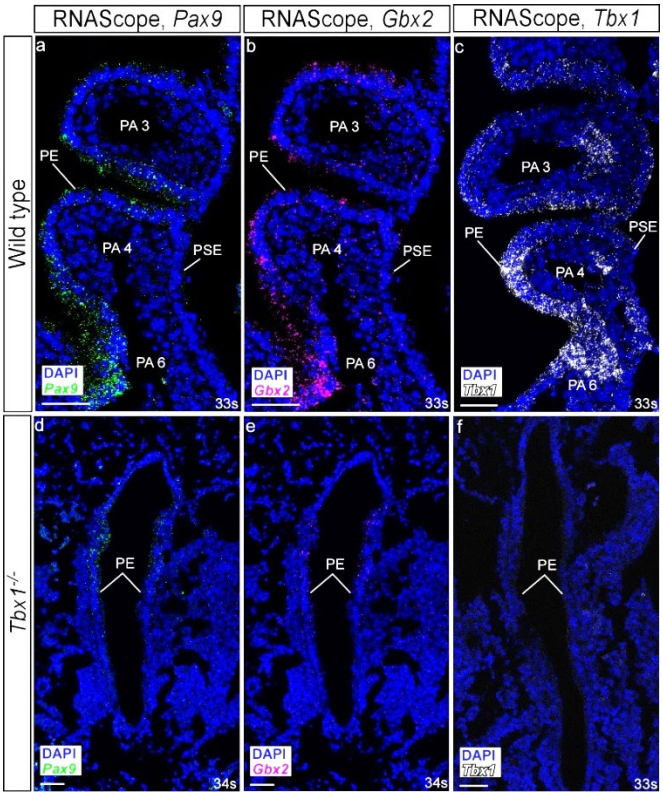

Figure 6.2. *Pax9* and *Gbx2* are downregulated in the pharyngeal endoderm of *Tbx1*$^{-/-}$ embryos.

Tbx1, Pax9 and *Gbx2* RNAScope probes were used on wild type (a, b, c, n=3, 33 somites) and *Tbx1*$^{-/-}$ (d, e, f, n=3, 31-34 somites) E10.5 sections. The caudal PAs (numbered) were observed in wild type embryos. The caudal PA are absent in *Tbx1*$^{-/-}$ embryos. An inner lining of pharyngeal endoderm (PE) can be observed. a) *Pax9* expression is clear in the PE layer of the arches. *Pax9* expression in the PE is reduced in the *Tbx1*$^{-/-}$ mutant (d). *Gbx2* is present in the pharyngeal endoderm and ectoderm of wild type embryos (b) but is reduced in the mutant (e). (c) *Tbx1* is expressed in the pharyngeal endoderm, ectoderm and mesoderm in wild type embryos. (f) *Tbx1*$^{-/-}$ embryo confirming lack of *Tbx1* expression. Abbreviations: PA, pharyngeal arch; PE, pharyngeal endoderm; PSE, pharyngeal surface ectoderm. Scale, 50μm.

Pax9 and *Gbx2* were downregulated in *Gbx2*$^{-/-}$ and *Pax9*$^{-/-}$ embryos respectively (Section 4.2). RNAScope was used to analyse the expression of *Tbx1* in *Pax9*$^{-/-}$ (n=3) and *Gbx2*$^{-/-}$ (n=3) embryos compared to wild type (n=4) at E9.5 (Figure 6.3). *Tbx1* expression was reduced in the *Pax9*$^{-/-}$ embryos (this data was published in Phillips et al., 2019). This reduction was more pronounced in the pharyngeal endoderm and ectoderm than the mesoderm. *Tbx1* expression appears downregulated in the pharyngeal ectoderm of *Gbx2*$^{-/-}$ embryos.

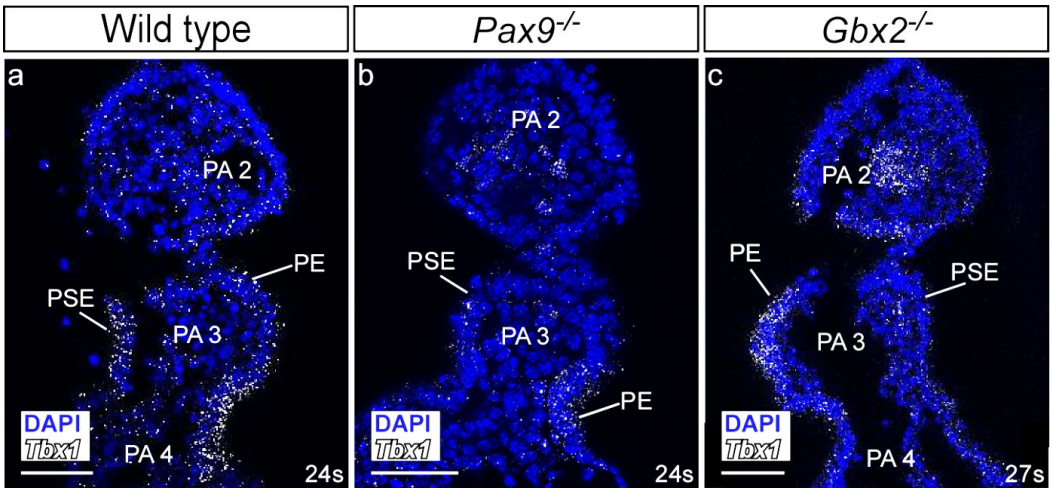

Figure 6.3. *Tbx1* expression *Pax9*$^{-/-}$ and *Gbx2*$^{-/-}$ embryos at E9.5.

RNAScope using a probe for *Tbx1* on wild type (a, n=4, 24-28 somites), *Pax9*$^{-/-}$ (b, n=3, 24-26 somites) and *Gbx2*$^{-/-}$ (c, n=3, 25-27 somites) embryos at E9.5. *Tbx1* expression was reduced in the pharyngeal endoderm and ectoderm of *Pax9*$^{-/-}$ embryos (b) and in the pharyngeal ectoderm of *Gbx2*$^{-/-}$ embryos (c). Abbreviations: PA, pharyngeal arch; PE, pharyngeal endoderm; PSE, pharyngeal surface ectoderm. Scale, 50μm.

Table 6.1 summarises the expression of *Tbx1*, *Pax9* and *Gbx2* in the mutant embryos, as assessed by RNAScope in this study (Section 4.2 and 6.2). All genes were downregulated in *Tbx1*$^{-/-}$ and *Pax9*$^{-/-}$ embryos. In *Gbx2*$^{-/-}$ embryos, *Pax9* was downregulated and *Tbx1* expression was downregulated in the pharyngeal ectoderm.

Table 6.1. Summary of RNAScope gene analysis in *Tbx1*$^{-/-}$, *Pax9*$^{-/-}$ and *Gbx2*$^{-/-}$ mutants.

	Downregulated genes		
Mutant	***Tbx1***	***Pax9***	***Gbx2***
***Tbx1*$^{-/-}$**	-	Y	Y
***Pax9*$^{-/-}$**	Y	-	Y
***Gbx2*$^{-/-}$**	Y	Y	-

6.3 *Gbx2* heterozygosity does not modify the *Tbx1*$^{+/-}$ phenotype

Calmont et al. (2009) investigated the interaction between *Tbx1* and *Gbx2* and observed a greater incidence of cardiovascular defects in *Tbx1*$^{+/-}$;*Gbx2*$^{+/-}$ mice compared to *Tbx1*$^{+/-}$ mice. However, the Calmont study used a different *Gbx2* mouse construct than used in this study (discussed in Section 3.7) which resulted in a discrepancy in the incidence of 4th PAA defects in *Gbx2*$^{-/-}$ mice between studies. Therefore, to establish a baseline phenotype on an enriched C57Bl/6 background, *Tbx1*$^{+/-}$ and *Tbx1*$^{+/-}$;*Gbx2*$^{+/-}$ mice were collected at E15.5 and analysed by MRI (Figure 6.4).

Tbx1$^{+/-}$ embryos previously collected in the laboratory, published in Phillips et al. (2019), were included in this dataset giving a total of 21 embryos. Appendix Table A.10 shows the phenotype of each *Tbx1*$^{+/-}$ embryo collected. 67% of *Tbx1*$^{+/-}$ mice (n=21 examined) presented with cardiovascular defects. The defects that occurred correlated with previously reported defects (34, 56, 97, 130-133). An abnormal RSA was most frequent, 43% had a RE-RSA and 24% had a CoRSA. A small fraction had IAA (5%) and VSD (5%) was also observed.

Similar defects were observed in the *Tbx1*$^{+/-}$;*Gbx2*$^{+/-}$ mice (Figure 6.4). Appendix Table A.11 shows the phenotype of each *Tbx1*$^{+/-}$;*Gbx2*$^{+/-}$ embryo collected. *Tbx1*$^{+/-}$;*Gbx2*$^{+/-}$ mice (n=10) had RE-RSA (20%), IAA (10%) and VSD (30%). One *Tbx1*$^{+/-}$;*Gbx2*$^{+/-}$ embryo (10%) had RAA. A defect not observed in *Tbx1*$^{+/-}$ mice collected here, however previously published data shows incidences of RAA in *Tbx1*$^{+/-}$ mice (132).

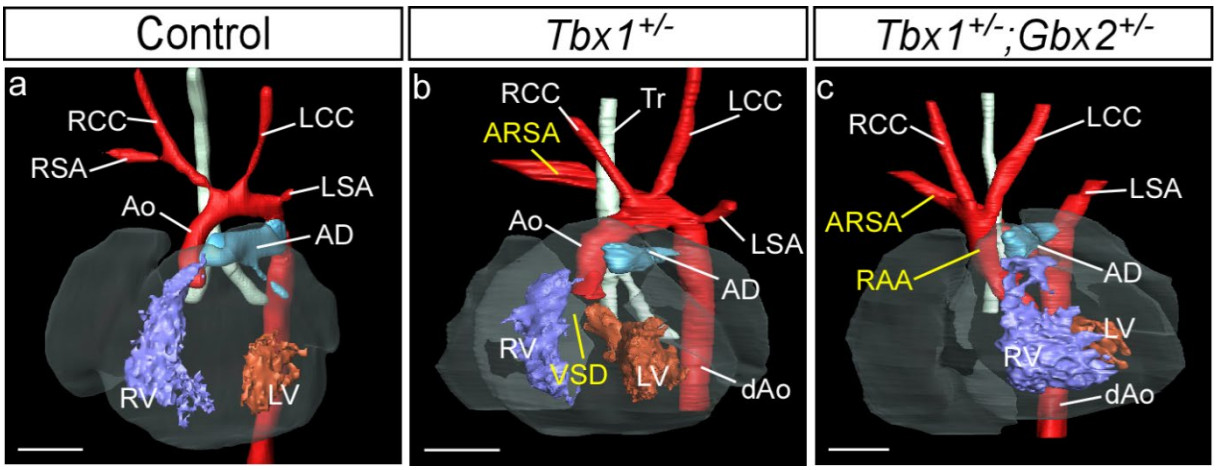

Figure 6.4. Cardiovascular defects present in *Tbx1*$^{+/-}$ and *Tbx1*$^{+/-}$;*Gbx2*$^{+/-}$ embryos at E15.5.

MRI reconstructions of a control embryo (a) showing normal cardiovascular development compared to *Tbx1*$^{+/-}$ (b) and *Tbx1*$^{+/-}$;*Gbx2*$^{+/-}$ (c) embryos. *Tbx1*$^{+/-}$ embryo has an ARSA (b). *Tbx1*$^{+/-}$;*Gbx2*$^{+/-}$ embryo has an ARSA and RAA. Abbreviations: AD, arterial duct; Ao, aorta; ARSA, aberrant right subclavian artery; dAo, dorsal aorta; DORV, double outlet right ventricle; LCC, left common carotid artery; LSA, left subclavian artery; LV, left ventricle; RAA, right aortic arch; RAD, right arterial duct; RCC, right common carotid artery; RSA, right subclavian artery; RV, right ventricle; Tr, trachea; VSD, ventricular septal defect. Scale, 500μm.

Table 6.2 compares the defects present in these mutant embryos. The penetrance of cardiovascular defects in *Tbx1*$^{+/-}$*Gbx2*$^{+/-}$ embryos was slightly lower that *Tbx1*$^{+/-}$ embryos at 50% (n=10 examined). There was a slight increase in the incidence of VSD and IAA in double heterozygotes, but overall there was no significant difference in the penetrance of individual defects. *Gbx2* heterozygosity did not modify the *Tbx1*$^{+/-}$ phenotype.

Table 6.2. Cardiovascular defects in *Tbx1*$^{+/-}$ embryos compared to *Tbx1*$^{+/-}$;*Gbx2*$^{+/-}$ embryos at E15.5.

Statistical significance was analysed by chi-squared for associations. Abbreviations: CV, cardiovascular; CoRSA, cervical right subclavian artery; IAA, interrupted aortic arch; RE-RSA, retro-oesophageal right subclavian artery; RAA, right aortic arch; VSD ventricular septal defect.

	Frequency					
Genotype	**CV Defect**	**VSD**	**IAA**	**RAA**	**RE-RSA**	**CoRSA**
***Tbx1*$^{+/-}$** n=21	14 (67%)	2 (10%)	1 (5%)	0	9 (43%)	5 (24%)
***Tbx1*$^{+/-}$;*Gbx2*$^{+/-}$** n=10	5 (50%)	3 (30%)	1 (10%)	1 (10%)	2 (20%)	0

6.4 *Gbx2* heterozygosity does not modify the *Tbx1*$^{+/-}$;*Pax9*$^{+/-}$ phenotype

Previous work in the laboratory showed that *Pax9* heterozygosity modified the *Tbx1*$^{+/-}$ phenotype, significantly increasing the incidence of IAA (134). *Tbx1*$^{+/-}$;*Pax9*$^{+/-}$;*Gbx2*$^{+/-}$ embryos were collected and compared to *Tbx1*$^{+/-}$;*Pax9*$^{+/-}$ mice to determine the effect of *Gbx2* heterozygosity (Figure 6.5).

Tbx1$^{+/-}$;*Pax9*$^{+/-}$ embryos previously collected in the laboratory, published in Phillips et al. (2019), were included in this dataset. All *Tbx1*$^{+/-}$;*Pax9*$^{+/-}$ embryos (n=24) had cardiovascular defects (Table Appendix A.12). The most frequent defects were IAA (63%) and defects to the RSA, namely RE-RSA (42%) and CoRSA (54%). RAA was also present in 8% of embryos. All *Tbx1*$^{+/-}$;*Pax9*$^{+/-}$;*Gbx2*$^{+/-}$ embryos (n=8) had cardiovascular defects (Appendix Table A.13) and shared the same defects as *Tbx1*$^{+/-}$;*Pax9*$^{+/-}$ embryos (Figure 6.5).

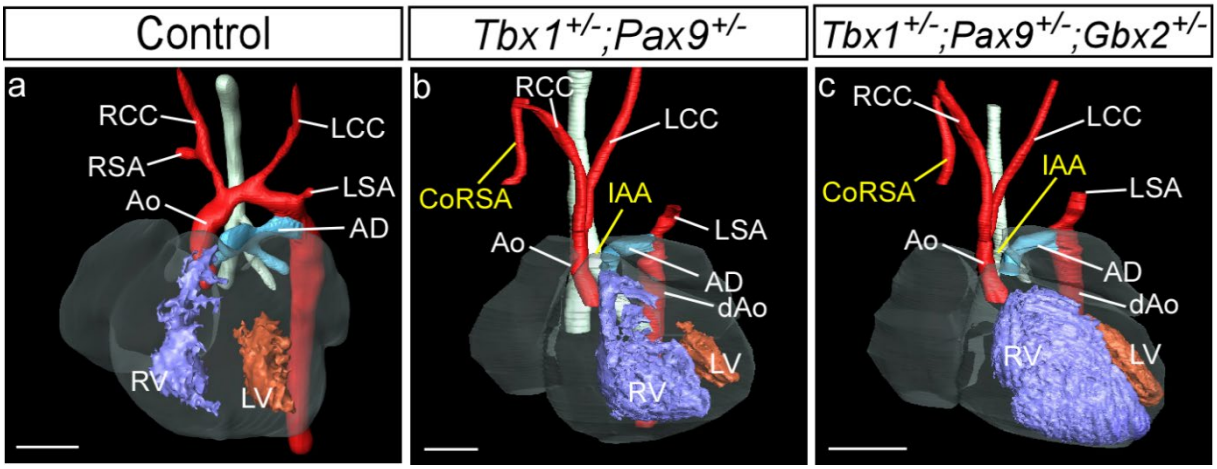

Figure 6.5. Cardiovascular defects present in *Tbx1*$^{+/-}$;*Pax9*$^{+/-}$ and *Tbx1*$^{+/-}$;*Pax9*$^{+/-}$;*Gbx2*$^{+/-}$ embryos at E15.5.

MRI reconstructions of a control embryo (a) showing normal cardiovascular development compared to *Tbx1*$^{+/-}$;*Pax9*$^{+/-}$ (b) and *Tbx1*$^{+/-}$;*Pax9*$^{+/-}$;*Gbx2*$^{+/-}$ (c) embryos. The mutant embryos (b, c) have the same cardiovascular defects with a CoRSA and IAA. Abbreviations: AD, arterial duct; Ao, aorta; ARSA, aberrant right subclavian artery; CoRSA, cervical right subclavian artery; dAo, dorsal aorta; DORV, double outlet right ventricle; IAA, interrupted aortic arch; LCC, left common carotid artery; LSA, left subclavian artery; LV, left ventricle; RAD, right arterial duct; RCC, right common carotid artery; RSA, right subclavian artery; RV, right ventricle; Tr, trachea. Scale, 500μm.

Table 6.3 summarises the cardiovascular defects present in *Tbx1*$^{+/-}$;*Pax9*$^{+/-}$ and *Tbx1*$^{+/-}$;*Pax9*$^{+/-}$;*Gbx2*$^{+/-}$ embryos. There was no significant difference in the incidence of cardiovascular defects between these mutants. *Gbx2* heterozygosity did not modify the *Tbx1*$^{+/-}$;*Pax9*$^{+/-}$ phenotype.

Table 6.3. Cardiovascular defects present in *Tbx1*$^{+/-}$;*Pax9*$^{+/-}$ embryos compared to *Tbx1*$^{+/-}$;*Pax9*$^{+/-}$;*Gbx2*$^{+/-}$ embryos at E15.5.

Statistical significance was analysed by chi-squared for associations. Abbreviations: CV, cardiovascular; CoRSA, cervical right subclavian artery; IAA, interrupted aortic arch; RE-RSA, retro-oesophageal right subclavian artery; RAA, right aortic arch, VSD; ventricular septal defect.

	Frequency					
Genotype	**CV Defect**	**VSD**	**IAA**	**RAA**	**RE-RSA**	**CoRSA**
***Tbx1*$^{+/-}$;*Pax9*$^{+/-}$** n=24	24 (100%)	7 (29%)	15 (63%)	2 (8%)	10 (42%)	13 (54%)
***Tbx1*$^{+/-}$;*Pax9*$^{+/-}$;*Gbx2*$^{+/-}$** n=8	8 (100%)	3 (38%)	4 (50%)	1 (13%)	5 (63%)	2 (25%)

6.5 Investigating the interaction of TBX1 and PAX9 with the *Gbx2* conserved region

Phenotyping data and gene expression analysis suggest that *Tbx1* and *Pax9* both act upstream of *Gbx2* in 4th PAA morphogenesis. The human and mouse *GBX2* sequences were aligned to analyse homology between the sequences. This identified a highly conserved (99%) region approximately 2kb downstream of exon 2. The *GBX2* gene was analysed using the MultiTF (https://multitf.dcode.org/) and JASPAR database (http://jaspar.genereg.net/) to screen for TBX (T-BE) and PAX (PAX-BE) binding elements. Analysis identified three PAX-BEs and one T-BE within the conserved region (Figure 6.6).

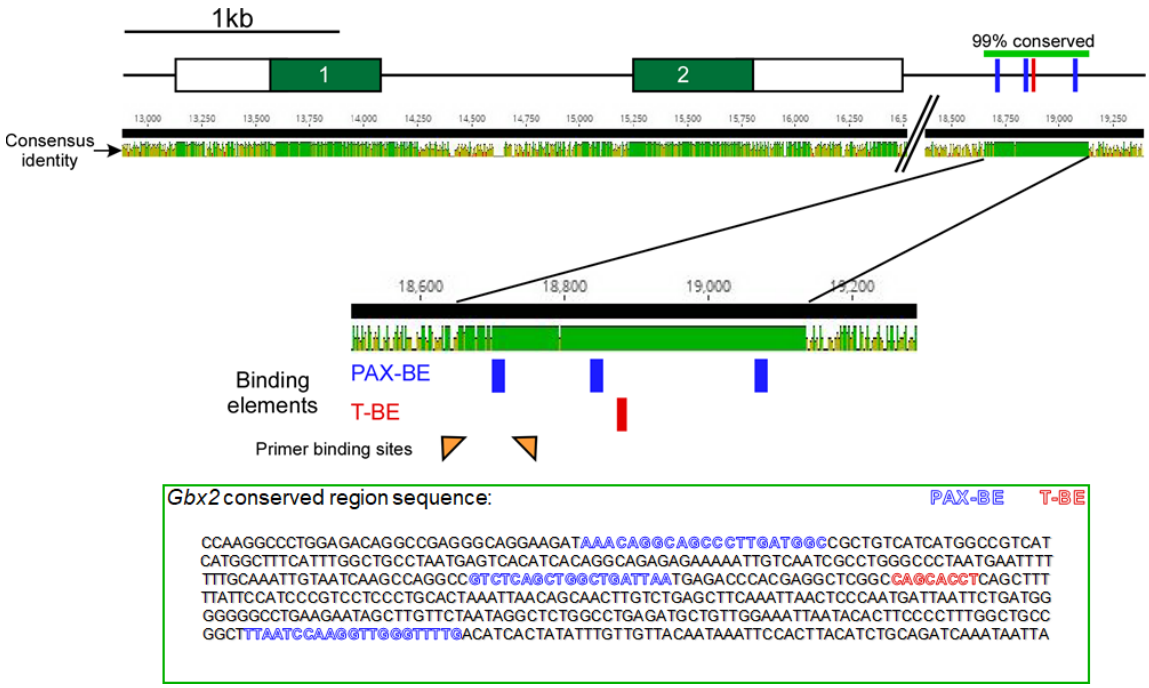

Figure 6.6. Schematic diagram of the *GBX2* conserved region.

Alignment of the human and mouse *GBX2* gene sequences showing conservation between the sequences. The conserved region is located approximately 2kb downstream of exon 2 and is 99% conserved. This region is ~500bp and possesses one TBX and three PAX binding elements. The sequence of the *Gbx2* conserved region is shown with the potential TBX and PAX binding sites. Abbreviations: kb, kilobase pair.

A luciferase assay was used to determine if TBX1 and PAX9 could activate the *GBX2* conserved region. This region was cloned into a luciferase expression vector. In this construct (referred to as GBX2-LUC), luciferase is downstream of a minimal promoter, under the control of the *Gbx2* enhancer region. Upon activation of this promoter, luciferase expression is increased. GBX2-LUC was transfected into JEG3 cells together with a *TBX1* and/or a *PAX9* cDNA expressing plasmid. The plasmid backbone (pcDNA3.1) was used as a control.

Luciferase reporter constructs containing a synthetic TBX (2xTtkGl2) or PAX (BMP4) binding site were used as a positive control. Both positive controls show a significant increase in luciferase activity (Figure 6.7a-b). A luciferase reporter lacking TBX and PAX binding sites (tkGl2) was used as a negative control. There was no significant change in luciferase activity with the addition of the TBX1 or PAX9 cDNA expressing plasmids in the negative control (Figure 6.7c).

Co-transfecting cells with the GBX2-LUC construct and TBX1 did not cause a significant increase in luciferase activity. Co-transfection of PAX9 caused a significant

increase in luciferase expression showing that PAX9 is able to bind and activate the conserved region. With the addition of TBX1 and PAX9, luciferase expression did not differ from the control. This suggests that TBX1 is repressing the PAX9-induced activation of *GBX2.*

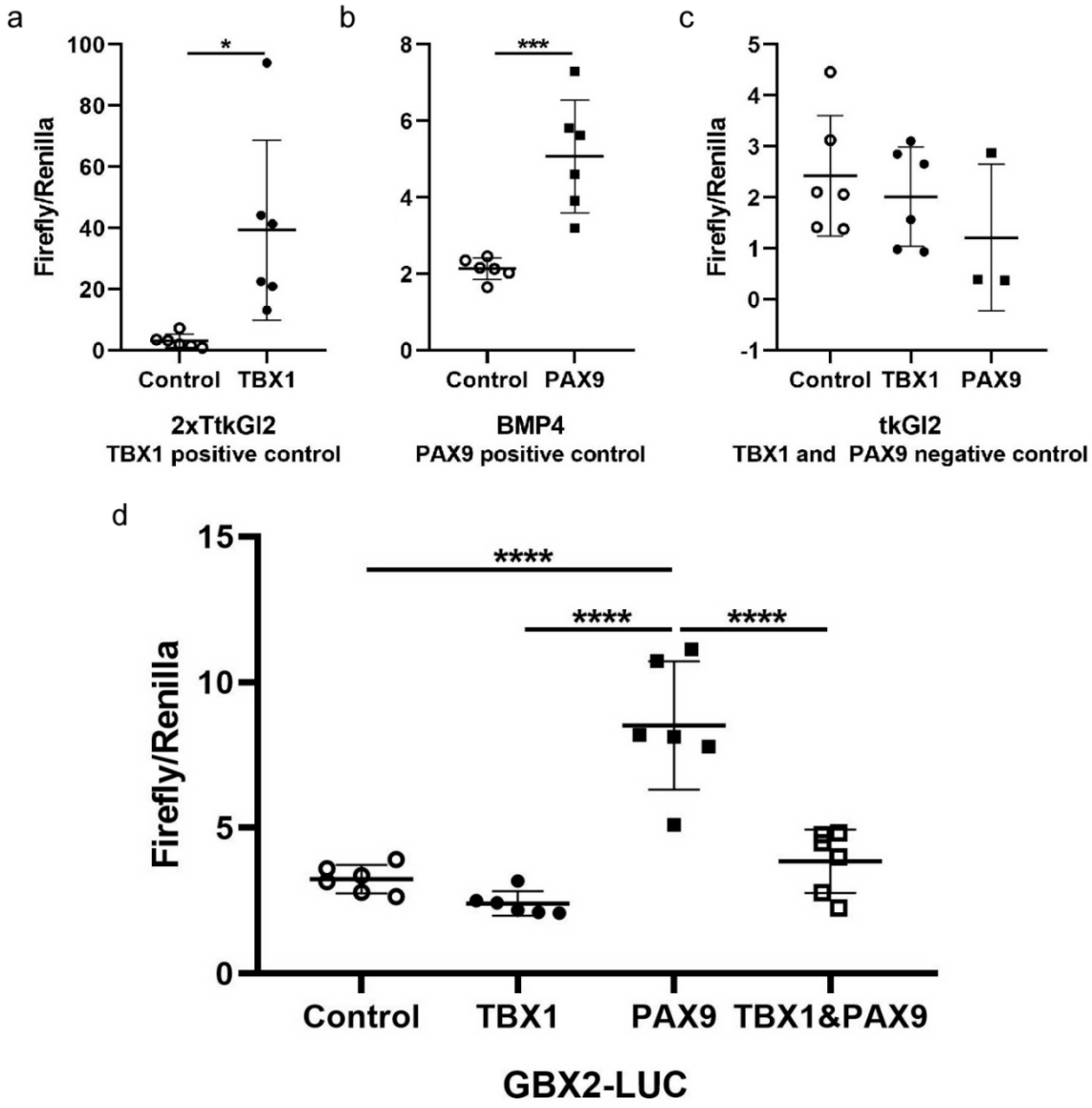

Figure 6.7. PAX9 activates the *GBX2* conserved region *in vitro*.

(a) The 2xTtkGl2 construct containing a synthetic T-BE was used as a TBX1 positive control (n=6). (b) The BMP4 construct was used as a PAX9 positive control (n=6). (c) The tkGl2 construct lacking both T-BEs and PAX-BEs was used as a negative control for TBX1 (n=6) and PAX9 (n=3). (d) TBX1 did not activate the GBX2-LUC construct. PAX9 significantly increased luciferase expression, confirming activation of the *GBX2* region. This activation was repressed with the combined addition of TBX1 and PAX9. Each plot point represents an independent experiment, each performed in triplicate. Statistical significance was calculated using an unpaired two-tail T-test (a, b) or a one-way ANOVA (c, d). *p<0.05**; ***p<0.001; ****p<0.0001.

The luciferase assays confirm activation of *GBX2* by PAX9. While TBX1 did not activate this region, *in vivo* phenotyping and expression data show the interaction between *Tbx1* and *Gbx2*. Therefore, the interaction of *Tbx1* with *Gbx2* cannot be disregarded. ChIP was used to investigate the interaction of Tbx1 and Pax9 with the *Gbx2* conserved region *in vivo.* Immunoprecipitation was carried out using antibodies against Tbx1, Pax9 and acetylated histone 3 lysine 27 (H3K27ac).

Chromatin regulators are key in the regulation of transcription. The state of chromatin determines the accessibility of a region of DNA, thereby determining its activation by transcription factors. Histone modifications and regulators control this state in developmental programs to maintain specific gene expression during embryogenesis. Acetylation of H3K27 marks active promoters and enhancers (201) and enrichment of H3K27ac would show that the *Gbx2* conserved region is in the open chromatin state.

Wild type CD1 embryos were collected at E10.5, pooled in groups of four, then briefly fixed in formaldehyde to crosslink the DNA and proteins. The chromatin was sonicated to 200-500bp fragments and a sample containing the total chromatin (input) was collected. Immunoprecipitation was carried out on the remaining sample using protein G beads and with antibodies raised against H3K27ac, Tbx1 or Pax9. A rabbit immunoglobulin (IgG) and a negative control sample without any antibody were also used. The immunoprecipitated samples were reverse crosslinked and the DNA was purified. The DNA was assessed by qPCR using primers designed to target the *Gbx2* conserved region (Figure 6.8).

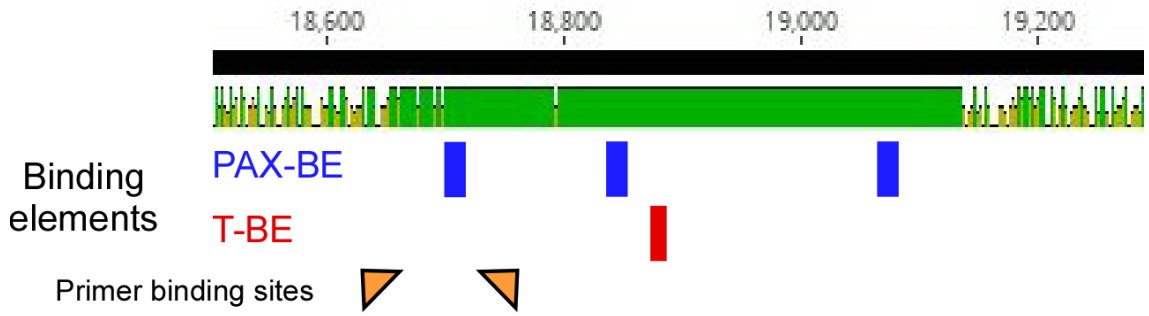

Figure 6.8. Location of primer binding sites used in the ChIP assay to target the *Gbx2* conserved region by qPCR.

Each sample was normalised to the input (total chromatin) sample and plotted as percentage of input and compared to the IgG negative control which represents background antibody binding. The *Gbx2* conserved region was significantly ($p<0.05$, one-way ANOVA corrected for multiple comparisons using the Holm-Šídák test) enriched for H3K27ac, Tbx1 and Pax9 compared to background IgG (Figure 6.9).

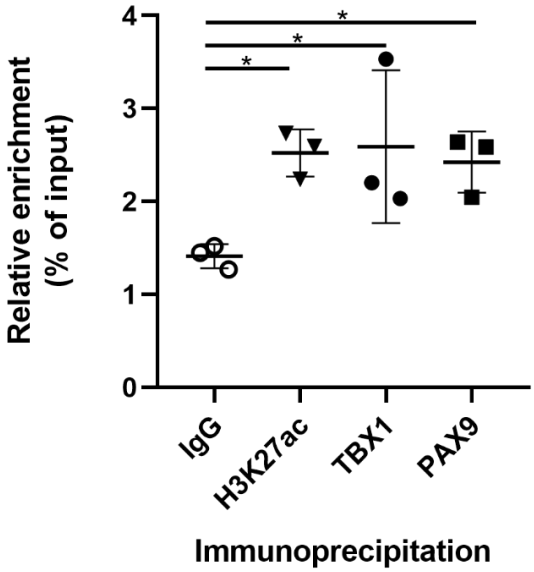

Figure 6.9. Chromatin immunoprecipitation of the *Gbx2* conserved region using E10.5 embryos.

DNA was purified from immunoprecipitated samples and analysed by qPCR using primers designed to target the *Gbx2* conserved region. IP of IgG was used as a negative control to show background antibody binding. The conserved region was significantly enriched for H3K27ac, TBX1 and PAX9 compared to IgG. Each plot point represents a biological replicate with four pooled E10.5 embryos in each experiment. Statistical analysis was calculated using a one-way ANOVA corrected for multiple comparisons using the Holm-Šídák test. *$p<0.05$.

The ChIP assay was repeated using CD1 embryos collected at E9.5, with nine embryos pooled in each experiment. The conserved region did not show significant enrichment for H3K27ac, TBX1 or PAX9 above background IgG (Figure 6.10).

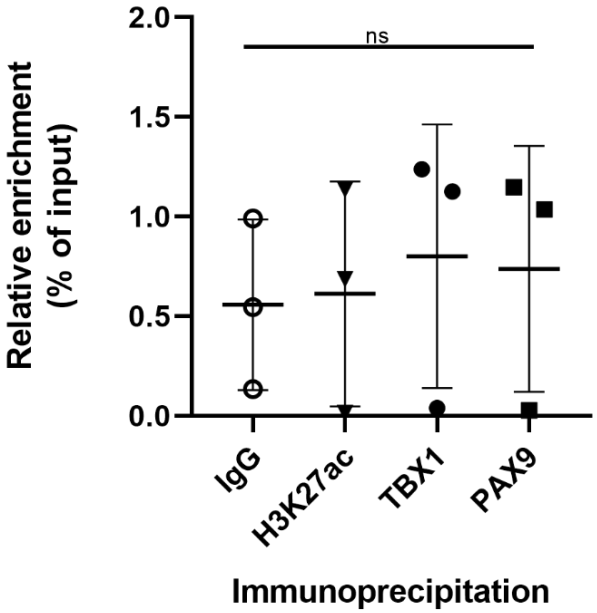

Figure 6.10. Chromatin immunoprecipitation of the *Gbx2* conserved region using E9.5 embryos.

DNA was purified from immunoprecipitated samples and analysed by qPCR using primers designed to target the *Gbx2* conserved region. IP of IgG was used as a negative control to show background antibody binding. The conserved region was not significantly enriched for H3K27ac, TBX1 or PAX9. Each plot point represents a biological replicate with nine pooled E9.5 embryos in each experiment. Statistical analysis was calculated using a one-way ANOVA corrected for multiple comparisons using the Holm-Šídák test. Abbreviations: ns, no significance.

As the expression of DNA-binding proteins varies in different tissues and stages of development, the amount of target protein present in IPs also varies. A large amount of tissue is needed in ChIP to detect a signal and the reason for low enrichment relative to total chromatin could be due to the small amount of chromatin present in the E9.5 sample. Embryos were pooled in each experiment, however the chromatin sheared from the E9.5 sample was low. At E10.5, there was 20.1-25.1µg of chromatin used for each IP whereas the chromatin available for each IP at E9.5 was lower at 10.1-12.1µg. The low signal observed in the E9.5 ChIP assay could be due to low levels of chromatin and further optimisation of this experiment is required to reliably investigate the conserved region at E9.5.

6.6 Discussion

This chapter aimed to investigate the potential *Tbx1-Pax9-Gbx2* genetic network in cardiovascular development. The first aim was to determine co-expression of these transcription factors in the PA and analyse gene expression in null mutants. Analysis of wild type embryos showed *Tbx1* expression within the pharyngeal endoderm, ectoderm and mesoderm, as previously reported (128, 129). This expression overlapped with *Pax9* and *Gbx2* in the pharyngeal endoderm at the time of 4th PAA specification at E9.5.

The endoderm is the only tissue within the PA in which all of these genes are expressed and, as *Tbx1*, *Pax9* and *Gbx2* mutants share overlapping 4th PAA defects, it is possible that these genes share a network in the pharyngeal endoderm for 4th PAA morphogenesis. Published studies (134) and the data presented in Chapter 5 suggest that *Tbx1* and *Gbx2* interact cell-autonomously with *Pax9* in the pharyngeal endoderm. This network is likely vast and involves the interaction of other genes. For example *Fgf8*, which has also been shown to interact with *Tbx1* and *Gbx2*, was downregulated specifically in the endoderm of *Tbx1*$^{-/-}$ mice (56, 166). Gene expression within the endoderm could be functioning as a signalling centre to interact with other tissue types required in PAA morphogenesis. *Tbx1* signals emanating from the endoderm are transduced via *Fgf8* to the mesenchyme, in which the PAA reside (56). The time of *Tbx1*, *Pax9* and *Gbx2* endoderm expression coincides with NCC migration into the PA. All of these genes are all needed for normal NCC behaviour (133, 135, 166), and could signal from the endoderm to affect NCC function.

The downregulation of *Pax9* and *Gbx2* in *Tbx1*$^{-/-}$ mice observed in the RNAScope analysis reflects that observed in previously published transcriptome analysis of *Tbx1*$^{-/-}$ embryos by Ivins et al. (2005). Analysis of *Pax9*$^{-/-}$ embryos showed the reduced expression of *Tbx1* in the epithelial layers of the PA. *Pax9* and *Tbx1* were each downregulated in *Tbx1*$^{-/-}$ and *Pax9*$^{-/-}$ embryos respectively, which supports the deduction that *Tbx1* and *Pax9* act in a non-hierarchal pathway (134).

The Calmont (2009) study showed an interaction between *Tbx1* and *Gbx2* in cardiovascular development, observing an increase in the penetrance of defects in *Tbx1*$^{+/-}$*;Gbx2*$^{+/-}$ mice compared to *Tbx1*$^{+/-}$ mice. This was not apparent, however, in the phenotyping data collected here, in which 67% of *Tbx1*$^{+/-}$ mice had cardiovascular defects compared to 50% of *Tbx1*$^{+/-}$*;Gbx2*$^{+/-}$ mice. Likewise, the penetrance of

individual defects, including IAA and RAA, did not significantly differ between these genotypes in this study showing that *Gbx2* heterozygosity did not modify the *Tbx1*$^{+/-}$ phenotype.

However, the 67% penetrance in the cardiovascular defects in *Tbx1*$^{+/-}$ embryos at E15.5 collected in this study was notably higher than the average reported penetrance in published data (29%). This difference could be due to deviations in genetic background between the studies (136). Table 6.4 summarises the penetrance of defects in *Tbx1*$^{+/-}$ and *Tbx1*$^{+/-}$*;Gbx2*$^{+/-}$ mice collected in this study and in published data in late development and neonatal stages. The higher baseline penetrance in *Tbx1*$^{+/-}$ mice collected in this study affects the interpretation of results when comparing to *Tbx1*$^{+/-}$*;Gbx2*$^{+/-}$ mutants. A similar penetrance of defects was observed in *Tbx1*$^{+/-}$*;Gbx2*$^{+/-}$ mice in this study (50%, n=10 examined) and the Calmont study (59%, n=22 examined). However when comparing to this baseline *Tbx1*$^{+/-}$ phenotype at 67%, there is no significant change which suggests that *Gbx2* heterozygosity does not modify the *Tbx1*$^{+/-}$ phenotype.

Table 6.4. Penetrance of cardiovascular defects in *Tbx1*$^{+/-}$ and *Tbx1*$^{+/-}$;*Gbx2*$^{+/-}$ mice E15.5-P2 in published data.

	Reference	Penetrance of CV Defects
***Tbx1*$^{+/-}$**	Calmont et al., 2009	26% (n=19)
	Vitelli et al., 2002	27% (n=41)
	Randall et al., 2009	24% (n=25)
	Guris et al., 2006	33% (n=18)
	Ryckebusch et al., 2010	25% (n=36)
	Papangeli and Scambler, 2012	29% (n=17)
	Zhang et al., 2008	38% (n=29)
	Average	29% (n=185)
	This study	67% (n=21)
***Tbx1*$^{+/-}$;*Gbx2*$^{+/-}$**	Calmont et al., 2009	59% (n=22)
	This study	50% (n=10)

Together with the analysis of *Tbx1*$^{+/-}$;*Pax9*$^{+/-}$;*Gbx2*$^{+/-}$ triple heterozygotes, which showed no difference to *Tbx1*$^{+/-}$;*Gbx2*$^{+/-}$ mice, it was concluded that *Gbx2* heterozygosity does not modify the phenotype. This correlates with the gene expression analysis in which *Tbx1* expression was unaffected in the pharyngeal endoderm of *Gbx2*$^{-/-}$ embryos suggesting that *Tbx1* acts upstream of *Gbx2.*

With the conclusion that *Gbx2* is a shared target of *Tbx1* and *Pax9,* the *Gbx2* gene was screened, which identified highly conserved T-BEs and PAX-BEs. The *Pax9-Gbx2* interaction apparent in phenotyping data was reflected in luciferase assays, while Tbx1 did not activate *Gbx2* in this assay. However, this assay only indicates the activation of *Gbx2*, not binding of this region. Hence the lack of activation by Tbx1 in the luciferase assay does not necessarily show a lack of Tbx1 binding.

The ChIP assay showed significant enrichment of the *Gbx2* conserved region for Tbx1 and Pax9 suggesting that these proteins could bind *Gbx2*. Likewise, this region was also significantly enriched for H3K27ac, a histone modification associated with active enhancers and open state chromatin (201). This suggests that the *Gbx2* conserved region is available for binding during the time of PAA formation and remodelling at E10.5.

However, while the statistical analysis suggests that *Gbx2* was significantly enriched for Tbx1, Pax9 and H3K27ac, the level of H3K27ac enrichment was arguably low for a histone modification enzyme. Therefore, the experiment does not conclusively show direct regulation of the *Gbx2* conserved region. This low level of enrichment could be explained due to low concentration of chromatin available, as a large amount of tissue is required to generate a signal.

Interestingly, Fulcoli et al. (2016) observed that Tbx1 was predominantly associated with lowly transcribed genes and low H3K27ac enrichment. *Tbx1* is an early regulator of histone modification and was shown positively regulated the methylation of histone 3 at lysine 4 (H3K4me1), a histone modification that marks primed enhancers (202-204). *Tbx1* acts as a poised enhancer to bind and keep DNA in the open state to then recruit other transcription or regulatory factors to consequently alter downstream transcription. For example, Tbx1 recruits P53 to *Gbx2* to modulate *Gbx2* expression through histone methylation (167). The active Tbx binding element identified by Caprio et al. (2014) is located within the *Gbx2* conserved region approximately 2kB downstream of exon 2. The T-BE and PAX-BEs identified in this study were in proximity, and it is tempting to speculate that *Tbx1* affects the state of local chromatin. In this context, Tbx1 could bind *Gbx2* and modify the chromatin to allow the binding of Pax9.

In the luciferase assay, Tbx1 prevented the activation of *Gbx2* by *Pax9* suggesting that Tbx1 represses Pax9 function. However, during cardiovascular development at mid-embryogenesis, gene expression is highly dynamic with the constant switching between gene activation and suppression. As Tbx1 regulates histone modification, it could have a potential role in controlling the timely activation of *Gbx2* by Pax9.

Pax9 has also been implicated in altering chromatin structure, as loss of Pax9 in mouse embryonic fibroblasts decreased trimethylation of histone 3 lysine 9 (H3K9me3) in heterochromatin (205). H3K9me3 represses repetitive elements and non-coding

regions of the genome (206). This histone modification has also been shown to influence cell fate by silencing lineage-inappropriate genes (206). Pax9 could modulate heterochromatin structure and have a potential role in determining cell fate. Additionally, Pax9 could have a role in the activation and expression of *Gbx2* through the interaction with the Tbx1-P53 complex.

While further work is required to determine if Tbx1 and Pax9 directly regulate the *Gbx1* conserved region, the luciferase assays and *in vivo* work presented in this chapter suggest the presence of a *Tbx1-Pax9-Gbx2* network in the morphogenesis of the 4th PAA.

Chapter 7. Final Discussion

7.1 Summary of findings and future work

The formation and remodelling of the PAA is highly complex, involving precise genetic interactions across multiple tissue types. This process is susceptible to genetic mutations and such perturbations result in life threatening CHDs. 22q11DS is the most common microdeletion in humans, with *TBX1* mutations identified as the leading cause of cardiovascular defects, however patients present with a varied phenotype (82, 207). Identifying the genetic interactors of *Tbx1* in cardiovascular development, could elucidate the modifiers of 22q11DS. Investigating the genetic networks and mechanisms underpinning cardiovascular and PAA morphogenesis is imperative in aiding the understanding in the manifestation of CHDs.

7.1.1 Gbx2 as a modifier of 22q11 deletion syndrome

To date, *GBX2* mutations have not been implicated in human patients with CHDs, however, studies have shown that *Gbx2* is required in cardiovascular development. The work in this thesis confirmed the necessity of *Gbx2*, thoroughly defining the null phenotype, and identified previously unreported defects in *Gbx2*$^{-/-}$ mice. Analysis revealed a new role for *Gbx2* in L-R patterning. These defects, including RPI and RAI, occurred simultaneously with 4th PAA and conotruncal abnormalities, however the mechanism by which *Gbx2* is involved in L-R patterning is unclear. *Gbx2* functions independent of *Pitx2* in L-R patterning. Analysis of the expression of other components of the complex nodal signalling pathways could reveal at which stage *Gbx2* is required. A large portion of *Gbx2*$^{-/-}$ embryos appeared to die prior to E8.5 suggesting a role of *Gbx2* in early embryogenesis. The early loss of *Gbx2*$^{-/-}$ embryos is likely due to abnormalities at gastrulation, during which *Gbx2* is expressed in all three germ layers (164).

The *Gbx2*$^{-/-}$ phenotype is varied between individual embryos and shows incomplete penetrance, a feature present in other mouse models including *Tbx1*$^{+/-}$ (53, 97, 130-134) and *Fgf8* hypomorphic mutant mice (61). This is not unlike the 22q11DS phenotype in which the penetrance cardiovascular defects is incomplete, present in approximately 75% of patients (84). The recovery of the 4th PAA phenotype (130) can

explain the incomplete penetrance in *Gbx2*$^{-/-}$ mice at later stages of development, but does not explain the 86% penetrance at E10.5. This incomplete penetrance is potentially due to genetic background. As different genetic strains possess genetic modifiers which can alter the phenotype (136).

Frequent defects in *Gbx2*$^{-/-}$ mice are RAA, aberrant subclavian arteries and DORV, all of which occur in 22q11DS, albeit at a lower frequency than IAA (85-89). IAA is one of the most commonly observed defects observed in 22q11DS (85). In this respect, *Gbx2*$^{-/-}$ mice do not present with the hallmark 22q11DS phenotype. Nonetheless, the *Gbx2*$^{-/-}$ phenotype still overlaps with the *Tbx1* and 22q11DS phenotype.

7.1.2 The Pax9-Gbx2 interaction in the pharyngeal endoderm

Pax9 is postulated as a more likely modifier of 22q11DS due to its strong interaction with *Tbx1* and the presentation of IAA in *Tbx1*$^{+/-}$*;Pax9*$^{+/-}$ and *Pax9*$^{-/-}$ mice (134). *Pax9* heterozygosity significantly modified the *Gbx2*$^{-/-}$ phenotype, increasing the severity and penetrance of defects. The presentation of *Pax9*$^{-/-}$ typical defects (IAA, absent common carotid arteries and thymus defects) in *Gbx2*$^{-/-}$*;Pax9*$^{+/-}$ embryos show that *Pax9* is a strong genetic modifier.

The *Pax9*$^{-/-}$ phenotype is relatively consistent between individual embryos and shows complete penetrance, therefore the modification with the simultaneous heterozygous deletion of *Gbx2* was more subtle. Together with the less pronounced downregulation of *Pax9* in *Gbx2*$^{-/-}$ embryos, phenotyping data suggests *Pax9* and *Gbx2* function hierarchically. *Pax9* likely acts upstream of *Gbx2* and *Gbx2* can feedback to act on *Pax9.*

This study validated the novel *Pax9Cre* allele, utilising this mouse to investigate the deletion of *Gbx2* from the pharyngeal endoderm in the context of *Pax9* heterozygosity. The presence of 4th PAA defects in *Pax9Cre;Gbx2*$^{f/-}$ embryos confirmed the cell-autonomous interaction between *Pax9* and *Gbx2* within this tissue, consistent with the *Tbx1-Pax9* interaction in the pharyngeal endoderm (134). The phenotype in the *Pax9Cre;Gbx2*$^{f/-}$ mutants could be a result of the *Pax9-Gbx2* interaction or the endoderm-specific loss of these genes. It is most likely a combined effect, although the individual role of *Gbx2* in the pharyngeal endoderm is yet to be determined. The

deletion of *Gbx2* from this tissue should be investigated using alternative pharyngeal endoderm-specific *Cre* lines, such as *Sox17Cre* (200).

Gbx2 is expressed in the pharyngeal endoderm and ectoderm and in *Pax9*$^{-/-}$ embryos, *Gbx2* expression was reduced in both tissues. This raises the question as to how the deletion of *Pax9* from the endoderm affects *Gbx2* expression in the ectoderm which would require extracellular signalling pathways.

Pax9 activity is required for the expression of multiple components of signalling pathways during the formation of the palate. The cleft palate in *Pax9*$^{-/-}$ mice occurs with the downregulation of Wnt signalling (208). The cleft palate phenotype was partially rescued through the inhibition of a Wnt antagonist. This suggests that, in normal development, *Pax9* functions through Wnt signalling during palate formation.

A similar effect was observed with Shh, Bmp and Fgf signalling. *Shh*, *Bmp4* and *Fgf10* expression in the palatal mesenchyme and epithelium are dependent on *Pax9* activity and are reduced in *Pax9*$^{-/-}$ mice (209). *Pax9* acts via Shh, Bmp and Fgf signalling to regulate expression of other transcription factors required in palate formation, such as *Osr2* (209, 210). These signalling pathways are all expressed in the pharyngeal endoderm, required for patterning of the PA and PAA (61, 63, 197, 211). *Tbx1* uses Fgf signalling to contact the mesoderm during PAA formation (56). *Pax9* relies on signalling pathways for contributing to organogenesis and development. In this context, *Pax9* expression in the pharyngeal endoderm may regulate *Gbx2* expression in the pharyngeal ectoderm via these signalling pathways.

The downregulation of *Gbx2* in both epithelial layers of *Pax9*$^{-/-}$ and *Tbx1*$^{-/-}$ embryos (133) indicates that *Gbx2* expression in both tissues contributes to PAA morphogenesis. The homozygous deletion of *Gbx2* from the ectoderm resulted in a similar penetrance of 4th PAA defects at E10.5 compared to the *Pax9Cre;Gbx2*$^{f/-}$ mutants in this study (133). The Calmont study (2009), however, failed to analyse conditional ectoderm mutants at later stages of development. To completely differentiate the tissue specific-role of *Gbx2*, conditional ectoderm and endoderm mutants need to be analysed and compared at late embryogenesis.

7.1.3 The Tbx1-Pax9-Gbx2 network

While *Gbx2* heterozygosity does not result in a strong modification of the *Tbx1*$^{+/-}$ phenotype, this does not negate the interaction between these genes. The downregulation of *Gbx2* in *Tbx1*$^{-/-}$ and *Pax9*$^{-/-}$ embryos suggests the interaction of these genes with *Gbx2* as a common downstream target. This is reflective of the non-hierarchal relationship of *Tbx1* and *Pax9* as both can independently interact with *Gbx2.*

The function of *Gbx2* depends on its interaction with downstream target genes and pathways. Using chromatin immunoprecipitation and direct sequencing on a human cell line, Roeseler et al. (2012) identified 286 potential target genes of *Gbx2*. Among the top candidate downstream targets were members of the Slit-Robo and Notch signalling pathway, both of which are needed in NCC migration (57, 212). *Robo1* and *Slit2* expression were reduced in *Gbx2*$^{-/-}$ embryos (133, 213). The implication of these pathways as a potential downstream target of *Gbx2* is consistent with the presentation of NCC migration defects in *Gbx2* mutant embryos (133, 166).

The combined transcriptome analysis of *Tbx1*$^{-/-}$ and *Pax9*$^{-/-}$ embryos highlighted 342 shared differentially regulated genes and resulted in the identification of *Gbx2* as a shared target (134). The transcriptome analysis of *Gbx2*$^{-/-}$ embryos would be highly informative in reviewing downstream targets of this gene and to further investigate the *Tbx1-Pax9-Gbx2* network.

7.1.4 The sensitivity of the 4th pharyngeal arch artery

It is worth commenting on the heightened sensitivity of the 4th PAA that occurs with genetic mutations and deletions. In mouse models investigating the genetic factors in the development of the PAA, it is primarily the 4th PAA that is affected. This is also true for *Tbx1*, *Pax9* and *Gbx2* mutants which show hypoplastic or absent 4th PAA. The 4th PAA appears to be more susceptible to genetic perturbations, although it is unknown as to why this is the case.

Each PAA forms a specific region of the aortic arch, the cranial PAA (1st and 2nd) regress, while the caudal PAA (3rd, 4th and 6th) persist and asymmetrically remodel; with the left and right 4th PAA forming part of the arch and RSA respectively. The fate of each PAA will be programmed early in embryogenesis, dependent on gene expression within the developing PA.

Transcriptome analysis showed distinct genetic profiles between the cranial and caudal PAA. For example, the caudal PAA were enriched for *Myocd*, a transcription factor that activates smooth muscle differentiation (214). Further investigation showed that smooth muscle cells fail to form around the 1st and 2nd PAA, while the caudal PAA, which form the mature aortic arch structure, were clearly invested in smooth muscle cells (214). The specific gene expression within each PA affects the formation of their respective PAA.

This is apparent in the mechanism of lumen formation between the cranial and caudal PAA. The endothelial cell lumen of the cranial PAA arises through angiogenesis while the caudal PAA are thought to form through *de novo* vasculogenesis (36). The PA show strict segmentation, with regionalised gene expression not only differing between cranial and caudal regions, but also between individual arches and the tissues of the PA (47).

The susceptibility of the 4th PAA has been noted throughout the literature, suggesting that there are also programmed differences between the 3rd, 4th and 6th caudal PAA. This heterogeneity in the fate of the different PAA is in part due to cellular differences. The smooth muscle layer of the PAA is derived from NCC that migrate into the PA (23). The composition of the 4th PAA smooth muscle and its derivatives differs from other vessel segments in that is has reduced actin and elastin content (215). There is no clear data proving the link between smooth muscle composition and predisposition to development defects of the 4th PAA however, 4th PAA hypoplasticity in *Tbx1*$^{+/-}$ mice occurs due to reduced smooth muscle formation (130). Additionally, the recovery of the 4th PAA is a result of the delayed differentiation of smooth muscle cells (130).

Molin et al. (2002) found that the smooth muscle composition of a vessel can affect its response to genetic perturbations. While the 4th PAA persists to form part of the mature aortic arch system, the right 6th PAA, carotid ducts and distal region of the right dorsal aorta regress. This regression is preceded by an increase in apoptosis in the mesenchyme surrounding the PAA. The apoptosis spreads to the smooth muscle layer of the regressing vessels (33). Molin et al. (2002) observed regression of the 4th PAA and the abnormal persistence of the right dorsal aorta in *Tgf-β2* knockout mice. This coincided with increased apoptosis around the 4th PAA segments and reduced apoptosis in the smooth muscle of the right dorsal aorta. The smooth muscle of the dorsal aorta is mesoderm-derived, unlike the NCC-derived smooth muscle of the PAA

(216). The forms of smooth muscle vary in their response to growth modifiers such as Tgf-β proteins (217) which will affect their response to developmental cues and genetic mutations.

Interestingly, *Tbx1*$^{+/-}$ mice show a low penetrance of IAA compared to ARSA while in *Tbx1*$^{+/-}$;*Pax9*$^{+/-}$ mice there is a shift towards an IAA dominant phenotype (130, 134). This suggests that the left and right 4th PAA differ in their sensitivity to genetic perturbations and the left 4th is more resistant. This is observed at E10.5 when an abnormal right PAA is more frequent than an abnormal left. As this discrepancy is present at mid-embryogenesis, it cannot be due to a difference in the ability of the right and left 4th to recover during development. The right and left 4th PAA have asymmetric development programs, however differences in the frequency of defects are present when the PAA are still symmetrical (130). This suggests that the 4th PAA is affected by genetic deletions at multiple stages: prior to development, initiation of asymmetric remodelling and the remodelling process.

7.1.5 The cause of the 4th PAA defects in Gbx2$^{-/-}$ mice

This study and previously published data have observed defects to the development of the 4th PAA in *Gbx2*$^{-/-}$ mice (133, 166). Published studies showed that NCC migratory streams are fused in *Gbx2* homozygous mutants which consequently leads to reduced NCC in the 4th PA. The lack of NCC in the 4th PA is also observed in *Tbx1*$^{+/-}$ and *Pax9*$^{-/-}$ mutants which results in absent smooth muscle around the 4th PAA (134). Byrd and Meyers (2005) did not detect deficient smooth muscle formation around the 4th PAA in *Gbx2*$^{-/-}$ mice. However, the phenotype reported by Byrd and Meyers was less severe than observed in this study, possibly due to differences in the *Gbx2* mouse construct. Therefore *Gbx2*$^{-/-}$ mice within this current cohort should be collected at E10.5 to assess smooth muscle investment around the 4th PAA prior to remodelling. Embryos should be assessed at E11.5 to determine if there is a delay in smooth muscle differentiation, as reported in *Tbx1*$^{+/-}$ mice with the recovery of the 4th PAA (130).

In *Tbx1* and *Gbx2* mutants, the NCC defects occur with reduced expression of the Slit-Robo pathway, which is implicated in NCC migration (218). NCC have a central role in the formation of the PAA and are additionally required in the septation of the OFT as they invade the OFT cushions and initiate this process (27). *Tbx1*, *Pax9* and *Gbx2* mouse mutants all show defects to OFT alignment and septation. DORV was

frequently observed in *Pax9*$^{-/-}$ and *Gbx2*$^{-/-}$ mice. This study shows that the simultaneous deletion of *Pax9* and *Gbx2* in complex mutants resulted in CAT, a more severe OFT abnormality, also observed in *Tbx1*$^{-/-}$ mice (50). This suggests that *Pax9* and *Gbx2* function both independently and together in controlling NCC function. The presentation of CAT in *Pax9;Gbx2* complex mutants and *Tbx1*-null mice, but not *Pax9*$^{-/-}$, *Gbx2*$^{-/-}$ or *Tbx1*$^{+/-}$ mice indicates that the normal behaviour of NCC is affected by gene dosage. This study and the literature show that NCC are a target in the *Tbx1-Pax9-Gbx2* network. The disruption of NCC, either to their migration or differentiation, results in structural abnormalities in the OFT and 4th PAA which develop into cardiovascular defects in later development. Figure 7.1 shows the proposed *Tbx1-Pax9-Gbx2* genetic network during the morphogenesis of the 4th PAA.

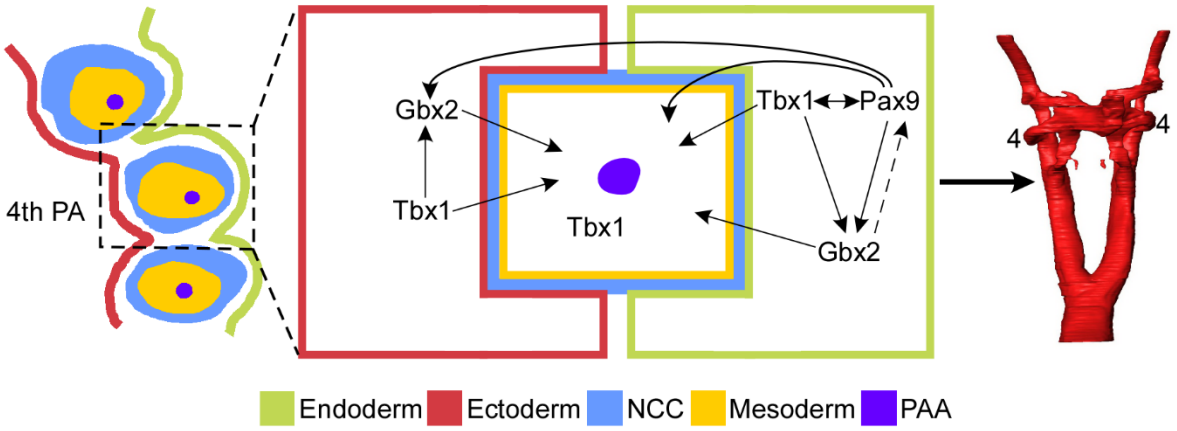

Figure 7.1. The proposed *Tbx1-Pax9-Gbx2* model in the morphogenesis of the 4th pharyngeal arch artery.

Tbx1, *Pax9* and *Gbx2* are all expressed within the pharyngeal endoderm of the PA and all independently influence the morphogenesis of the 4th PAA. *Tbx1* and *Pax9* interact cell-autonomously within the pharyngeal endoderm (134), where they function upstream of *Gbx2. Gbx2* appears to feedback to *Pax9* within this tissue. *Tbx1* and *Gbx2* expression within the pharyngeal ectoderm is also required in 4th PAA morphogenesis (132, 133). *Pax9* is able to signal to modulate *Gbx2* expression within the pharyngeal ectoderm. Abbreviations: NCC, neural crest cell; PA, pharyngeal arch; PAA pharyngeal arch artery.

7.2 Conclusion

The data presented in this thesis defined a cell-autonomous *Pax9-Gbx2* interaction within the pharyngeal endoderm during 4th PAA and cardiovascular development. This thesis effectively established the *Gbx2*-null phenotype at multiple stages of

development, identifying previously unreported defects. This work has investigated the specific interactions in the *Tbx1-Pax9-Gbx2* genetic network, suggesting that *Gbx2* is a shared downstream target of *Tbx1* and *Pax9*, and implicates *Gbx2* as a potential modifier of the 22q11DS phenotype.

Appendix

A. Phenotyping data for each genotype

The following tables provide the phenotyping data of each mutant mouse collected at E13.5-P0.

Abbreviations: cAoA, cervical aortic arch; CAT, common arterial trunk; CC, common carotid artery; CoRSA, cervical origin of the right subclavian artery; DORV, double outlet right ventricle; IAA, interrupted aortic arch; IRSA, isolated right subclavian artery; LCC, left common carotid artery; pCAT, partial common arterial trunk; RAA, right aortic arch; RAD, right arterial duct; RAI, right atrial isomerism; RCC, right common carotid artery; RE-LSA, retro-oesophageal left subclavian artery; RE-RSA, retro-oesophageal right subclavian artery; RPI, right pulmonary isomerism; TGA, transposition of the great arteries; VR, vascular ring; VSD, ventricular septal defect.

Table A.1. Phenotype of each *Gbx2*$^{-/-}$ mouse at E15.5.

Mouse number	Age	Phenotype
1	E15.5	-
2		RE-RSA, RAD, midline dorsal aorta, DORV, VSD, mesocardia, vestigial right thymus lobe
3		-
4		IRSA, DORV, VSD, mesocardia
5		RAA, RAD, RE-LSA, right dorsal aorta, DORV, VSD, mesocardia, mirror image aortic arch, RAI, RPI
6		RAA, RAD, right dorsal aorta, DORV, VSD, dextrocardia, mirror image aortic arch, RAI, RPI
7		RAA, RE-RSA, DORV, VSD, dextrocardia, RPI
8		-
9		-
10		RAA, RAD, RE-LSA, right dorsal aorta, mesocardia, mirror image aortic arch
11		DORV, VSD, RAI, exencephaly
12		RAD, VR, RE-LSA, right dorsal aorta, VSD, TGA, mesocardia, mirror image aortic arch, RAI, RPI
13		-
14		RAA, RAD, right dorsal aorta, mesocardia, mirror image aortic arch, RAI, RPI, cleft palate
15		RAA, RAD, right dorsal aorta, DORV, VSD, mesocardia, mirror image aortic arch, RAI, RPI
16		-
17		DORV, VSD
18		IRSA, DORV, VSD
19		RE-RSA, DORV, VSD
20		VR, RE-RSA, RAI, RPI, bilateral hypoplastic thymus
21		VSD, mesocardia
22		-
23		-
24		-
25		RAD, IRSA, midline dorsal aorta

Table A.2. Phenotype of each *Gbx2*$^{+/-}$;*Pax9*$^{+/-}$ mouse at E15.5 and P0.

Mouse number	Age	Phenotype
1	E15.5	-
2		-
3		-
4		-
5		-
6		-
7		RE-RSA
8		-
9		-
10		-
11		-
12		-
13		RAA, RE-RSA
14		-
15		-
16		-
17	P0	-
18		-
19		RAA, RE-RSA
20		IAA
21		-
22		RAA
23		IAA
24		-
25		-
26		-
27		-
28		-

Table A.3. Phenotype of each *Gbx2*$^{-/-}$;*Pax9*$^{+/-}$ mouse at E13.5-15.5 and P0.

Mouse number	Age	Phenotype
1	E13.5	IAA, CoRSA, absent RCC, DORV, VSD, vestigial and hypoplastic thymus
2		IAA, hypoplastic aorta, RAD RE-RSA, absent CC, pCAT, RPI, absent thymus
3		IAA, DORV, VSD, RAI, RPI, vestigial thymus
4		IAA, VR, IRSA, midline dorsal aorta, RAI, RPI, absent thymus
5		VR, IRSA, midline dorsal aorta, absent RCC, DORV, VSD, absent thymus
6	E15.5	RAA, RAD, RE-LSA, right dorsal aorta, DORV, VSD, mirror image aortic arch, hypoplastic and vestigial left thymus lobe
7		RAA, RE-RSA, VSD, absent left thymus lobe
8		DORV, VSD
9		RE-RSA, DORV, VSD
10		RAA, midline dorsal aorta, DORV, VSD
11		RAA, VSD, absent thymus
12		RAD, VR, RE-RSA, midline dorsal aorta, VSD, TGA, mesocardia, RAI, RPI
13		RE-RSA, absent right thymus lobe
14	P0	IAA, RE-RSA, absent LCC, absent thymus

Table A.4. Phenotype of each *Pax9*$^{-/-}$ mouse at E15.5 and P0.

Mouse number	Age	Phenotype
1	E15.5	IAA, hypoplastic aorta, RE-RSA, absent CC, VSD, absent thymus, cleft palate, pre-axial digit duplication
2		IAA, hypoplastic aorta, RE-RSA, absent CC, overriding aorta, VSD, absent thymus, cleft palate, pre-axial digit duplication
3		IAA, absent thymus, cleft palate, pre-axial digit duplication
4		IRSA, absent thymus, cleft palate, pre-axial digit duplication
5		IAA, hypoplastic aorta, RE-RSA, absent CC, DORV, VSD, absent thymus, cleft palate, pre-axial digit duplication
6		IAA, hypoplastic aorta, RE-RSA, absent CC, DORV, VSD, absent thymus, cleft palate, pre-axial digit duplication
7		IAA, hypoplastic aorta, absent CC, DORV, VSD, absent thymus, cleft palate, pre-axial digit duplication
8	P0	IAA, RE-RSA, absent thymus
9		IAA, RE-RSA, absent thymus

Table A.5. Phenotype of each *Pax9*$^{-/-}$;*Gbx2*$^{+/-}$ mouse at E15.5 and P0.

Mouse number	Age	Phenotype
1	E15.5	RAA, RE-RSA, DORV, VSD, absent thymus, cleft palate, pre-axial digit duplication
2		IAA, hypoplastic aorta, RE-RSA, absent CC, DORV, VSD, absent thymus, cleft palate, pre-axial digit duplication
3		IAA, hypoplastic aorta, RE-RSA, absent CC, DORV, VSD, absent thymus, cleft palate, pre-axial digit duplication
4		IAA, hypoplastic aorta, RE-RSA, absent CC, pCAT, VSD, absent thymus, cleft palate, pre-axial digit duplication
5		IAA, hypoplastic aorta, RE-RSA, absent CC, pCAT, VSD, mesocardia, absent thymus, cleft palate, pre-axial digit duplication
6		IAA, hypoplastic aorta, RE-RSA, absent CC, DORV, VSD, mesocardia, absent thymus, cleft palate, pre-axial digit duplication
7		IAA, hypoplastic aorta, absent CC, DORV, VSD, absent thymus, cleft palate, pre-axial digit duplication
8	P0	IAA, RE-RSA, absent thymus
9		IAA, RE-RSA, absent thymus

Table A.6. Phenotype of each *Pax9*$^{-/-}$;*Gbx2*$^{-/-}$ mouse at E15.5-P0.

Mouse number	Age	Phenotype
1	E15.5	CAT, IRSA, absent CC, AVSD, absent thymus, cleft palate, pre-axial digit duplication
2	P0	IAA, hypoplastic aorta, IRSA, absent thymus

Table A.7. Phenotype of each *Pax9Cre;Gbx2$^{f/f}$* mouse at E15.5.

Embryo number	Age	Phenotype
1	E15.5	-
2		-
3		RE-RSA
4		-
5		-
6		-
7		DORV, VSD
8		-
9		-
10		-
11		-
12		-
13		-
14		-
15		-
16		-

Table A.8. Phenotype of each *Pax9Cre;Gbx2$^{f/-}$* mouse at E15.5.

Embryo number	Age	Phenotype
1	E15.5	RAA, RE-RSA, absent LCC
2		-
3		-
4		RE-RSA
5		-
6		-
7		RE-RSA, ASD, common AV valve, mesocardia
8		-
9		-
10		-
11		-
12		-
13		-
14		-

Table A.9. Phenotype of each *Pax9Cre;Gbx2*$^{+/f}$ mouse at E15.5.

Embryo number	Age	Phenotype
1	E15.5	-
2		-
3		-
4		RAA, RAD, right dorsal aorta, DORV, VSD, mirror image aortic arch
5		-
6		-
7		-
8		-
9		-
10		-
11		-
12		-
13		-
14		-
15		-

Table A.10. Phenotype of each *Tbx1*$^{+/-}$ mouse at E15.5.

Embryos 4-21 were collected in previous datasets (Phillips et al., 2019).

Embryo number	Age	Phenotype
1	E15.5	RE-RSA
2		-
3		RE-RSA, VSD
4		-
5		cAoA, CoRSA
6		RE-RSA
7		RE-RSA
8		RE-RSA
9		RE-RSA
10		RE-RSA
11		CoRSA
12		IAA, CoRSA, VSD
13		RE-RSA
14		-
15		RE-RSA
16		-
17		-
18		-
19		-
20		cAoA, CoRSA
21		CoRSA

Table A.11. Phenotype of each *Tbx1*$^{+/-}$;*Gbx2*$^{+/-}$ mouse at E15.5.

Embryo number	Age	Phenotype
1	E15.5	VSD
2		RAA, RE-RSA
3		Hypoplastic thymus
4		IAA
5		VSD
6		-
7		-
8		-
9		RE-RSA, VSD
10		-

Table A.12. Phenotype of each *Tbx1*$^{+/-}$;*Pax9*$^{+/-}$ mouse at E15.5.

Embryos 4-24 were collected in previous datasets (Phillips et al., 2019).

Embryo number	Age	Phenotype
1	E15.5	IAA, CoRSA
2		VR, RE-RSA, absent thymus
3		IAA, hypoplastic aorta, hypoplastic thymus
4		RAA, VR, RE-RSA,
5		IAA, CoRSA
6		IAA, CoRSA
7		cAoA, CoRSA
8		IAA, RE-RSA
9		IAA, CoRSA, VSD
10		RE-RSA
11		cAoA, CoRSA
12		RE-RSA
13		IAA, RE-RSA
14		IAA, CoRSA
15		IAA, CoRSA, VSD
16		IAA, CoRSA, VSD
17		RE-RSA
18		IAA, CoRSA
19		IAA, CoRSA, VSD
20		IAA, RE-RSA, VSD
21		RAA, RE-RSA, absent thymus
22		cAoA, CoRSA
23		IAA, CoRSA
24		IAA, RE-RSA

Table A.13. Phenotype of each *Tbx1*$^{+/-}$;*Pax9*$^{+/-}$;*Gbx2*$^{+/-}$ mouse at E15.5.

Embryo number	Age	Phenotype
1	E15.5	IAA, VSD, hypoplastic thymus
2		CAoA, RE-RSA
3		CoRSA, VSD
4		RE-RSA
5		IAA, RE-RSA, VSD
6		IAA, RE-RSA
7		IAA
8		RAA, VR, RE-RSA

References

1. Andersen TA, Troelsen Kde L, Larsen LA. Of mice and men: molecular genetics of congenital heart disease. Cellular and molecular life sciences : CMLS. 2014;71(8):1327-52.
2. Mary ER. The Heart-Forming Areas of the Early Chick Blastoderm. Physiological Zoology. 1943;16(1):22-43.
3. Rosenquist GC. Location and movements of cardiogenic cells in the chick embryo: The heart-forming portion of the primitive streak. Developmental Biology. 1970;22(3):461-75.
4. Garcia-Martinez V, Schoenwolf GC. Primitive-streak origin of the cardiovascular system in avian embryos. Dev Biol. 1993;159(2):706-19.
5. Zaffran S, Kelly RG, Meilhac SM, Buckingham ME, Brown NA. Right ventricular myocardium derives from the anterior heart field. Circulation Research. 2004;95(3):261-8.
6. Kelly RG, Brown NA, Buckingham ME. The Arterial Pole of the Mouse Heart Forms from Fgf10-Expressing Cells in Pharyngeal Mesoderm. Developmental Cell. 2001;1(3):435-40.
7. Waldo KL, Kumiski DH, Wallis KT, Stadt HA, Hutson MR, Platt DH, et al. Conotruncal myocardium arises from a secondary heart field. Development. 2001;128(16):3179-88.
8. Christoffels VM, Habets PEMH, Franco D, Campione M, De Jong F, Lamers WH, et al. Chamber formation and morphogenesis in the developing mammalian heart. Developmental Biology. 2000;223(2):266-78.
9. Kaufman MH, Navaratnam V. Early differentiation of the heart in mouse embryos. Journal of Anatomy. 1981;133(2):235-46.
10. Eisenberg LM, Markwald RR. Molecular Regulation of Atrioventricular Valvuloseptal Morphogenesis. Circulation Research. 2005;77(1).
11. Kim JS, Virágh S, Moorman AFM, Anderson RH, Lamers WH. Development of the myocardium of the atrioventricular canal and the vestibular spine in the human heart. Circulation Research. 2001;88(4):395-402.
12. De Jong F, Virágh S, Moorman AFM. Cardiac development: A morphologically integrated molecular approach. Cardiology in the Young. 1997;7(2):131-46.
13. Van Den Hoff MJB, Moorman AFM, Ruijter JM, Lamers WH, Bennington RW, Markwald RR, et al. Myocardialization of the cardiac outflow tract. Developmental Biology. 1999;212(2):477-90.
14. Lamers WH, Viragh S, Wessels A, Moorman AF, Anderson RH. Formation of the tricuspid valve in the human heart. Circulation. 1995;91(1):111-21.
15. Komiyama M, Ito K, Shimada Y. Origin and development of the epicardium in the mouse embryo. Anat Embryol (Berl). 1987;176(2):183-9.
16. Dettman RW, Denetclaw Jr W, Ordahl CP, Bristow J. Common epicardial origin of coronary vascular smooth muscle, perivascular fibroblasts, and intermyocardial fibroblasts in the avian heart. Developmental Biology. 1998;193(2):169-81.
17. Sedmera D, McQuinn T. Embryogenesis of the heart muscle. Heart failure clinics. 2008;4(3):235-45.
18. Ben-Shachar G, Arcilla RA, Lucas RV, Manasek FJ. Ventricular trabeculations in the chick embryo heart and their contribution to ventricular and muscular septal development. Circulation Research. 1985;57(5):759-66.
19. Sedmera D, Pexieder T, Vuillemin M, Thompson RP, Anderson RH. Developmental patterning of the myocardium. The Anatomical record. 2000;258(4):319-37.

20. High FA, Epstein JA. The multifaceted role of Notch in cardiac development and disease. Nature Reviews Genetics. 2008;9(1):49-61.
21. Kirby ML, Turnage KL, 3rd, Hays BM. Characterization of conotruncal malformations following ablation of "cardiac" neural crest. The Anatomical record. 1985;213(1):87-93.
22. Lumsden A, Sprawson N, Graham A. Segmental origin and migration of neural crest cells in the hindbrain region of the chick embryo. Development. 1991;113(4):1281-91.
23. Waldo KL, Kumiski D, Kirby ML. Cardiac neural crest is essential for the persistence rather than the formation of an arch artery. Developmental dynamics : an official publication of the American Association of Anatomists. 1996;205(3):281-92.
24. Hutson MR, Kirby ML. Seminars in Cell and Developmental Biology Model Systems for

the Study of Heart Development and Disease Cardiac Neural Crest

and Conotruncal Malformations. Semin Cell Dev Biol. 2007;18(1):101-10.
25. Bockman DE, Kirby ML. Dependence of thymus development on derivatives of the neural crest. Science. 1984;223(4635):498-500.
26. Nakamura T, Colbert MC, Robbins J. Neural crest cells retain multipotential characteristics in the developing valves and label the cardiac conduction system. Circ Res. 2006;98(12):1547-54.
27. Kirby ML, Gale TF, Stewart DE. Neural crest cells contribute to normal aorticopulmonary septation. Science. 1983;220(4601):1059-61.
28. Nishibatake M, Kirby ML, Van Mierop LHS. Pathogenesis of persistent truncus arteriosus and dextroposed aorta in the chick embryo after neural crest ablation. Circulation. 1987;75(1):255-64.
29. Waldo KL, Hutson MR, Stadt HA, Zdanowicz M, Zdanowicz J, Kirby ML. Cardiac neural crest is necessary for normal addition of the myocardium to the arterial pole from the secondary heart field. Dev Biol. 2005;281(1):66-77.
30. Bajolle F, Zaffran S, Kelly RG, Hadchouel J, Bonnet D, Brown NA, et al. Rotation of the myocardial wall of the outflow tract is implicated in the normal positioning of the great arteries. Circulation Research. 2006;98(3):421-8.
31. Bamforth SD, Chaudhry B, Bennett M, Wilson R, Mohun TJ, Van Mierop LHS, et al. Clarification of the identity of the mammalian fifth pharyngeal arch artery. Clinical Anatomy. 2013;26(2):173-82.
32. Hiruma T, Nakajima Y. Development of pharyngeal arch arteries in early mouse embryo. Journal of Anatomy. 2002;201(1):15-29.
33. Molin DG, DeRuiter MC, Wisse LJ, Azhar M, Doetschman T, Poelmann RE, et al. Altered apoptosis pattern during pharyngeal arch artery remodelling is associated with aortic arch malformations in Tgfbeta2 knock-out mice. Cardiovasc Res. 2002;56(2):312-22.
34. Papangeli I, Scambler PJ. Tbx1 genetically interacts with the transforming growth factor-beta/bone morphogenetic protein inhibitor Smad7 during great vessel remodeling. Circ Res. 2013;112(1):90-102.
35. Bergwerff M, Verberne ME, DeRuiter MC, Poelmann RE, Gittenberger-de Groot AC. Neural crest cell contribution to the developing circulatory system: implications for vascular morphology? Circ Res. 1998;82(2):221-31.
36. Noden DM. Origins and assembly of avian embryonic blood vessels. Annals of the New York Academy of Sciences. 1990;588:236-49.
37. Anderson MJ, Pham VN, Vogel AM, Weinstein BM, Roman BL. Loss of unc45a precipitates arteriovenous shunting in the aortic arches. Dev Biol. 2008;318(2):258-67.

38. Coffin JD, Poole TJ. Embryonic vascular development: immunohistochemical identification of the origin and subsequent morphogenesis of the major vessel primordia in quail embryos. Development. 1988;102(4):735-48.
39. Congdon ED. Transformation of the aortic-arch system during the development of the human embryo1922.
40. Wang X, Chen D, Chen K, Jubran A, Ramirez A, Astrof S. Endothelium in the pharyngeal arches 3, 4 and 6 is derived from the second heart field. Developmental Biology. 2017;421(2):108-17.
41. Li P, Pashmforoush M, Sucov HM. Mesodermal retinoic acid signaling regulates endothelial cell coalescence in caudal pharyngeal arch artery vasculogenesis. Dev Biol. 2012;361(1):116-24.
42. Liang J, Song G, Li Q, Bian Z. Novel missense mutations in PAX9 causing oligodontia. Archives of Oral Biology. 2012;57(6):784-9.
43. Le Lievre CS, Le Douarin NM. Mesenchymal derivatives of the neural crest: analysis of chimaeric quail and chick embryos. Journal of embryology and experimental morphology. 1975;34(1):125-54.
44. Gordon J, Wilson VA, Blair NF, Sheridan J, Farley A, Wilson L, et al. Functional evidence for a single endodermal origin for the thymic epithelium. Nature Immunology. 2004;5(5):546-53.
45. Noden DM. The role of the neural crest in patterning of avian cranial skeletal, connective, and muscle tissues. Developmental Biology. 1983;96(1):144-65.
46. Veitch E, Begbie J, Schilling TF, Smith MM, Graham A. Pharyngeal arch patterning in the absence of neural crest. Current Biology. 1999;9(24):1481-4.
47. Graham A, Okabe M, Quinlan R. The role of the endoderm in the development and evolution of the pharyngeal arches. J Anat. 2005;207:479-87.
48. Haworth KE, Wilson JM, Grevellec A, Cobourne MT, Healy C, Helms JA, et al. Sonic hedgehog in the pharyngeal endoderm controls arch pattern via regulation of Fgf8 in head ectoderm. Dev Biol. 2007;303(1):244-58.
49. Piotrowski T, Nusslein-Volhard C. The Endoderm Plays an Important Role

in Patterning the Segmented Pharyngeal

Region in Zebrafish (Danio rerio). Developmental Biology. 2000;225:339-56.
50. Jerome LA, Papaioannou VE. DiGeorge syndrome phenotype in mice mutant for the T-box gene, Tbx1. Nature Genetics. 2001;27(3):286-91.
51. Jackson A, Kasah S, Mansour SL, Morrow B, Basson MA. Endoderm-specific deletion of Tbx1 reveals an FGF-independent role for Tbx1 in pharyngeal apparatus morphogenesis. Developmental dynamics : an official publication of the American Association of Anatomists. 2014;243(9):1143-51.
52. Arnold J, Werling U, Braunstein EM, Liao J, Nowotschin S. Inactivation of Tbx1 in the pharyngeal endoderm results in 22q11DS malformations. Development and Disease. 2006;133:977-87.
53. Vitelli F, Morishima M, Taddei I, Lindsay EA, Baldini A. Tbx1 mutation causes multiple cardiovascular defects and disrupts neural crest and cranial nerve migratory pathways. Human Molecular Genetics. 2002;11(8):915-22.
54. Trokovic N, Trokovic R, Mai P, Partanen J. Fgfr1 regulates patterning of the pharyngeal region. Genes Dev. 2003;17(1):141-53.
55. Walshe J, Mason I. Fgf signalling is required for formation of cartilage in the head. Dev Biol. 2003;264(2):522-36.
56. Vitelli F, Taddei I, Morishima M, Meyers EN, Lindsay EA, Baldini A. A genetic link between Tbx1 and fibroblast growth factor signaling. Development. 2002;129(19):4605-11.

57. High FA, Zhang M, Proweller A, Tu L, Parmacek MS, Pear WS, et al. An essential role for Notch in neural crest during cardiovascular development and smooth muscle differentiation. Journal of Clinical Investigation. 2007;117(2):353-63.
58. Itoh N, Ohta H, Nakayama Y, Konishi M. Roles of FGF Signals in Heart Development, Health, and Disease. Frontiers in cell and developmental biology. 2016;4:110.
59. Crossley PH, Martin GR. The mouse Fgf8 gene encodes a family of polypeptides and is expressed in regions that direct outgrowth and patterning in the developing embryo. Development. 1995;121(2):439-51.
60. Trumpp A, Depew MJ, Rubenstein JL, Bishop JM, Martin GR. Cre-mediated gene inactivation demonstrates that FGF8 is required for cell survival and patterning of the first branchial arch. Genes Dev. 1999;13(23):3136-48.
61. Abu-Issa R, Smyth G, Smoak I, Yamamura K, Meyers EN. Fgf8 is required for pharyngeal arch and cardiovascular development in the mouse. Development. 2002;129(19):4613-25.
62. Cesario JM, Malt AL, Jeong J. Developmental Genetics of the Pharyngeal Arch System. Colloquium Series on Developmental Biology. 2015;2(1):1-108.
63. Moore-Scott BA, Manley NR. Differential expression of Sonic hedgehog along the anterior-posterior axis regulates patterning of pharyngeal pouch endoderm and pharyngeal endoderm-derived organs. Dev Biol. 2005;278(2):323-35.
64. Chiang C, Litingtung Y, Lee E, Young KE, Corden JL, Westphal H, et al. Cyclopia and defective axial patterning in mice lacking Sonic hedgehog gene function. Nature. 1996;383(6599):407-13.
65. Washington Smoak I, Byrd NA, Abu-Issa R, Goddeeris MM, Anderson R, Morris J, et al. Sonic hedgehog is required for cardiac outflow tract and neural crest cell development. Dev Biol. 2005;283(2):357-72.
66. Delot EC, Bahamonde ME, Zhao M, Lyons KM. BMP signaling is required for septation of the outflow tract of the mammalian heart. Development. 2003;130(1):209-20.
67. Abdelwahid E, Rice D, Pelliniemi LJ, Jokinen E. Overlapping and differential localization of Bmp-2, Bmp-4, Msx-2 and apoptosis in the endocardial cushion and adjacent tissues of the developing mouse heart. Cell and tissue research. 2001;305(1):67-78.
68. Liu W, Selever J, Wang D, Lu MF, Moses KA, Schwartz RJ, et al. Bmp4 signaling is required for outflow-tract septation and branchial-arch artery remodeling. Proc Natl Acad Sci U S A. 2004;101(13):4489-94.
69. Sun Y, Teng I, Huo R, Rosenfeld MG, Olson LE, Li X, et al. Asymmetric requirement of surface epithelial beta-catenin during the upper and lower jaw development. Developmental dynamics : an official publication of the American Association of Anatomists. 2012;241(4):663-74.
70. Maretto S, Cordenonsi M, Dupont S, Braghetta P, Broccoli V, Hassan AB, et al. Mapping Wnt/beta-catenin signaling during mouse development and in colorectal tumors. Proc Natl Acad Sci U S A. 2003;100(6):3299-304.
71. Ikeya M, Lee SM, Johnson JE, McMahon AP, Takada S. Wnt signalling required for expansion of neural crest and CNS progenitors. Nature. 1997;389(6654):966-70.
72. Brault V, Moore R, Kutsch S, Ishibashi M, Rowitch DH, McMahon AP, et al. Inactivation of the beta-catenin gene by Wnt1-Cre-mediated deletion results in dramatic brain malformation and failure of craniofacial development. Development. 2001;128(8):1253-64.
73. Huh SH, Ornitz DM. Beta-catenin deficiency causes DiGeorge syndrome-like phenotypes through regulation of Tbx1. Development. 2010;137(7):1137-47.

74. Reller MD, Strickland MJ, Riehle-Colarusso T, Mahle WT, Correa A. Prevalence of congenital heart defects in metropolitan Atlanta, 1998-2005. The Journal of pediatrics. 2008;153(6):807-13.
75. Thom T, Haase N, Rosamond W, Howard VJ, Rumsfeld J, Manolio T, et al. Heart disease and stroke statistics--2006 update: a report from the American Heart Association Statistics Committee and Stroke Statistics Subcommittee. Circulation. 2006;113(6):e85-151.
76. Venables AW, Campbell PE. Double outlet right ventricle. A review of 16 cases with 10 necropsy specimens. British heart journal. 1966;28(4):461-71.
77. Unolt M, Putotto C, Silvestri LM, Marino D, Scarabotti A, Valerio M, et al. Transposition of great arteries: new insights into the pathogenesis. Frontiers in pediatrics. 2013;1:11.
78. Reardon MJ, Hallman GL, Cooley DA. Interrupted aortic arch: brief review and summary of an eighteen-year experience. Texas Heart Institute journal. 1984;11(3):250-9.
79. Hanneman K, Newman B, Chan F. Congenital Variants and Anomalies of the Aortic Arch. Radiographics : a review publication of the Radiological Society of North America, Inc. 2017;37(1):32-51.
80. Shuford WH, Sybers RG, Milledge RD, Brinsfield D. The cervical aortic arch. The American journal of roentgenology, radium therapy, and nuclear medicine. 1972;116(3):519-27.
81. Ezzeldin M, Youssef EW, Bansal V, Qurraie AS, Zaidat O. Cervical Origin of the Right Subclavian Artery with a Nonbifurcating Left Cervical Carotid Artery. Interventional neurology. 2018;7(6):399-402.
82. Scambler PJ. The 22q11 deletion syndromes. Human Molecular Genetics. 2000;9(16 REV. ISS.):2421-6.
83. Digilio M, Marino B, Capolino R, Dallapiccola B. Clinical manifestations of Deletion 22q11.2 syndrome (DiGeorge/Velo-Cardio-Facial syndrome). Images in paediatric cardiology. 2005;7(2):23-34.
84. Ryan AK, Goodship JA, Wilson DI, Philip N, Levy A, Seidel H, et al. Spectrum of clinical features associated with interstitial chromosome 22q11 deletions: A European collaborative study. Journal of Medical Genetics. 1997;34(10):798-804.
85. Unolt M, Versacci P, Anaclerio S, Lambiase C, Calcagni G, Trezzi M, et al. Congenital heart diseases and cardiovascular abnormalities in 22q11.2 deletion syndrome: From well-established knowledge to new frontiers. American journal of medical genetics Part A. 2018;176(10):2087-98.
86. Babaoglu K, Altun G, Binnetoglu K, Donmez M, Kayabey O, Anik Y. Crossed pulmonary arteries: a report on 20 cases with an emphasis on the clinical features and the genetic and cardiac abnormalities. Pediatric cardiology. 2013;34(8):1785-90.
87. Lee MY, Won HS, Baek JW, Cho JH, Shim JY, Lee PR, et al. Variety of prenatally diagnosed congenital heart disease in 22q11.2 deletion syndrome. Obstetrics & gynecology science. 2014;57(1):11-6.
88. Momma K, Ando M, Matsuoka R, Joo K. Interruption of the aortic arch associated with deletion of chromosome 22q11 is associated with a subarterial and doubly committed ventricular septal defect in Japanese patients. Cardiol Young. 1999;9(5):463-7.
89. Marino B, Digilio MC, Grazioli S, Formigari R, Mingarelli R, Giannotti A, et al. Associated cardiac anomalies in isolated and syndromic patients with tetralogy of Fallot. The American journal of cardiology. 1996;77(7):505-8.
90. Morrow B, Goldberg R, Carlson C, Das Gupta R, Sirotkin H, Collins J, et al. Molecular definition of the 22q11 deletions in velo-cardio-facial syndrome. American journal of human genetics. 1995;56(6):1391-403.

91. Morrow BE, McDonald-McGinn DM, Emanuel BS, Vermeesch JR, Scambler PJ. Molecular genetics of 22q11.2 deletion syndrome. American journal of medical genetics Part A. 2018;176(10):2070-81.
92. Motahari Z, Moody SA, Maynard TM, LaMantia AS. In the line-up: deleted genes associated with DiGeorge/22q11.2 deletion syndrome: are they all suspects? Journal of neurodevelopmental disorders. 2019;11(1):7.
93. Lindsay EA. Chromosomal microdeletions: Dissecting DEL22Q11 syndrome. Nature Reviews Genetics. 2001;2(11):858-68.
94. McDonald-McGinn DM, Sullivan KE, Marino B, Philip N, Swillen A, Vorstman JA, et al. 22q11.2 deletion syndrome. Nature reviews Disease primers. 2015;1:15071.
95. Sellier C, Hwang VJ, Dandekar R, Durbin-Johnson B, Charlet-Berguerand N, Ander BP, et al. Decreased DGCR8 expression and miRNA dysregulation in individuals with 22q11.2 deletion syndrome. PLoS One. 2014;9(8):e103884.
96. Guris DL, Fantes J, Tara D, Druker BJ, Imamoto A. Mice lacking the homologue of the human 22q11.2 gene CRKL phenocopy neurocristopathies of DiGeorge syndrome. Nat Genet. 2001;27(3):293-8.
97. Guris DL, Duester G, Papaioannou VE, Imamoto A. Dose-dependent interaction of Tbx1 and Crkl and locally aberrant RA signaling in a model of del22q11 syndrome. Dev Cell. 2006;10(1):81-92.
98. Lindsay EA, Vitelli F, Su H, Morishima M, Huynh T, Pramparo T, et al. Tbx1 haploinsufficiency in the DiGeorge syndrome region causes aortic arch defects in mice. Nature. 2001;410(6824):97-101.
99. Lindsay EA, Botta A, Jurecic V, Carattini-Rivera S, Cheah YC, Rosenblatt HM, et al. Congenital heart disease in mice deficient for the DiGeorge syndrome region. Nature. 1999;401(6751):379-83.
100. Merscher S, Funke B, Epstein JA, Heyer J, Puech A, Lu MM, et al. TBX1 is responsible for cardiovascular defects in velo-cardio-facial/DiGeorge syndrome. Cell. 2001;104(4):619-29.
101. Aggarwal VS, Morrow BE. Genetic modifiers of the physical malformations in velo-cardio-facial syndrome/DiGeorge syndrome. Developmental Disabilities Research Reviews. 2008;14(1):19-25.
102. Fliegauf M, Benzing T, Omran H. When cilia go bad: cilia defects and ciliopathies. Nature reviews Molecular cell biology. 2007;8(11):880-93.
103. Melchionda S, Digilio MC, Mingarelli R, Novelli G, Scambler P, Marino B, et al. Transposition of the great arteries associated with deletion of chromosome 22q11. The American journal of cardiology. 1995;75(1):95-8.
104. Rankin CT, Bunton T, Lawler AM, Lee SJ. Regulation of left-right patterning in mice by growth/differentiation factor-1. Nat Genet. 2000;24(3):262-5.
105. Brennan J, Norris DP, Robertson EJ. Nodal activity in the node governs left-right asymmetry. Genes Dev. 2002;16(18):2339-44.
106. Yasui H, Nakazawa M, Morishima M, Miyagawa-Tomita S, Momma K. Morphological observations on the pathogenetic process of transposition of the great arteries induced by retinoic acid in mice. Circulation. 1995;91(9):2478-86.
107. Nonaka S, Shiratori H, Saijoh Y, Hamada H. Determination of left-right patterning of the mouse embryo by artificial nodal flow. Nature. 2002;418(6893):96-9.
108. Okada Y, Nonaka S, Tanaka Y, Saijoh Y, Hamada H, Hirokawa N. Abnormal nodal flow precedes situs inversus in iv and inv mice. Molecular Cell. 1999;4(4):459-68.
109. Schweickert A, Campione M, Steinbeisser H, Blum M. Pitx2 isoforms: involvement of Pitx2c but not Pitx2a or Pitx2b in vertebrate left-right asymmetry. Mech Dev. 2000;90(1):41-51.

110. Shiratori H, Sakuma R, Watanabe M, Hashiguchi H, Mochida K, Sakai Y, et al. Two-step regulation of left-right asymmetric expression of Pitx2: initiation by nodal signaling and maintenance by Nkx2. Mol Cell. 2001;7(1):137-49.
111. Logan M, Pagan-Westphal SM, Smith DM, Paganessi L, Tabin CJ. The transcription factor Pitx2 mediates situs-specific morphogenesis in response to left-right asymmetric signals. Cell. 1998;94(3):307-17.
112. Shiratori H, Yashiro K, Shen MM, Hamada H. Conserved regulation and role of Pitx2 in situs-specific morphogenesis of visceral organs. Development. 2006;133(15):3015-25.
113. Liu C, Liu W, Palie J, Lu MF, Brown NA, Martin JF. Pitx2c patterns anterior myocardium and aortic arch vessels and is required for local cell movement into atrioventricular cushions. Development. 2002;129(21):5081-91.
114. Bamforth SD, Braganca J, Farthing CR, Schneider JE, Broadbent C, Michell AC, et al. Cited2 controls left-right patterning and heart development through a Nodal-Pitx2c pathway. Nat Genet. 2004;36(11):1189-96.
115. Purandare SM, Ware SM, Kwan KM, Gebbia M, Bassi MT, Deng JM, et al. A complex syndrome of left-right axis, central nervous system and axial skeleton defects in Zic3 mutant mice. Development. 2002;129(9):2293-302.
116. Komatsu Y, Kaartinen V, Mishina Y. Cell cycle arrest in node cells governs ciliogenesis at the node to break left-right symmetry. Development. 2011;138(18):3915-20.
117. Fujiwara T, Dehart DB, Sulik KK, Hogan BL. Distinct requirements for extra-embryonic and embryonic bone morphogenetic protein 4 in the formation of the node and primitive streak and coordination of left-right asymmetry in the mouse. Development. 2002;129(20):4685-96.
118. Raya A, Kawakami Y, Rodriguez-Esteban C, Buscher D, Koth CM, Itoh T, et al. Notch activity induces Nodal expression and mediates the establishment of left-right asymmetry in vertebrate embryos. Genes Dev. 2003;17(10):1213-8.
119. Shiratori H, Hamada H. The left-right axis in the mouse: from origin to morphology. Development. 2006;133(11):2095-104.
120. Bollag RJ, Siegfried Z, Cebra-Thomas JA, Garvey N, Davison EM, Silver LM. An ancient family of embryonically expressed mouse genes sharing a conserved protein motif with the T locus. Nature Genetics. 1994;7(3):383-9.
121. El Omari K, de Mesmaeker J, Karia D, Ginn H, Bhattacharya S, Mancini EJ. Structure of the DNA-bound T-box domain of human TBX1, a transcription factor associated with the DiGeorge syndrome. Proteins: Structure, Function and Bioinformatics. 2012;80(2):655-60.
122. Kispert A, Herrmann BG. The Brachyury gene encodes a novel DNA binding protein. EMBO Journal. 1993;12(8):3211-20.
123. Conlon FL, Fairclough L, Price BMJ, Casey ES, Smith JC. Determinants of T box protein specificity. Development. 2001;128(19):3749-58.
124. Castellanos R, Xie Q, Zheng D, Cvekl A, Morrow BE. Mammalian TBX1 preferentially binds and regulates downstream targets via a tandem T-site repeat. PLoS One. 2014;9(5):e95151.
125. Basson CT, Bachinsky DR, Lin RC, Levi T, Elkins JA, Soults J, et al. Mutations in human TBX5 [corrected] cause limb and cardiac malformation in Holt-Oram syndrome. Nat Genet. 1997;15(1):30-5.
126. Linden H, Williams R, King J, Blair E, Kini U. Ulnar Mammary syndrome and TBX3: expanding the phenotype. American journal of medical genetics Part A. 2009;149a(12):2809-12.

127. Liu C, Shen A, Li X, Jiao W, Zhang X, Li Z. T-box transcription factor TBX20 mutations in Chinese patients with congenital heart disease. European journal of medical genetics. 2008;51(6):580-7.
128. Chapman DL, Garvey N, Hancock S, Alexiou M, Agulnik SI, Gibson-Brown JJ, et al. Expression of the T-box family genes, Tbx1-Tbx5, during early mouse development. Developmental Dynamics. 1996;206(4):379-90.
129. Zhang Z, Cerrato F, Xu H, Vitelli F, Morishima M, Vincentz J, et al. Tbx1 expression in pharyngeal epithelia is necessary for pharyngeal arch artery development. Development. 2005;132(23):5307-15.
130. Lindsay EA, Baldini A. Recovery from arterial growth delay reduces penetrance of cardiovascular defects in mice deleted for the DiGeorge syndrome region. Human Molecular Genetics. 2001;10(9):997-1002.
131. Ryckebusch L, Bertrand N, Mesbah K, Bajolle F, Niederreither K, Kelly RG, et al. Decreased levels of embryonic retinoic acid synthesis accelerate recovery from arterial growth delay in a mouse model of DiGeorge syndrome. Circ Res. 2010;106(4):686-94.
132. Randall V, McCue K, Roberts C, Kyriakopoulou V, Beddow S, Barrett AN, et al. Great vessel development requires biallelic expression of Chd7 and Tbx1 in pharyngeal ectoderm in mice. J Clin Invest. 2009;119(11):3301-10.
133. Calmont A, Ivins S, Van Bueren KL, Papangeli I, Kyriakopoulou V, Andrews WD, et al. Tbx1 controls cardiac neural crest cell migration during arch artery development by regulating Gbx2 expression in thepharyngeal ectoderm. Development. 2009;136(18):3173-83.
134. Phillips HM, Stothard CA, Qureshi WMS, Kousa AI, Briones-Leon JA, Khasawneh RR, et al. Pax9 is required for cardiovascular development and interacts with Tbx1 in the pharyngeal endoderm to control 4(th) pharyngeal arch artery morphogenesis. Development. 2019.
135. Kochilas L, Merscher-Gomez S, Lu MM, Potluri V, Liao J, Kucherlapati R, et al. Role of neural crest during cardiac development in a mouse model of DiGeorge syndrome. Developmental Biology. 2002;251(1):157-66.
136. Taddei I, Morishima M, Huynh T, Lindsay EA. Genetic factors are major determinants of phenotypic variability in a mouse model of the DiGeorge/del22q11 syndromes. Proc Natl Acad Sci U S A. 2001;98(20):11428-31.
137. Ivins S, Van Beuren KL, Roberts C, James C, Lindsay E, Baldini A, et al. Microarray analysis detects differentially expressed genes in the pharyngeal region of mice lacking Tbx1. Developmental Biology. 2005;285(2):554-69.
138. Stapleton P, Weith A, Urbánek P, Kozmik Z, Busslinger M. Chromosomal localization of seven PAX genes and cloning of a novel family member, PAX-9. Nature Genetics. 1993;3(4):292-8.
139. Walther C, Guenet JL, Simon D, Deutsch U, Jostes B, Goulding MD, et al. Pax: A murine multigene family of paired box-containing genes. Genomics. 1991;11(2):424-34.
140. Bopp D, Burri M, Baumgartner S, Frigerio G, Noll M. Conservation of a large protein domain in the segmentation gene paired and in functionally related genes of Drosophila. Cell. 1986;47(6):1033-40.
141. Stuart ET, Kioussi C, Gruss P. Mammalian Pax genes. Annual review of genetics. 1994;28:219-36.
142. Wang Q, Fang WH, Krupinski J, Kumar S, Slevin M, Kumar P. Pax genes in embryogenesis and oncogenesis. Journal of cellular and molecular medicine. 2008;12(6a):2281-94.
143. Torres M, Gomez-Pardo E, Dressler GR, Gruss P. Pax-2 controls multiple steps of urogenital development. Development. 1995;121(12):4057-65.

144. Nishimoto K, Iijima K, Shirakawa T, Kitagawa K, Satomura K, Nakamura H, et al. PAX2 gene mutation in a family with isolated renal hypoplasia. Journal of the American Society of Nephrology : JASN. 2001;12(8):1769-72.
145. Chalepakis G, Goulding M, Read A, Strachan T, Gruss P. Molecular basis of splotch and Waardenburg Pax-3 mutations. Proc Natl Acad Sci U S A. 1994;91(9):3685-9.
146. Lalwani AK, Brister JR, Fex J, Grundfast KM, Ploplis B, San Agustin TB, et al. Further elucidation of the genomic structure of PAX3, and identification of two different point mutations within the PAX3 homeobox that cause Waardenburg syndrome type 1 in two families. American journal of human genetics. 1995;56(1):75-83.
147. Santen GWE, Sun Y, Gijsbers ACJ, Carré A, Holvoet M, van Haeringen A, et al. Further delineation of the phenotype of chromosome 14q13 deletions: (Positional) involvement of FOXG1 appears the main determinant of phenotype severity, with no evidence for a holoprosencephaly locus. Journal of Medical Genetics. 2012;49(6):366-72.
148. Schuffenhauer S, Leifheit HJ, Lichtner P, Peters H, Murken J, Emmerich P. De novo deletion (14)(q11.2q13) including PAX9: Clinical and molecular findings. Journal of Medical Genetics. 1999;36(3):233-6.
149. Bonczek O, Balcar VJ, Sery O. PAX9 gene mutations and tooth agenesis: A review. Clinical genetics. 2017;92(5):467-76.
150. Wallin J, Mizutani Y, Imai K, Myashita N, Moriwaki K, Taniquchi M, et al. A new Pax gene, Pax-9, maps to mouse chromosome 12. Mamm Genome. 1993;4(7):354-8.
151. Neubuser A, Koseki H, Balling R. Characterization and developmental expression of Pax9, a paired-box-containing gene related to Pax1. Developmental Biology. 1995;170(2):701-16.
152. Peters H, Neubüser A, Kratochwil K, Balling R. Pax9-deficient mice lack pharyngeal pouch derivatives and teeth and exhibit craniofacial and limb abnormalities. Genes and Development. 1998;12(17):2735-47.
153. Kist R, Greally E, Peters H. Derivation of a mouse model for conditional inactivation of Pax9. Genesis. 2007;45(7):460-4.
154. Kimura S, Hara Y, Pineau T, Fernandez-Salguero P, Fox CH, Ward JM, et al. The T/ebp null mouse: thyroid-specific enhancer-binding protein is essential for the organogenesis of the thyroid, lung, ventral forebrain, and pituitary. Genes Dev. 1996;10(1):60-9.
155. Pabst O, Rummelies J, Winter B, Arnold HH. Targeted disruption of the homeobox gene Nkx2.9 reveals a role in development of the spinal accessory nerve. Development. 2003;130(6):1193-202.
156. McGinnis W, Levine MS, Hafen E, Kuroiwa A, Gehring WJ. A conserved DNA sequence in homoeotic genes of the Drosophila Antennapedia and bithorax complexes. Nature. 1984;308(5958):428-33.
157. Gehring WJ, Qian YQ, Billeter M, Furukubo-Tokunaga K, Schier AF, Resendez-Perez D, et al. Homeodomain-DNA recognition. Cell. 1994;78(2):211-23.
158. Matsui T, Hirai M, Hirano M, Kurosawa Y. The HOX complex neighbored by the EVX gene, as well as two other homeobox-containing genes, the GBX-class and the EN-class, are located on the same chromosomes 2 and 7 in humans. FEBS Letters. 1993;336(1):107-10.
159. Waters ST, Wilson CP, Lewandoski M. Cloning and embryonic expression analysis of the mouse Gbx1 gene. Gene expression patterns : GEP. 2003;3(3):313-7.
160. Buckley DM, Burroughs-Garcia J, Lewandoski M, Waters ST. Characterization of the Gbx1-/- mouse mutant: a requirement for Gbx1 in normal locomotion and sensorimotor circuit development. PLoS One. 2013;8(2):e56214.

161. Meziane H, Fraulob V, Riet F, Krezel W, Selloum M, Geffarth M, et al. The homeodomain factor Gbx1 is required for locomotion and cell specification in the dorsal spinal cord. PeerJ. 2013;1:e142.
162. Heimbucher T, Murko C, Bajoghli B, Aghaallaei N, Huber A, Stebegg R, et al. Gbx2 and Otx2 interact with the WD40 domain of Groucho/Tle corepressors. Mol Cell Biol. 2007;27(1):340-51.
163. Bouillet P, Chazaud C, Oulad-Abdelghani M, Dolle P, Chambon P. Sequence and expression pattern of the Stra7 (Gbx-2) homeobox-containing gene induced by retinoic acid in P19 embryonal carcinoma cells. Developmental dynamics : an official publication of the American Association of Anatomists. 1995;204(4):372-82.
164. Chapman G, Remiszewski JL, Webb GC, Schulz TC, Bottema CDK, Rathjen PD. The mouse homeobox gene, Gbx2: Genomic organization and expression in pluripotent cells in vitro and in vivo. Genomics. 1997;46(2):223-33.
165. Wassarman KM, Lewandoski M, Campbell K, Joyner AL, Rubenstein JLR, Martinez S, et al. Specification of the anterior hindbrain and establishment of a normal mid/hindbrain organizer is dependent on Gbx2 gene function. Development. 1997;124(15):2923-34.
166. Byrd NA, Meyers EN. Loss of Gbx2 results in neural crest cell patterning and pharyngeal arch artery defects in the mouse embryo. Developmental Biology. 2005;284(1):233-45.
167. Caprio C, Baldini A. p53 suppression partially rescues the mutant phenotype in mouse models of DiGeorge syndrome. Proceedings of the National Academy of Sciences of the United States of America. 2014;111(37):13385-90.
168. Li JY, Lao Z, Joyner AL. Changing requirements for Gbx2 in development of the cerebellum and maintenance of the mid/hindbrain organizer. Neuron. 2002;36(1):31-43.
169. Srinivas S, Watanabe T, Lin C-S, William CM, Tanabe Y, Jessell TM, et al. Cre reporter strains produced by targeted insertion of EYFP and ECFP into the ROSA26 locus. BMC Developmental Biology. 2001;1(1):4.
170. Soriano P. Generalized lacZ expression with the ROSA26 Cre reporter strain. Nat Genet. 1999;21(1):70-1.
171. Bamforth SD, Schneider JE, Bhattacharya S. High-throughput analysis of mouse embryos by magnetic resonance imaging. Cold Spring Harbor Protocols. 2012;7(1):93-101.
172. Zweier C, Sticht H, Aydin-Yaylagul I, Campbell CE, Rauch A. Human TBX1 missense mutations cause gain of function resulting in the same phenotype as 22q11.2 deletions. American journal of human genetics. 2007;80(3):510-7.
173. Ogawa T, Kapadia H, Feng JQ, Raghow R, Peters H, D'Souza RN. Functional consequences of interactions between Pax9 and Msx1 genes in normal and abnormal tooth development. The Journal of biological chemistry. 2006;281(27):18363-9.
174. Boudjemline Y, Fermont L, Le Bidois J, Lyonnet S, Sidi D, Bonnet D. Prevalence of 22q11 deletion in fetuses with conotruncal cardiac defects: a 6-year prospective study. The Journal of pediatrics. 2001;138(4):520-4.
175. Haaning AM, Quinn ME, Ware SM. Heterotaxy-spectrum heart defects in Zic3 hypomorphic mice. Pediatric research. 2013;74(5):494-502.
176. Kitamura K, Miura H, Miyagawa-Tomita S, Yanazawa M, Katoh-Fukui Y, Suzuki R, et al. Mouse Pitx2 deficiency leads to anomalies of the ventral body wall, heart, extra- and periocular mesoderm and right pulmonary isomerism. Development. 1999;126(24):5749-58.
177. Haber MA, Iranmahboob A, Thomas C, Liu M, Najjar A, Zagzag D. ERG is a novel and reliable marker for endothelial cells in central nervous system tumors. Clinical neuropathology. 2015;34(3):117-27.

178. Zhang W, Behringer RR, Olson EN. Inactivation of the myogenic bHLH gene MRF4 results in up-regulation of myogenin and rib anomalies. Genes Dev. 1995;9(11):1388-99.
179. Braun T, Arnold HH. Inactivation of Myf-6 and Myf-5 genes in mice leads to alterations in skeletal muscle development. The EMBO journal. 1995;14(6):1176-86.
180. Patapoutian A, Yoon JK, Miner JH, Wang S, Stark K, Wold B. Disruption of the mouse MRF4 gene identifies multiple waves of myogenesis in the myotome. Development. 1995;121(10):3347-58.
181. Olson EN, Arnold HH, Rigby PW, Wold BJ. Know your neighbors: three phenotypes in null mutants of the myogenic bHLH gene MRF4. Cell. 1996;85(1):1-4.
182. Meyers EN, Lewandoski M, Martin GR. An Fgf8 mutant allelic series generated by Cre- and Flp-mediated recombination. Nat Genet. 1998;18(2):136-41.
183. Carmeliet P, Ferreira V, Breier G, Pollefeyt S, Kieckens L, Gertsenstein M, et al. Abnormal blood vessel development and lethality in embryos lacking a single VEGF allele. Nature. 1996;380(6573):435-9.
184. Jacks T, Shih TS, Schmitt EM, Bronson RT, Bernards A, Weinberg RA. Tumour predisposition in mice heterozygous for a targeted mutation in Nf1. Nat Genet. 1994;7(3):353-61.
185. Kist R, Watson M, Wang X, Cairns P, Miles C, Reid DJ, et al. Reduction of Pax9 gene dosage in an allelic series of mouse mutants causes hypodontia and oligodontia. Hum Mol Genet. 2005;14(23):3605-17.
186. Fujita M, Sakabe M, Ioka T, Watanabe Y, Kinugasa-Katayama Y, Tsuchihashi T, et al. Pharyngeal arch artery defects and lethal malformations of the aortic arch and its branches in mice deficient for the Hrt1/Hey1 transcription factor. Mechanisms of Development. 2016;139:65-73.
187. Tossell K, Kiecker C, Wizenmann A, Lang E, Irving C. Notch signalling stabilises boundary formation at the midbrain-hindbrain organiser. Development. 2011;138(17):3745-57.
188. Crump JG, Maves L, Lawson ND, Weinstein BM, Kimmel CB. An essential role for Fgfs in endodermal pouch formation influences later craniofacial skeletal patterning. Development. 2004;131(22):5703-16.
189. Yashiro K, Shiratori H, Hamada H. Haemodynamics determined by a genetic programme govern asymmetric development of the aortic arch. Nature. 2007;450(7167):285-8.
190. Guo T, McDonald-McGinn D, Blonska A, Shanske A, Bassett AS, Chow E, et al. Genotype and cardiovascular phenotype correlations with TBX1 in 1,022 velo-cardio-facial/DiGeorge/22q11.2 deletion syndrome patients. Human mutation. 2011;32(11):1278-89.
191. Lin Z, Cantos R, Patente M, Wu DK. Gbx2 is required for the morphogenesis of the mouse inner ear: a downstream candidate of hindbrain signaling. Development. 2005;132(10):2309-18.
192. Gabriel SB, Salomon R, Pelet A, Angrist M, Amiel J, Fornage M, et al. Segregation at three loci explains familial and population risk in Hirschsprung disease. Nat Genet. 2002;31(1):89-93.
193. Frank DU, Fotheringham LK, Brewer JA, Muglia LJ, Tristani-Firouzi M, Capecchi MR, et al. An Fgf8 mouse mutant phenocopies human 22q11 deletion syndrome. Development. 2002;129(19):4591-603.
194. Rosamond W, Flegal K, Friday G, Furie K, Go A, Greenlund K, et al. Heart disease and stroke statistics--2007 update: a report from the American Heart Association Statistics Committee and Stroke Statistics Subcommittee. Circulation. 2007;115(5):e69-171.

195. Parisot P, Mesbah K, Theveniau-Ruissy M, Kelly RG. Tbx1, subpulmonary myocardium and conotruncal congenital heart defects. Birth defects research Part A, Clinical and molecular teratology. 2011;91(6):477-84.
196. Vincent SD, Mayeuf-Louchart A, Watanabe Y, Brzezinski JAt, Miyagawa-Tomita S, Kelly RG, et al. Prdm1 functions in the mesoderm of the second heart field, where it interacts genetically with Tbx1, during outflow tract morphogenesis in the mouse embryo. Hum Mol Genet. 2014;23(19):5087-101.
197. Lin L, Cui L, Zhou W, Dufort D, Zhang X, Cai CL, et al. Beta-catenin directly regulates Islet1 expression in cardiovascular progenitors and is required for multiple aspects of cardiogenesis. Proc Natl Acad Sci U S A. 2007;104(22):9313-8.
198. Tian Y, Yuan L, Goss AM, Wang T, Yang J, Lepore JJ, et al. Characterization and in vivo pharmacological rescue of a Wnt2-Gata6 pathway required for cardiac inflow tract development. Dev Cell. 2010;18(2):275-87.
199. Cai CL, Liang X, Shi Y, Chu PH, Pfaff SL, Chen J, et al. Isl1 identifies a cardiac progenitor population that proliferates prior to differentiation and contributes a majority of cells to the heart. Dev Cell. 2003;5(6):877-89.
200. Engert S, Liao WP, Burtscher I, Lickert H. Sox17-2A-iCre: a knock-in mouse line expressing Cre recombinase in endoderm and vascular endothelial cells. Genesis. 2009;47(9):603-10.
201. Creyghton MP, Cheng AW, Welstead GG, Kooistra T, Carey BW, Steine EJ, et al. Histone H3K27ac separates active from poised enhancers and predicts developmental state. Proc Natl Acad Sci U S A. 2010;107(50):21931-6.
202. Local A, Huang H, Albuquerque CP, Singh N, Lee AY, Wang W, et al. Identification of H3K4me1-associated proteins at mammalian enhancers. Nat Genet. 2018;50(1):73-82.
203. Sharifi-Zarchi A, Gerovska D, Adachi K, Totonchi M, Pezeshk H, Taft RJ, et al. DNA methylation regulates discrimination of enhancers from promoters through a H3K4me1-H3K4me3 seesaw mechanism. BMC genomics. 2017;18(1):964.
204. Fulcoli FG, Franzese M, Liu X, Zhang Z, Angelini C, Baldini A. Rebalancing gene haploinsufficiency in vivo by targeting chromatin. Nature communications. 2016;7:11688.
205. Bulut-Karslioglu A, Perrera V, Scaranaro M, de la Rosa-Velazquez IA, van de Nobelen S, Shukeir N, et al. A transcription factor-based mechanism for mouse heterochromatin formation. Nature structural & molecular biology. 2012;19(10):1023-30.
206. Nicetto D, Zaret KS. Role of H3K9me3 heterochromatin in cell identity establishment and maintenance. Current opinion in genetics & development. 2019;55:1-10.
207. Yagi H, Furutani Y, Hamada H, Sasaki T, Asakawa S, Minoshima S, et al. Role of TBX1 in human del22q11.2 syndrome. Lancet. 2003;362(9393):1366-73.
208. Li C, Lan Y, Krumlauf R, Jiang R. Modulating Wnt Signaling Rescues Palate Morphogenesis in Pax9 Mutant Mice. Journal of dental research. 2017;96(11):1273-81.
209. Zhou J, Gao Y, Lan Y, Jia S, Jiang R. Pax9 regulates a molecular network involving Bmp4, Fgf10, Shh signaling and the Osr2 transcription factor to control palate morphogenesis. Development. 2013;140(23):4709-18.
210. Lan Y, Xu J, Jiang R. Cellular and Molecular Mechanisms of Palatogenesis. Current topics in developmental biology. 2015;115:59-84.
211. Bachiller D, Klingensmith J, Shneyder N, Tran U, Anderson R, Rossant J, et al. The role of chordin/Bmp signals in mammalian pharyngeal development and DiGeorge syndrome. Development. 2003;130(15):3567-78.

212. De Bellard ME, Rao Y, Bronner-Fraser M. Dual function of Slit2 in repulsion and enhanced migration of trunk, but not vagal, neural crest cells. The Journal of cell biology. 2003;162(2):269-79.
213. Roeseler DA, Sachdev S, Buckley DM, Joshi T, Wu DK, Xu D, et al. Elongation factor 1 alpha1 and genes associated with Usher syndromes are downstream targets of GBX2. PLoS One. 2012;7(11):e47366.
214. Losa M, Latorre V, Andrabi M, Ladam F, Sagerstrom C, Novoa A, et al. A tissue-specific, Gata6-driven transcriptional program instructs remodeling of the mature arterial tree. eLife. 2017;6.
215. Bergwerff M, DeRuiter MC, Hall S, Poelmann RE, Gittenberger-de Groot AC. Unique vascular morphology of the fourth aortic arches: possible implications for pathogenesis of type-B aortic arch interruption and anomalous right subclavian artery. Cardiovasc Res. 1999;44(1):185-96.
216. Esner M, Meilhac SM, Relaix F, Nicolas JF, Cossu G, Buckingham ME. Smooth muscle of the dorsal aorta shares a common clonal origin with skeletal muscle of the myotome. Development. 2006;133(4):737-49.
217. Topouzis S, Majesky MW. Smooth muscle lineage diversity in the chick embryo. Two types of aortic smooth muscle cell differ in growth and receptor-mediated transcriptional responses to transforming growth factor-beta. Dev Biol. 1996;178(2):430-45.
218. Jia L, Cheng L, Raper J. Slit/Robo signaling is necessary to confine early neural crest cells to the ventral migratory pathway in the trunk. Dev Biol. 2005;282(2):411-21.